# Diamond Regrowth in High Pressure High Temperature Sintered Polycrystalline Diamond and its Impact on Mechanical Performance

Tuoran Chen
St Catherine's College


University of Oxford
A thesis presented for the degree of

Doctor of Philosophy

MT 2023

# Abstract

Polycrystalline diamond (PCD) composite is an amazing ultra-hard material for cutting, drilling and machining. Its synthesis involves binder-catalysed diamond regrowth through high-pressure high-temperature (HPHT) liquid phase sintering. During sintering, individual diamond grains are connected by regrown diamond to form a continuous structure, strengthening the mechanical performance.

However, the fundamental sintering mechanisms are yet to be fully understood. This is for several reasons. Firstly, it is challenging to directly identify regrown diamond. Secondly, a comprehensive diamond regrowth mechanism is absent in the literature. Lastly, the impact of diamond regrowth on the mechanical performance of PCD materials remains unknown. This work aims to gain more knowledge in these three aspects.

By comparing the characterization results from reference and normal samples, criteria are established to identify regrown diamond by its characteristic crystal defects. A diamond grain is determined as a regrown grain if its GOS value, acquired from EBSD, is less than 1°. Based on the different nitrogen-vacancy ($NV_0$) CL intensities between regrown and old diamond, a distinct contour separating them is revealed by SEM-CL. CL emissions from nitrogen-vacancy-nitrogen (NVN or H3) centres occur exclusively in regrown diamond. TEM reveals the inhomogeneous distribution of dislocations, rich in old diamond and sparse in regrown diamond.

By studying microstructures of samples terminated at different stages of sintering, two mechanisms, the direct transformation of graphite to diamond and graphite-diamond dissolution-reprecipitation are confirmed as being predominant separately prior to the binder infiltration and prior to dwell stage of sintering. Through investigating the orientations and distributions of the graphite inside and outside of diamond grains and the enclosed binder particles, it is concluded that diamond graphitization, graphite dissolution and epitaxially redeposition of dissolved carbon atoms are the three key steps in the graphite-diamond dissolution-reprecipitation mechanism. A model

incorporating the change of microstructures and functions of binder during the dissolution-reprecipitation process is proposed.

Bent twins are identified as the characteristic microstructural features of regrown diamond from the direct transformation of graphite.

During the dwell, a third mechanism, the classical dissolution reprecipitation diamond regrowth occurs by spheroidization of the binder particles, regulated by the minimization of interfacial energy. Sphericity of binder particles serves as a parameter to indirectly describe diamond regrowth at this stage, with higher sphericity reflecting increased diamond-diamond connection.

By varying graphite content and dwell duration, four samples were prepared to investigate the relationships between diamond regrowth and wear resistance and transverse rupture strength (TRS). It is found that increasing the dwell by a factor of 10 improves the TRS by 7.6% and 5.7% for samples with and without graphite, while 5 wt% extra graphite leads to reduction of TRS by about 5%. The longer dwell is thought to increase the toughness and potentially decrease the size of the largest residual flaw to increase the TRS. The increase of the largest residual flaw due to a higher average grain size and increasing density of coarse grains is considered to be the explanation for the TRS reduction resulting from graphite additions. There was no effect of longer dwell time on wear resistance. However, wear resistance was reduced for samples with extra graphite. The possible reasons might again be related to the increase in average flaw size associated with the consequent increase in grain size.

# List of Abbreviations

AGG: Abnormally Grown Grain

AsB: A type of SEM image with the signal mostly from backscattered electrons

BF: Bright Field

BSE: Backscattered Electron

B-S Line: Berman-Simon Line

CDF: Centered Dark Field

CL: Cathodoluminescences

CIE: International Commission on Illumination

CVD: Chemical Vapor Deposition

DDC: diamond-diamond connectivity

DF: Dark Field

DLS: Dynamic Light Scattering

DP: Diffraction Pattern

EADGS: Estimated Average Diamond Grain Size

EBSD: Electron Backscatter Diffraction

ECCI: Electron Channelling Contrast Imaging

EDM: Electrical Discharge Machining.

EDX: Energy Dispersive X-ray (Spectroscopy)

EELS: Electron Energy Loss Spectroscopy

EM: Electron Microscope

EsB: A type of SEM image with the signal almost from backscattered electrons

FCC: Face Centred Cubic

FIB: Focussed Ion Beam

GIC: Global Innovation Centre of Element Six Ltd.

GOS: Grain Orientation Spread

HAADF: High-Angle Annular Dark-Field

HCP: Hexagonal Close Packed

HPHT: High Pressure High Temperature

HR: High Resolution

ICP-MS: Inductively Coupled Plasma Mass Spectroscopy

Inlens: A type of SEM image with the signal almost from secondary electrons

LAADF: Low-Angle Annular Dark-Field

$LN_2$: Liquid Nitrogen

PCA: Principal Component Analysis

PCD: Polycrystalline Diamond

PCDM: Polycrystalline Diamond Material – the focused composite material of study in this thesis.

PDC: Polycrystalline Diamond Compact or Polycrystalline Diamond Cutter – They are always used interchangeably in industry literature. But usually they mean the same thing, which is the cutter made of PCDM and the corresponding super hard alloy substrate.

SE: Secondary Electron

SE2: A type of SEM image with the signal from both secondary and backscattered electrons with a ratio of 1:1.

SEM: Scanning Electron Microscope

SPCD: The standard PCD sample defined in section 3.1.1

STEM: Scanning Transmission Electron Microscope

TEM: Transmission Electron Microscope

TRS: Transverse Rupture Strength

VBA: Vertical Borer Analysis

WSA: Wear Scar Area

XRD: X-ray Diffraction/Diffractometer

ZPL: Zero Phonon Line

# Table of Contents

# List of Abbreviations

AGG: Abnormally Grown Grain

AsB: A type of SEM image with the signal mostly from backscattered electrons

BF: Bright Field

BSE: Backscattered Electron

B-S Line: Berman-Simon Line

CDF: Centered Dark Field

CL: Cathodoluminescences

CIE: International Commission on Illumination

CVD: Chemical Vapor Deposition

DDC: diamond-diamond connectivity

DDR: Degree of Diamond Regrowth

DLS: Dynamic Light Scattering

DP: Diffraction Pattern

EADGS: Estimated Average Diamond Grain Size

EBSD: Electron Backscatter Diffraction

ECCI: Electron Channelling Contrast Imaging

EDM: Electrical Discharge Machining.

EDX: Energy Dispersive X-ray (Spectroscopy)

EELS: Electron Energy Loss Spectroscopy

EM: Electron Microscope

EsB: A type of SEM image with the signal almost from backscattered electrons

FCC: Face Centred Cubic

FIB: Focussed Ion Beam

GIC: Global Innovation Centre of Element Six Ltd.

GOS: Grain Orientation Spread

HAADF: High-Angle Annular Dark-Field

HCP: Hexagonal Close Packed

HPHT: High Pressure High Temperature

ICP-MS: Inductively Coupled Plasma Mass Spectroscopy

Inlens: A type of SEM image with the signal almost from secondary electrons

LAADF: Low-Angle Annular Dark-Field

$LN_2$: Liquid Nitrogen

PCA: Principal Component Analysis

PCD: Polycrystalline Diamond

PCDM: Polycrystalline Diamond Material – the focused composite material of study in this thesis.

PDC: Polycrystalline Diamond Compact or Polycrystalline Diamond Cutter – They are always used interchangeably in industry literature. But usually they mean the same thing.

SE: Secondary Electron

SE2: A type of SEM image with the signal from both secondary and backscattered electrons with a ratio of 1:1.

SEM: Scanning Electron Microscope

SPCD: The standard PCD sample defined in section 3.2.1

STEM: Scanning Transmission Electron Microscope

TEM: Transmission Electron Microscope

TRS: Transverse Rupture Strength

VBA: Vertical Borer Analysis

WSA: Wear Scar Area

XRD: X-ray Diffraction/Diffractometer

ZPL: Zero Phonon Line

# 1 Introduction

# Table of Contents



Polycrystalline diamond (PCD) material, defined as a continuous network of multiple diamond grains bonded together, accompanied by an interpenetrating network of transition metal and high carbon alloys, has found use in many industries, such as oil and gas, mining and construction, automobile and aerospace.

Compared to other cutting tool materials such as polycrystalline cubic boron carbide, Co-WC, SiC and single crystal diamond in figure 1.1, PCD material possesses the third best hardness (about 50-70 GPa)[1] and improved toughness (~ 7-9 $MPam^{0.5}$)[2,3] than single crystal diamond, which renders the superior wear resistance of PCD material, especially at high temperature[3,4]. Moreover, the chemical and bio inertness, bulk Young's modulus and thermal conductivity of PCD are higher than other non-diamond cutting tool materials[5].

Due to these extreme properties which give it great drilling efficiencies, PCD stands out as one of the best drilling tools, especially in the oil and gas industry. 65% of the footage was drilled by PCD material in this field and this portion of footage was projected to rise to 80% in 2016[3,6]. This market domination has made PCD material a significant contributor to the economics of oil and gas over the past 40 years.

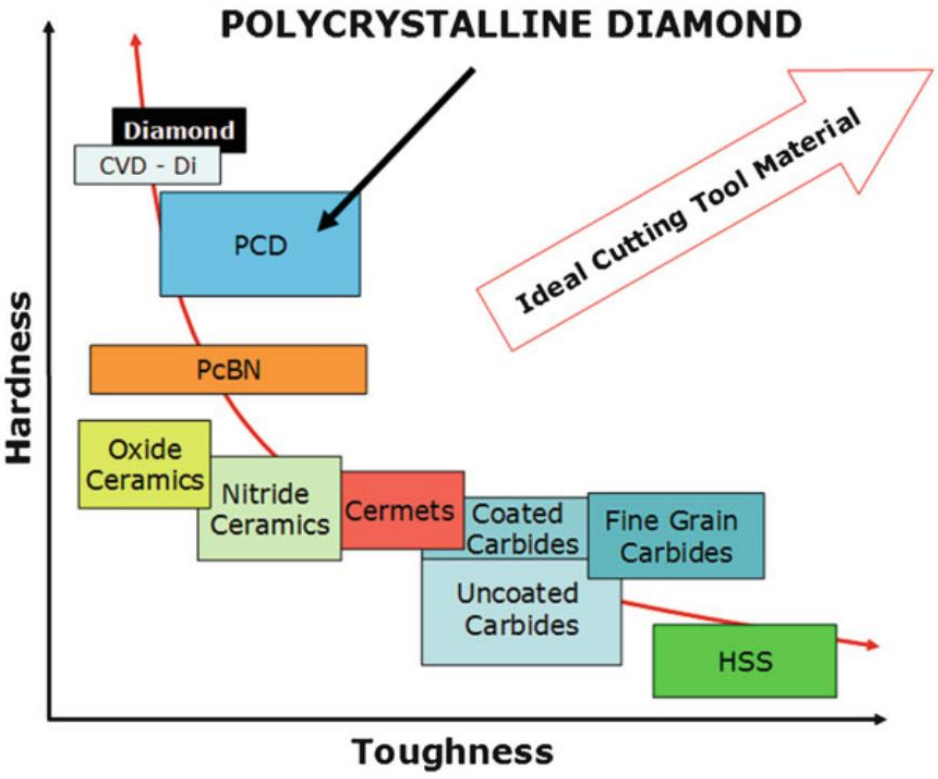


*Figure 1: the ideal cutting tool graph*[7].

PCD material is synthesized by the high pressure high temperature (HPHT) sintering of diamond powders and transition metal binders, which is a specific type of liquid phase sintering. This HPHT liquid phase sintering involves diamond regrowth, a process of partial diamond recrystallization. When entering into the HPHT diamond stable region in the carbon phase diagram, the metallic binder phase, which is usually liquid under these conditions, will catalyse the transformation of non-diamond carbon to diamond carbon by reducing the corresponding energy barrier. The most frequently used binders are transition metals, such as Ni, Fe, and Co or alloys derived from these elements.

After HPHT sintering, individual compacted diamond grains turn into a dense and continuous integral structure via the infiltration of a binder phase and more importantly, diamond regrowth. Although a denser diamond structure undoubtedly improves the overall mechanical properties of PCD materials, it is the connection between diamond grains after diamond regrowth that enables the utilization the astonishing hardness and strength of single crystal diamond, while avoiding the

weakness of its relatively poor toughness. By forming diamond-diamond bonding or connections during diamond regrowth, the microscopical whole grain fracture is averted and the wear resistance of PCD materials is improved. Furthermore, the connected diamond grains take advantage of their isotropic texture to avoid easy fracture along the cleavage plane, thus, to enhance the toughness of PCD materials[8,9]. Therefore, one of the most crucial factors influencing the mechanical properties of PCD materials is believed to be diamond regrowth, which predominantly governs the interconnections between diamonds.

However, in spite of its importance, diamond regrowth is still not well understood. There are three main questions regarding diamond regrowth:

1. What are the potentially unique microstructural features of regrown diamonds that can be utilized to establish a method for their characterization techniques?
2. What are the mechanisms of diamond regrowth during the HPHT sintering process?
3. What are the relationships between the diamond regrowth and the mechanical properties/performance of PCD materials?

It is claimed that the old diamond, diamond grit fed into the press before the HPHT sintering, experiences heavy plastic deformation during sintering, while the regrown diamond is supposedly almost defect free[10–12]. This is supported by the Transmission Electron Microscope (TEM) results from Walmsley *et al.*[6] and Westraadt *et al.*[13,14]. They demonstrated a large number of TEM images mainly showing the distinct difference in dislocation densities between old and regrown diamond. However, these results cannot address some questions. Firstly, they cannot exclude the possibility that an old diamond protected by its surrounding diamond networks would be only slightly plastically deformed, generating as few dislocations as in the regrown diamond. Secondly, there is a lack of evidence from a confirmed regrown diamond as a reference. And finally, TEM results only focus on a small region of sample, so cannot represent the prevalent microstructure features at a large scale. Daniel[15] noticed a difference in the density of diamond NV centres before and after the

plastic deformation. Further investigation was hindered however by the limitations of the cathodoluminescence (CL) technique available at that time.

There are many reported mechanisms to describe the diamond regrowth process, such as grain growth, the direct transformation from graphite to diamond, Ostwald ripening and the dissolution and reprecipitation mechanisms[16–19]. However, these proposed mechanisms have either provided incomplete evidence or lacked key evidence due to the limitations in characterization methods used in previous studies, making them insufficiently convincing.

In the end, since studying regrown diamond is generally very difficult, the challenges encountered in addressing the first two questions about further complicate attempts to answer the third one definitively, as the following examples demonstrate. Shul'zhenko *et al.*[20] reported an increase of strength and wear resistance in PCD materials with the addition graphite, attributing these benefits to the improved diamond regrowth. Akaishi[21] also linked the diamond regrowth to the wear resistance of PCD materials. Gigl[2] reasoned a decrease of transverse rupture strength (TRS) was linked to poor diamond regrowth, while Lima *et al.* [22] claimed a sufficient diamond regrowth is crucial for achieving high hardness. Unfortunately, none of the above-mentioned studies presented a method to assess the diamond-diamond connectivity (DDC), such as a parameter to qualitatively and/or quantitatively describe it.

## 1.1 Motivation for this work

By utilizing state-of-the-art characterization techniques, such as (S)TEM, SEM, EDX, CL, EELS, EBSD, FIB-SEM 3D tomography, ECCI, XRD, as well as routine methods like VBA, TRS testing, ICP-OES, this thesis aims to deepen the understanding of the diamond regrowth process and its influence on mechanical performance. Each chapter seeks to address the one of the three main questions described above through comprehensive analysis.

The fourth chapter focuses on investigating the microstructural features of regrown diamonds. It examines the microstructures of single crystal diamond grits and the abnormally grown grains (a known regrown diamond), comparing them with standardly sintered PCD materials and standardly sintered PCD materials with additional graphite. By identifying differences and similarities in crystal defects and microstructure between these materials, a method for accurately assessing regrown diamonds can be established.

The fifth chapter studies samples from different stages of sintering, such as cold compaction, hot compaction and during dwelling. By chronologically analysing the changes in phase, composition and microstructure of these PCD samples, the process of diamond regrowth can be deduced. Various potential mechanisms of diamond regrowth are discussed.

In the sixth chapter, samples with different amounts of graphite additions and different dwell time periods are compared to evaluate the DDC before and during dwell.

In the seventh chapter, mechanical performance is assessed through vertical borer analysis (VBA) and 3-point bend testing. These experimental results aim to establish a potential relationship between diamond regrowth and the mechanical performance of PCD materials.

This fundamental study endeavours to pave the way for the development of the next generation of PCD cutting tools of with lower cost, a broader range of applications and more environmentally friendly production methods.

## 1.2 Reference


(1) Li, Q.; Zhan, G.; Li, D.; He, D.; Moellendick, T. E.; Gooneratne, C. P.; Alalsayednassir, A. G. Ultrastrong Catalyst-Free Polycrystalline Diamond. *Sci. Rep.* **2020**, *10* (1), 1–10.

(2) Lammer, A. Mechanical Properties of Polycrystalline Diamonds. *Mater. Sci. Technol. (United Kingdom)* **1988**, *4* (11), 949–955.

(3) Scott, T. A. The Influence of Microstructure on the Mechanical Properties of Polycrystalline Diamond: A Literature Review*. *Adv. Appl. Ceram.* **2018**, *117* (3), 161–176.

(4) Childerhouse, T.; M'Saoubi, R.; Franca, L. F. P.; Crawforth, P.; Jackson, M. Machining Performance and Wear Behaviour of Polycrystalline Diamond and Coated Carbide Tools during Milling of Titanium Alloy Ti-54M. *Wear* **2023**, *523* (January).

(5) García-Marro, F.; Mestra, A.; Kanyanta, V.; Maweja, K.; Ozbayraktar, S.; Llanes, L. Contact Damage and Residual Strength in Polycrystalline Diamond (PCD). *Diam. Relat. Mater.* **2016**, *65*, 131–136.

(6) Bellin, F.; Dourfaye, A.; King, W.; Thigpen, M. The Current State of PDC Bit Technology. *World Oil* **2010**, *231* (11), 67–71.

(7) Kanyanta, V. *Microstructure-Property Correlations for Hard, Superhard, and Ultrahard Materials*; 2016.

(8) Telling, R. H.; Pickard, C. J.; Payne, M. C.; Field, J. E. Theoretical Strength and Cleavage of Diamond. *Phys. Rev. Lett.* **2000**, *84* (22), 5160–5163.

(9) Field, J. E.; Pickles, C. S. J. Strength, Fracture and Friction Properties of Diamond. *Diam. Relat. Mater.* **1996**, *5* (6–8), 625–634.

(10) Britun, V. F.; Oleynik, G. S.; Semenenko, N. P. Deformation Processes during High-Pressure Sintering of the Diamond Powders Produced by Catalytic Synthesis. *J. Mater. Sci.* **1992**, *27*

(16), 4472–4476.

(11) Walmsley, J. C.; Lang, A. R. *Transmission Electron Microscopic Observations of Deformation and Microtwinning in a Synthetic Diamond Compact*; 1983; Vol. 2.

(12) Yu, X.; Raterron, P.; Zhang, J.; Lin, Z.; Wang, L.; Zhao, Y. Constitutive Law and Flow Mechanism in Diamond Deformation. *Sci. Rep.* **2012**, *2*, 1–7.

(13) Walmsley, J. C.; Lang, A. R. Characteristics of Diamond Regrowth in a Synthetic Diamond Compact. *J. Mater. Sci.* **1988**, *23* (5), 1829–1834.

(14) Westraadt, J. E.; Dubrovinskaia, N.; Neethling, J. H.; Sigalas, I. Thermally Stable Polycrystalline Diamond Sintered with Calcium Carbonate. *Diam. Relat. Mater.* **2007**, *16* (11), 1929–1935.

(15) Daniel, R. D. The Influence of Nitrogen on the Plasticity of Diamond, University of Hull, 2000.

(16) Park, J. K.; Akaishi, M.; Yamaoka, S.; Fukunaga, O.; Eun, K. Y.; Yoon, D. N. Formation of Bridges between Diamond Particles during Sintering in Molten Cobalt Matrix. *J. Mater. Sci.* **1992**, *27* (17), 4695–4697.

(17) Luo, K.; Liu, B.; Hu, W.; Dong, X.; Wang, Y.; Huang, Q.; Gao, Y.; Sun, L.; Zhao, Z.; Wu, Y.; et al. Coherent Interfaces Govern Direct Transformation from Graphite to Diamond. *Nature* **2022**, *607* (7919), 486–491.

(18) Uehara, K.; Yamaya, S. High Pressure Sintering of Diamond by Cobalt Infiltration. *Int. J. Refract. Met. Hard Mater.* **1988**, *7* (4), 219–223.

(19) German, R. M. Sintering Window and Sintering Mechanism for Diamond. *Int. J. Refract. Met. Hard Mater.* **2023**, *117*, 151–160.

(20) Shul'zhenko, A. A.; Jaworska, L.; Sokolov, A. N.; Gargin, V. G.; Petasyuk, G. A.; Belyavina, N. N.; Zakora, A. P.; Suprun, M. V.; Tkach, V. N. Novel Wear-Resistant Superhard Diamond Composite Polycrystalline Material. *J. Superhard Mater.* **2018**, *40* (1), 1–7.

(21) Akaishi, M.; Ohsawa, T.; Yamaoka, S. Synthesis of Fine-Grained Polycrystalline Diamond Compact and Its Microstructure. *J. Am. Ceram. Soc.* **1991**, *74* (1), 5–10.

(22) Lima, F. T. C.; Bobrovnitchii, G. S.; Filgueira, M. Study of the Diamond 5%wt- Cobalt Sintering under the HPHT Lowest Limit. *Mater. Sci. Forum* **2005**, *498–499*, 225–230.

# 2 The Study of Diamond Regrowth During HPHT Sintering in Polycrystalline Diamond (PCD) Materials

## Table of Contents

## 2.1 Identifying the Regrown Diamond

There are two types of diamond in the PCD materials after HPHT liquid phase sintering. The first type is commonly referred to by industries as “old diamond” whose crystal structure is maintained as diamond crystal through the entire sintering process. The second type is known as “regrown diamond”, also referred as “new diamond” or “newly formed diamond”[1]. The carbon atoms in this type of diamond experience a transformation, from a non-diamond structure, amorphous carbon or even dissolved carbon atoms at some point during the HPHT sintering to a diamond crystal structure, then existing in this form until the end of the process. In terms of chemical bonding, if ignoring impurities and various defects in diamond, the carbon atoms of old diamond keep their four $sp^3$ bonds from the beginning to the end of HPHT sintering, while the carbon atoms of new diamond undergo a $sp^3$ hybridisation at some point during sintering and then maintain their four σ bonds till the end. Because both old and regrown diamond have identical crystal structures and chemical bonds after HPHT sintering, it is technically challenging to identify the regrown diamond in PCD materials. And if the diamond regrowth is epitaxial, this identification becomes further complicated as the regrown diamond could form either a whole diamond grain or be merely a part of a diamond grain.

One difference between these two types of diamond is from their morphologies. It is claimed from academia and industry that the regrown diamond exhibits different morphologies compared to those of old diamond. These morphology differences are categorized as being crystal defect differences, such as different types of defects and crystallinity, or microstructural morphology differences, such as a difference in the shape of diamond[2], diamond grain size or the existence of a second phase.

### 2.1.1 The Microstructural Difference Between Regrown and Old Diamonds

There is a limited amount of research available regarding the microstructural differences between regrown and old diamond. In term of the shape of diamond, one study conducted by Park *et al*.[2] focused on intentionally varying the sintering time to form bridges between diamond grains. These recognizable bridges are protrusions from one diamond grain to connecting to the adjacent one. An example of a bridge is shown in figure 2.1 below.

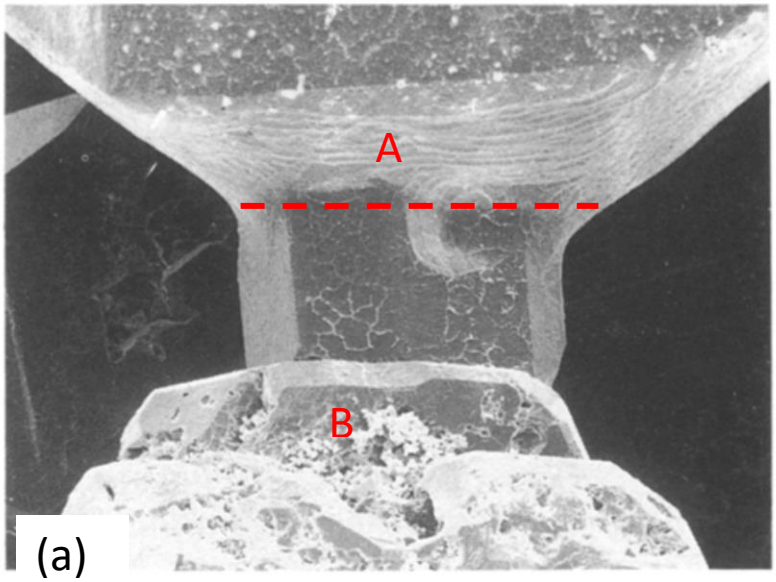
A
B
(a)

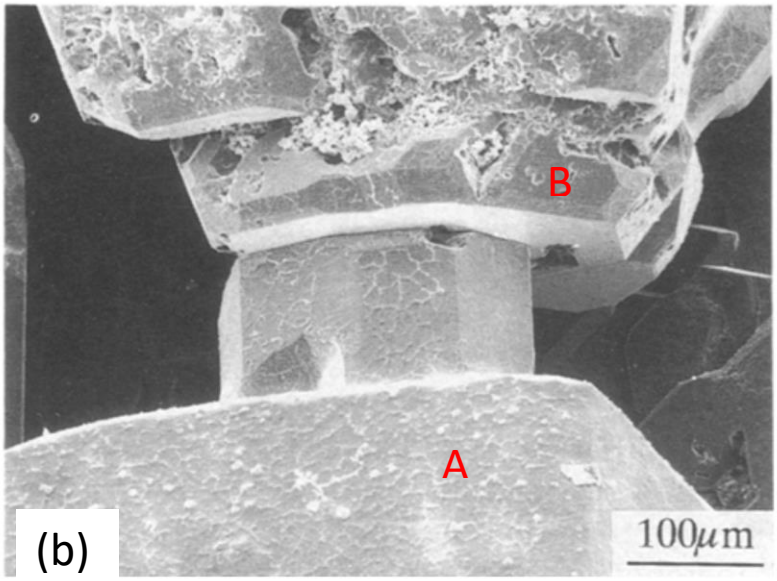
B
A
(b)
100μm

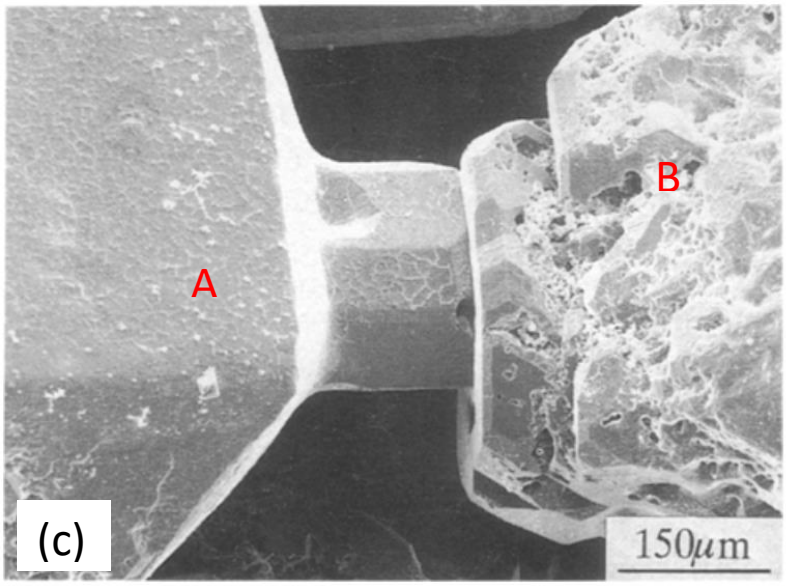
B
A
(c)
150μm

*Figure 2.1: SEM image of a diamond bridge after long time sintering by Park et al. a) front view b) back view. c) side view.*

However, it is challenging to accurately identify the interface between regrown and old diamond to study the mechanism of diamond regrowth. An imaginary section along the red dashed line in figure 2.1 can be approximately referred to as the interface separating the regrown and old diamond. Alongside the diamond protrusions, another distinctive feature is the disparity of diamond facets. The facets of diamond grain A are relatively flat and smooth, whereas those of grain B appear porous, rough and contain pits and cavities. Park *et al*.[2] attribute this porous morphology to the dissolution of diamond during the HPHT sintering but did not elaborate with further explanation. A possible explanation provided by the present author might be the uneven distribution of the vertically uniaxial pressure generated by the belt type press during sintering[3,4]. The pressure on grain A is above the Berman-Simon line and the diamond regrowth occurs at the contact point between A and B, growing toward B. In contrast, the dissolution occurred randomly on grain B without specific preferential locations, due to some local pressures being below the Berman-Simon line.

A special type of diamond grain emerging during HPHT sintering is the abnormally grown grain (AGG), as the most recognizable regrown diamond, simply because of its several times larger size compared to that of a normal grain[5]. The AGG also exhibits facets and residual binder phases which will be discussed later[5,6]. Consequently, as identifiable regrown diamond, the AGG serves as a useful reference for comparing the microstructure difference between regrown and old diamond. One potential danger is that the regrowth mechanisms of the normal regrown diamond and abnormal grown growth might be different, resulting in different microstructures.

Regarding the secondary phases, both Minnaar *et al*.[7] and Walmsley & Lang[1] discovered Co inclusions and residual graphite enclosed within the diamond host after HPHT sintering. The Co inclusions were found to have the same orientation as its diamond host, while the graphite was randomly oriented[1]. One interesting observation that warrants attention, though not explicitly mentioned, is that these binder inclusions are generally in a spherical morphology, whereas the

phase boundary actually consists of multiple short-length low-angle facets. As aforementioned, the binder phases were also detected in abnormally grown grains in a wide range of sizes[5].

### 2.1.2 The Crystal Defect Difference Between Regrown and Old Diamonds

Crystal defects like dislocations, micro twins, stacking faults and certain colour centres are introduced to the old diamond due to the plastic deformation during the hot compaction and perhaps the initial stage of sintering. This will be discussed in detail in section 2.2.3.

The regrown diamond, nevertheless, is supposed to have fewer of these defects or even to be defect free. During the regrowth, the temperature and the stress field inside the press remain stable and thermodynamically favourable for diamond regrowth. Therefore, a difference in defect density between regrown and old diamond is anticipated.

#### 2.1.2.1 Study of the Microstructure by TEM

A different dislocation density is examined electron-microscopically from various studies. Walmsley & Lang[8] were the first to notice distinct dislocation densities in different regions of HPHT sintered PCD grains. They later reported that the epitaxially regrown diamond on the original old diamond grains showed a lower dislocation density compared to the original diamond grain in a HPHT sintered sample[1]. However, they cannot entirely exclude the possibility that a small number of old diamond grains may contain a low dislocation density after less plastic deformation due to the heterogeneous stress field surrounding them. This uncertainty poses challenges in merely relying on the relative dislocation density to identify the regrown diamond.

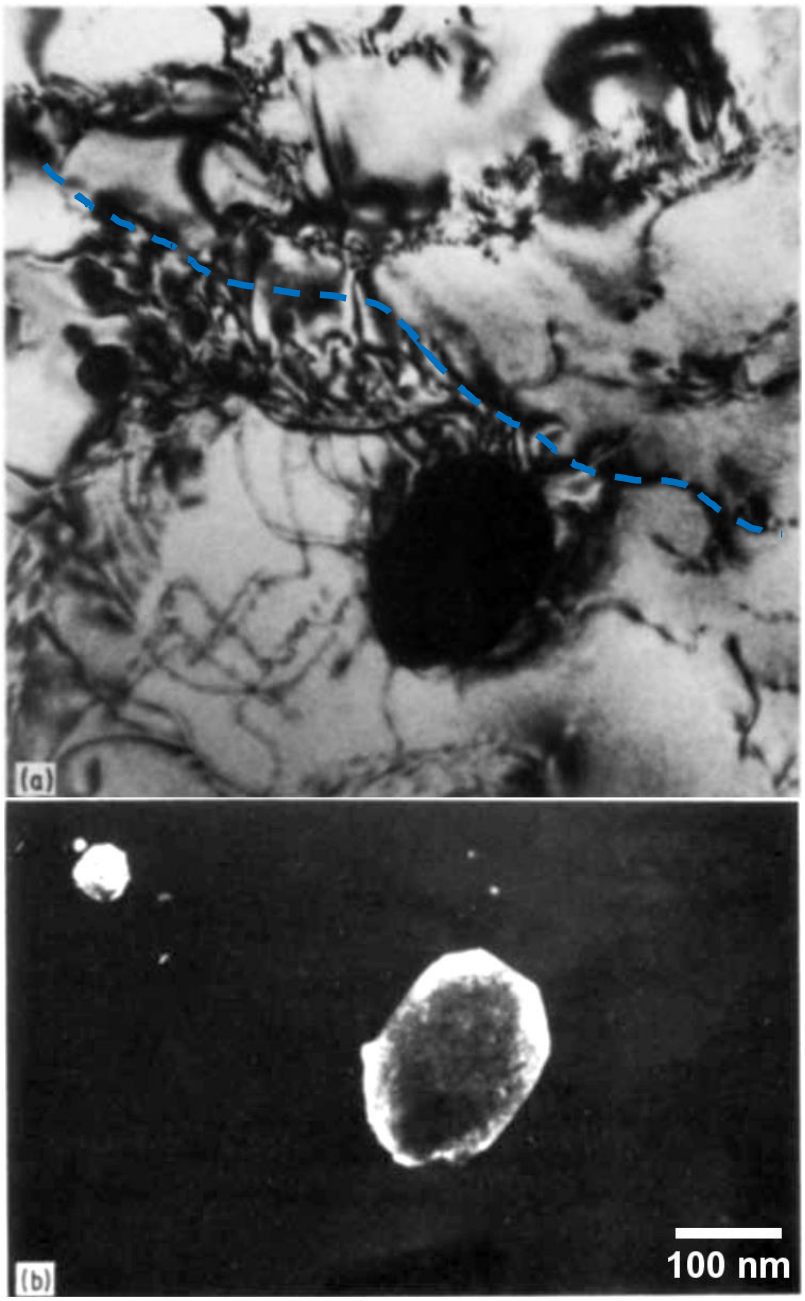


*Figure 2.2: the a) BF and b) DF TEM images showing a regrown diamond enclosing some binder particles. The [002] zone axis is aligned with the electron beam. In a), the 220 reflection is chosen as a two-beam condition to illustrate dislocations (thin dark lines). Note that some dark contrast at the top of image could arise from local strain like bending contours. In b), the 200 reflection is selected as another two-beam condition to exhibit the diffraction contrast of binder particles. Notably, both the binder particles and this diamond grain share the same orientation.*

In these less deformed diamond grains, as seen in figure 2.2 a), they claimed that sporadic dislocations may be formed at binder inclusions (relative positions shown in figure 2.2 b)) where the regrowth happens, and then grow along the diamond regrowth direction. However, this dislocation formation mechanism can be disputed. Firstly, dislocations can originate from the plastic deformation resulting from diamond point-to-point contact during the hot compaction when the

liquid binder has not yet infiltrated. During liquid binder infiltration, they evenly redistribute the stress within PCD skeleton. Diamond grains are more likely under the hydraulic stress to compress the volume rather than the deviatoric stress to change the shape of its grain via slip and rotation. Secondly, even if the dislocation formation is somehow related to the binder, the distribution of dislocations should be homogeneous around binder pools, which is not the case in figure 2.2 a) where only the right big binder particle is partially surrounded by dislocations in the bright field TEM image. One could argue there is the presence of large thermal stress between the binder and diamond during cooling, but that would lead to cracking rather than slipping if the stress were large enough. Another possible explanation of these dislocations is that they might have originated from the old diamond during hot compaction and migrated towards regrown diamond until trapped by binders during dwelling.

Another noteworthy microstructural feature claimed by them is the presence of low-angle boundary resulting from misorientation between the regrown and old diamond, as indicated by the blue dashed line in the BF TEM image. The regrown diamond is situated in the upper part of the image, clearly separated from this boundary. However, when considering the relative dislocation density, it becomes challenging to identify the regrown diamond at the right side of the big binder particle below or above the low-angle boundary since there is little difference in the dislocation density; This contradicts their conclusion, which suggests a clear dislocation density difference between the regrown and old diamond.

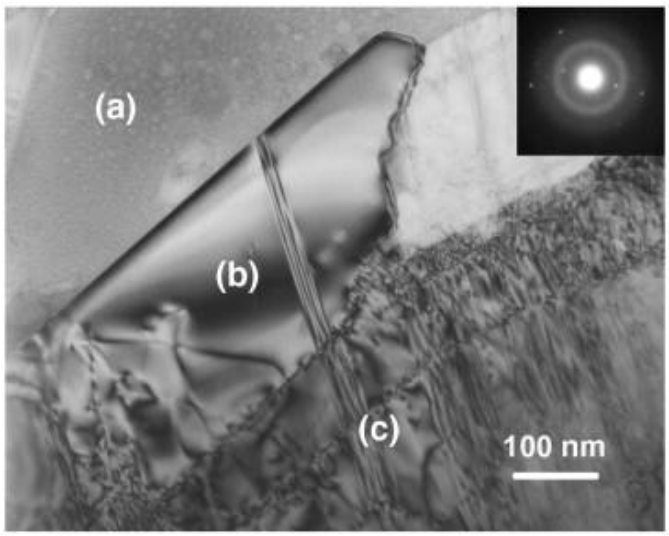


*Figure 2.3: the bright field TEM image of a diamond-binder interface. (a) the partly amorphous binder, (b) the regrown diamond rim, (c) the deformed old diamond.*[9]

Westraadt *et al*. [9] re-evaluated this dislocation density difference in the HPHT sintered PCD materials catalysed by a different binder. Their findings further supported that the regrown diamond has less dislocations, which are claimed to grow from the old diamond grain. However, upon examining the TEM image in figure 2.3 below, two notable features are focused on. Firstly, the obvious broad straight strip from (c) to (b) looks like a twin in terms of its width and its periodic contrast. Secondly, there is a dense network of dislocations present in the lower left region at the left bottom region of (b), while only minimal dislocations are observed adjacent to the scale bar in region (c).

Unfortunately, these comparisons are based on the regional relative difference in dislocation density. None provided a quantitative judgement of dislocation density to identify the regrown diamond.

Deformation twins may play a similar, but opposite, role in identifying the regrown diamond. Twinning is one of the fundamental modes of diamond plastic deformation and is prevalent in PCD materials[11]. In diamond crystal structure, there are two common types of twins, the 60° <111> twin and the 70.5° <110> twin[12]. Their details are listed in table 2.1 below.

| Rotation angle | Rotation axis | Twin plane | Type |
|---|---|---|---|
| 60° | <111> | {111} | Growth or deformation twins |
| 70.5° | <110> | {111} | Mostly deformation twin |

*Table 2.1: Rotation angles, rotation axes and twin planes of the most two common twins in diamond crystal.*

In the case of the 70.5° <110> twin, its formation involves the dissociation of a perfect dislocation to a sessile Frank <111> partial dislocation and a glissile Shockley <112> partial dislocation, subsequent to the slip of this Shockley partial dislocation on {111} planes[11,13]. This twin is identifiable by its typical moiré fringes in the bright and dark field images, along with faint twin diffracted spots in the diffraction pattern with either set of {111} planes as its symmetric plane pattern[8,14].

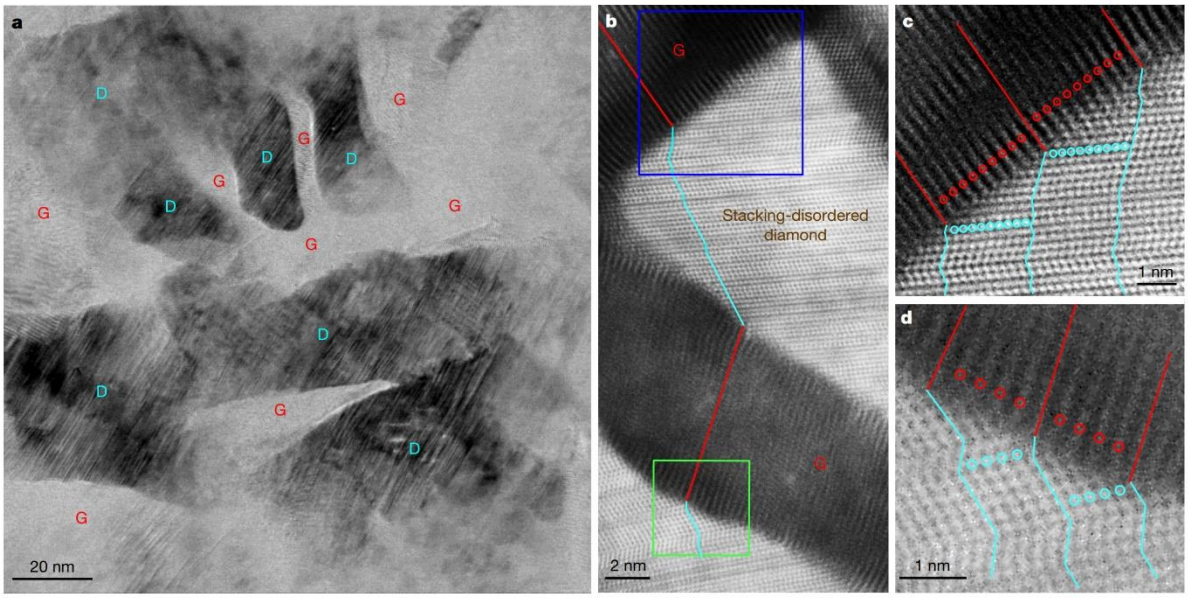


*Figure 2.4: the microstructure of nano diamond after binderless sintering at 15GPa, 1200 °C. a) the STEM BF image. G is graphite and D is diamond. b) the HRs image of the interface between the diamond and graphite. c) enlargement of the blue area in b). The stacking faults are pointed by cyan lines. d) enlargement of the green area in b). The stacking faults are pointed by cyan lines[15].*

Luo *et al.*[15] reported the synthesis of diamond through the binderless direct transformation of graphite. Under more than 15 GPa and with the temperature exceeding 1200 °C, the binderless direct transformation from graphite to diamond is achievable. However, the resultant diamond is stacking disordered. In the BF STEM image in figure 2.4 a), there are numerous bent strips manifesting in white contrast in the black diamond domain. In the high resolution (HRs) images b) and c), the stacking disorder in diamond is labelled in cyan. Luo *et al.*[15] attributed these bent stacking

faults or disorder to the significant external pressure during the direct graphite-to-diamond transformation, which is discussed further in section 2.2.3.3.

An interesting feature that Luo *et al.*[15] didn't mention is that the angles between these faults are approximately around 141°, which is a characteristic of the 70.5° <110> twin (141° is equal to a 70.5° rotation around a <110> axis plus the 70.5° between two sets of {111} planes in that (110) vertical plane). In diamond, 70.5° <110> twins appear as straight strips pointing in the same orientation in <110> zone axis TEM images[8], similar to the stripes observed in figure 2.4 a). Therefore, it is suggested that the stacking faults found in Luo's study are 70.5° <110> twins with some degree of bending due to the considerable external pressure during the binderless graphite-to-diamond transformation. Consequently, contrary to the relatively low dislocation density observed in HPHT sintered regrown diamond, there would be massive bent 70.5° <110> twins in the regrown diamond resulting from the binderless direct transformation of graphite. However, in old diamond, these twins are straight and relatively sporadic. Nevertheless, it is unknown if the criterion of identifying regrown diamond based on dislocation density difference remains applicable for the diamond regrown directly from graphite, as no evidence regarding the presence or absence of dislocations is shown in the STEM results from Luo *et al*[15].

### 2.1.2.2 Study of the Microstructure by SEM-CL

SEM-CL can be applied to locate the position of colour centres like $NV^0$ and NVN centres and dislocations in diamond. The regrown diamond could potentially be distinguished from the old diamond based on its different CL emissions. In a CL image, only diamond will be recorded, as the conductive metallic binder phases and carbides barely emit CL.

Building upon the discussion of different dislocation densities in regrown and old diamond in Section 2.1.2.1, this difference could also be examined by SEM-CL. Collins and Robertson[16] reasoned that a special blue emission from PCD is related to the density of defects like dislocations and twinning, which was later echoed by Marinelli *et al*[17]. This CL emission appears as a distinct band in the blue

wavelength range in CL spectrum and is called Band-A. Many studies claimed this Band-A is related to a band structure of dislocation decorated with a donor-acceptor pair[18–20]. Some argued the acceptor might be merely the substitutional single boron atom or boron atoms decorating dislocations[21,22]. However, through a comparison of CL spectra between boron doped and undoped high-purity CVD diamond films, Ruan *et al.*[23] refuted both the donor-acceptor pair model and the boron decoration model.

Though there is no clear theory to explain the band structure of Band-A, researchers agree that this Band-A is associated with dislocations. The most straightforward and convincing evidence to support this relation are from the observation of Band-A CL emissions from various single dislocations via STEM-CL by Pennycook *et al.*[24] and Yamamo *et al.*[19] Hence, by comparing panchromatic CL images to CL images with Band-A emission only, diamond exhibiting no Band-A emission could be designated as regrown diamond. Glenn *et al.*[25] employed this method in reverse to distinguish defective nano diamond for biological labelling purpose.

Other remarkable defects are the 484nm, NVN and $NV^0$ centres. For diamond synthesized from a nickel-based catalyst, the 484 nm centre, which is related to the substitutional nickel in diamond, can be detected mostly in the {111} growth faces [16,26]. The formation of NVN centre is linked to the mobile vacancies and the A-centre, a pair of substitutional nitrogen atoms. At high temperature when the vacancy is mobile and the concentration of vacancy is approximately equal to that of A-centre, the A-centre will capture an vacancy to form the NVN centre[27,28]. For $NV^0$ centres, Collins and Robertson[16] reported a broadened $NV^0$ peak due to the residual strain and the disappearance of NVN centres in PCD after HPHT sintering. Furthermore, R. Daniel found new CL emissions from $NV^0$ centres in regions after high-temperature plastic deformation in HPHT-sintered diamond[29]. Based on his research, the industry believes that a large amount of $NV^0$ centres will be created during the HPHT sintering. This is likely because of the relatively high nitrogen concentration in raw diamond powders present to enhance strength of PCD[14]. Additionally vacancies can be emitted by jogging or

climbing of dislocations during HPHT sintering[30,31]. Finally it is well-known that a 800–900 °C annealing can facilitate the formation of $NV^0$ centres via the diffusion of vacancies and their capture on the substitutional nitrogen[32,33]. The $NV^0$ centres could be also from the interaction between NVN centres and mobile vacancies after a HPHT annealing[34]. Thus, the old diamond might be rich in NV centres with a broadened peak, but deficient in NVN centres compared to the regrown diamond. CL images showing emissions from either $NV^0$ or NVN centres could be used to potentially identify regrown diamond.

Although SEM-CL offers the advantage of less cumbersome lab work, flexibility and large-scale characterization area compared to TEM, there is, nonetheless, a resolution limit in the PCD bulk specimen for SEM-CL. By reducing the resolution, the minority carrier diffusion in CL will introduce inaccuracy when locating the position of various defects in diamond[35]. This issue becomes more pronounced in less defective diamond crystals as the minority carrier can travel a longer distance before recombination occurs[36]. When the minority carrier diffusion length exceeds the size of the defect-free regrown diamond, and the dwell time of CL imaging is not extremely short, the electrons and holes can freely diffuse to adjacent old diamond when the electron probe is on the regrown diamond. As a result, they recombine in the old diamond, emitting the characteristic CL from old diamond. Consequently, in the CL image, the regrown diamond will exhibit characteristic CL emissions from adjacent old diamond. To mitigate this issue, using a low SEM voltage to shrink the electron-sample interaction volume and a cryo stage to decrease the minority carrier diffusion length are recommended when studying regrown diamond with SEM-CL.

Additionally, non-radiative recombination via multiple phonon emissions, the Auger effect and surface states (dangling bonds and reconstructed surface) and potential non-electron-induced luminescence can either reduce the actual CL intensities or cause unexpected noise in the CL spectrum[37]. These factors influence the quantitative analysis of CL results. Extra attention is needed when studying diamond with CL.

### 2.1.2.3 Study of Microstructure by EBSD

The grain orientation spread (GOS) approach based on EBSD data has been widely applied to quantitatively study dynamic recrystallization in metallic materials[38–41]. GOS represents the average misorientation of all EBSD scanned pixels within a grain compared to the average orientation of that grain. Its mathematical expression is:

$$GOS_{grain\ i} = \frac{1}{N}\sum_{j=1}^{N} misorientation_{N_{(j)}}$$

where $N$ is the number of pixels in the grain $i$, $N_{(j)}$ is the j th pixel and $misorientation_{N_{(j)}}$ is the minimum misorientation between the j th pixel and grain's average orientation[38,39]. GOS is in the unit of degrees (°).

The GOS value of a grain depends on the degree of recrystallization within that grain. The recrystallized part of the grain is anticipated to be free of dislocations and deformation twins, which reduces the misorientation with respect to the grain average orientation and consequently lowers the GOS value[40]. Mandal *et al*.[38] reported that the GOS value decreases with the increase of the recrystallized fraction in that grain. Miller and Pollock[41] linked the GOS value to the density of geometrically necessary dislocations and argued that for a fully recrystallized grain, its GOS value should be below a threshold value. Different threshold values of GOS from 1° to 5° are reported to distinguish the dynamically recrystallized grains from previously deformed grains[39–41].

The GOS approach was applied to characterize the crystallinity of bulk single crystal or polycrystalline CVD diamond by Mohapatra *et al.*[42] In their study, the maximum GOS value of the CVD PCD was less than 1° and for a single crystal CVD diamond, the GOS value peaked at 1.1° at a thickness around 10 µm and then quickly dropped below 1° with increasing thickness[42]. Since CVD diamond has a good reputation for high crystallinity, the current author asserts that any diamond grain from HPHT sintered PCD with a GOS value less than 1° can be regarded as partially or fully regrown diamond grain. Though the GOS approach has not been used to study the PCD materials,

Britun *et al*.[11] found a local high misorientation from azimuthal broadening of TEM diffraction spots caused by heavy plastic deformation, and this misorientation can extend throughout the whole grain even with temperature exceeding 2000 °C. This locally high misorientation would reflect a high GOS value, contrary to the low-GOS-value regrown diamond. Thus, the GOS approach could also be potentially applied to quantitatively distinguish regrown diamond from old diamond in PCD materials.

However, the disadvantage of the GOS approach is that it can only reflect the crystallinity of a whole diamond grain and does not show the regrown part locally. A local misorientation, also known as kernel average misorientation, map might be a supplement as it can present the average misorientation between each pixel and its nearby pixels locally (for example, its surrounding 7x7 pixels). The local misorientation in that pixel in the unit of degrees (°) is obtained by:

$$Local\ Misorientation_{i,j} = \frac{1}{\left|N_{(i,j)}\right|} \sum_{(k,l)\in N_{(i,j)}} w(o_{i,j}, o_{k,l})$$

where $\left|N_{(i,j)}\right|$ is the number of all neighbouring pixels, e.g. for a 7x7 matrix, $\left|N_{(7,7)}\right|$ =48. $w(o_{i,j}, o_{k,l})$ is the disorientation angle between the centre pixel $o_{i,j}$ and any neighbouring pixel $o_{k,l}$[43].

By setting a threshold value to the local average misorientation, it is possible to highlight the regrown part in a diamond grain. The highest average local misorientation recorded by Mohapatra *et al.* [42] is around 0.7°. This value can be referred to when analysing the local misorientation map of PCD materials. However, Britun *et al*.[11] emphasized the misorientation across the interface between the regrown and old diamond is smooth, complicating the identification of this interface.

Since both the GOS approach and the local misorientation map are very sensitive to the pixel size, a high-resolution EBSD might be required to accurately measure the regrown diamond part.

In conclusion, the regrown diamond should exhibit one or several different crystal defects and/or microstructural morphologies compared to that of old diamond. Different characterization methods can be used to investigate different aspects of the morphology difference. However, there is no perfect characterization technique which could cover most of the characteristic morphologies. Each of the above-mentioned characterization techniques has its own limitations, either requiring enormous lab work or potentially bringing uncertainty, lacking regional sensitivity or being too general. On the other hand, from the literature, none of the morphological features is decisive in identifying regrown diamond, especially determining the interface between the regrown and old diamond. Therefore, for accurately identifying regrown diamond, it is recommended to employ multiply characterization techniques to investigate different morphological features in same specimen.

## 2.2 HPHT Polycrystalline Diamond Synthesis

The synthesis of PCD materials can be divided into four main stages: pre-treatment, cold compaction, hot compaction and liquid state sintering, where diamond grits regrow. Though the diamond regrowth may not happen during the first three stages, its occurrence is closely linked with them.

### 2.2.1 Pre-treatment

The assembly of diamond grits and binder powders into a PCD green body before compaction in a cubic press is referred to as pre-treatment. There are two purposes in pre-treatments: to achieve a homogeneous green structure and to improve composition purity[44].

Homogeneity in the PCD green structure is crucial to avoid the formation of weak microstructures. For example, a "soft spot" in PCD materials occurs when diamond particles are fully isolated in binder phases, resulting in no diamond-diamond bonding due to incomplete sintering[45]. Binder phases infiltrate to wet the diamond surface in these regions, yet the extent of diamond regrowth is

far from sufficient to form connections between these particles. Another weak microstructure is the aggregation of fine or coarse diamond grits when a multi-modal mix of diamond grits is used. Vibrational mixing can help alleviate the inhomogeneity in the green structure, while another effective but more expensive method involves coating binders onto diamond grits[44].

During the pre-treatment stage, the assembled powders are enclosed in rare metallic canisters. However, these canisters may still contain volatile impurities like reactive gases and unstable carbon species. These contaminants can be largely eliminated by outgassing, a high temperature treatment in medium to high vacuum[44,46]. One effect of outgassing is the initiation of surface graphitization of diamond grits. Kamali[47] observed a change in colour of diamond grits from opaque to black after outgassing. He then characterized and compared the diamond grits before and after outgassing, confirming the surface graphitization from multiple characterization results. The HR-TEM results in figure 2.5 display the observed surface graphitization. Surface graphite can play a dual role, as a lubricant during later compaction and as a carbon source during diamond regrowth[48].

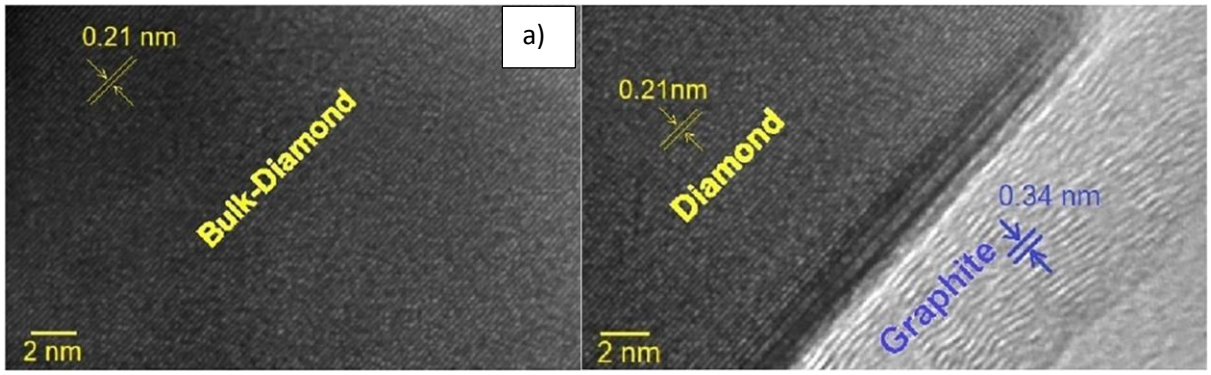


*Figure 2.5: HR-TEM images of diamond grit (a) before and (b) after outgassing. The graphite layer onto diamond can be located in (b)[47].*

## 2.2.2 Cold Compaction

Upon insertion into the cubic press, the period when the PCD green structure is compressed hydrostatically from 0 up to several GPa without heating is called cold compaction[48]. This compression undoubtedly alters the PCD compact's microstructure, transforming it to a dense and stable mass via two sub-processes: particle crushing and rearrangement[49,50]. Particle crushing and

rearrangement act as driving forces for changes of PCD microstructure, while densification is the consequence of iterations of particle crushing and rearrangement. In the first two images of the schematic description of cold compaction in Figure 2.3. diamond particles crush against each through point or surface contacts. Although the external loading is usually lower than the fracture strength of single crystal diamond (~50-100GPa), cracks can still be generated if the local concentrated contact stress exceeds this fracture strength[51,52]. With an increase of loading, cracking leads to the brittle fragmentation of diamond particles, resulting in changes in the size and shape of diamond particles[53]. Crushed diamond particles exhibit rough surfaces and sharp edges[51]. Simultaneously, the majority of diamond particles and fragments rearrange their relative positions via the mutual sliding and voids are filled by finer fragments, as shown in Figure 2.6 (c). Ideally, the particle movement does not cease until the space is unavailable for sliding, which means every particle is anchored by the directly contacted surrounding particles. This state corresponds to Figure 2.6 (d). At the end of cold compaction, diamond particles become stable under the applied pressure and the PCD compact has become denser[51].

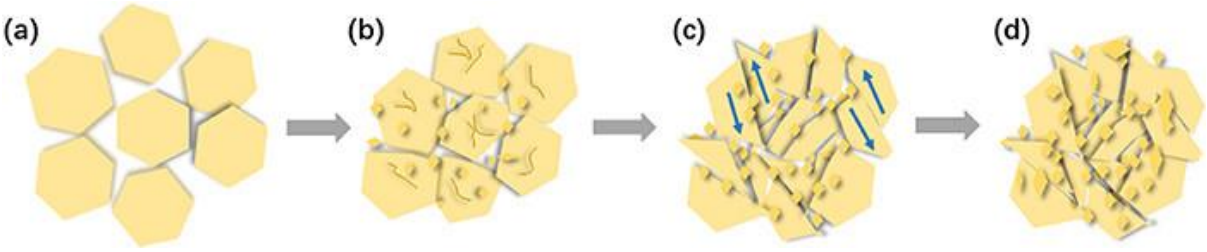


*Figure 2.6: the schematic description of cold compression. a) is the initial status. (b) corresponds to particle crushing, cracking, fragmentation and rearrangement. Cracks and small diamond fragments can be found. (c) shows the further rearrangement by mutual sliding and the finer fragments fill the voids in the PCD compact. (d) the stable and denser status of the PCD compact*[51].

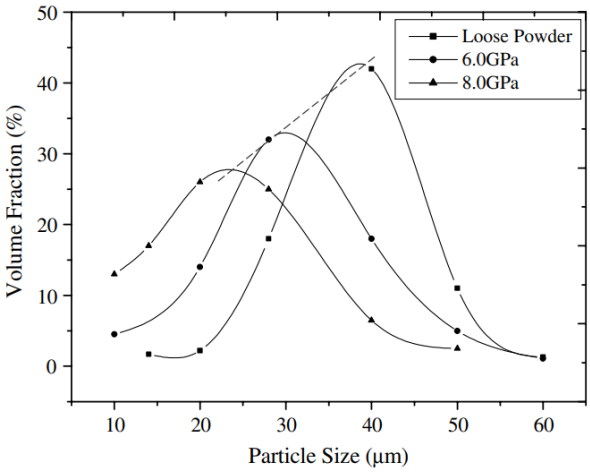


*Figure 2.7: Size distribution of diamond crystals for two compaction pressures and loose powder at room temperature*[52].

Three main changes after cold compaction are the density of the PCD compact, the size distribution and the shape of diamond particles. Based on Figure 2.7, Bobrovnitchii *et al.*[52] concluded that the size distribution becomes flatter, and the peak value of distribution decreases with the increase of external loading; these trends become more evident as pressure increases.

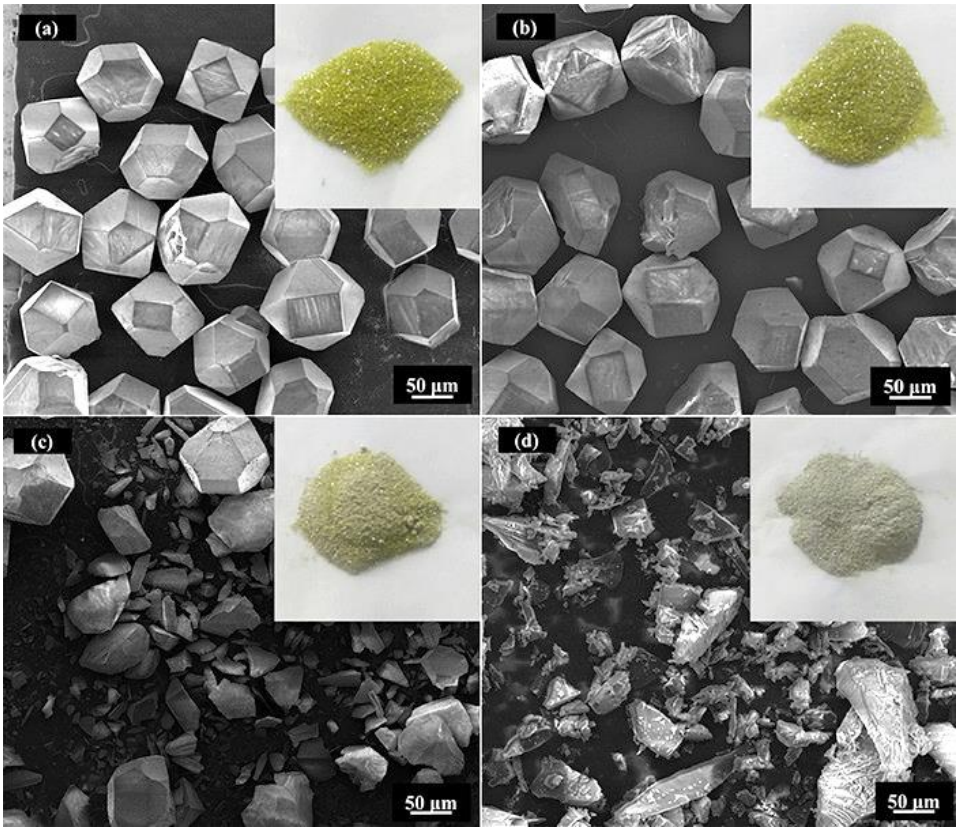


*Figure 2.8:(a) Secondary electron images of original diamond powders before pressing. (b) After pressing at 200 MPa. (c) After pressing at 400 MPa. d) After pressing at 600 MPa. The inset images at the top right of each image are the optical photos of the corresponding powders*[51].

These conclusions are also supported by the SEM images in Figure 2.8 , where higher pressure results in more small diamond fragments. [51]. Another feature noticeable in Figure 2.8 is the sharper shape of diamond particles with the increase of pressure. Almost every diamond particle shows an irregular shape in Figure 2.8 (d). However, depending on the applied pressure and composition, some diamond particles, whether cracked or intact, remain unaffected, indicating a complex and heterogeneous stress field within the PCD compact.

Owing to this heterogeneous stress field, upon heating, some diamond remain within the diamond stable region, while others enter the graphite stable region in the carbon phase diagram, complicating the diamond regrowth during sintering[51,52].

Nearly every study about the PCD cold compaction mentions a reduction in porosity; but none demonstrates a characteristic method to measure this reduction[51,52,54].

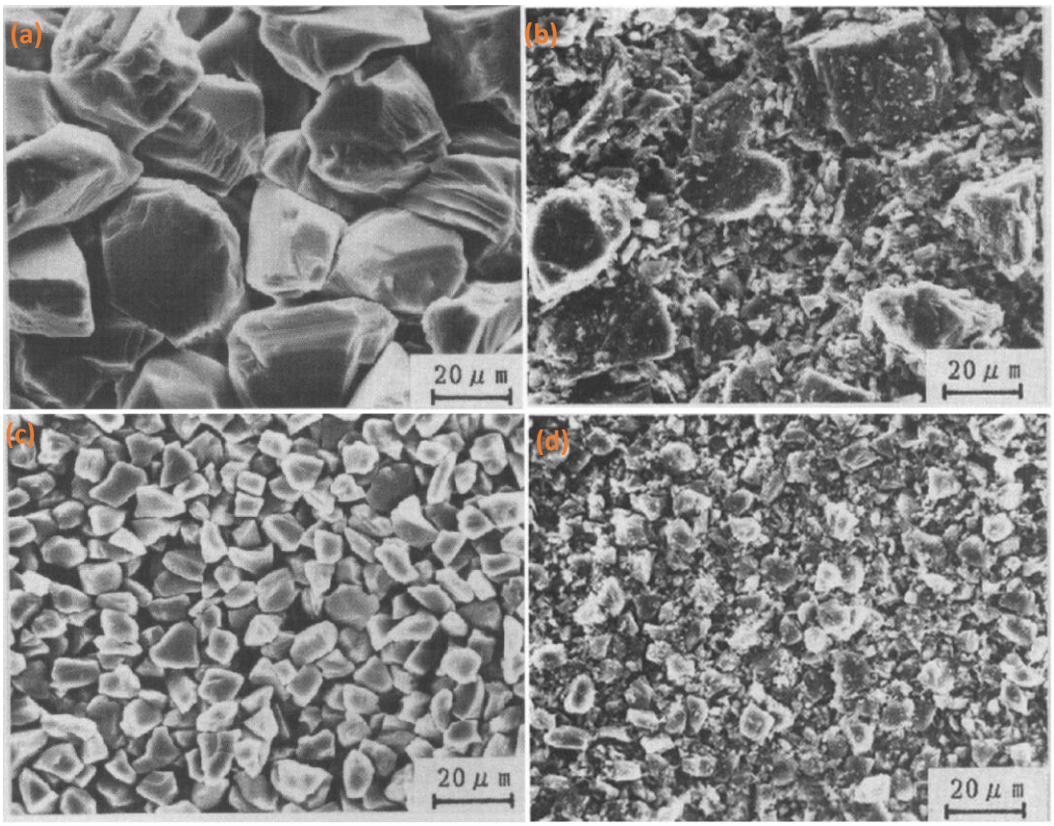


*Figure 2.9: 40-60 µm and 10-15 µm grades diamond powders before(a),(c) and after(b),(d) cold compaction at 5.5GPa*[55].

It is summarized that the degree of all three changes is dependent on the initial diamond size and morphology[52,54,55]. An example of initial diamond size impact on the size distribution and shape is presented in Figure 2.9.

Additionally, local surface graphitization is possible during cold compaction. Wang *et al.*[56] simulated the grinding of a SiC tip onto a diamond bulk at room temperature with the highest compressive stress at 2.6 GPa. They observed very shallow surface graphitization on diamond upon friction, as the local temperature can reach 600 K. Despite the lack of direct evidence of surface graphitization after cold compaction, the idea of surface graphitization may be supported by the gradual change of diamond colour when increasing the loading pressure in Figure 2.8 [51]. As mentioned before, the change of colour of diamond powders from non-black to black is a sign of surface graphitization[47].

In conclusion, the three main changes described and the possible graphitization will profoundly influence the diamond regrowth during sintering and the final microstructure of PCD materials. These will be discussed in detail in section 2.2.4.

## 2.2.3 Hot Compaction

Hot compaction is defined as the period from the start of press heating until reaching the predetermined temperature while the external loading slowly increases from about 85% to 100%. During this stage, three main phenomena occur: the plastic deformation of diamond particles, the diamond surface graphitization, and the binder infiltration.

### 2.2.3.1 Plastic Deformation

During hot compaction, diamond can be plastic, with its brittle to ductile transition temperature typically around 800 °C, depending on the size, shape, synthesis process, impurity and external pressure [11,57,58]. Given that the maximum sintering temperature is usually beyond 1300 °C, old diamond can undergo plastic deformation during HPHT sintering. This process introduces three types of defects into the diamond: dislocations, twinning, and stacking faults.

In diamond, perfect dislocations are usually found on the {111} <110> system, while partial dislocations can have slip directions along <112> and <111>[14]. Yu *et al*.[14] uniaxially deformed PCD powders at different temperatures (25 °C, 1000 °C, and 1200 °C), which simulates the hot compaction stage of HPHT sintering. They discovered an extremely high density of perfect <110> dislocations entangled with each other. Britun *et al*.[11] identified rich concentration of perfect <110> and Shockley partial <112> dislocations in PCD materials after heating up to 700-1400 °C. The interesting finding from Mussi *et al*.[59] is the capture of some dislocation dipole annihilations at a maximum heating temperature of only 1200 °C, which indicates an extremely high dislocation density, shown in figure 2.10. Walmsley and Lang[8] reported an inhomogeneous dislocation distribution in diamond grain. The low dislocation density region was attributed to diamond regrowth in their following study. Overall, it is confirmed that the old diamond is supposed to be filled with superabundant dislocations.

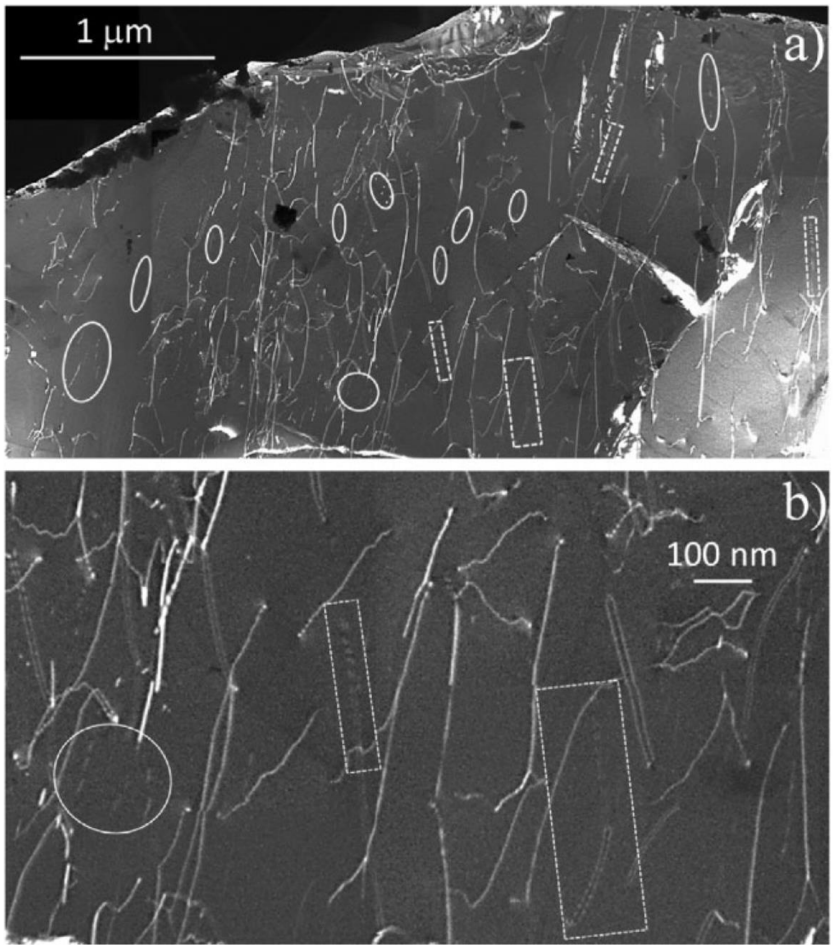

*Figure 2.10: a weak beam dark field TEM image of synthetic type Ib diamond after deformation under 5 GPa and 900-1200 °C. The zone axis is along <111>. a) Massive dislocations. b) Zoom in to show the faint dislocation annihilation dipoles*[59].

Deformation twins were also observed in conjunction with dislocations in all the above-mentioned studies. This is reasonable since twinning is the other major deformation mechanism[60]. The details of two types of twins in diamond are discussed in section 2.1.2.1. However, except Luo *et al*. [15], none of the studies mentioned whether both types of twins will form in the regrown diamond. In the author's opinion, this might be possible; the growth twin can be formed to accommodate the external pressure during carbon atom reprecipitation onto existing diamond surfaces. While the deformation twin, which is associated to the glide of the Shockley partial dislocation, could occur under less stress compared that to trigger the perfect dislocation slip during diamond regrowth[13,60].

Several studies claimed the formation of stacking faults in PCD materials after hot compaction[11,14]. Unfortunately, aside Woods'[61] and Yin's[62] researches about the stacking faults in single crystal diamond, no studies presented convincing evidence of stacking faults in PCD and explained their potential formation mechanism under a HPHT condition[11,14]. Contradictorily, in their hot compaction alike experiment, Yu *et al*.[14] announced the absence of large stacking faults in their TEM results.

It should be noted that this heavy plastic deformation is not universal to all old diamond. Some diamond grits, especially smaller ones, might be protected from severe plastic deformation by the surrounding diamond due to the heterogeneous stress field between diamond particles[1]. As plastic deformation is a vital process that creates the different crystal defect in old diamond, those portions of old diamond that undergo less plastic deformation can further complicate the identification of regrown diamond.

#### 2.2.3.2 Graphitization

Diamond simultaneously undergoes partial graphitization during hot compaction. There are two kinds of diamond graphitization: binderless graphitization and binder-assisted graphitization. In both cases, the graphitization happens at diamond surface where the pressure is below the Berman-

Simon line[52,63]. Thus, the graphite-to-diamond transformation is thermodynamically favourable until the local pressure surpasses the Berman-Simon line.

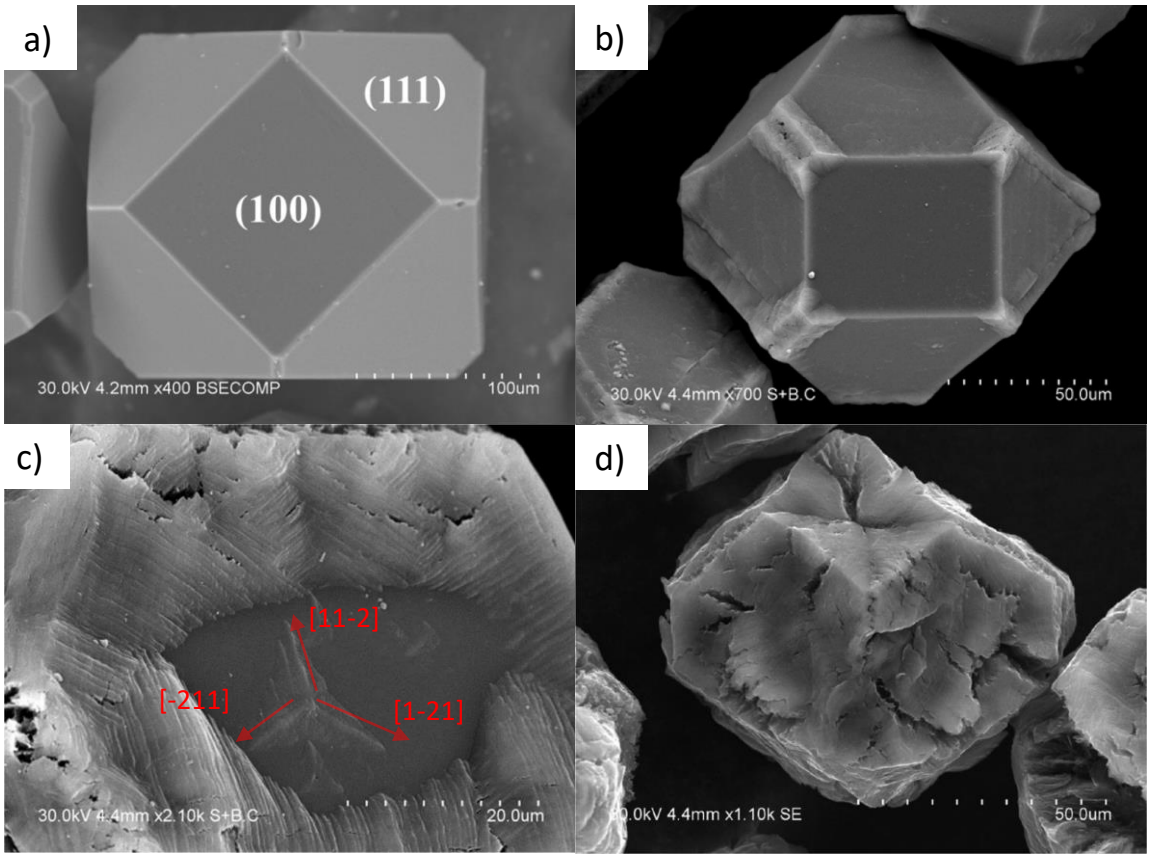


*Figure 2.11: the gradual graphitization on diamond particle with a vacuum annealing at 1600 °C. a) the morphology of diamond particle before vacuum annealing. b) after annealing for 2mins. c) after annealing for 4 mins. d) after annealing for 4 mins* [64].

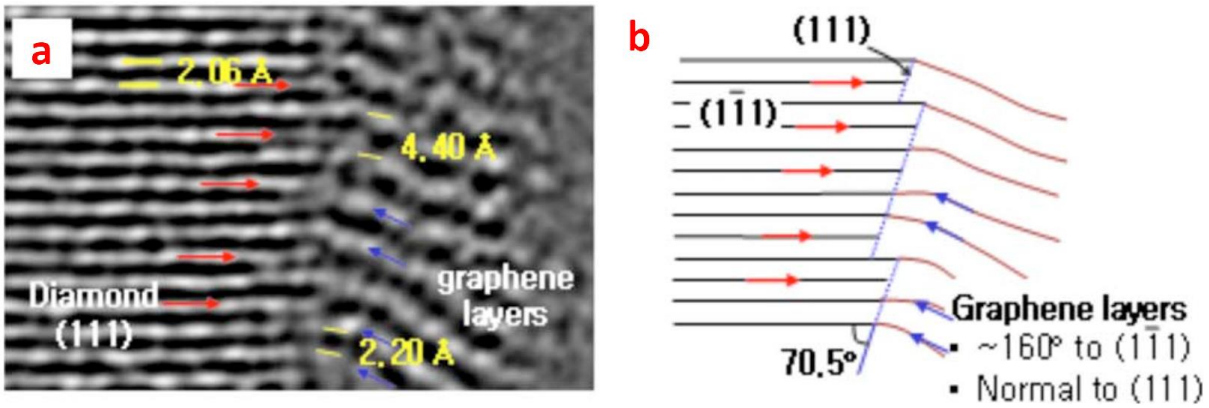


*Figure 2.12: a) A HRs TEM image of the cross section of diamond-graphite interface. b) The corresponding sketch of a).* [65]

Binderless graphitization on diamond surfaces has been studied. Bokhonov *et al*.[64] investigated diamond graphitization during a vacuum annealing at 1600 °C. The gradual graphitization on the

diamond surface is illustrated in figure 2.11 above. Graphitization initializes from the edges of the diamond and propagates toward the centres of facets. After full graphitization, clear diamond facets are no longer recognizable. The orientation of dendrites on the [111] diamond plane in figure 2.11 c) indicates an orientation relationship between diamond and its surface graphite. They concluded that the $(002)_{graphite}$ // $(111)_{diamond}$. This orientation relationship is echoed by the HR-TEM image of graphitized diamond powder in figure 2.5[47]. However, in a study of the graphitization of CVD diamond shown in figure 2.12, Lee *et al*.[65] discovered a different orientation relationship: the $(002)_{graphite}$ is 160° to the $(111)_{diamond}$. As they didn't mention the annealing environment and some gases, like oxygen, can intensively intervene in the process of binderless diamond graphitization, this distinct orientation relationship could be partially attributed to a different annealing environment[65]. During the HPHT sintering of PCD materials, the capsule is completely sealed and the residual gases are at low concentrations after outgassing. The gas mediated diamond graphitization, therefore, is outside the scope of this thesis. Another key parameter influencing the orientation relationship is the temperature. Though not in a vacuum environment, Khmelnitsky and Gippius[66] found varying thermal stabilities on different diamond facets with the increase of temperature, indicating a different threshold temperature of graphitization on different diamond facet.

Meanwhile, the kinetic barrier of binderless diamond graphitization is reduced by an increase of temperature Fedoseev *et al*.[67] generally claimed that old diamond graphitizes more with the increase of temperature. This claim is also supported by an increase in the intensity of graphite XRD peaks with elevated temperature[68]. However, when the temperature exceeds 1700 °C, some graphite may be transformed back to diamond. The kinetics also depends on the area-to-volume ratio; finer diamond powders are prone to be graphitized[69].

In a similar study of the HPHT sintering of PCD materials, Akaishi[69] compacted the diamond powder at 5.8 GPa and heated it up to 1400 °C with and without Co infiltration. Strong graphite peaks were recorded in the Raman spectrum for diamond powder without Co infiltration. Since the binder does

not infiltrate into the PCD table before reaching the eutectic point of the Co-WC-C system (above 1400 °C for 5.5 GPa), during HPHT sintering, the diamond surface without binder contact continues to graphitize until interrupted by the infiltration of liquid binder[69,70]. As aforementioned in section 2.2.1, the graphite layer on diamond formed during outgassing will become almost homogeneously thicker during the hot compaction.

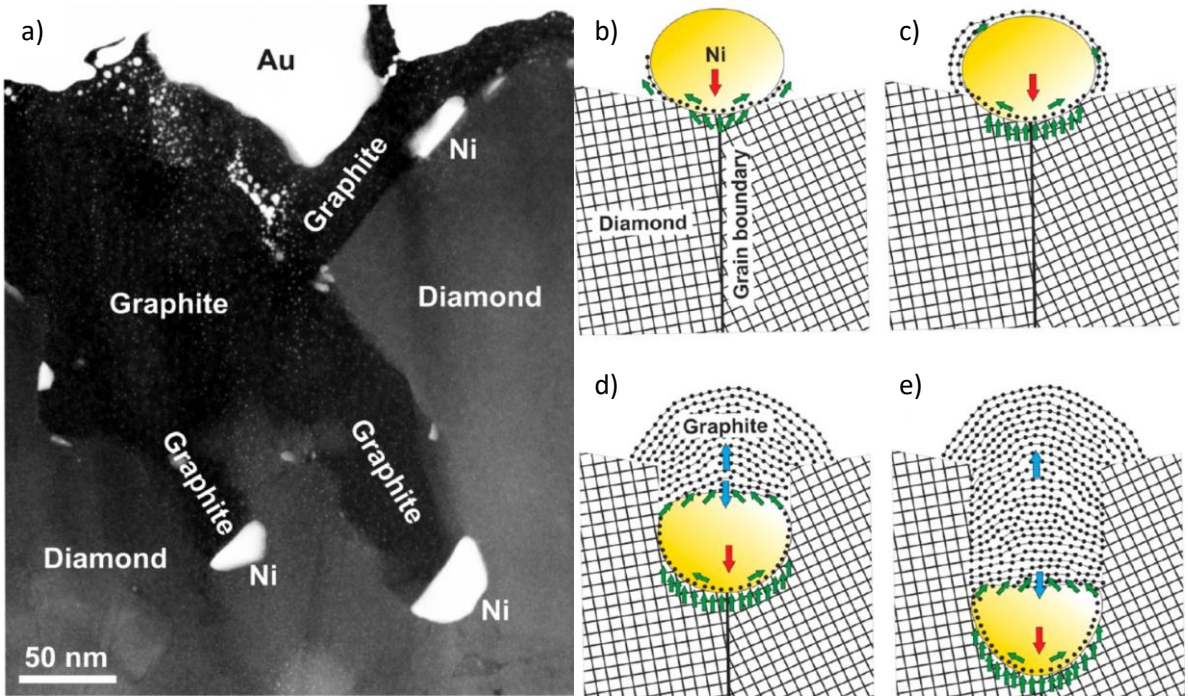


*Figure 2.13: a) the HAADF image of drilling channels along GBs filled by Ni-assisted graphitization. b-e) the sketches of different stage of this graphitizaton.* [71]

Binder-assisted graphitization takes place at the binder-diamond contact, even when the binder remains a solid state. Tian *et al*.[72] wrapped the single crystal diamond with solid cobalt and studied the solubility of diamond in solid Co under constant 5 GPa, but varying temperatures. They proved the dissolution of diamond atoms to form a C-Co solid solution via the interstitial solid-state diffusion, as evidenced by their EDX and weight measurement results. Though they claimed that diamond regrowth occurred via the reprecipitation of dissolved carbon atoms at 5 GPa and 1300 °C after Co reached carbon saturation, the morphology on diamond facet and the sintering condition situated in the graphite stable region (at 1300 °C, the diamond stable region in the P-T phase diagram should be above 5.11 GPa) indicate that the precipitate should be graphite rather than

diamond. In another study, as shown in figure 2.13 a), Tulic *et al.*[71] discovered the drilling channels along the GB of CVD nano diamond, left by Ni particles after annealing at 800 °C for 10mins. Newly formed graphite filled these channels. Due to the limited space and constraints from nearby diamond, this graphite was detected to be heavily bent, as seen via HRs STEM images and diffraction patterns. The graphitization mechanism is described in sketches in figure 2.13 b)-e). It resembles a dissolution-reprecipitation like process. Diamond carbon-carbon bonds are catalytically broken by the nickel particle and isolated carbon atoms undergo nickel surface diffusion toward the spacious region behind the particle, rather than directly diffuse across the binder, eventually precipitate out as graphite behind the nickel[71]. This mechanism is similar to proposed mechanisms from several other catalytic graphitization studies[73,74]. However, no evidence supports the surface diffusion path. In terms of the orientation relationship between graphite and diamond, some concluded a $(002)_{graphite}$ // $(111)_{diamond}$ orientation relationship from different binders[11,73,74], which aligns with the orientation relationship identified by Bokhonov *et al*.[64] from the binderless diamond graphitization described above.

Regarding the HPHT sintering of PCD materials using a cobalt binder, firstly the catalytic nature of cobalt is close to that of nickel and iron[75]. Secondly admixed cobalt and/or the front of infiltrated Co-WC melt have extensive surface contact with the diamond. Therefore, unlike the homogeneous binderless diamond graphitization, the binder-assisted graphitization is expected to occur heterogeneously at the diamond-binder contact in PCD material, probably during liquid binder infiltration. Some residual graphite was indeed examined by TEM and XRD/Raman separately in a Co-catalyzed HPHT sintering of PCD materials, though none of them provided quantitative information[1,69].

In conclusion, it has been established that both ways of graphitization will occur during the hot compaction. The graphite profoundly influences the following sintering in two aspects; one is as the lubricant to assist the rearrangement of diamond particles to a denser green body; the other is as

the carbon source for the later diamond regrowth. However, in the Co-catalyzed HPHT sintering of PCD materials, it is unknown which graphitization mechanism dominates and whether voids are filled by graphite in the PCD table before binder infiltration[69].

#### 2.2.3.3 Direct Transformation of Graphite to Diamond

Before the infiltration of liquid binder, some diamond-diamond bonds could potentially be formed through the direct transformation from graphite. In a study of the binderless HPHT sintering of PCD at 1600°C with only 8 MPa, Fedoseev *et al*.[67] implied that the function of the GB is to connect the isolated diamond powders and form a unified structure, although no microstructural evidence was presented. In a similar study at 14 GPa, Liu *et al*.[68] speculated that the direct transformation of graphite to diamond occured in light of the change in relative XRD peak intensities of both graphite and diamond occurred. The PCD sample in their study was depicted as a diamond skeleton formed by mutually bonded micron-sized diamond grains.

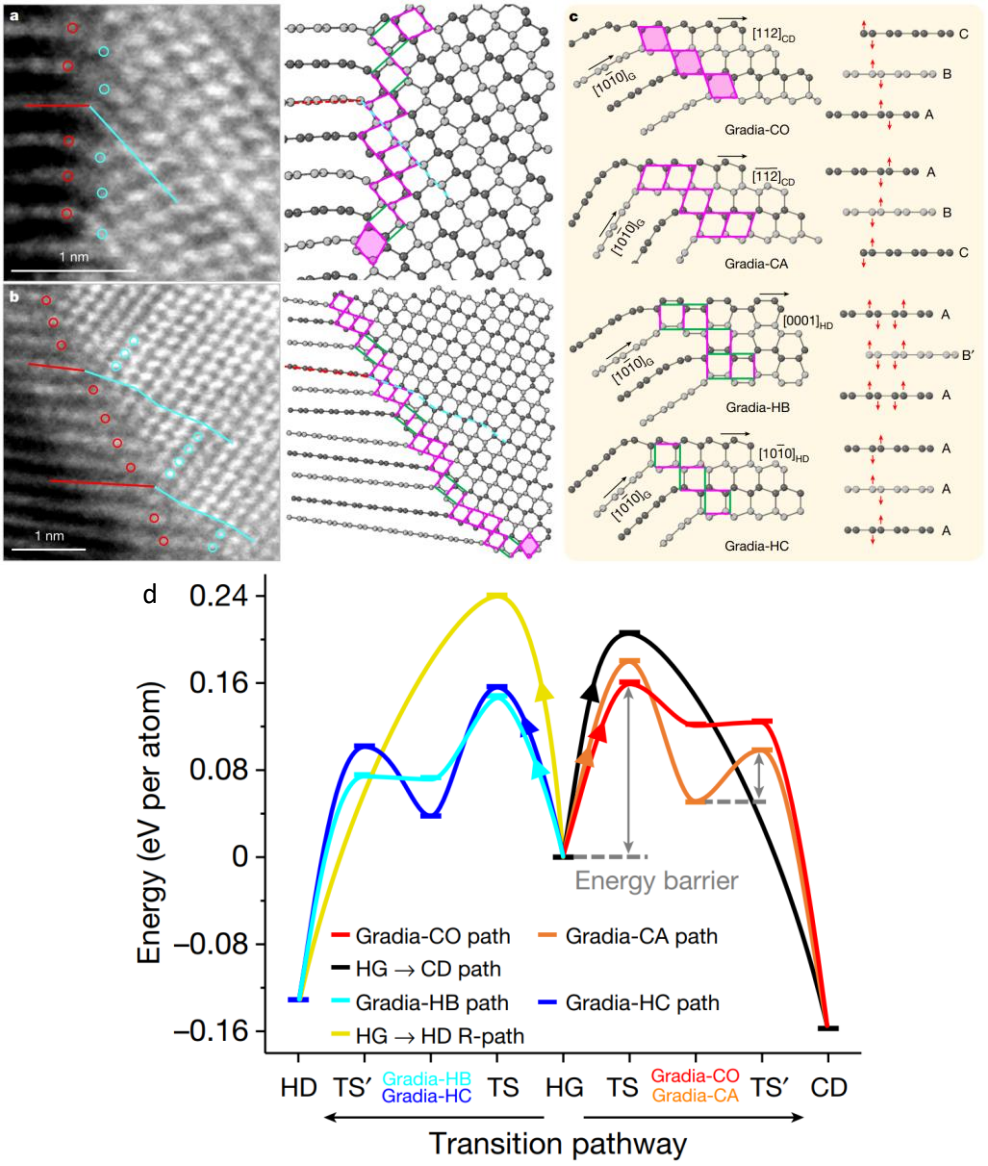


*Figure 2.14: HRs HAADF STEM image of graphite-diamond (Gradia) interfaces a) with an obtuse angle (CO) and its corresponding atomic models, b) with an acute angle (CA) and its corresponding models. Red and cyan circles and lines correspond to graphite and diamond atoms respectively. c) Four representative graphite-diamond interfaces. The red arrows indicating their moving positions when transferring to diamond structure from graphite. d) First principle calculation of energy barriers for the transformation for different routes at 10 GPa. (HD, the hexagonal diamond, is out of the scope of this thesis. But more details can be found in their paper)* [15]

A more systematic study of the direct transformation of graphite to diamond was carried out by Luo. *et al*[15]. Under an external pressure greater than 10 GPa, carbon atoms in graphite undergo compression, bending and slipping to form local disordered wave-like structure to accommodate this pressure. This wave-like disorder in graphite leads to local variations in atomic stacking and interplanar distance, which in turn nucleates cubic diamond via additional bonding across surrounding carbon atoms from multiple graphite layers. Depending on the orientation relationships between diamond and graphite, the diamond-graphite interfaces are named Gradia-CO for an

obtuse angle and Gradia-CA for an acute angle between <1010>$_{graphite}$ and <112>$_{diamond}$. An HRs HAADF STEM image showing these two coherent diamond-graphite interfaces and their corresponding atomic models is inserted in figure 2.14 a) and b). Figure 2.14 c) illustrates the relative movement of the graphite carbon atoms near the interface to compose a diamond structure. Based on the results of first principle calculations in figure 2.14 d), once this diamond-graphite interface is formed, its propagation or the diamond growth along graphite is thermodynamically favourable. The XRD microstructural features of this regrown diamond is discussed in section 2.1.2.1.

In the HPHT sintering of PCD materials, since the diamond powder undergo surface graphitisation during outgassing and at some point, during hot compaction, it is very likely that raw diamond powders are covered with a layer of graphite with varying thickness. Hence, at a non-slip, heavily compressed diamond-diamond contact with a rising temperature prior to triggering the liquid binder infiltration, it is conceivable that the regrown diamond to bond these two diamond grains could be directly transformed from this layer of graphite, following the mechanism discussed above. Should no graphite exist between the diamond-diamond contact, the transformation remains less plausible due to the high transformation energy battier between two differently oriented diamond, although substantiating evidence is required.

#### 2.2.3.4 Binder Infiltration

Unlike the pressureless liquid phase sintering, where the wetting is dependent on the dihedral angle determined by interfacial energies, upon reaching the eutectic point of the binder system in substrate, the liquid binder infiltration into the PCD table is mainly driven by the overwhelming applied pressure[76,77]. The capillary force at local gaps between diamond powders can have a positive or negative influence depending on the local geometry. Regarding the quantitative estimation of the capillary attraction, German[70] hypothesized that the infiltration becomes immediately at 7 GPa and 1500 °C for a cobalt viscosity of 27 mPa. However, this idealised estimation is less plausible due to the various pore sizes and the change in liquid binder viscosity when WC is introduced and carbon is

saturated. Moreover, at 1500 °C, the substrate comprises solid WC and liquid Co-WC; the applied pressure is mainly exerted on the solid WC skeleton, and is not like squeezing a bottle of liquid solely. The effective external pressure to facilitate the binder infiltration might be much lower than the applied pressure. Experimental observations by Hong *et al*.[77] and Uehara & Yamaya[55] noted incomplete Co infiltration in their studies with limited temperature increases. Furthermore, Hong *et al*.[77] commented that the infiltration process correlates with the size of diamond raw powder, generally the bigger the grain size is, the easier the infiltration is. Because the size of diamond raw powder actually determines the pore size in the PCD table, which indirectly affects the regional capillary force, it restates the considerable importance of the capillary forces. Achieving 100% dense PCD materials necessitates overcoming the largest capillary force through effective external pressure.

As discussed in the previous section, the mode of liquid binder infiltration can dictate the process of binder-assisted graphitization. Rapid infiltration of the liquid binder would promptly dissolve graphite, while slower infiltration might trigger regional binder-assisted graphitization through the protrusion of liquid binder or isolated binder particles[76,77]. This, in turn, has the potential to impact diamond regrowth.

### 2.2.4 Dwell

The dwell stage is referred to as the period when both mean temperature and pressure remain constant at their maximum values, surpassing both the eutectic line of the binder system and the Berman-Simon line in the P-T diagram. Since the sintering condition thermodynamically favours the formation of diamond and the molten binder could catalyse this formation by lowering the energy barrier for the transformation from non-diamond carbon to diamond carbon, it is widely believed that the diamond regrowth predominantly occurs during this stage.

In addition to the previously discussed the direct transformation from graphite to diamond, there are two mechanisms that describe the process of diamond regrowth: the binder assisted dissolution and reprecipitation mechanism and the grain growth mechanism.

### 2.2.4.1 Grain Growth via Dissolution and Reprecipitation Mechanism

The dissolution and reprecipitation mechanism has been predominantly reported, albeit with only a few studies offering a detailed description of this process[50,55,69,70,72,78–80].

This mechanism can be described in several steps. The first step is the dissolution of carbon atoms into the binder. During the liquid binder infiltration, both graphite and potentially amorphous carbon preferentially dissolve compared to diamond, possibly due to the relatively weak π bond and lower atomic density[70]. The molten binder, usually composed of the transition metal, can dissolve the carbon atoms from diamond or graphite by overlapping the *d* orbitals with carbon's *p* orbitals to break σ/ π bonds[75]. The dissolved carbon atoms can occupy the tetragonal voids in transition metal binders.

The more vacancies are in the 3*d* & 4*s* orbitals of the transition metal binder, the stronger the reaction is between the binder and diamond and the easier the formation of carbides is due to the decrease of carbon mobility. In the case of cobalt, which possesses three vacant 3d orbitals, carbon solubility is relatively high (reaching 11.9 atomic % in liquid at the eutectic point), and the mobility of carbon is also enhanced[75]. Owing to a higher carbon diffusion rate in cobalt and more thermal energy, both the diamond solubility and carbon diffusivity increase significantly with the elevation of temperature, allowing for quicker dissolution [72,81]. Under conditions of 5 GPa and 1350 °C for 20 mins, the presence of graphite precipitates indicates carbon saturation in cobalt[72]. Although the diamond solubility in Co increases with temperature, it seems the dissolution rate increases more rapidly with this temperature increase, implying that carbon saturation can be achieved in a relatively short time span, less than 20 mins, when a single crystal diamond grit is wrapped by solid Co shell at 5 GPa and 1350 °C [72]. In scenarios where the binder turns liquid, carbon saturation is

expected to occur swiftly in PCD materials because, firstly, the contact between diamond or graphite and molten binder increases, especially along the gaps between coarse and fine diamond grains, expediting total dissolution of carbon atoms in liquid binder; secondly, the high temperature exceeding 1500 °C improves the kinetics of dissolution and diffusion process and lastly the binder volume is only less than 1/10 of diamond, compared to the study by Tian *et al*.[72] where diamond was surround by Co binder.

It is claimed within the industry that there is a preferential dissolution of diamond. This is attributed to the high area-to-volume ratio of fine diamond powders, sharp diamond edges, kinks, and adatom carbon atoms, all of which are susceptible to dissolution. Regions abundant in dangling bonds, such as heavily plastically deformed regions and microcracks, are also prone to dissolution. Uehara & Yamaya[55] described the regrowth mechanism in an Ostwald ripening manner at the cost of fine diamond, despite the lack of evidence.

The diffusion in the HPHT synthesis of PCD materials is possibly to be short-range due to the relatively narrow gaps between diamond powders during binder infiltration[70,82].

The resulting precipitation, either as graphite or diamond depending on the specific sintering conditions, stems from carbon saturation in the binder[75]. In figure 2.15, Tian *et al*.[72] discovered recrystallized diamond crystals on the surface of feed diamond seed after the solid Co reached a carbon saturation at 5 GPa and 1100 °C for 200 mins. Upon raising the temperature to 1350 °C, the conditions favour graphite thermodynamically, resulting in newly formed graphite, which is confirmed through XRD patterns.

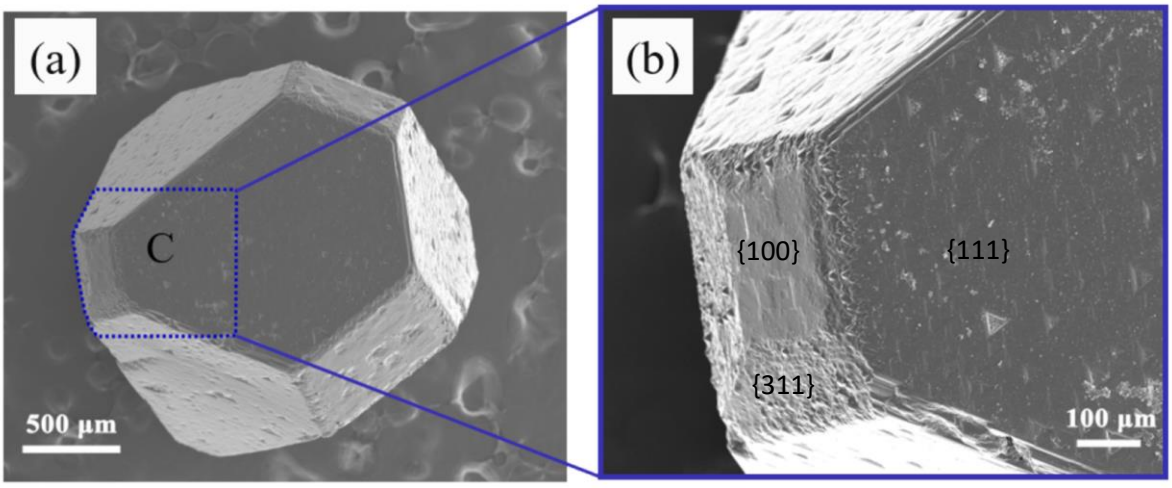


*Figure 2.15: single crystal diamond wrapped with solid Co in press under 5 GPa and 1100 °C for 200 mins. a) the single crystal. b) enlarged diamond surface with some claimed regrown diamond. Diamond facets are labelled.* [72]

The reprecipitation process is still under debate. Sung and Tai[75] presumed the undissolved graphite flakes floating on molten binder are puckered via the pressure assisted interactions, with the puckered graphite presenting a diamond-like structure and serving as nuclei, whereas the deposition of individual diamond atoms onto diamond surfaces is thought to occur under lower pressure, driven by the different solubility between graphite and diamond under HPHT. For example, at 5.7GPa and 1400 °C, compared to diamond, more than 1.2 atom% of metastable graphite will be dissolved in molten nickel[83].

Another perspective suggests that C-C bond formation from $Co_3C$ within the molten binder leads to reprecipitation[84]. The C-C bond in $Co_3C$ has a similar length to that of the diamond σ bond. The metastable $Co_3C$ decomposes at high temperatures due to the more intensive vibration of carbon atoms, resulting in C-C bonds that are then compressed to a diamond-like structure and eventually deposited onto diamond surfaces. Fan *et al*.[85] located the similar key intermediate product, $Fe_3C$, at the diamond/binder film interface in the Fe-Ni-C system using TEM. Yin *et al*.[86] used $Fe_3C$ as a carbon source for the synthesis of diamond under HPHT. However, Esconjauregui *et al*.[87] also invoked this reprecipitation process to explain the catalytically assisted synthesis of carbon nanotubes, even though carbon nanotubes possess a different crystal structure from diamond. The divergence in crystal structures raises questions about how the same process leads to different outcomes.

Moreover, a lack of kinetic studies related to this transition metal carbide-mediated reprecipitation process is notable. Given that this process entails the formation and decomposition of metastable transition metal carbides, whereas diamond regrowth can occur immediately, a comprehensive kinetic study becomes crucial. Lastly, other catalysts, like Cu and Zn, can also catalyse the diamond regrowth, whereas none have vacant 3*d* or 4*s* orbitals to form any carbides at 6 GPa and 1600 °C[88]. The solid Co could also assist the diamond growth through the solid state diffusion and saturation under appropriate conditions[72].

In summary, investigating the reprecipitation process poses challenges, primarily in capturing metastable carbides or observing carbon deposition in-situ within a molten binder. However, the abovementioned findings strongly indicate that the reprecipitation process could be straightforward and universally applicable, such that, when diamond is the thermodynamically stable phase, the freely mobile carbon atoms in molten binder diffuse to the diamond/binder interface and, due to the difference in solubility between diamond and graphite, deposit onto the diamond surface via the $sp^3$ hybridisation, forming robust σ bonds. It is unknown, when all the non-diamond carbon atoms are dissolved and deposited, what would happen between the molten binder and diamond.

#### 2.2.4.2 Grain Growth via Movement of Grain Boundaries at Solid/Solid Interfaces

Another mechanism that has received little attention but is common in metal and other ceramic sintering studies is grain growth via movement of grain boundaries at solid/solid interfaces. This mechanism was only mentioned in a few earlier studies. Hong. *et al*.[89] firstly proposed an adhesion-and-coalescence process based on fracture surface observations of Co catalysed HPHT PCD materials after acid treatment, though with no supporting evidence, like EBSD mapping of GBs in attached fine and coarse grains. Park *et al*.[2] conducted a 12-hour-long Co catalysed HPHT dwell and obtained a diamond bridge between diamond grains as seen in figure 2.1. They attributed this bridge to grain boundary migration, a characteristic feature of grain growth, even though they also suggested

dissolution and reprecipitation as the regrowth mechanism. Likewise, due to limitations in available characterization techniques at that time, no further crucial evidence was presented. In contrast , Britun[11] merely reported an absence of diamond regrowth under binderless sintering conditions at 7.7 GPa and 2400-2500 °C, with no supporting evidence. There are no thermodynamic nor kinetic studies about this grain growth in PCD materials.

The most distinctive change associated with this grain growth is supposed to be the increase of the average grain size. This might be the most important evidence to prove the occurrence of movement of grain boundaries at solid/solid interfaces.

Conclusively, neither of these two diamond regrowth mechanisms provides a comprehensive explanation of how the GB is formed to connect diamond grains during dwell, which is the vital aspect of the whole HPHT sintering process.

## 2.3 The Relationship Between Diamond Regrowth and Mechanical Performance of PCD Materials

Because of the challenge in identifying regrown diamond and then quantitatively judging the degree of diamond regrowth, to the author's knowledge, no study has specifically focused on the relationship between diamond regrowth and the mechanical performance of PCD materials. Many studies simply speculated about the relationships between mechanical performance and diamond regrowth. The review concentrates on the potential impact of diamond regrowth on the two most commonly assessed mechanical properties, namely the wear resistance and the transverse rupture strength, also known as the flexural strength or the bend strength.

The influence of diamond regrowth on fracture toughness is not included owing to the difficulty of producing sufficiently sharp notches, which is not emphasized in many studies. If the radius of the notch tip is much larger than the inherent flaw size of the material, the toughness measured from

these notches is overestimated[90]. But it is in general anticipated that the formation of direct diamond-diamond bonding after sintering would increase the toughness of PCD materials [91].

### 2.3.1 Wear resistance

It is stated that diamond regrowth leads to the enlargement and reinforcement of connections between diamond grains, often referred to as "necks". German[70] mathematically postulated a relationship between neck size and sintering time, as shown in figure 2.16, implying that the diamond neck size will soar at the initial stages of sintering. This enhanced diamond connections, consequently, would generally improve the wear resistance of PCD materials[92]. Hibbs and Lee noticed the occasional abnormally large wear debris which they attributed to potential poor intergranular bonding or extensive fractured grains[93]. In their conclusion, poor diamond connections could lead to a catastrophic whole-grain fracturing mechanism. Pretorius commented that strong necks between diamond grains might inhibit this wear mechanism, favouring other, slower wear mechanism[94]. However, none of these studies treated the diamond connection as an isolated variable to study its impact on wear resistance.

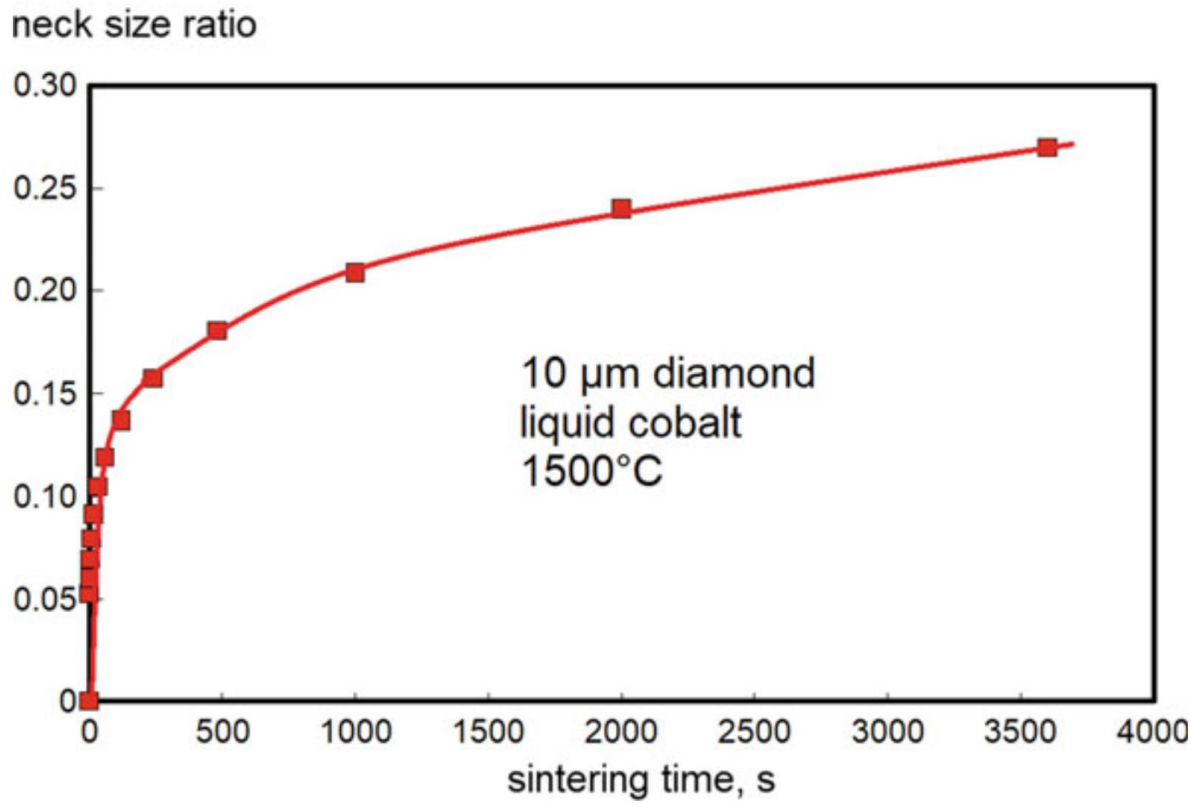


*Figure 2.16: Neck size ratio vs sintering time for a PCD materials diamond starting with a 10 µm average diamond grains and sintered at 1500 °C. [70]*

Shul'zhenko *et al.*[48] deliberately introduced n-layers graphene into PCD compacts as a carbon source to assist diamond regrowth during Si-assisted sintering at 7-7.5 GPa and 1250-1350 °C. They found a 7 times lower wear mass loss with the addition of 0.1wt% n-layers graphene, accompanied by smaller wear debris or fragments. These outcomes led to the deduction of strong necking between diamond grains when graphene was added. Chen *et al.*[95] similarly added pure graphene at 0.1wt% concentration into their PCD materials before sintering. A 33% improvement of the wear ratio and a 75% enhancement of the hardness were reported. However, these studies have a limitation in that the additional graphite source indirectly promotes the degree of diamond regrowth; practical evidence establishing the formation of more connections following these additions is lacking.

## 2.3.2 Transverse Rupture Strength (TRS)

Only a few studies have established a direct link between diamond regrowth and the Transverse Rupture Strength (TRS), despite the fact that the bonding between diamond grains can potentially

reduce the size of flaws on the tensile surface between diamond and binder. Lammer[96] restated that poor bonding between diamond grains could potentially lead to a decrease in the TRS. While noticing different TRS values between PCD materials with a different average grain sizes and remarking that the interfacial flaws, whose size would be affected by diamond regrowth, determine the TRS, Petrovic *et al*.[97] failed to establish a clear connection between this TRS difference and diamond connections. Qiu *et a.l*[98], claimed that the TRS is dependent on the bonding between diamond grains in PCD materials with a high diamond content. Regrettably, the presence of different types and amounts of binders within their PCD materials hindered their ability to further explore this dependent relationship.

## 2.4 Reference


(1) Walmsley, J. C.; Lang, A. R. Characteristics of Diamond Regrowth in a Synthetic Diamond Compact. *J. Mater. Sci.* **1988**, *23* (5), 1829–1834.

(2) Park, J. K.; Akaishi, M.; Yamaoka, S.; Fukunaga, O.; Eun, K. Y.; Yoon, D. N. Formation of Bridges between Diamond Particles during Sintering in Molten Cobalt Matrix. *J. Mater. Sci.* **1992**, *27* (17), 4695–4697.

(3) Moriyoshi, Y.; Akaishi, M.; Fukunaga, O. The Microstructure of WC and WC-4.3 Wt% Co Sintered at High Pressure. *J. Mater. Sci.* **1986**, *21* (12), 4250–4256.

(4) Bellin, F.; Dourfaye, A.; King, W.; Thigpen, M. The Current State of PDC Bit Technology. *World Oil* **2010**, *231* (11), 67–71.

(5) McKie, A.; Herrmann, M.; Sigalas, I.; Sempf, K.; Nilen, R. Suppression of Abnormal Grain Growth in Fine Grained Polycrystalline Diamond Materials (PCD). *Int. J. Refract. Met. Hard Mater.* **2013**, *41*, 66–72.

(6) Shin, T. J.; Oh, J. O.; Oh, K. H.; Lee, D. N. The Mechanism of Abnormal Grain Growth in Polycrystalline Diamond during High Pressure-High Temperature Sintering. *Diam. Relat. Mater.* **2004**, *13* (3), 488–494.

(7) Minnaar, E. G.; Westraadt, J. E.; Neethling, J. H. Microstructural Characterization of Polycrystalline Diamond Sintered at Ultrahigh Pressures. *Microsc. Microanal.* **2017**, *23* (S1), 2288–2289.

(8) Walmsley, J. C.; Lang, A. R. *Transmission Electron Microscopic Observations of Deformation and Microtwinning in a Synthetic Diamond Compact*; 1983; Vol. 2.

(9) Westraadt, J. E.; Dubrovinskaia, N.; Neethling, J. H.; Sigalas, I. Thermally Stable Polycrystalline Diamond Sintered with Calcium Carbonate. *Diam. Relat. Mater.* **2007**, *16* (11), 1929–1935.

(10) Westraadt, J. E.; Sigalas, I.; Neethling, J. H. Characterisation of Thermally Degraded Polycrystalline Diamond. *Int. J. Refract. Met. Hard Mater.* **2015**, *48*, 286–292.

(11) Britun, V. F.; Oleynik, G. S.; Semenenko, N. P. Deformation Processes during High-Pressure Sintering of the Diamond Powders Produced by Catalytic Synthesis. *J. Mater. Sci.* **1992**, *27* (16), 4472–4476.

(12) Abou-Ras, D.; Schorr, S.; Schock, H. W. Grain-Size Distributions and Grain Boundaries of Chalcopyrite-Type Thin Films. *J. Appl. Crystallogr.* **2007**, *40* (5), 841–848.

(13) Mahajan, S. Critique of Mechanisms of Formation of Deformation, Annealing and Growth Twins: Face-Centered Cubic Metals and Alloys. *Scr. Mater.* **2013**, *68* (2), 95–99.

(14) Yu, X.; Raterron, P.; Zhang, J.; Lin, Z.; Wang, L.; Zhao, Y. Constitutive Law and Flow Mechanism in Diamond Deformation. *Sci. Rep.* **2012**, *2*, 1–7.

(15) Luo, K.; Liu, B.; Hu, W.; Dong, X.; Wang, Y.; Huang, Q.; Gao, Y.; Sun, L.; Zhao, Z.; Wu, Y.; et al. Coherent Interfaces Govern Direct Transformation from Graphite to Diamond. *Nature* **2022**, *607* (7919), 486–491.

(16) Collins, A. T.; Robertson, S. H. Cathodoluminescence Studies of Sintered Diamond. *J. Mater. Sci. Lett.* **1985**, *4* (6), 681–684.

(17) Marinelli, M.; Hatta, A.; Ito, T.; Hiraki, A.; Nishino, T. Band-A Emission in Synthetic Diamond Films: A Systematic Investigation. *Applied Physics Letters*. 1996, pp 1631–1633.

(18) Dean, P. J. Bound Excitons and Donor-Acceptor Pairs in Natural and Synthetic Diamond. *Phys. Rev.* **1965**, *139* (2A).

(19) Yamamoto, N.; Spence, J. C. H.; Fathy, D. Cathodoluminescence and Polarization Studies from Individual Dislocations in Diamond. *Philos. Mag. B Phys. Condens. Matter; Stat. Mech. Electron. Opt. Magn. Prop.* **1984**, *49* (6), 609–629.

(20) Graham, R. J.; Moustakas, T. D.; Disko, M. M. Cathodoluminescence Imaging of Defects and Impurities in Diamond Films Grown by Chemical Vapor Deposition. *J. Appl. Phys.* **1991**, *69* (5), 3212–3218.

(21) Koizumi, S.; Watanabe, K.; Hasegawa, M.; Kanda, H. Ultraviolet Emission from a Diamond Pn Junction. *Science (80-. ).* **2001**, *292* (5523), 1899–1901.

(22) Kawarada, H.; Yokota, Y.; Mori, Y.; Nishimura, K.; Hiraki, A. Cathodoluminescence and Electroluminescence of Undoped and Boron-Doped Diamond Formed by Plasma Chemical Vapor Deposition. *J. Appl. Phys.* **1990**, *67* (2), 983–989.

(23) Ruan, J.; Kobashi, K.; Choyke, W. J. On the "Band-A" Emission and Boron Related Luminescence in Diamond. *Applied Physics Letters*. 1992, pp 3138–3140.

(24) Pennycook, S. J.; Brown, L. M.; Craven, A. J. Observation of Cathodoluminescence at Single Dislocations by STEM. *Philos. Mag. A Phys. Condens. Matter, Struct. Defects Mech. Prop.* **1980**, *41* (4), 589–600.

(25) Glenn, D. R.; Zhang, H.; Kasthuri, N.; Schalek, R.; Lo, P. K.; Trifonov, A. S.; Park, H.; Lichtman, J. W.; Walsworth, R. L. Correlative Light and Electron Microscopy Using Cathodoluminescence from Nanoparticles with Distinguishable Colours. *Sci. Rep.* **2012**, *2*, 1–6.

(26) Collins, A. T.; Kanda, H.; Burns, R. C. The Segregation of Nickel-Related Optical Centres in the Octahedral Growth Sectors of Synthetic Diamond. *Philos. Mag. B Phys. Condens. Matter; Stat. Mech. Electron. Opt. Magn. Prop.* **1990**, *61* (5), 797–810.

(27) Van Enckevort, W. J.; Visser, E. P. Photoluminescence Microtomography of Diamond. *Philos. Mag. B Phys. Condens. Matter; Stat. Mech. Electron. Opt. Magn. Prop.* **1990**, *62* (6), 597–614.

(28) Collins, A. T. The Characterisation of Point Defects in Diamond by Luminescence Spectroscopy. *Diam. Relat. Mater.* **1992**, *1* (5–6), 457–469.

(29) Daniel, R. D. The Influence of Nitrogen on the Plasticity of Diamond, University of Hull, 2000.

(30) Jones, R. Dislocations, Vacancies and the Brown Colour of CVD and Natural Diamond. *Diam. Relat. Mater.* **2009**, *18* (5–8), 820–826.

(31) Laidlaw, F. H. J.; Diggle, P. L.; Breeze, B. G.; Dale, M. W.; Fisher, D.; Beanland, R. Spatial Distribution of Defects in a Plastically Deformed Natural Brown Diamond. *Diam. Relat. Mater.* **2021**, *117* (March).

(32) Soltamova, A. A.; Il'in, I. V.; Shakhov, F. M.; Kidalov, S. V.; Vul', A. Y.; Yavkin, B. V.; Mamin, G. V.; Orlinskii, S. B.; Baranov, P. G. Electron Paramagnetic Resonance Detection of the Giant Concentration of Nitrogen Vacancy Defects in Sintered Detonation Nanodiamonds. *JETP Lett.* **2010**, *92* (2), 102–106.

(33) Baranov, P. G.; Soltamova, A. A.; Tolmachev, D. O.; Romanov, N. G.; Babunts, R. A.; Shakhov, F. M.; Kidalov, S. V.; Vul', A. Y.; Mamin, G. V.; Orlinskii, S. B.; et al. Enormously High Concentrations of Fluorescent Nitrogen-Vacancy Centers Fabricated by Sintering of Detonation Nanodiamonds. *Small* **2011**, *7* (11), 1533–1537.

(34) Webb, S. W.; Jackson, W. E. Synthetic Diamond Crystal Strength Enhancement through Annealing at 50 Kbar and 1500 °C. *J. Mater. Res.* **1995**, *10* (7), 1700–1709.

(35) Toth, M.; Phillips, M. R. Monte Carlo Modeling of Cathodoluminescence Generation Using Electron Energy Loss Curves. *Scanning* **1998**, *20* (6), 425–432.

(36) Malinauskas, T.; Jarasiunas, K.; Ivakin, E.; Ralchenko, V.; Gontar, A.; Ivakhnenko, S. Optical Evaluation of Carrier Lifetime and Diffusion Length in Synthetic Diamonds. *Diamond and Related Materials*. 2008, pp 1212–1215.

(37) Yacobi, B. G.; Holt, D. B. *Cathodoluminescence Microscopy of Inorganic Solids*; Springer US: Boston, MA, 1990.

(38) Mandal, S.; Bhaduri, A. K.; Subramanya Sarma, V. A Study on Microstructural Evolution and Dynamic Recrystallization during Isothermal Deformation of a Ti-Modified Austenitic Stainless Steel. *Metall. Mater. Trans. A Phys. Metall. Mater. Sci.* **2011**, *42* (4), 1062–1072.

(39) Hadadzadeh, A.; Mokdad, F.; Wells, M. A.; Chen, D. L. A New Grain Orientation Spread Approach to Analyze the Dynamic Recrystallization Behavior of a Cast-Homogenized Mg-Zn-Zr Alloy Using Electron Backscattered Diffraction. *Mater. Sci. Eng. A* **2018**, *709* (October 2017), 285–289.

(40) Cao, Y.; Di, H.; Zhang, J.; Zhang, J.; Ma, T.; Misra, R. D. K. An Electron Backscattered Diffraction Study on the Dynamic Recrystallization Behavior of a Nickel-Chromium Alloy (800H) during Hot Deformation. *Mater. Sci. Eng. A* **2013**, *585*, 71–85.

(41) Miller, V. M.; Pollock, T. M. Texture Modification in a Magnesium-Aluminum-Calcium Alloy During Uniaxial Compression. *Metall. Mater. Trans. A Phys. Metall. Mater. Sci.* **2016**, *47* (4), 1854–1864.

(42) Mohapatra, D. R.; Jain, L.; Rai, P.; Hazra, K. S.; Samajdar, I.; Misra, D. S. Development of Crystallographic Texture and In-Grain Misorientation in CVD-Produced Single and Polycrystalline Diamond. *Chemical Vapor Deposition*. 2011, pp 107–113.

(43) Brewer, L. N.; Field, D. P.; Merriman, C. C. Mapping and Assessing Plastic Deformation Using EBSD. *Electron Backscatter Diffr. Mater. Sci.* **2009**, 251–262.

(44) Akaishi, M.; Yamaoka, S.; Tanaka, J.; Ohsawa, T.; Fukunaga, O. Synthesis of Sintered Diamond with a High Electrical Resitivity and High Hardness. *Mater. Sci. Eng. A* **1988**, *105–106* (PART 2), 517–523.

(45) Robert H, F. Composite Polycrystalline Diamond Compact with Improved Impact and Thermal Stability. 5,645,617, 1997.

(46) Fries, R.; Sigalas, I.; Nebelung, M. Polycrystalline Abrasive Grit. US 6,913,633 B2, July 5, 2005.

(47) Kamali, A. R. Black Diamond Powder: On the Thermal Oxidation and Surface Graphitization. *Appl. Surf. Sci.* **2021**, *551* (January).

(48) Shul'zhenko, A. A.; Jaworska, L.; Sokolov, A. N.; Gargin, V. G.; Petasyuk, G. A.; Belyavina, N. N.; Zakora, A. P.; Suprun, M. V.; Tkach, V. N. Novel Wear-Resistant Superhard Diamond Composite Polycrystalline Material. *J. Superhard Mater.* **2018**, *40* (1), 1–7.

(49) Sigalas, I.; Caveney, R. J.; Bailey, M. W. Diamond Materials and Their Applications. In *Handbook of Ceramic Hard Materials*; Wiley-VCH Verlag GmbH: Weinheim, Germany, 2008; pp 478–572.

(50) Walmsley, J. C. The Microstructure of Ultrahard Material Compacts Studied by Transmission Electron Microscopy. *Mater. Sci. Eng.* **1988**, *105–106* (PART 2), 549–553.

(51) Guan, S.; Peng, F.; Liang, H.; Fan, C.; Tan, L.; Wang, Z.; Zhang, Y.; Zhang, J.; Yu, H.; He, D. Fragmentation and Stress Diversification in Diamond Powder under High Pressure. *J. Appl. Phys.* **2018**, *124* (21).

(52) Bobrovnitchii, G. S.; Osipov, O. S.; Filgueira, M. Some Peculiarities of the Diamond Micro-Powder Sintering. *Int. J. Refract. Met. Hard Mater.* **2003**, *21* (5–6), 251–258.

(53) Deng, L.; Nilen, R.; Ozbayraktar, S. The Effects of Diamond Grit Characteristics on the Microstructure and Abrasion Resistance of Pcds Sintered by HPHT. *Ceram. Eng. Sci. Proc.* **2018**, *38* (2), 3–10.

(54) Deng, F.; Yang, X.; Deng, W.; Zhou, L.; Wang, H.; Zhang, Z. Law of Crushing of Diamond Powders by Ultra-High Pressure Extrusion. *Diam. Relat. Mater.* **2019**, *96* (January), 25–30.

(55) Uehara, K.; Yamaya, S. High Pressure Sintering of Diamond by Cobalt Infiltration. *Int. J. Refract. Met. Hard Mater.* **1988**, *7* (4), 219–223.

(56) Wang, C.; Song, X.; Shen, X.; Sun, F. Molecular Dynamics Simulation and Experimental

Investigation of Structural Transformation and Graphitization in Diamond during Friction. *Comput. Mater. Sci.* **2020**, *184*.

(57) Dang, C.; Chou, J. P.; Dai, B.; Chou, C. T.; Yang, Y.; Fan, R.; Lin, W.; Meng, F.; Hu, A.; Zhu, J.; et al. Achieving Large Uniform Tensile Elasticity in Microfabricated Diamond. *Science (80-. ).* **2021**, *371* (6524), 76–78.

(58) Regan, B.; Aghajamali, A.; Froech, J.; Tran, T. T.; Scott, J.; Bishop, J.; Suarez-Martinez, I.; Liu, Y.; Cairney, J. M.; Marks, N. A.; et al. Plastic Deformation of Single-Crystal Diamond Nanopillars. *Adv. Mater.* **2020**, *32* (9).

(59) Mussi, A.; Eyidi, D.; Shiryaev, A.; Rabier, J. TEM Observations of Dislocations in Plastically Deformed Diamond. *Phys. Status Solidi Appl. Mater. Sci.* **2013**, *210* (1), 191–194.

(60) Christian, J. W.; Mahajan, S. Deformation Twinning. *Progress in Materials Science*. 1995, pp 1–157.

(61) Woods, G. S. Electron Microscope Observations of Stacking Faults and Microtwins in Synthetic Diamond. *Philos. Mag.* **1971**, *23* (182), 473–484.

(62) Yin, L. W.; Li, M. Sen; Cui, J. J.; Bai, Y. J.; Xu, B.; Gong, J. H.; Hao, Z. Y. Planar Defects and Dislocations in HPHT As-Grown Diamond Crystals. *Diam. Relat. Mater.* **2002**, *11* (2), 268–272.

(63) Kondo, K.; Sawai, S.; Akaishi, M.; Yamaoka, S. Deformation Behaviour of Shock-Synthesized Diamond Powder under High Pressures and High Temperatures. *J. Mater. Sci. Lett.* **1993**, *12* (17), 1383–1385.

(64) Bokhonov, B. B.; Dudina, D. V.; Sharafutdinov, M. R. Graphitization of Synthetic Diamond Crystals: A Morphological Study. *Diam. Relat. Mater.* **2021**, *118* (August).

(65) Lee, J. K.; Lee, S. C.; Ahn, J. P.; Kim, S. C.; Wilson, J. I. B.; John, P. The Growth of AA Graphite on (111) Diamond. *J. Chem. Phys.* **2008**, *129* (23), 127–130.

(66) Khmelnitsky, R. A.; Gippius, A. A. Transformation of Diamond to Graphite under Heat Treatment at Low Pressure. *Phase Transitions* **2014**, *87* (2), 175–192.

(67) Fedoseev, D. V.; Sokolina, G. A.; Yakovlev, E. N.; Lavrent'ev, A. V.; Lazareva, O. I.; Afanas'eva, L. F. Porosity Changes in the Sintering of Diamond Powders. *Sov. Powder Metall. Met. Ceram.* **1984**, *23* (9), 683–686.

(68) Liu, J.; Zhan, G.; Wang, Q.; Yan, X.; Liu, F.; Wang, P.; Lei, L.; Peng, F.; Kou, Z.; He, D. Superstrong Micro-Grained Polycrystalline Diamond Compact through Work Hardening under High Pressure. *Appl. Phys. Lett.* **2018**, *112* (6).

(69) Akaishi, M.; Kanda, H.; Sato, Y.; Setaka, N.; Ohsawa, T.; Fukunaga, O. Sintering Behaviour of the Diamond-Cobalt System at High Temperature and Pressure. *J. Mater. Sci.* **1982**, *17* (1), 193–198.

(70) German, R. M. Sintering Window and Sintering Mechanism for Diamond. *Int. J. Refract. Met. Hard Mater.* **2023**, *117*, 151–160.

(71) Tulić, S.; Waitz, T.; Čaplovičová, M.; Habler, G.; Varga, M.; Kotlár, M.; Vretenár, V.; Romanyuk, O.; Kromka, A.; Rezek, B.; et al. Covalent Diamond-Graphite Bonding: Mechanism of Catalytic Transformation. *ACS Nano* **2019**, *13* (4), 4621–4630.

(72) Tian, Y.; Wang, J.; Zhang, J.; Guan, S.; Zhang, L.; Wu, B.; Su, Y.; Huang, M.; Zhou, L.; He, D. Solubility and Stability of Diamond in Cobalt under 5 GPa. *Diam. Relat. Mater.* **2020**, *110* (September), 1–7.

(73) Shen, B.; Ji, Z.; Lin, Q.; Gong, P.; Xuan, N.; Chen, S.; Liu, H.; Huang, Z.; Xiao, T.; Sun, Z. Graphenization of Diamond. *Chem. Mater.* **2022**, *34* (9), 3941–3947.

(74) Tulić, S.; Waitz, T.; Čaplovičová, M.; Habler, G.; Vretenár, V.; Susi, T.; Skákalová, V. Catalytic Graphitization of Single-Crystal Diamond. *Carbon N. Y.* **2021**, *185*, 300–313.

(75) Sung, C. M.; Tai, M. F. Reactivities of Transition Metals with Carbon: Implications to the Mechanism of Diamond Synthesis Under High Pressure. *Int. J. Refract. Met. Hard Mater.* **1997**, *15* (4), 237–256.

(76) Belnap, J. D. Sintering of Ultrahard Materials. *Sinter. Adv. Mater.* **2010**, 389–414.

(77) Hong, S. M.; Akaishi, M.; Kanda, H.; Osawa, T.; Yamaoka, S.; Fukunaga, O. Behaviour of Cobalt Infiltration and Abnormal Grain Growth during Sintering of Diamond on Cobalt Substrate. *J. Mater. Sci.* **1988**, *23* (11), 3821–3826.

(78) Katzman, H.; Libby, W. F. Sintered Diamond Compacts with a Cobalt Binder. *Science (80-. ).* **1971**, *172* (3988), 1132–1134.

(79) Notsu, Y.; Nakajima, T.; Kawai, N. Sintering of Diamond with Cobalt. *Mater. Res. Bull.* **1977**, *12* (11), 1079–1085.

(80) De, S.; Heaney, P. J.; Fei, Y.; Vicenzi, E. P. Microstructural Study of Synthetic Sintered Diamond and Comparison with Carbonado, a Natural Polycrystalline Diamond. *American Mineralogist*. 2004, pp 438–445.

(81) Sibanda, M.; Eric, R. H.; Koursaris, A. Solid State Diffusion of Carbon in the Co-5% Fe-C System at High Pressure: Metallography and Phase Equilibrium. *J. South African Inst. Min. Metall.* **2005**, *105* (7), 465–472.

(82) Fedoseev, D. V.; Sokolina, G. A.; Yakovlev, E. N.; Lavrent'ev, A. V.; Lazareva, O. I.; Afanas'eva, L. F. Porosity Changes in the Sintering of Diamond Powders. *Sov. Powder Metall. Met. Ceram.* **1984**, *23* (9), 683–686.

(83) Strong, H. M.; Hanneman, R. E. Crystallization of Diamond and Graphite. *J. Chem. Phys.* **1967**, *46* (9), 3668–3676.

(84) Liu, Z.; Zhilin, L. I.; Sun, Z. Catalysis Mechanism and Catalyst Design of Diamond Growth.

*Metall. Mater. Trans. A Phys. Metall. Mater. Sci.* **1999**, *30* (11), 2757–2766.

(85) Fan, X. H.; Xu, B.; Tian, B.; Guo, X. F.; Wang, X. L. Microstructures of Diamond/Metallic Film Interface and Growth Mechanism of Diamond in Fe-Ni-C System at High Pressure and High Temperature. *Mater. Res. Innov.* **2013**, *17* (SUPPL. 1), 45–48.

(86) Yin, L. W.; Li, M. Sen; Cui, J. J.; Zou, Z. Da; Liu, P.; Hao, Z. Y. Diamond Formation Using Fe3C as a Carbon Source at High Temperature and High Pressure. *J. Cryst. Growth* **2002**, *234* (1), 1–4.

(87) Esconjauregui, S.; Whelan, C. M.; Maex, K. The Reasons Why Metals Catalyze the Nucleation and Growth of Carbon Nanotubes and Other Carbon Nanomorphologies. *Carbon N. Y.* **2009**, *47* (3), 659–669.

(88) Kanda, H.; Akaishi, M.; Yamaoka, S. New Catalysts for Diamond Growth under High Pressure and High Temperature. *Appl. Phys. Lett.* **1994**, *65* (6), 784–786.

(89) Hong, S. M.; Akaishi, M.; Kanda, H.; Osawa, T.; Yamaoka, S. Dissolution Behaviour of Fine Particles of Diamond under High Pressure Sintering Conditions. *J. Mater. Sci. Lett.* **1991**, *10* (3), 164–166.

(90) Scott, T. The Effect of High Temperature on Polycrystalline Diamond, Oxford, 2019.

(91) Wentorf, R. H.; DeVries, R. C.; Bundy, F. P. Sintered Superhard Materials. *Science (80-. ).* **1980**, *208* (4446), 873–880.

(92) Yahiaoui, M.; Paris, J. Y.; Delbé, K.; Denape, J.; Gerbaud, L.; Colin, C.; Ther, O.; Dourfaye, A. Quality and Wear Behavior of Graded Polycrystalline Diamond Compact Cutters. *Int. J. Refract. Met. Hard Mater.* **2016**, *56*, 87–95.

(93) Hibbs, L. E.; Lee, M. Some Aspects of the Wear of Polycrystalline Diamond Tools in Rock Removal Processes. *Wear* **1978**, *46* (1), 141–147.

(94) Pretorius, C. J.; Soo, S. L.; Aspinwall, D. K.; Harden, P. M.; M'Saoubi, R.; Mantle, A. L. Tool

Wear Behaviour and Workpiece Surface Integrity When Turning Ti-6Al-2Sn-4Zr-6Mo with Polycrystalline Diamond Tooling. *CIRP Ann.* **2015**, *64* (1), 109–112.

(95) Chen, Z.; Ma, D.; Wang, S.; Dai, W.; Li, S.; Zhu, Y.; Liu, B. Effects of Graphene Addition on Mechanical Properties of Polycrystalline Diamond Compact. *Ceram. Int.* **2020**, *46* (8), 11255–11260.

(96) Lammer, A. Mechanical Properties of Polycrystalline Diamonds. *Mater. Sci. Technol. (United Kingdom)* **1988**, *4* (11), 949–955.

(97) Petrovic, M.; Ivankovic, A.; Murphy, N. The Mechanical Properties of Polycrystalline Diamond as a Function of Strain Rate and Temperature. *J. Eur. Ceram. Soc.* **2012**, *32* (12), 3021–3027.

(98) Qiu, T.; Feng, J.; Cai, B.; Fan, G.; Zhang, W.; Liu, Y. Microstructural Evolution of Diamond-Based Composites at High Temperature and High Pressure. *Materials (Basel).* **2022**, *15* (24).

# 3 Experimental

# Table of Contents

## 3.1 Introduction

This chapter describes all the experimental methods throughout the thesis, other techniques specific to each chapter will be described in those chapters.

## 3.2 PCD Sample Preparation

All of the PCD samples mentioned in this thesis were provided by Element Six Ltd. Herein, a standard PCD sample (SPCD) is defined as one manufactured via the processes described in section 3.2.1. Any deviation from the SPCD is highlighted and discussed in the respective "Materials and Sample Preparation" section in each chapter.

### 3.2.1 PCD Cutter Manufacturing

In the production of SPCDs, the PCD raw powders were composed of diamond powders and Co powders (mean diameter 1 μm) with a weight ratio of 100:1. The diamond powders consisted of coarse powders (95 wt%, mean diameter 22 μm) and fine powders (5 wt%, mean diameter 2 μm). A SE2 image of PCD raw powders is shown in figure 3.1:

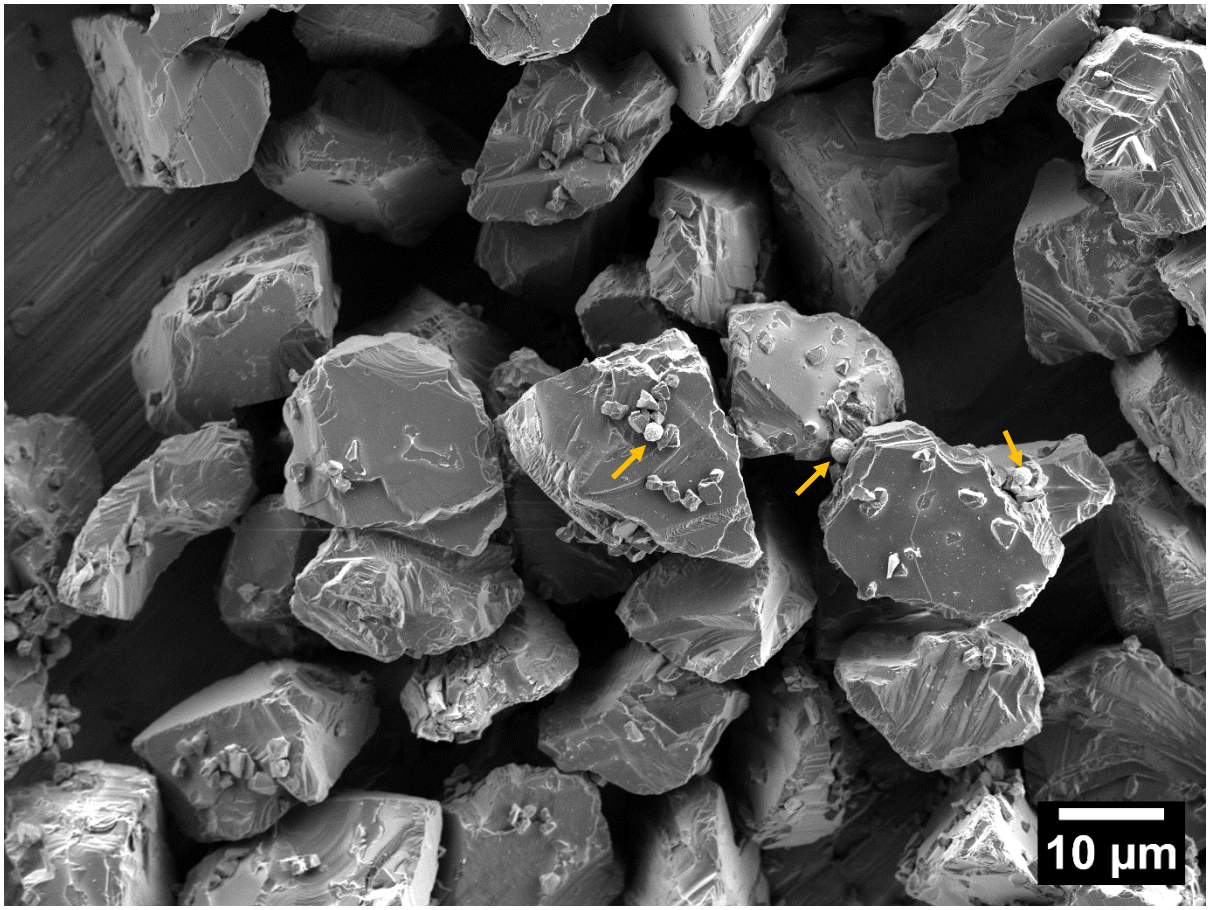


*Figure 3.1: The SE2 image of the PCD raw powder. The Co powders (labelled in orange arrows) are spherical, while the diamond powders are less regular shaped with steps and kinks.*

After confirming the powder composition, the PCD cutters were manufactured via the flow chart in figure 3.2.


*Figure 3.2: the flow chart of the PCD cutter manufacturing processes*

1. Powder mixing: At a clean room, PCD raw powders were added to a Resodym LabRAM II acoustic mixer (Resodyn Acoustic Mixer, USA) for admixing. The details of the time and power used for admixing are confidential. The aim of this step is to enable a uniform admixed PCD raw powder.
2. Pre-composite assembly: The admixed PCD raw powder was transferred into an inner alloyed cup on the tray inside a mixing machine (Retsch As200, Germany) for further admixing. The details of the time and power used for admixing are confidential. Subsequently, the inner cup

was sealed with the cutter substrate, rich in binder. Now it had a two-layer structure, a thin layer of PCD table admixed with Co powders and a thick substrate layer rich in Co. The assembled composite was stored in this clean room. A PCD skeleton refers to the structure of the contacted diamond and Co powders with interstitial voids and gaps between them.

3. Vacuum heated outgassing: The assembled composite was placed into a furnace (Cambridge Vacuum Engineering, UK) to heat in vacuum to more than 800 °C. The detail is confidential. The purpose of this step is to minimise non-diamond impurities on diamond surfaces.
4. Electron beam welding: The outgassed samples were double-cupped in outer metal cups, one on the top and one on the bottom. The overlapping regions of the cups in the middle of the sample were welded in a low vacuum environment to prevent further contamination from oxygen in the air. It also aids in sintering as the pressure-transfer medium will be prevented from contaminating the PCD powders.
5. Sintering: the sealed outgassed samples were assembled into a cubic press capsule and placed in the HPHT press. The identical pressure was applied onto each of the six surfaces of this cubic press capsule from the HPHT press. More details of the cubic press can be found in literature[1]. The P-T parameters related to the HPHT sintering are depicted in figure 3.3.

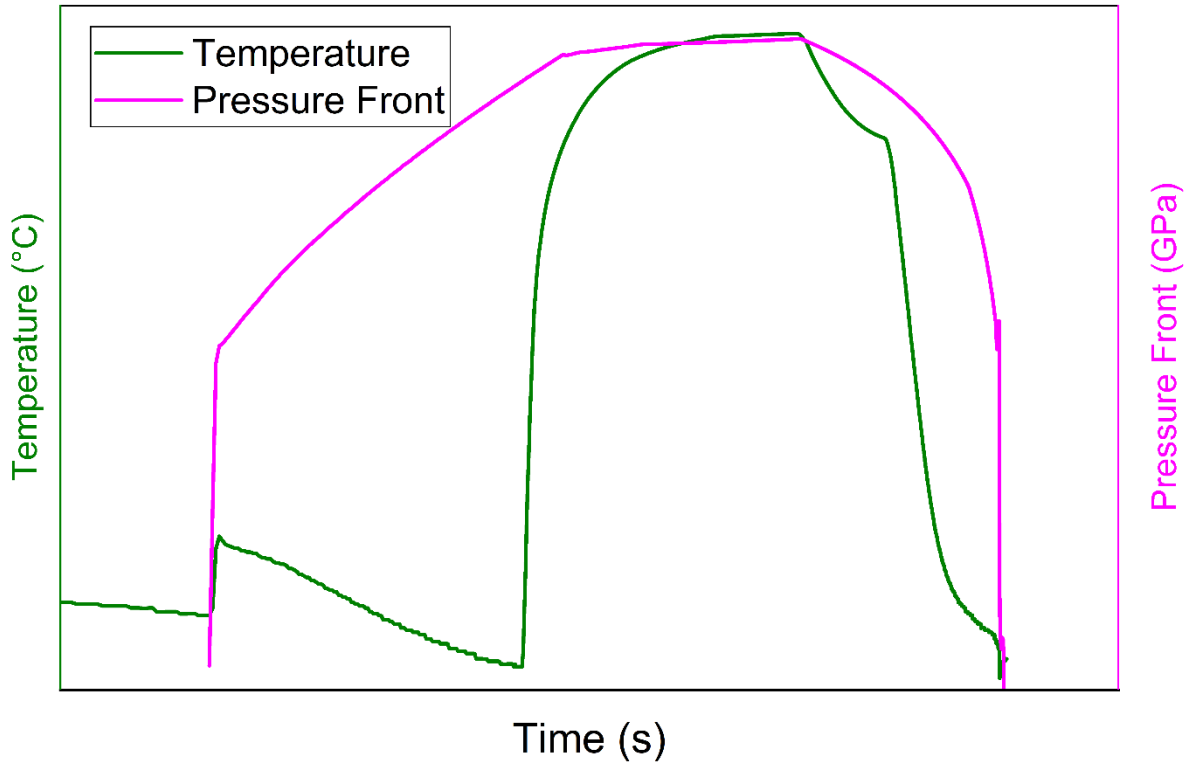


*Figure 3.3: the HPHT sintering profile for the SPCD.* ***Most of the details were wiped due to confidentiality requirement. Tmax ranges from 1500- 1800 °C. Pmax ranges from 6.5-8.5 GPa.***

6. Post-treatment: After the sintering process, the sintered PCD cutters were cleaned to remove the dust and ash residues from the capsule. They were then Electrical Discharge Machined (EDM) cut, ground to remove large amounts of material and lapped to achieve the designed geometry. The residual stress could be partially alleviated via a confidential post-fabrication vacuum heat treatment. This was done by the fast prototype processing team at Element Six Ltd.

A typical PCD cutter is shown in figure 3.4.

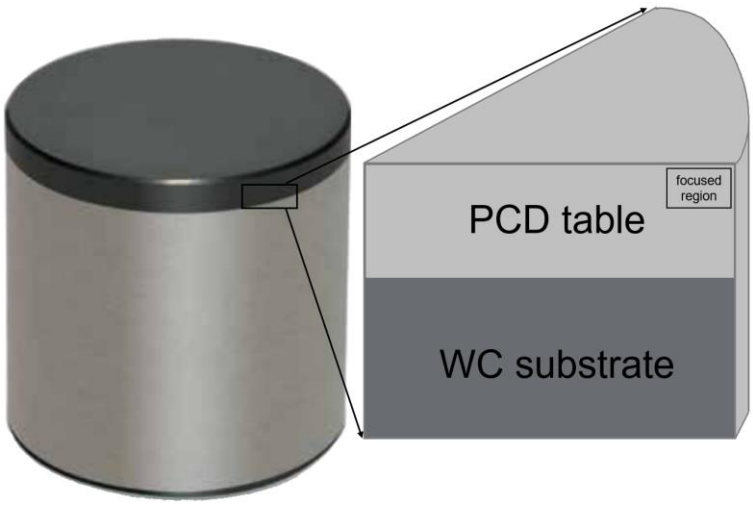


*Figure 3.4: a typical PCD cutter. The enlarged region is the cross section of a SEM sample. All the TEM samples are lifted out from the rectangular research focused region.*

### 3.2.2 SEM Sample Preparation

Once the PCD cutter was prepared, a piece of SEM sample (4*6 cm) was fabricated by the same methods as were used for the post treatment described above. The subsequent fine preparation took place at Oxford. Firstly, a PCD SEM sample was washed in acetone ultrasonically for 5 mins. It was then transferred to a PIPS 2 Ar Plasma Precision Etching System (Gatan, USA) for surface polishing. The polishing was carried out at 3kV with a 3° tilt of the Ar gun, and lasted for 30 minutes. Lastly, the sample was cleaned in the Fischione 1020 plasma cleaner (Fischione, USA) using a mixed gas of Ar (75 vol%) and $O_2$ (25 vol%) for 1 to 2 mins.

Figure 3.5 a) and b) are the SE2 and EsB images of a typical surface of PCD materials after all treatments and preparations.

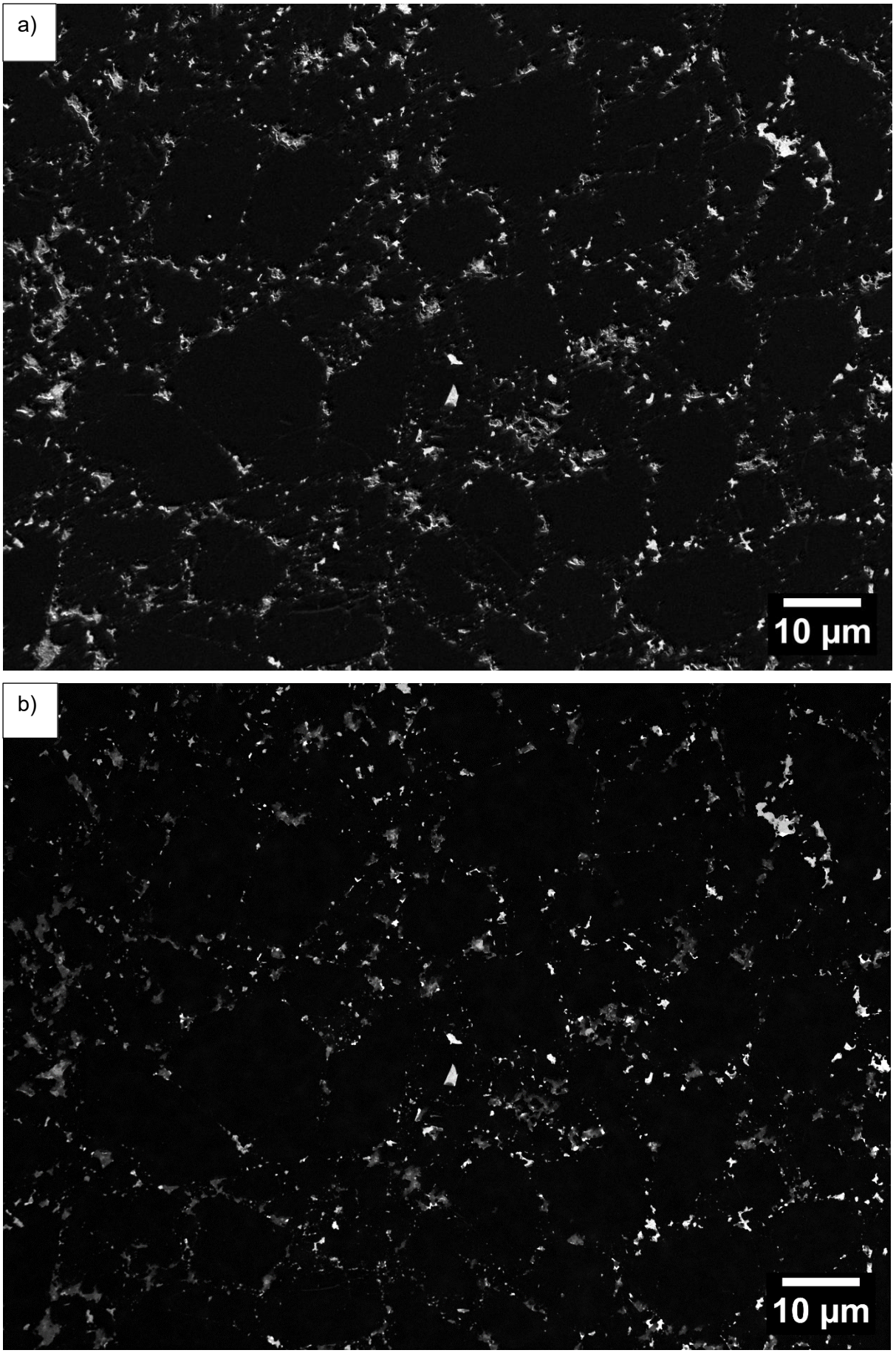


*Figure 3.5: a typical surface of a SPCD. a) an SE2 image b) an EsB image. Diamond is black, Co is grey and WC is white*

### 3.2.3 TEM Sample Preparation

EM samples were prepared via Zeiss Nvision SEM-FIB (Zeiss, Germany). The target region is selected from the SEM PCD sample and covered with an amorphous carbon protective layer. The surrounding regions were trenched. The remained target region was undercut and lifted out *in-situ* to be transformed to an Omniprobe Cu grid. The lamella was thinned until it reached a good electron transparency. A successfully fabricated PCD TEM sample is shown in figure 3.6.

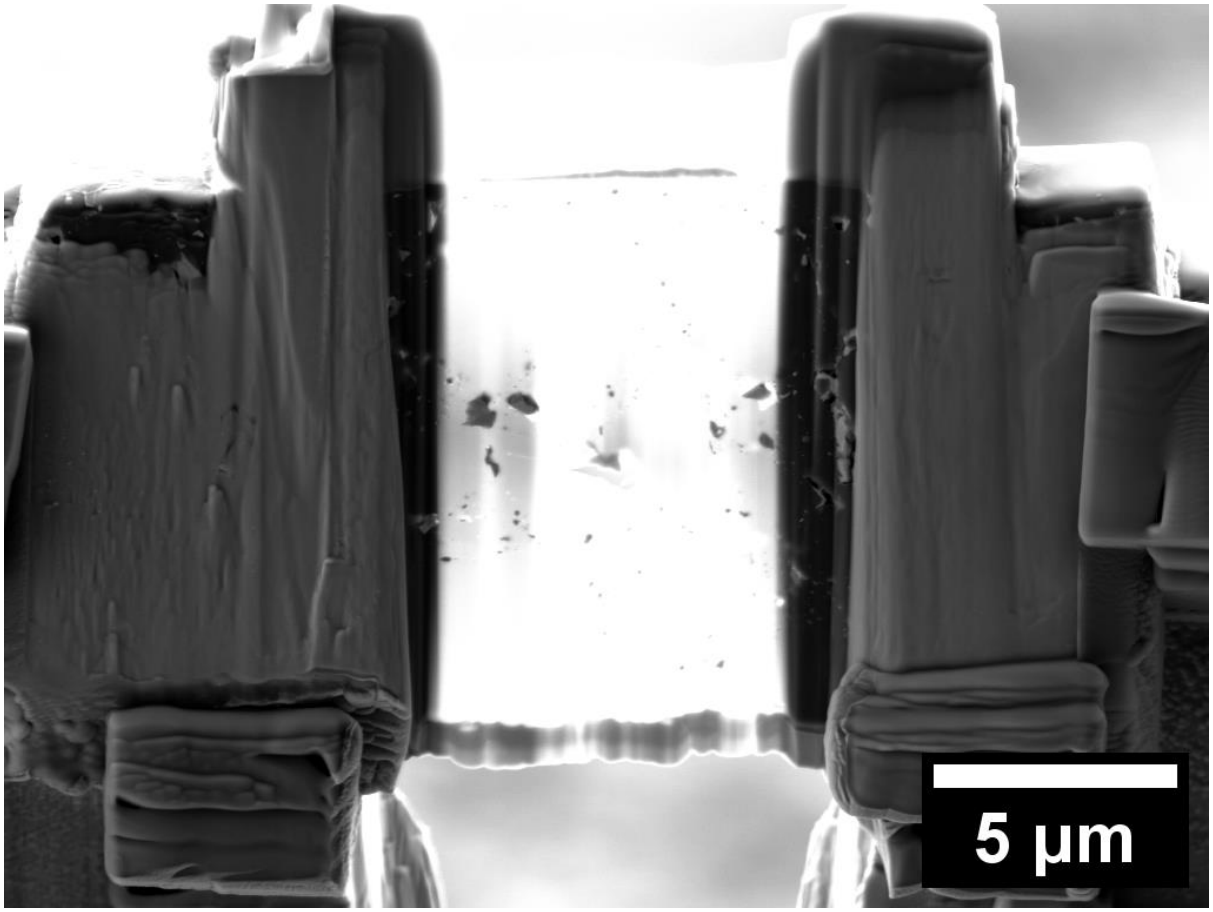


*Figure 3.6: an SE2 image of a fabricated PCD TEM sample. The image was taken at 5 kV.*

## 3.3 Electron Microscopy Characterization

### 3.3.1 Scanning Electron Microscopy

All the SEM images were taken from either Zeiss Merlin EBSD SEM (Zeiss, Germany) or Zeiss Merlin EDX SEM (Zeiss, Germany). With the different emphases, different types of SEM images were taken. Table 3.1 below lists the different types of SEM images from different electron detectors:

| Type | Detector | Signals | Voltage | Current | Remarks |
|---|---|---|---|---|---|
| SE2 | an Everhart–Thornley type detector | SE+BSE (1:1) | 2 kV | 350 pA | **Surface topography contrast** + some **compositional contrast** |
| Inlens | In-lens SE detector | Mostly SE | | | **Shallow surface structure (~10 nm)** |
| EsB | Energy selective backscattered detector | Mostly BSE | 2-5 kV | 350-1000 pA | **Pure compositional contrast** |
| AsB | Angular selective backscattered detector | Mostly BSE with a tiny portion of SE | 7 kV | 500 pA | Mainly **compositional contrast** |

*Table 3.1: the details of different types of SEM images of the corresponding detectors.*

The SEM operating voltage, if not specifically mentioned in captions, is referenced as the values listed in table 3.1. SEM images were usually captured at 2 kV, 350 pA to minimise the local charging in the semi-conductive PCD material[2,3]. Therefore, no conductive coating was applied as the impact of charging is negligible during imaging.

### 3.3.2 Electron Backscatter Diffraction (EBSD) Mapping

All EBSD maps were taken using a Zeiss Merlin EBSD SEM (Zeiss, Germany) with a Bruker Quantax EBSD system and forward scattered electron detectors, usually at 10 kV, 10 nA to boost the mapping resolution. The lowest pixel step was set to 31 nm, which was estimated from the Monte Carlo simulation. From the view point of configuration, the SEM PCD sample was tilted to 70° with an 18-

mm working distance and a detector distance ranging from 13.5 to 18 mm. Though the higher voltage and current settings of EBSD, compared to SEM imaging, may cause significant charging on the sample surface, the 70° sample tilt helps mitigate this issue. It enhances both secondary and backscattered electron coefficients, leading to more SE and BSE being scattered out of sample surface[4,5]. In practice, relatively high-energy diffracted BSEs are less affected by the weaker charging field after the 70° tilt and consequently a clear Kikuchi pattern with a good signal-to-noise ratio can be obtained and recognized by detectors.

All the EBSD data were analysed via the HKL Channel 5 software (Oxford instrument, UK).

### 3.3.3 ARGUS™ Forescattered Imaging

Taken from the Zeiss Merlin EBSD signal, the ARGUS images present the channelling contrast of diamond grains. The imaging setting resembles that of EBSD with little differences in a longer detector distance of 31 mm, an extra 6.7° tilt of detector and a longer working distance of 19 mm. Three forescattered detectors are mounted under the EBSD detector, recording the intensity of forescattered electrons from one pixel in red, green and blue colours respectively. The three different colours are then mixed to form an RGB colour designated to this pixel. Consequently, pixels from different orientations will display different colours in the ARGUS image. Owing to its special configuration, the ARGUS image shows a high orientation sensitivity[6]. A grain with a low misorientation within it will display a uniform colour, while a heavily deformed grain will likely display colour gradients or even several colours within it. A grain boundary can be quickly recognized by discerning the different colours by its two sides.

### 3.3.4 Linear Intercept Analysis

The average linear intercept of grains in 2D is linked to the average 3D grain size via a parameter $S_v$ (grain boundary surface area to grain volume ratio)[7]. In polycrystalline ceramics with some reasonable estimations,

$$\overline{D} = S_v \times \overline{L} = 1.558 \times \overline{L}$$

where $\overline{D}$ is the average grain size and $\overline{L}$ is the average linear intercept[7,8]. $\overline{L}$ can be derived from EM images that show the grain boundaries of the PCD.

The linear interception analysis was conducted on ARGUS images. Specifically, five ARGUS images were captured at x1000 magnification with a step size of 33 nm from five distinct regions in PCD, including the top-right, top-left, middle, bottom-left, and bottom-right regions. For some undersintered samples, ten ARGUS images from those five same regions were taken due to its lower grain density. An evenly distributed 6x6 grid was superimposed on each ARGUS image to generate the intercepts on diamond grains. The length of each interception was measured and labelled using ImageJ[9]. An example of a measured and labelled ARGUS image is demonstrated in figure 3.7.

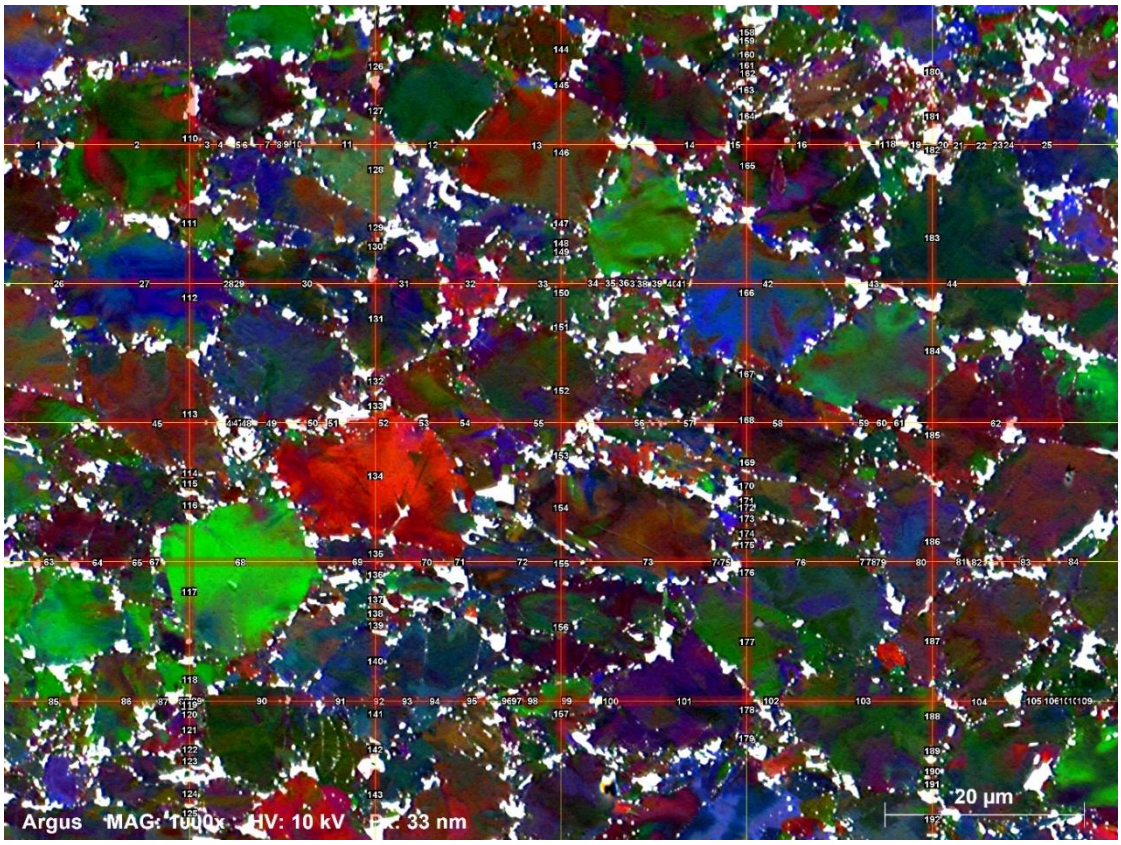


*Figure 3.7: ARGUS image from the top left region of sample No.5.An evenly distributed 6x6 yellow grid is superimposed and the effective interceptions within each grain are measured and labelled in red with corresponding numbers.*

To reduce the ambiguity in intercept measurement, only intercept longer than 15 step sizes (approximately 0.5 µm) is defined as effective. Approximately 1000 effective intercepts were

recorded for each sample. The average grain size is determined by multiplying the measured average intercept length by the constant factor of 1.558.

### 3.3.5 Energy Dispersive X-ray Spectroscopy

All EDX maps and spectra were taken using a Zeiss Merlin EDX SEM with an Oxford instruments Xmax 150 EDX detector. The voltage was set to 5 kV which is sufficient to include the Kα1 peak of Carbon, $L\alpha_{1,2}$ peaks of Co and $M\alpha_1$ peak of W in the EDX spectrum for qualitative and relative quantitative analysis. The dwell time was set to more than 100 μs to give enough signal to the X-ray detectors. All EDX data are processed via the Aztec Oxford Instruments software.

### 3.3.6 Transmission Electron Microscopy

All TEM images, including bright field images, centred dark field images and diffraction patterns, were captured at 200 kV via the JEOL JEM-2100 TEM (JEOL, Japan) with an Oxford Instruments 80mm thin window EDS detector and a Gatan Orius CCD camera.

### 3.3.7 Scanning Transmission Electron Microscopy

All STEM images, EELS & EDX spectrums and EDX maps were taken at 200 kV from JEOL ARM-200F STEM (JEOL, Japan) with a 100 $mm^2$ Centurion EDX detector and a Gatan GIF Quantum 965 ER. All results from STEM were acquired and analysed by PhD candidate Ruomu Zhang.

High-Angle Annular Dark-Field (HAADF) images were taken to show the Z contrast mainly between diamond and binder.

Low-Angle Annular Dark-Field (LAADF) images were taken to show the diffraction contrast mainly between diamond and graphite.

## 3.3.8 FIB-SEM 3D tomography

The FIB-SEM 3D tomography was performed on a Zeiss Auriga FIB-SEM (Zeiss, Germany) using ZEISS Atlas 3D software.

The SEM PCD sample was tilted to 54°. A 5 µm thick top-platinum bottom-carbon protective layer was coated on the target region. A surface mark was carved on the protective layer for alignment and the auto focus of SEM imaging was used during sectioning. Three sides of the coated region were trenched to avoid re-deposition on the cross section of the target region. A PCD sample ready for 3D sectioning is shown in figure 3.8.

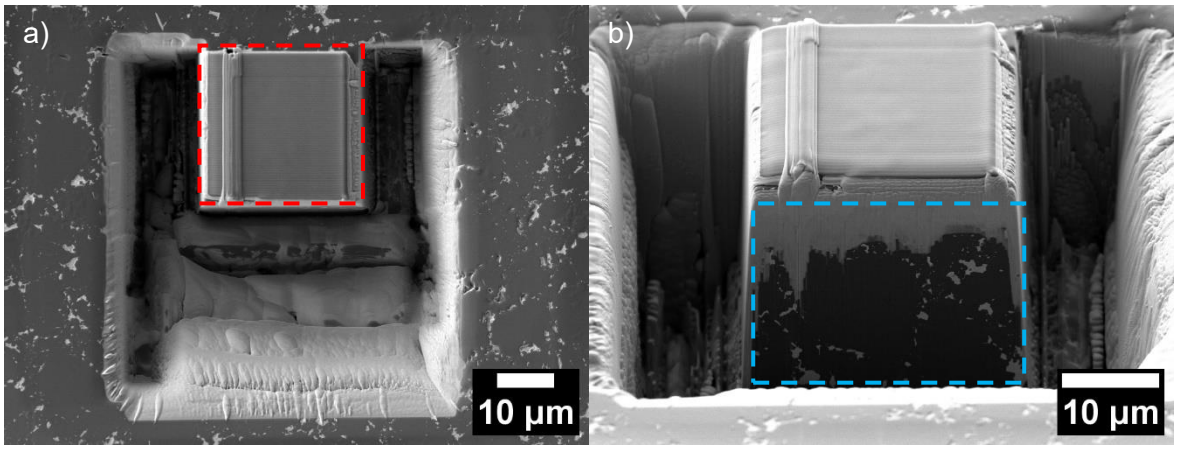


*Figure 3.8: SEM images of a PCD sample prepared before sectioning. a) at 0° tilt b) at 54° tilt. The red rectangle in a) is the plan view of the carbon protective layer before deposing another Pt layer. The blue rectangle in b) is the cross section.*

The SEM imaging condition was at 2 kV and 300 pA. The FIB was set to 30 kV, 2 nA to enable a relatively smooth finish on the cross section and a desirable sectioning speed. With a pre-set voxel size of 10x10x20 nm in the stack of SEM images, the sectioning speed between neighbouring SEM images depends on the size of the cross section and ranges from 10 to 15 nm/min in this study. Both the Inlens and the EsB SEM images were captured on the cross section along the sectioning. The configuration of FIB-SEM is sketched in figure 3.9. The 3D tomography sectioning images were taken by Dr Gareth M. Hughes.


*Figure 3.9: the configuration of FIB-SEM 3D tomography.*

The SEM images were aligned, resized, filtered with a Median filter with radius of 2 pixels and their brightness and contrast were adjusted and enhanced. In the next stage, the SEM images were imported in sequence to Avizo. The W, Co and diamond were segmented out based on their different intensities in EsB images. Each element was visualized in 3D tomography and quantified the total vol % respectively. Lastly, relative positions of voxel of each element were recorded. If two voxels share on common face, they are defined as connected. A particle was defined as a cluster of connected voxels.

Figure 3.10 is a flow chart showing the steps of image analysis in 3D tomography.

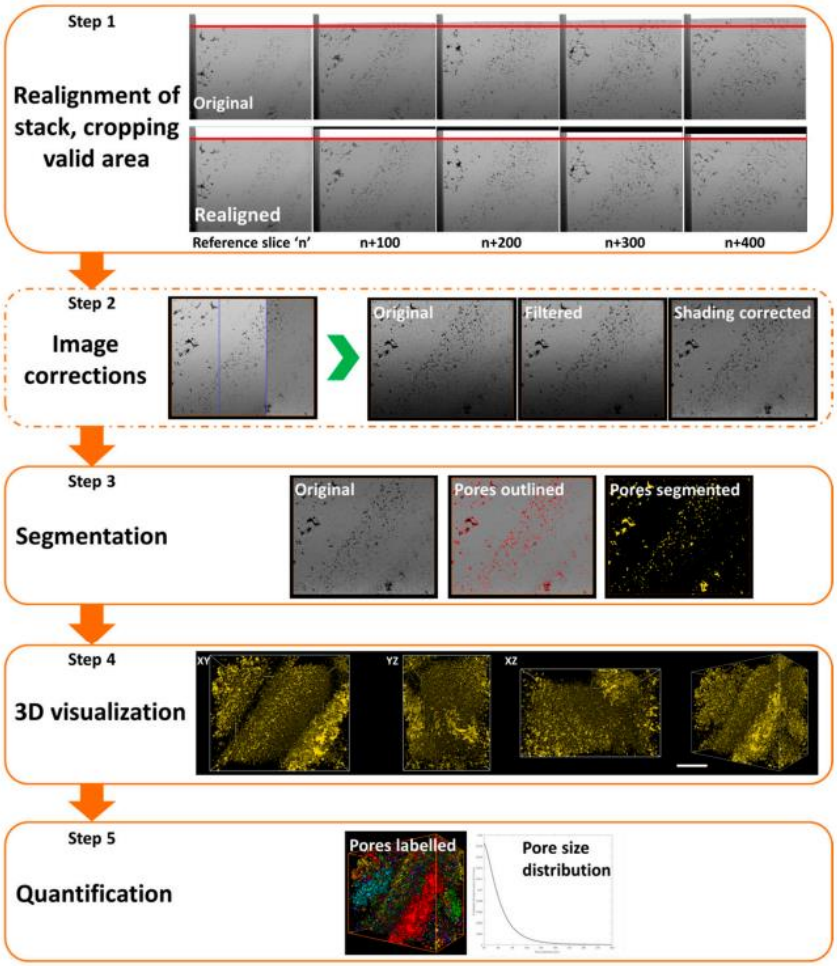


*Figure 3.10: the image processing steps on tomography data*[10].

### 3.3.9 Image Processing

The renowned image processing program, ImageJ[9], was used to process all the EM images, such as adjusting the brightness, contrast and gamma, applying various image filters, performing Fast Fourier transforms, etc.

## 3.4 Other Experimental Techniques

### 3.4.1 Laboratory X-ray Diffraction

The XRD patterns were obtained with the assistance of Dr. Roger Nilen at the GIC via a PANalytical X'Pert Pro diffractometer (Malvern, UK) with a customized Co source ($\lambda_{Co}$ is longer than $\lambda_{Cu}$) to further separate the overlapped XRD peaks for better indexing. The sample was mounted on a

spinning stage. 2θ was scanned from 20° to 100° with a step size of 0.0167° and a speed of 200 s/step at room temperature. The data were transformed from Co X-ray diffraction angles to the equivalent Cu X-ray angles for the Rietveld Refinement (Profex[11]) to estimate quantitative data like the weight percentage of graphite. Since both the atomic scattering factor and structure factor remain unchanged with the transition from a cobalt X-ray source to a copper X-ray source, XRD intensities should not vary with this transition. Ultimately, the weight ratio between graphite and diamond is unchanged after the X-rays transition.

### 3.4.2 Inductively Coupled Plasma Optical Emission Spectroscopy (ICP-OES)

The composition of each element in PCD materials was quantitatively measured using ICP-OES at the GIC. The data were obtained by staff from Element Six Ltd. Generally, some strong solvents like $HNO_3$ were used to dissolve the Co and W in the PCD. The PCD sample was shaped to a disk and was initially soaked into the solvent for a fixed period such as 24 hrs or 72 hrs to partially dissolve metallic elements. The same disk PCD sample was then crushed to pieces and further soaked in solvent, enabling a full dissolution of the remained metallic elements. The quoted accuracy is within 0.1 wt%. Due to confidentiality requirements, the details of the ICP-OES experiment are not discussed here.

## 3.5 Reference


(1) Bellin, F.; Dourfaye, A.; King, W.; Thigpen, M. The Current State of PDC Bit Technology. *World Oil* **2010**, *231* (11), 67–71.

(2) Joy, D. C.; Luo, S. An Empirical Stopping Power Relationship for Low-energy Electrons. *Scanning* **1989**, *11* (4), 176–180.

(3) Joy, D. C.; Joy, C. S. Low Voltage Scanning Electron Microscopy. *Micron*. 1996, pp 247–263.

(4) Schwartz, A. J.; Kumar, M.; Adams, B. L.; Field, D. P. *Electron Backscatter Diffraction in Materials Science*; 2009.

(5) Postek, M. T.; Vladár, A. E. Does Your SEM Really Tell the Truth? How Would You Know? Part 4: Charging and Its Mitigation. *Scanning Microsc. 2015* **2015**, *9636* (3), 963605.

(6) Bruker. Quantax CrystAlign. 2017.

(7) Mendelson, M. I. Average Grain Size in Polycrystalline Ceramics. *J. Am. Ceram. Soc.* **1969**, *52* (8), 443–446.

(8) Greer, A. L.; Bunn, A. M.; Tronche, A.; Evans, P. V.; Bristow, D. J. Modelling of Inoculation of Metallic Melts: Application to Grain Refinement of Aluminium by Al-Ti-B. *Acta Mater.* **2000**, *48* (11), 2823–2835.

(9) Schneider, C. A.; Rasband, W. S.; Eliceiri, K. W. NIH Image to ImageJ: 25 Years of Image Analysis. *Nat. Methods 2012 97* **2012**, *9* (7), 671–675.

(10) Liu, Y.; King, H. E.; van Huis, M. A.; Drury, M. R.; Plümper, O. Nano-Tomography of Porous Geological Materials Using Focused Ion Beam-Scanning Electron Microscopy. *Minerals* **2016**,

*6* (4).

(11) Doebelin, N.; Kleeberg, R. Profex: A Graphical User Interface for the Rietveld Refinement Program BGMN. *urn:issn:1600-5767* **2015**, *48* (5), 1573–1580.

# 4 Identifying Regrown Diamond via EBSD, SEM-CL and (S)TEM

## Table of Contents

## 4.1 Introduction

Studying regrown diamond in PCD materials has always been a challenge, primarily due to the absence of universally accepted criteria to identify it. This gap hinders investigations into the relationship between diamond regrowth and the mechanical performance of PCD materials.

The objective of this chapter is to establish a set of criteria that can effectively distinguish regrown diamond from old diamond. This requires the identification of potentially distinctive microstructural features in both regrown diamond and old diamond. To identify these microstructural features, various characterization techniques such as EBSD, SEM-CL, TEM and analytical STEM are employed to examine crystal defects and microstructural morphologies in these two types of diamond.

Regarding samples, one reference sample is some single crystal, raw diamond grits synthesized from graphite. The other reference sample, some abnormally grown grains (AGG) from a PCD sample, is examined, as there are known regrown diamond grains. As references, they can help to identify the microstructural features of regrown diamond. The normal grains of the standard PCD (SPCD), as described in section 3.21.1., along with those from standard PCD with additional graphite feed (SPCDG), as experimental samples, are characterized and compared to the references to try to find any different morphological features to distinguish them from regrown diamond.

## 4.2 Material and Sample Preparation

1. **Single crystal diamond grits** (Element Six, UK): these are the raw diamond powders fed into the press before sintering, as shown in figure 3.1 a). Generally, they were directly synthesized from graphite via HPHT sintering, then crushed to meet specific size requirements. However, details of the synthesis are confidential.

Diamond single crystal grits from this synthesis are of relatively high crystal quality compared to the heavily plastically deformed PCD grains[1,2]. This observation is supported by the manufacturer.

2. **Abnormally grown diamond grains**: exceptionally large diamond grains due to the abnormal grown growth in SPCD. An SE2 image of the AGG is displayed in figure 4.1. The reason for the formation of AGGs in PCD materials is still debated[3]. However, empirically, the addition of graphite will enhance the probability of the formation of AGGs in PCD materials.
3. **Normal grains of SPCD**: randomly selected normal diamond grains from a SPCD sample. The details of SPCD can be found in section 3.1.1.
4. **The region from SPCDG**: a selected region consisting of suspected partially regrown diamond grains from a SPCDG sample, referred as “the region from SPCDG”. SPCDG is a new type of PCD sample with a different mixed powder compared to SPCD. Before the admixing of diamond and cobalt powders, extra graphite (Element Six, UK) was added to the PCD raw powders, with a diamond/graphite weight ratio of 20:1. The mean diameter of the graphite particles was 30 μm. The addition of graphite is to boost the scale of diamond regrowth. The subsequent steps in SPCDG manufacturing were the same as for the SPCD.

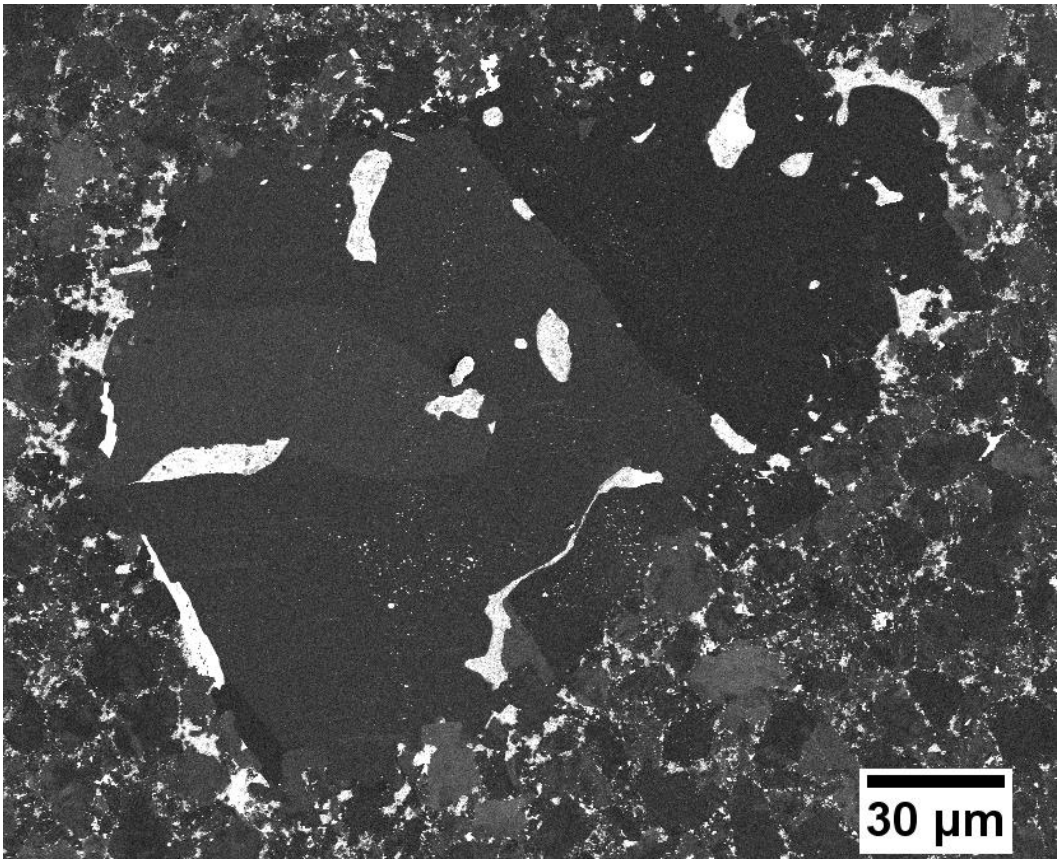


*Figure 4.1: An SE2 image of AGGs*

## 4.3 Experimental

### 4.3.1 Characterization Techniques

#### 4.3.1.1 Electron Microscopies

The details of the EM-related general characterization have been previously discussed and can be found in Section 3.3 Therefore, they will not be repeated here.

#### 4.3.1.2 Cathodoluminescence (CL)

The CL study of diamond was in collaboration with Dr. Paul Edwards from the Semiconductor Spectroscopy and Devices group at the University of Strathclyde. CL data were acquired from the FEI Quanta 250FEG SEM-CL system at an $LN_2$ temperature (−

196 °C). Hyperspectral CL images were captured at 10 kV with a 400 line/mm grating blazed at 500 nm and centred at 450 nm. The spatial resolution of the CL maps is estimated to be 50 nm from the Monte Carlo simulation[4]. CL images and spectra were acquired by Dr. Paul Edwards. All the CL data were processed and analysed with a software called “Chimp” by the present author[5].

One special type of map derived from the hyperspectral CL is the real colour CL map. This map calculates the chromaticity coordinates of each pixel's spectrum in International Commission on Illumination (CIE) 1931 colour space (figure 4.2) from three CIE's colour matching functions, converts these chromaticity coordinates into RGB values and finally plots a colour bitmap based on these RGB values[5,6]. This can reflect the corresponding colour in CIE 1931 colour space from the dominant wavelength in the spectrum of that pixel.

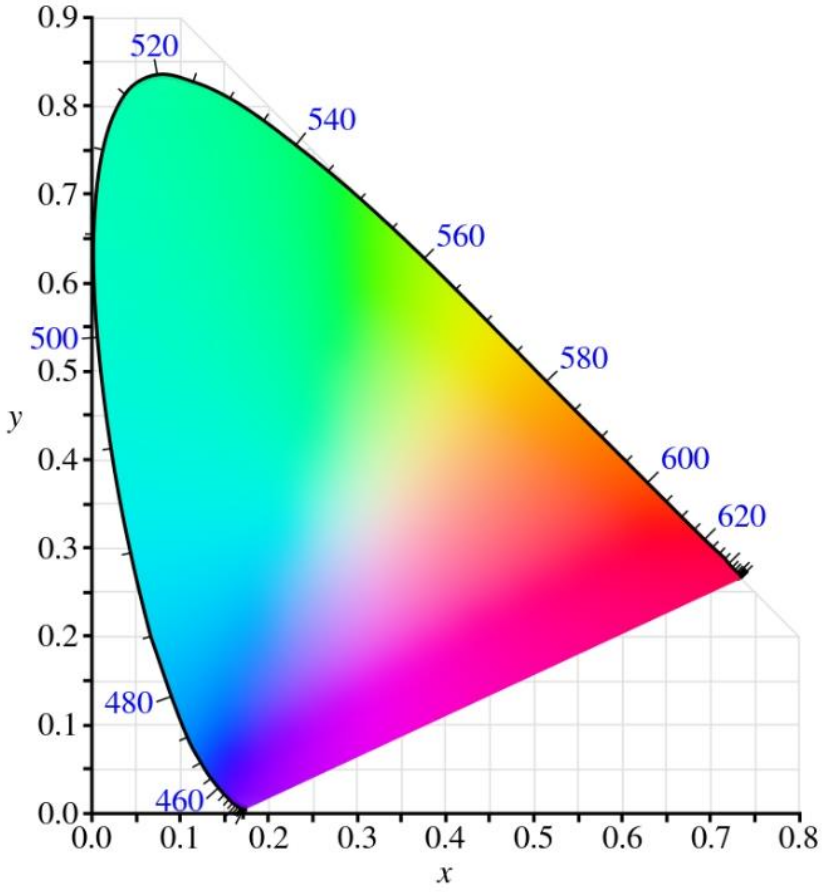


*Figure 4.2: A CIE 1931 chromaticity diagram generated using Chimp. The axes are scaled so that the chromaticity co-ordinates (x,y) vary from 0,0 (bottom left) to 1,1 (top right)[7]. The outer curved boundary is the spectral (or monochromatic) locus, with wavelengths shown in nanometres.*

By the non-linear iterative partial least squares algorithm, principal component analysis (PCA) was used to decompose all spectra in a hyperspectral-CL image into several variant components nonorthogonally[5]. This allows one or several of the most significant fitted components with different variances to be identified as a form of spectrum. These decomposed components were then used to generate the corresponding CL map, which is re-coloured[5]. This empirical approach was utilized to extract the specific CL intensities from the corresponding colour centre from a complete CL spectrum.

## 4.4 Results and Discussion

For reference samples, more than eight randomly selected diamond grits, along with an AGG, were investigated by EBSD and CL. Results from both EBSD and CL analyses were consistent in these samples. The focus of the characterization on a limited number of reference samples is due to several factors: firstly, the scarcity of suitable reference samples, like the AGG; secondly the time-consuming nature of the measurements; thirdly, the large number of individual measurements (pixels) for each grain, which are consistent in both CL and EBSD, allowing for a high degree of confidence in the characterization of each reference sample. Lastly, although the number of reference samples is small, they all showed low GOS value and these were consistently smaller than those in normal old diamond grains.

## 4.4.1 Identifying Regrown Diamond by EBSD

### 4.4.1.1 EBSD Results of Diamond Grits

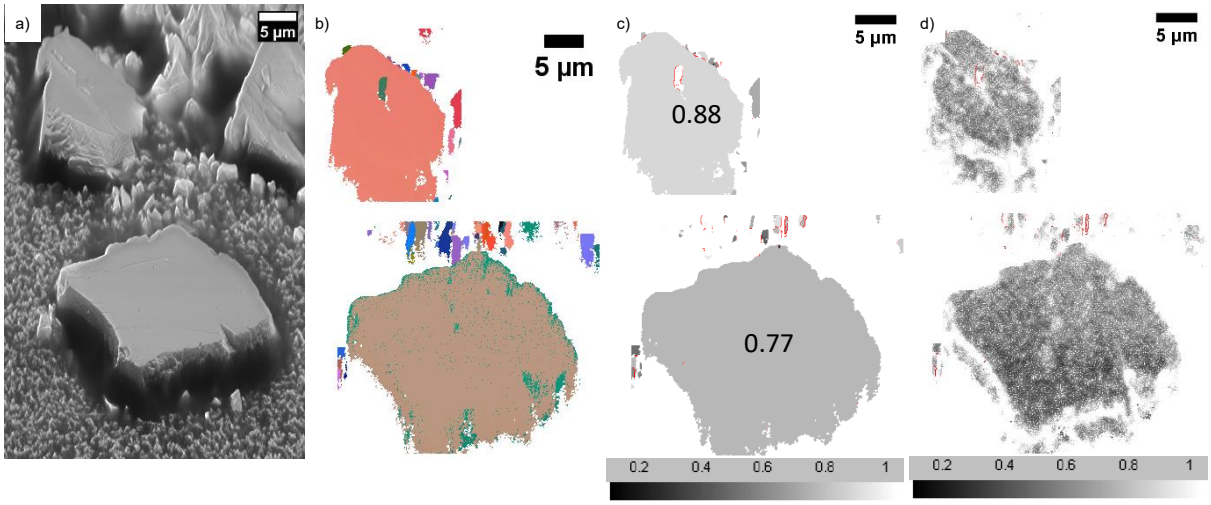


*Figure 4.3: An SEM image and EBSD maps of diamond grits. a) An SE2 image with a 70° tilt correction. b) An EBSD Euler map. c) An EBSD GOS map only showing diamond grains with a GOS value less than 1°. The GOS values of two diamond grains are labelled. d) An EBSD local misorientation map only showing pixels with a local misorientation value less than 1°. The red boundaries in c) and d) are GBs.*

Two relatively flat surfaces of coarse diamond grits were targeted in figure 4.3 a) for EBSD mapping. From the EBSD Euler map in figure 4.3 b), each colour denotes a specific orientation with an angular resolution of 0.1°. In the bottom coarse grit, most of the green pixels aggregate near the edge of the diamond. This phenomenon arises from the slopes and local indentations near the edge of grit, leading to slight differences in orientations of backscattered electrons.

As reviewed in section 2.1.2.3, the grain orientation spread (GOS) approach based on EBSD data could help identify the regrown diamond grains. GOS values of two coarse grains are labelled in figure 4.3 c). In the local misorientation map in figure 4.3 d), blank strips at the bottom of two coarse grits are also attributed to slopes around diamond edges. Despite this negative influence, GOS values of both coarse diamond grits still remain below 1°. The actual GOS values should be even lower if excluding the apparent local misorientation from edge effects. Some fine diamond grits exhibit a GOS value above 1° due to their complex geometries, which increase the apparent local misorientation and the GOS value.

#### 4.4.1.2 EBSD Results of AGGs

The SE2 image and EBSD maps of AGGs are displayed in figure 4.4 a)-d). In the EBSD Euler map (figure 4.4 b), the large green, purple and dark pink sub grains, from the top to the bottom of the AGG, share mutual twinning relationships (confirmed by EBSD map not shown). As illustrated in figure 4.4 c), their GOS values correspond to 0.77°, 0.67° and 0.59° respectively. This aligns with the darker colours in figure 4.4 d), meaning a low local misorientation within these AGGs. The smaller light pink AGG, with a GOS value of 0.83°, is separated from the coarse AGGs by a thin layer of binder as shown in figure 4.4 b). The binder pools and the vast majority of surrounding normal grains exhibit GOS values of more than 1°, reflected as blank in figure 4.4 c).

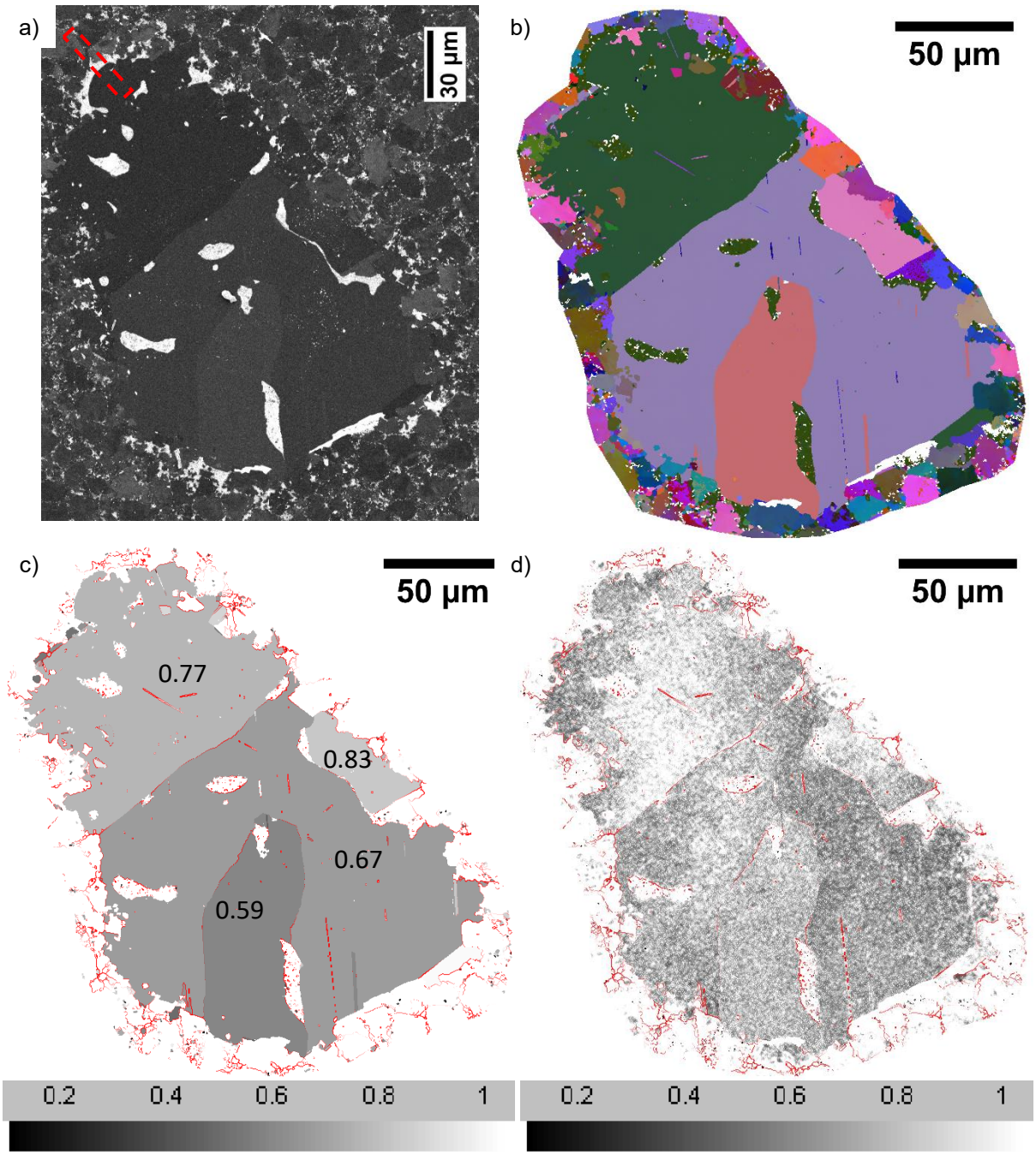


*Figure 4.4: An SEM image and EBSD maps of AGGs. a) An SE2 image. A TEM sample was taken from the red rectangular region. b) An EBSD Euler map. c) An EBSD GOS map only showing diamond grains with a GOS value less than 1°. The GOS value of sub-grains in AGG are labelled. d) An EBSD local misorientation map only shows pixels with a local misorientation value less than 1°. The red boundaries in c) and d) are GBs, but the boundaries between AGGs are twin boundaries.*

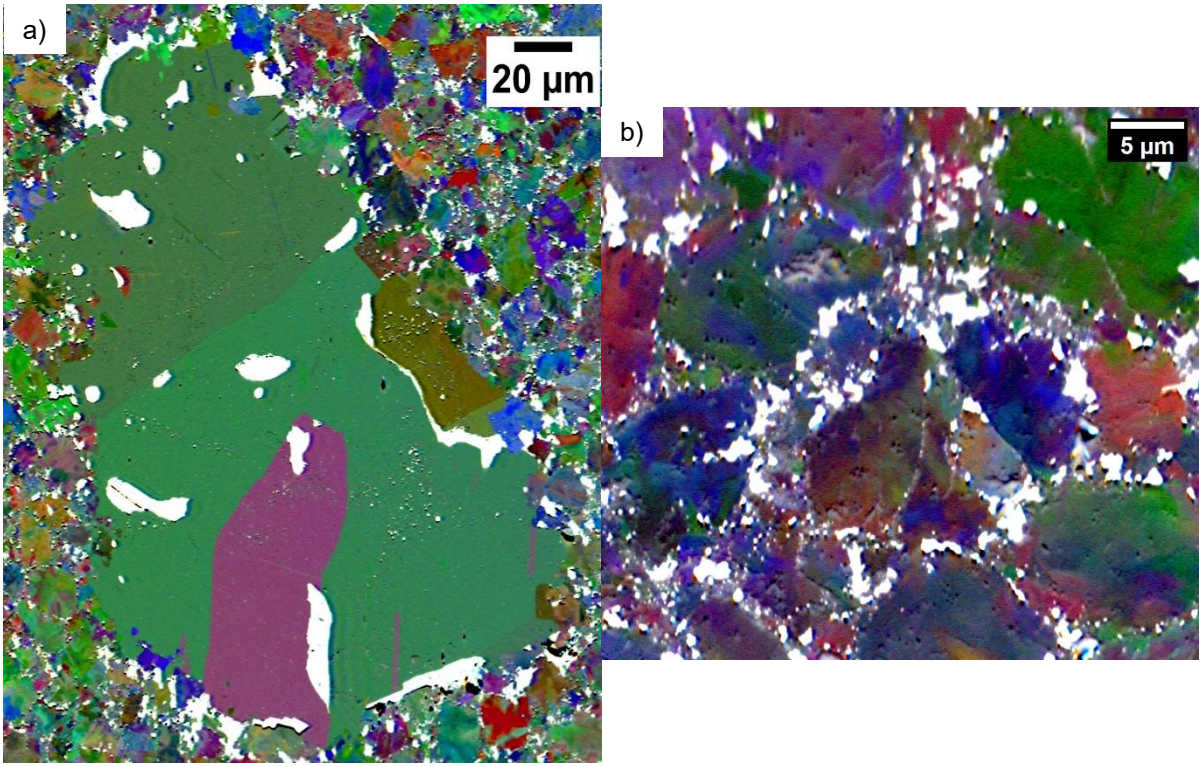


*Figure 4.5: ARGUS images of a) AGGs and b) normal grains in SPCD. Each colour represents an orientation and the colour is extremely sensitive to the orientation.*

The GOS value and local misorientation can also be qualitatively reflected in the high orientation resolution ARGUS imaging. In figure 4.5 a), colour distributions appear uniform within all AGGs. In normal grains surrounding AGGs, colour distributions are inhomogeneous, indicating a significant local misorientation. This high misorientation is clearly displayed in figure 4.5 b), a randomly selected region of normal grains of SPCD at higher magnification. Given that ARGUS imaging takes merely a few minutes, it serves as a rapid method for a preliminary search for diamond grains with low GOS value.

### 4.4.1.3 EBSD Results of SPCD

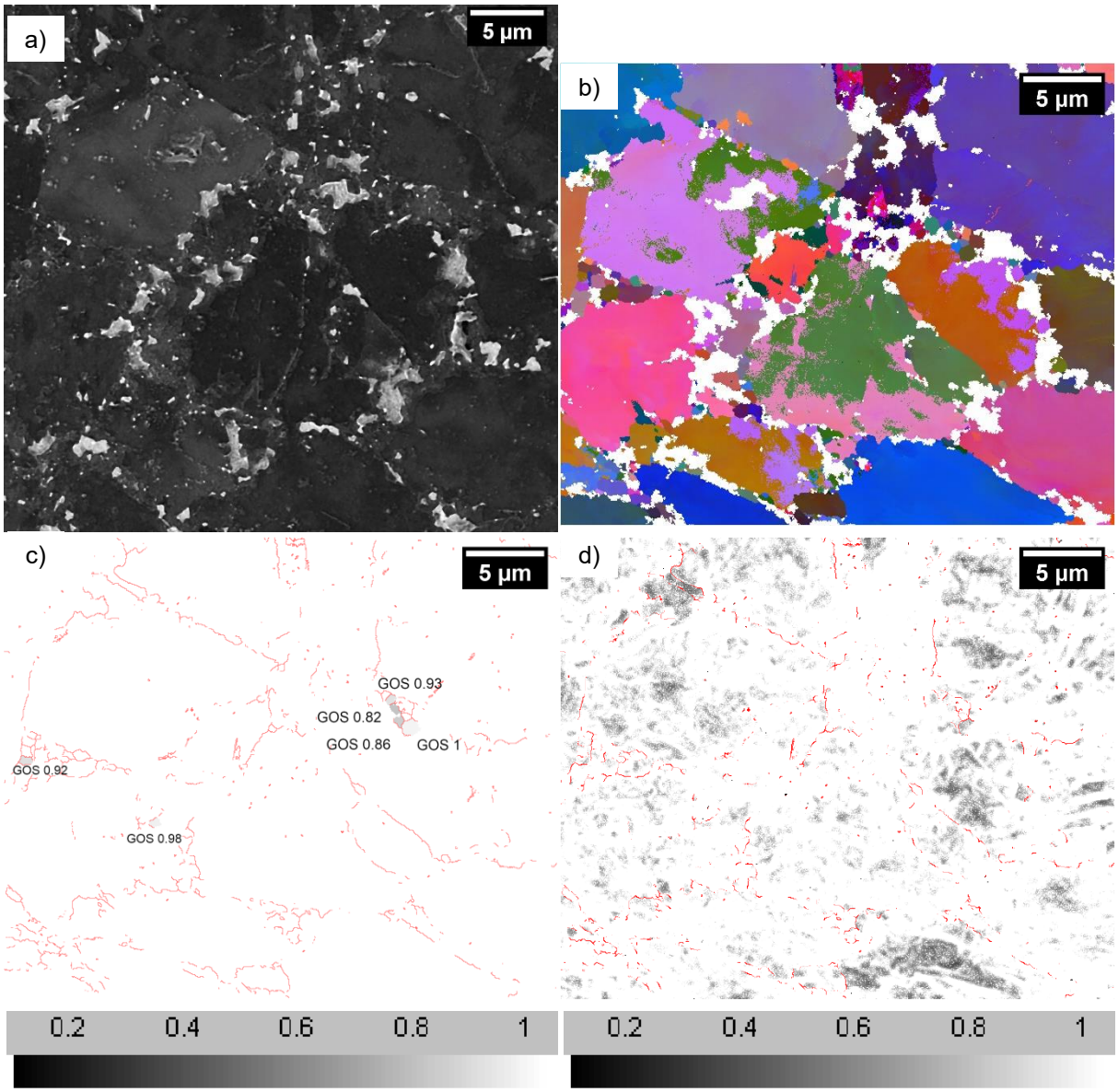


*Figure 4.6: An SEM image and EBSD maps of a region from SPCD. a) An SE2 image. b) An EBSD Euler map. c) An EBSD GOS map only showing diamond grains with a GOS value less than 1°. The GOS value of some fine diamond grains are labelled. d) An EBSD local misorientation map only showing pixel with a local misorientation value less than 1°. The red boundaries in c) and d) are GBs*

Figure 4.6 a) - d) are the SE2 image and EBSD maps of the same randomly selected region from SPCD as in figure 4.5 b). This region contains several normal diamond grains. The corresponding Euler map in figure 4.6 b) and ARGUS image in figure 4.5 b) suggest a large misorientation within these grains. The mainly blank GOS map and local misorientation map in figure 4.6 c) and d) provide further quantitative evidence supporting this suggestion. The mean GOS value of relatively large normal grains (>1 $\mu m^2$) is 3.2°±0.9°.

#### 4.4.1.4 EBSD Results of SPCD with Additional Graphite Feed

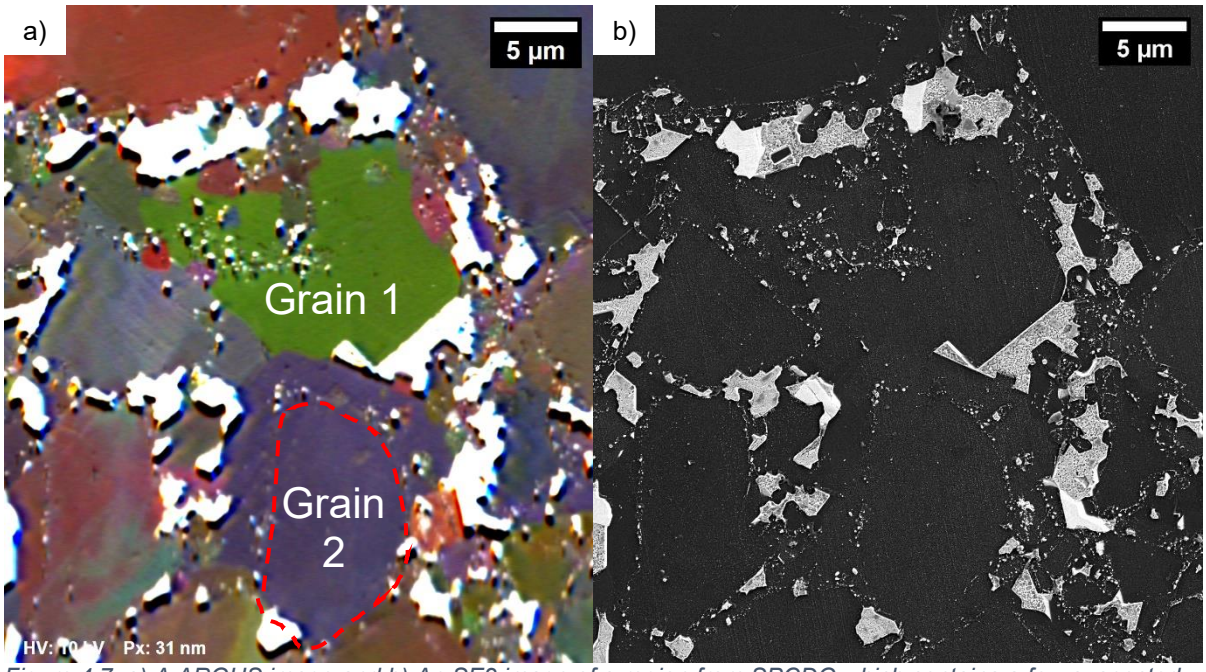


*Figure 4.7: a) A ARGUS image and b) An SE2 image of a region from SPCDG which contains a few suspected regrown grains. Two grains are numbered 1 and 2 in a). A contour is outlined in the grain 2 as a red dash line.*

In the region from SPCDG, the microstructures are different. Figure 4.7 a) and b) are the ARGUS and SE2 images of this region. Labelled in the ARGUS image, two grains, labelled 1 and 2, are targeted in the region from SPCDG. The homogeneous green colour in grain 1 resembles the uniform colour in AGGs in figure 4.5 a). Beneath it lies grain 2, separated into two parts by a red dash contour mostly aligned with the positions of enclosed binder particles within grain 2.

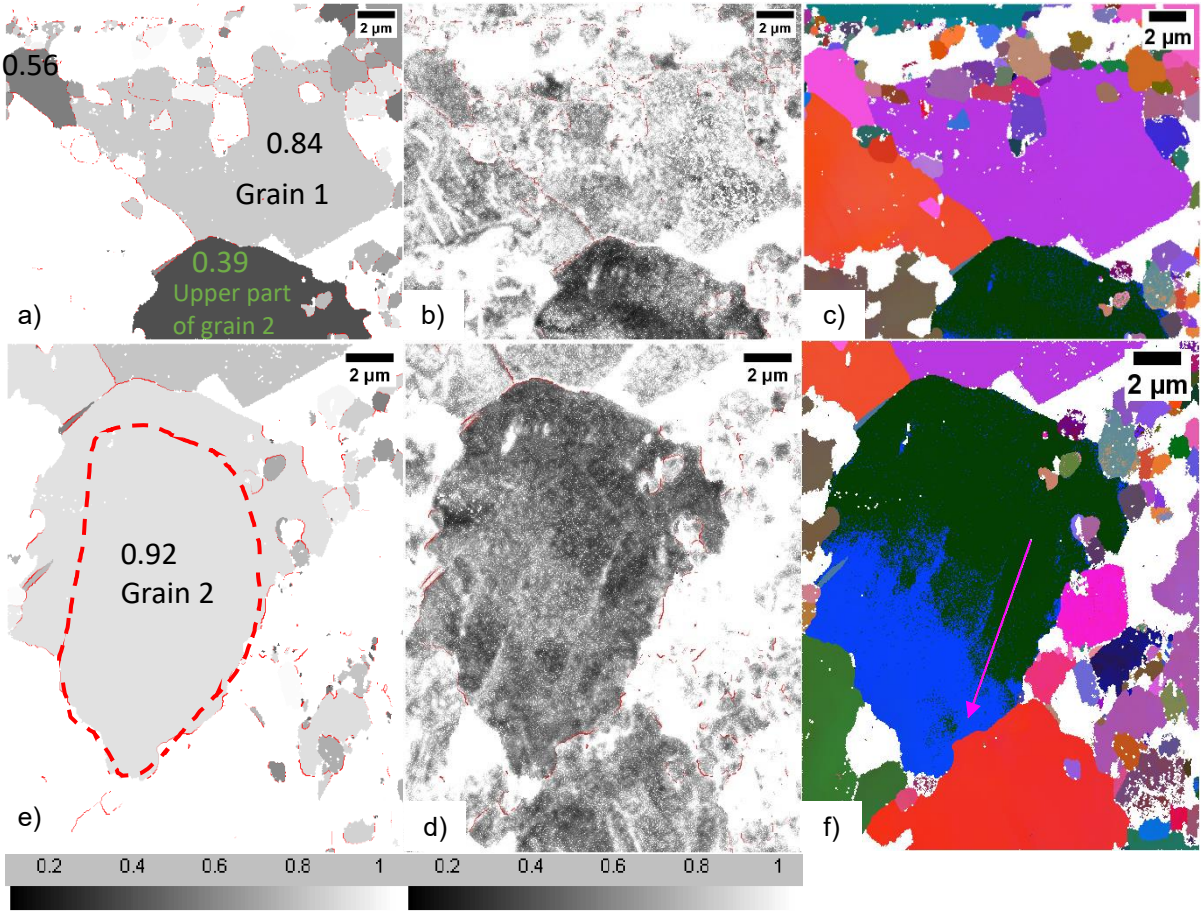


*Figure 4.8: The EBSD maps corresponding to figure 4.7. a) and d) GOS EBSD maps. b) and e) local misorientation maps and c) and f) Euler maps. The colour scale bars and map properties are consistent with figure 4.6. A contour is outlined in the grain 2 as a red dash line, same as that in figure 4.7 a). The largest misorientation along the pink line in grain 2 in f) is about 2.6°.*

Figure 4.8 shows the GOS, local misorientation and Euler maps of grains 1 and 2. Their respective GOS values, as illustrated in figure 4.8 a) and d), are 0.84 and 0.92°. Notably, a GOS value of 0.39° is assigned to the upper part of grain 2 as shown in dark in figure 4.8 a). This upper part consists of regions mostly outside the red contour in grain 2. The two different GOS values (0.39° and 0.92°) of the same grain 2 are also evidently reflected in both the local misorientation map (figure 4.8 e) and the Euler map (figure 4.8 f)). In the local misorientation map, this upper part presents a slightly darker colour due to low local misorientation, whereas a gradual increase of misorientation is observed from the top right to bottom left within the red contour. In the Euler map, this upper part shows a dark green colour, while inside the red contour the dark green colour transforms to blue, indicating a relatively large change of orientation.

#### 4.4.1.5 Discussion of EBSD Results

As reviewed in section 2.1.2.3, the EBSD-based GOS approach is a widely accepted and standardized method for identifying recrystallized grains in metallic materials[8–11]. A low GOS value indicates a high crystallinity of a grain since most crystal defects including deformation twins and geometrically necessary dislocations can introduce misorientation within a crystal and consequently significantly raise the value of GOS[11]. Mohapatra *et al*[12] reported that GOS values of most diamond grains in CVD diamond film, usually with a high crystallinity, are less than 1°. In line with these findings, GOS values of both reference diamond grits and AGGs are below 1°.

Contrary to the two reference samples, in figure 4.6, the majority of normal diamond grains in randomly selected region from SPCD exhibit a GOS above 1°. This consistently high mean GOS value (3.2°) for normal diamond grains is universal throughout the SPCD.

Since AGGs are known regrown diamond grains and diamond grits directly transformed from graphite can also be considered as regrown diamond, it is reasonable to set the threshold GOS value for the identification of regrown diamond grain to 1°. This low (1°) threshold aligns well with the claim in section 2.1.2.3 that the regrown diamond is supposed to have fewer crystal defects or even to be defect free. According to this GOS threshold, most of normal diamond grains from SPCD should be old diamond.

By contrast, in the region from SPCDG investigated, according to this GOS threshold, both grains 1 and 2 can be identified as regrown diamond due to their GOS values less than 1°. From figure 4.8 b) and c), there is no inhomogeneity of misorientation through the grain 1. However, such inhomogeneity of misorientation is revealed by all three EBSD maps in grain 2. The low GOS value (0.39°) of the upper part of grain 2, along with the low local misorientation from the same part, all indicate that this part is from diamond regrowth. Assuming the ratio of areas inside and outside of the red contour in grain 2 is roughly 1:1.5 and the GOS value for area outside the red contour to 0.5°, the calculation based on these

assumptions indicate the area inside the red contour has a GOS value > 1°, and therefore to be old diamond.

Other ARGUS images from the SPCDG showed a random distribution of regions similar to the one analysed in detail here, apparently containing regrown diamond. It is speculated that these regions are probably related to the addition of extra graphite before sintering.

### 4.4.2 Identifying Regrown Diamond by SEM-CL

To find the potentially different colour centres and their distribution in old and regrown diamond grains, diamond grits, the same AGGs and the same region from SPCDG as in the previous section were probed by SEM-CL at liquid nitrogen temperature. Due to the limited access to the SEM-CL system and the high GOS values of diamond grains from SPCD, SPCD was not characterized by SEM-CL.

Table 4.1 summarizes the name, starting wavelength from zero-phonon line, colour and structure of the four most predominant colour centres in PCD in this section. Nickel, as a component of binder composition, is introduced to diamond raw powder during powder synthesis. Cobalt related colour centres (669.3 nm 623.2 nm 580.6 nm), which are associated with cobalt-nitrogen complexes, are not apparently present in all CL spectra[13].

| Name | Starting Wavelength | Colour in CL maps | Structure |
|---|---|---|---|
| Band-A | A band from 400 – 500 nm | Blue | Dislocation related[14–16] |
| 484 nm centre | 484 nm | Green | A substitutional nickel atom related centre[17,18] |
| NVN centre | 503 nm | Green | Two substitutional nitrogen atoms paired with a vacancy in the middle[19,20] |
| $NV^0$ centre | 575 nm | Red | A substitutional nitrogen atom paired with a vacancy; not charged[21,22] |

*Table 4.1: the general information of four main colour centres in PCD.*

### 4.4.2.1 SEM-CL Results from Diamond Grits

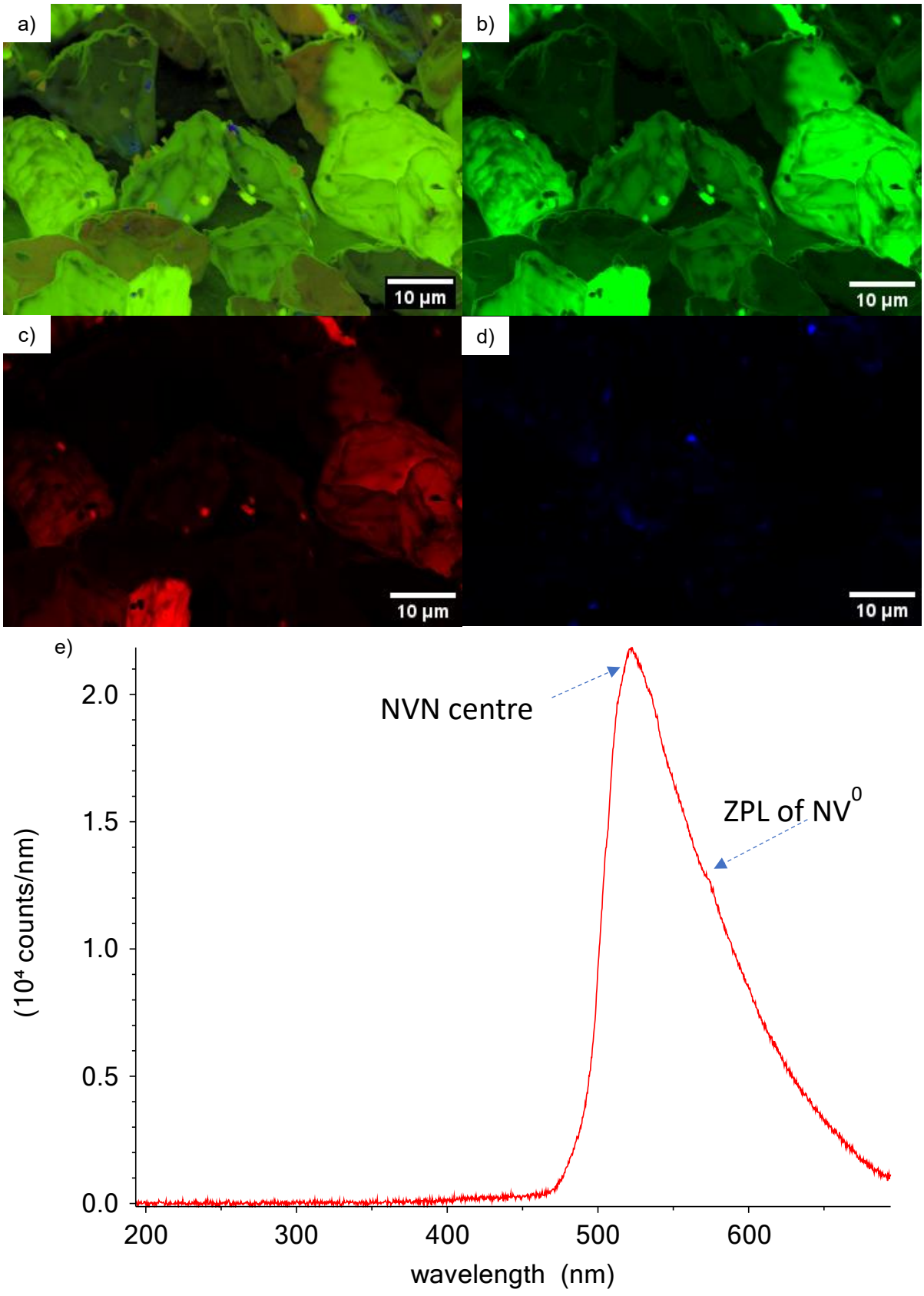


*Figure 4.9: CL maps of diamond grits. a) A real colour map. b) Green CL map. c) Red CL map. d) Blue CL map. e) Mean CL spectrum.*

Figure 4.9 a) is a real colour map of diamond grits. Figure 4.9 b), c) and d) are the corresponding CL maps associated respectively with CL emissions from NVN centres, $NV^0$ centres and dislocations after PCA. Since CL emissions from these defects are green, red and blue respectively, these three specific CL maps were coloured accordingly. Figure 4.9 e) is the corresponding mean spectrum of diamond grits. It indicates dominant CL from NVN centres starting from around 500 nm, with a less distinctive shoulder at 575 nm, which is the zero-phonon line (ZPL), the wavelength at which a relaxation is not phonon assisted, of $NV^0$ centres[21,22]. The presence of both NVN centres and $NV^0$ centres is consistent with the CL result from Collins and Robertson[21] and the photoluminescence results from Lysenko *et al*.[22]. However, unlike the typical CL band from NVN centres[20], no obvious ZPL or phonon replicas, the wavelength at which a relaxation involves the lattice vibration to lose energy, of the NVN centre are observed in figure 4.9 e). This peculiarity is also noticed in figure 4.10 f), which also shows no ZPL and phonon replicas of the NVN centre.

There is almost no blue CL contribution from dislocations in coarse diamond grits, but some fine diamond grits exhibit relatively intense blue CL emissions from dislocations, while others display strong $NV^0$ CL with or without intense NVN CL emissions in figure 4.9 c).

### 4.4.2.2 SEM-CL Results from AGGs

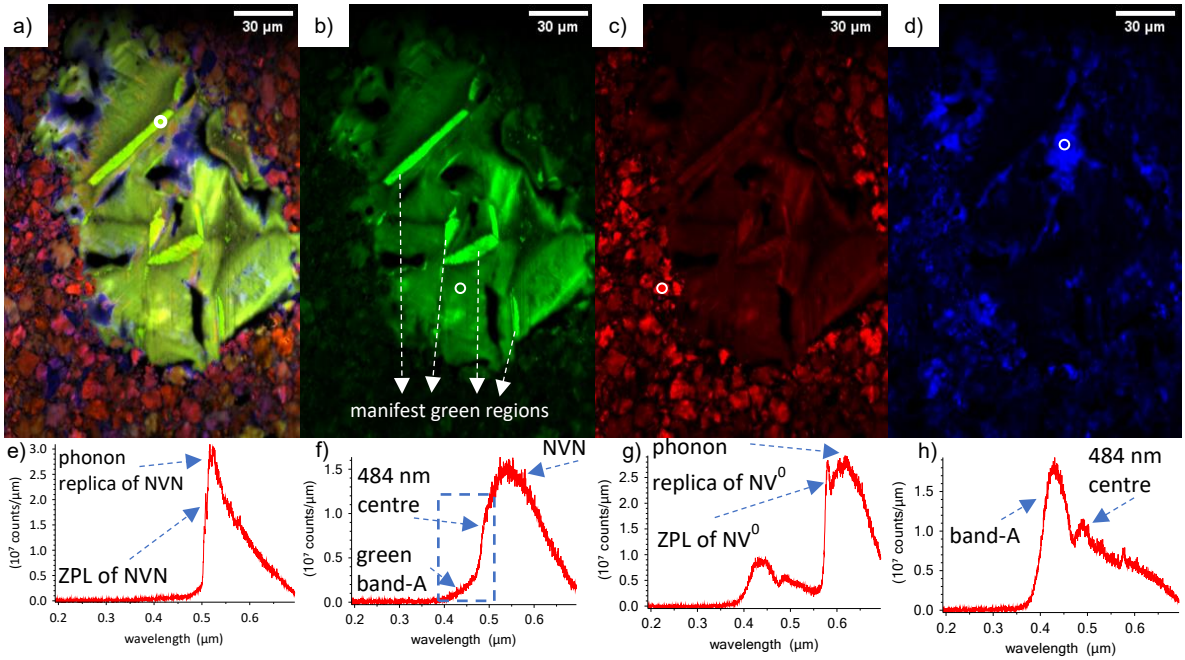


*Figure 4.10: CL maps of the AGG region. a) A real colour map. b) Green CL map. c) Red CL map. d) Blue CL map. CL spectra e)-h) under each map are from the circled region in each CL map.*

The presence of NVN centres was also captured within the same AGGs as were shown in figure 4.5. Figure 4.10 a) - d) are the real colour, green, red and blue CL maps of AGGs, with corresponding spectra e) - h) from the circled regions in each map. In the real colour map, there are some manifest green luminescent regions, which are more pronounced and labelled in the green CL map. The CL spectrum (figure 4.10 e)) captured from a white circle marked in one green luminescent region in figure 4.10 a) demonstrates a typical CL edge emission of NVN centres, displaying a clear ZPL and its phonon replica[19,20]. It slightly overlaps with $NV^0$ CL starting from 575 nm, while no detectable CL from the 484 nm centre was observed. The other interesting observation in figure 4.10 a) is the different colours from AGGs (green) and normal grains (red), suggesting different dominant CL emissions from them.

A CL spectrum was also taken from a less green region within the AGG circled in figure 4.10 b). This CL spectrum (figure 4.10 f)) differs from 10 e) in that it shows a broad asymmetric band from around 400nm to more than 700 nm. This asymmetric band likely comprises 3 components: CL emissions from NVN centres, from 484 nm centres and the green band-A

which is the band-A decorated by impurity boron atoms, resulting a 100-nm increase in wavelength of blue band-A[23–25].

Upon moving to a neighbouring normal grain circled in figure 4.10 c), its corresponding CL spectrum (figure 4.10 g)) is very different. The CL emissions from NVN centres disappear and the CL emissions from $NV^0$ centres become dominant. The blue band-A ranging from 400 to 500 nm and the CL emissions from 484 nm centres are also exhibited.

Lastly, when probing a blue region in AGG marked in figure 4.10 d), band-A becomes the dominant CL in figure 4.10 h), while the CL emissions from 484 nm centres keep a relatively constant intensity compared to that in figure 4.10 f). The CL intensity from $NV^0$ centres drops by about 80% compared to that from the normal grain in figure 4.10 g).

### 4.4.2.3 SEM-CL Results from SPCD with Additional Graphite Feed

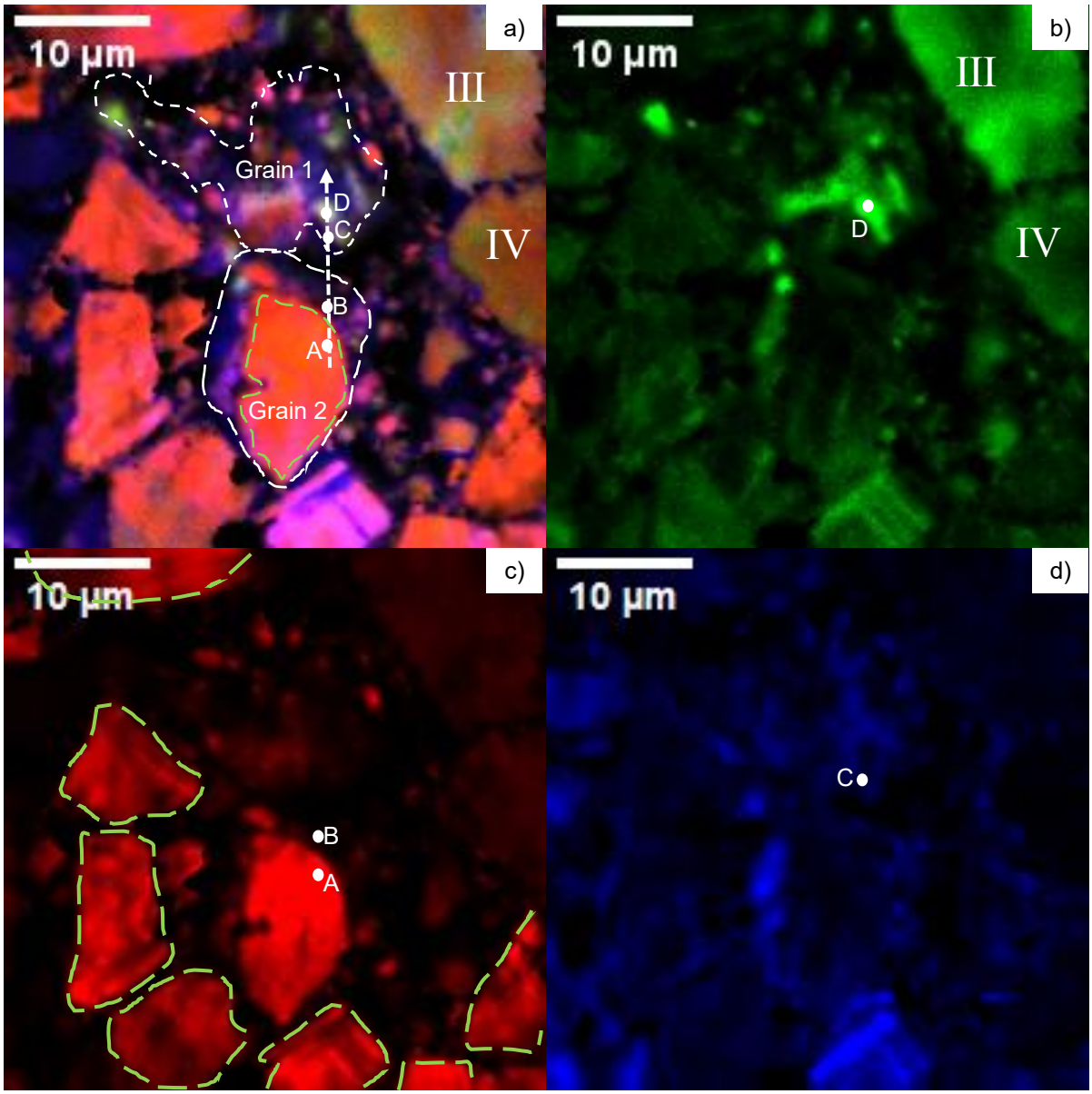


*Figure 4.11: CL maps of the region from SPCDG shown in* ***figure 4.7*** *including grains 1 and 2. a) A real colour map. The spectra from the marked points here are illustrated in figure 4.12. b) A green CL map. c) A red CL map. d) A blue CL map. Two grain at the north-east corner are marked with roman numeral III and IV.*

Figure 4.11 a) – d) are the real colour map and the green, red and blue CL maps of the region from SPCDG containing both grains 1 and 2. Since both GBs and binder particles are non-luminescent in CL maps, features in CL maps look different from those in EBSD maps, and ARGUS and SE2 images. GBs of grains 1 and 2 are approximately outlined in white dashed lines in figure 4.11 a).

In figure 4.11 a), grain 1 exhibits varied and uneven luminescence. Grain 2 consists of two parts, separated by the periphery of a red area, marked by green dashed line. This periphery almost overlaps with the contour (the red dashed line) in figure 4.7 a) and from now will be referred to as the "distinct contour" for brevity. The part of grain 2 inside this distinct contour emits red CL, while the part outside of it appears mainly purplish, with some local green and red luminescent clusters. The similar peripheries of red areas of other coarse grains are outlined with green dashed lines in figure 4.11 c).

In figure 4.11 b), apart from entirely greenish grains III and IV whose green CL emissions are from 484 nm centres by examination of their CL spectra, other intensively green luminescent regions exhibit green CL emissions are because of the presence of NVN centres, with a typical NVN CL band marked in figure 4.12 d) which shows the spectrum from point D. These luminescent green regions are located outside of all peripheries of red areas (green dashed lines in figure 4.11 a) and c)).

In figure 4.11 c), red CL emissions are concentrated within the peripheries of red areas in coarse grains and some fine diamond grains. As evidenced by the representative CL spectrum in figure 4.12 a) which shows the spectrum from point A in figure 4.11 c), $NV^0$ centre is the dominant colour centre in these red areas, yielding red CL emissions. There are fewer $NV^0$ CL emissions from grain 1.

Finally, the distribution of blue CL is shown in figure 4.11 d). The blue CL is associated with the presence of dislocations.

To study the characteristic CL from both grains 1 and 2, four points, marked with A, B, C and D, are selected along a vertical dashed line, drawn in figure 4.11 a). To clearly present their positions, these 4 points are re-labelled in the different CL colour maps (figure 4.11 b) – d)) respectively. Points A and B are positioned inside and outside of the distinct contour in grain 2. Points C and D are from grain 1, with point D from an intensively green luminescent

region and point C in adjacent to it. The CL spectra corresponding to these 4 points are inserted in figure 4.12 a) - d).

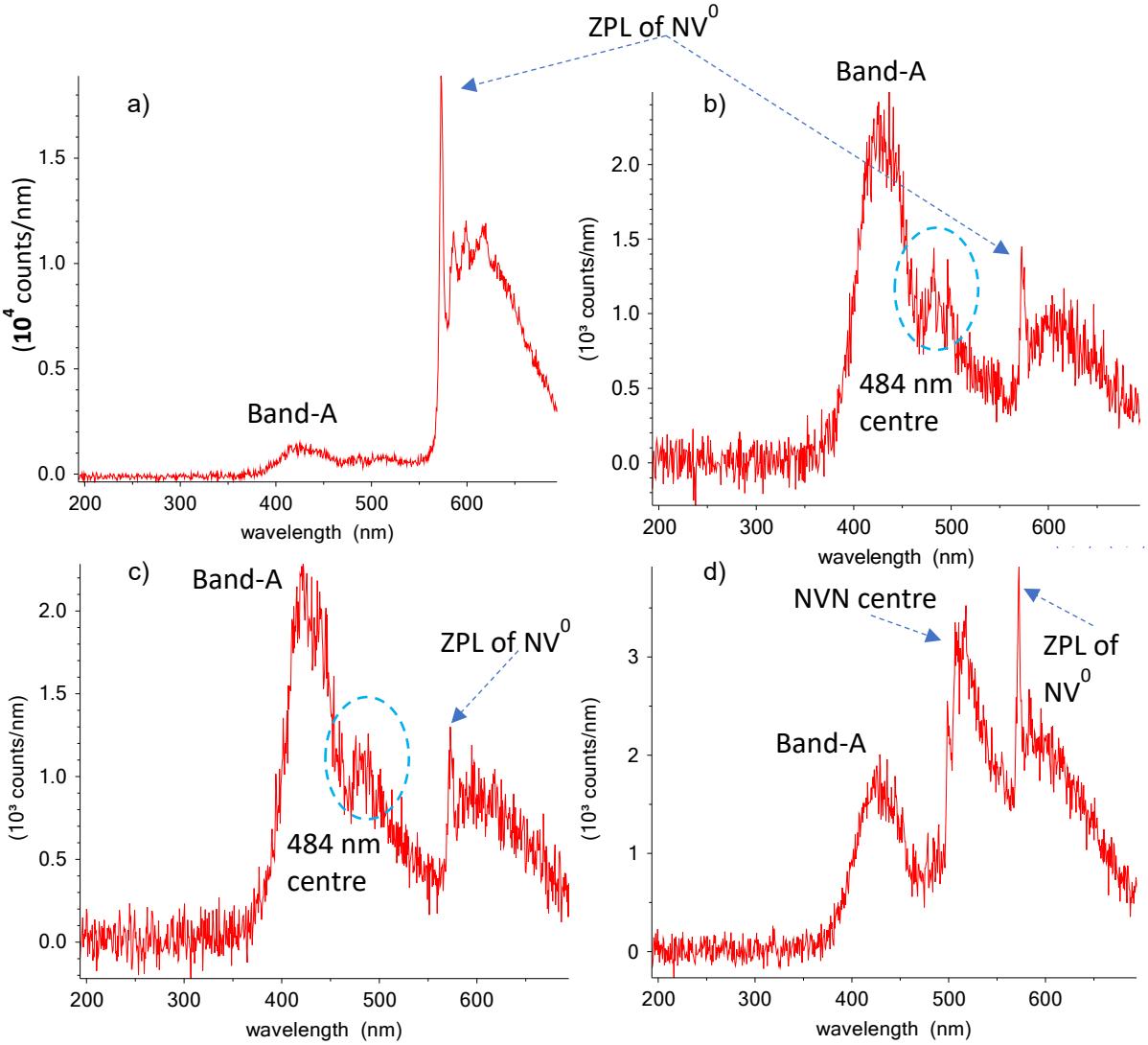


*Figure 4.12: CL spectra from the letter labelled regions in figure 4.11 a). a), b), c) and d), corresponding to region A, B, C and D respectively.*

Though CL is not a fully quantitative characterization technique, it is still possible to compare CL intensities from a small region of the same material under the same imaging conditions[26]. Evidently, the dominant CL emission at point A is from the $NV^0$ centre, with its ZPL reaching more than $1.5x10^4$ counts. However, when moving to point B, the CL intensity of the ZPL of $NV^0$ centre drastically reduces to less than 1/10 of that in the point A, whereas the intensity of band-A barely changes from point A to B. Interestingly, the overall shape of the spectrum remains almost unchanged from point B, in grain 2, to point C in the grain 1. Both points show strong CL from 484 nm centres, marked with blue circles in figure 4.12. However, the

CL spectrum (figure 4.12 d)) from the intensively green point D changes again, with an increase of the CL intensity of the NVN centre. Due to an overlap of the tail of NVN CL emission with the initial part of $NV^0$ CL emission, the CL intensity of $NV^0$ in figure 4.12 d) appears higher than those in figure 4.12 b) and c).

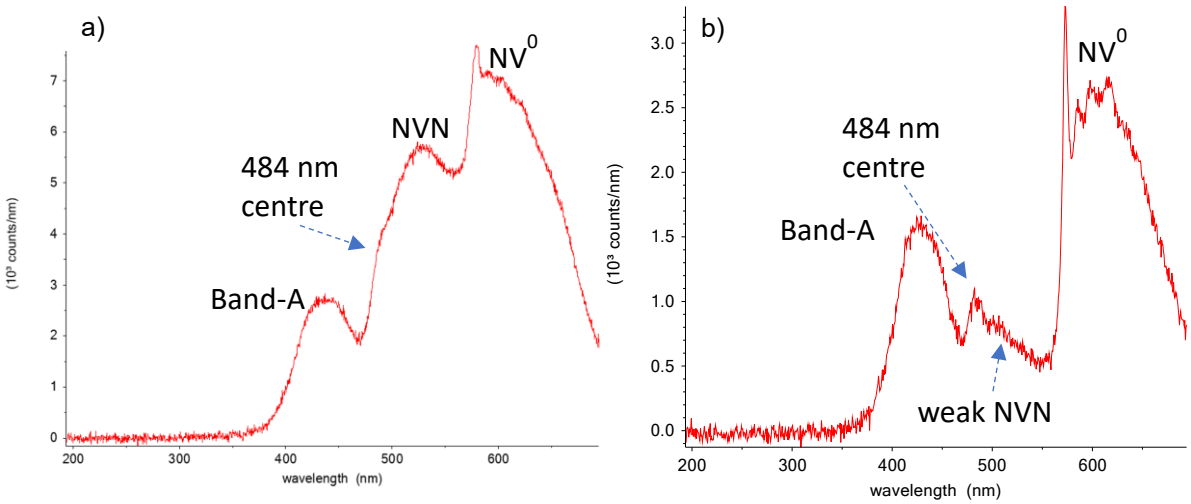


*Figure 4.13: a) The mean CL spectrum of the whole region, including AGGs, in figure 4.10 a). b) The mean CL spectrum of the whole region in figure 4.11. The weak NVN shoulder is labelled.*

Figure 4.13 compare the mean spectrum from the AGGs and the region from SPCDG. The most obvious difference between them is the presence of strong and weak the NVN CL emissions in the AGG and the region from SPCDG respectively.

### 4.4.2.4 Discussion of SEM-CL results

The overlap of different CL edges/bands introduces difficulties in the interpretation of the results. Because a portion of the sideband of NVN CL overlaps with the majority of $NV^0$ CL, a pixel with an intensive NVN emission can also be luminescent in the red $NV^0$ CL map after PCA. Therefore, the intensity distribution in figure 4.9 b) is similar to that in figure 4.9 c) to some degree. Similarly, when plotting the green CL map after PCA, CL intensities from the 484 nm centre were partially included in the green CL maps. Thus, in figure 4.11 b), from their CL spectra, green CL emissions from entire grains Ⅲ and Ⅳ are attributed to the presence of 484 nm centres, rather than NVN centres.

The overlap of different CL contributions alters the band shape in spectra as well. Three different CL emissions, green band-A, emissions from 484 nm centres and from NVN centres, overlap to form the asymmetric band in figure 4.10 f). Due to this overlap, the characteristic CL peaks from NVN centres are buried within a large asymmetric CL band. According to their photoluminescence result from nickel catalysed synthetic diamond grits, O. G. Lysenko *et al.*[22] also attributed this asymmetric CL band to the overlap between the NVN centre and the 484 nm centre. The overlap between the CL from the NVN centre and the 484 nm centre might also be the reason to explain the peculiar band shape in figure 4.9 e), though more evidence is needed to deconvolve the CL overlap.

In terms of the distribution of colour centres, some colour centres tend to aggregate at preferential diamond growth sectors during synthesis[13,27]. The {100} growth sector is a preferential location for the NVN centre during synthesis [13]. This potentially explains the inhomogeneity of CL intensities among diamond grits due to differently exposed growth sectors in figure 4.9 b). However, in figure 4.10 b), the reason for the formation of distinct green regions within single AGG, which is related with the aggregation of NVN centres, remains unclear. As the distribution of these distinct green regions is along twin boundaries in AGGs (detected by EBSD maps not shown), their formation might be associated with twinning. Additionally, $NV^0$ centre can be derived from the NVN centres during annealing[28]. This potentially explains the observed difference in $NV^0$ CL intensities among normal diamond grains in figure 4.10 c), as the distribution of NVN centres is inhomogeneous due to the different exposure of growth sectors across the polished surface. Lastly, the 484 nm centre is commonly observed in {111} growth sectors of synthetic diamond catalysed by a nickel based binder[29]. Therefore, normal diamond grains with a {111} growth sector exposed on the surface exhibit a higher CL intensity than others in figure 4.10 b) and figure 4.11 b).

As reviewed in section 2.1.2.2, regrown diamond could emit strong or weak specific CL luminescence due to the presence or absence of different colour centres. From the present CL results, the NVN centre is a sufficient but not necessary characteristic colour centre for

regrown diamond. NVN centres are consistently found in the two reference samples, yet are only sporadically distributed in grain 1, a suspected regrown grain. This suggests that, either only the regrown part contains NVN centres or not all regrown parts do. The latter claim is more likely because, when considering the overall size of grain 1, it is difficult to see how only a limited number of small regions could be the regrown within the grain. Such a scenario would contradict the low GOS value and uniform distribution of local misorientation in grain 1.The inhomogeneous distribution of NVN centres in regrown parts of diamond might be ascribed to either insufficient vacancies or excessive A-centres (a substitutional nitrogen pair) during NVN centre formation[23,30]. Therefore, the NVN centre can be regarded as a characteristic of diamond regrowth, but not a necessary one.

For grain 1, the relatively low CL intensities shown in figure 4.11 c) and d), associated with $NV^0$ centres and dislocations respectively, along with some NVN centre aggregated regions shown in figure 4.11 b), suggest that the majority of it originates from the diamond regrowth.

The most exciting finding from CL is the discovery of the distinct contour in grain 2, partially aligned with the enclosed binder particles. One order of magnitude of difference in the $NV^0$ CL intensity has been confirmed between the inside and outside of this distinct contour, with higher intensity observed inside and lower outside the contour. The CL spectrum from the outside of the contour resembles the spectrum from grain 1; both exhibit relatively low CL intensities from the 484 nm centre, $NV^0$ centre and dislocations. Therefore, the region outside of the distinct contour is regarded as regrown diamond. As for the region inside the distinct contour, its relatively abundant $NV^0$ centres, which are created from interactions either between NVN centres and vacancies or between substitutional nitrogen atoms and vacancies during hot compaction[23,31,32], suggest it is old diamond.

Turning now to the band-A emissions, all band-A CL maps present a random distribution. There are two potential explanations. Firstly, not all dislocations luminesce when scanned by electrons[33,34]. Yamamo *et al.*[33] claimed that only partial dislocations are luminescent while perfect dislocations emit little CL. Secondly, CL is not related to the type and shape of

dislocations. Both 60° mixed and screw dislocations were observed to be sometimes luminescent and sometimes non-luminescent by STEM-CL[34]. Though band-A CL is related to diamond dislocations, these two observations suggest that CL might not be suitable for studying diamond dislocation distributions. Other characterization techniques, such as TEM, are demanded.

### 4.4.3 Identifying Regrown Diamond by (S)TEM

To investigate dislocations, twins, and stacking faults in diamond, (S)TEM was employed.

#### 4.4.3.1 TEM Results of Diamond Grits

In Figure 4.14 a) and b), BF TEM images with different g vectors show no detectable dislocations, twins, or stacking faults in diamond grits; the contrast shows representative bending contours (two examples are outlined in red dashed lines in figure 4.14 a)) and thickness fringes (an example is outlined in blue dashed lines in figure 4.14 b))[35].

#### 4.4.3.2 TEM Results of AGGs

The microstructural features in AGGs are similar. In BF TEM images (Figure 4.14 c) and d)), no dislocations, twins, or stacking faults were detected with different g vectors.

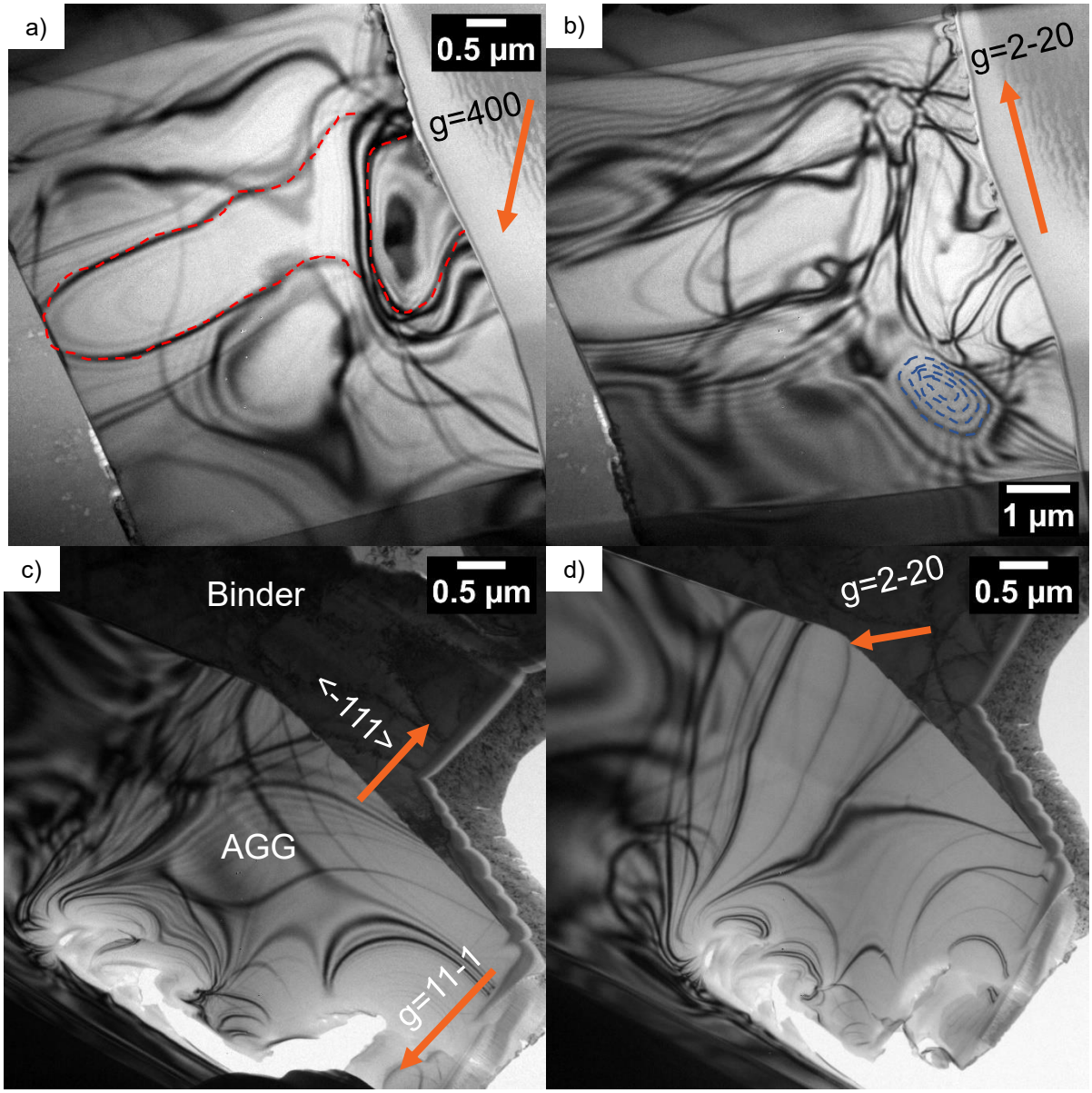


*Figure 4.14: TEM images of a diamond grit TEM sample. a) A BF TEM image. The electron beam is parallel to <011> of diamond. The g vector of (400) is marked. b) A BF TEM image. The electron beam is parallel to <111> of diamond. The g vector of (2-20) is marked. c) & d) are BF TEM images on the AGG side of a region across an AGG and normal grains outlined in figure 4.4 a). c) A BF TEM image with the electron beam parallel to <101> of AGG. The g vector of (11-1) is marked. d) A BF TEM image with the electron beam parallel to another <110> zone axis of AGG. The g vector of (2-20) is marked.*

### 4.4.3.3 TEM Results of Diamond Grits After Hot Compaction

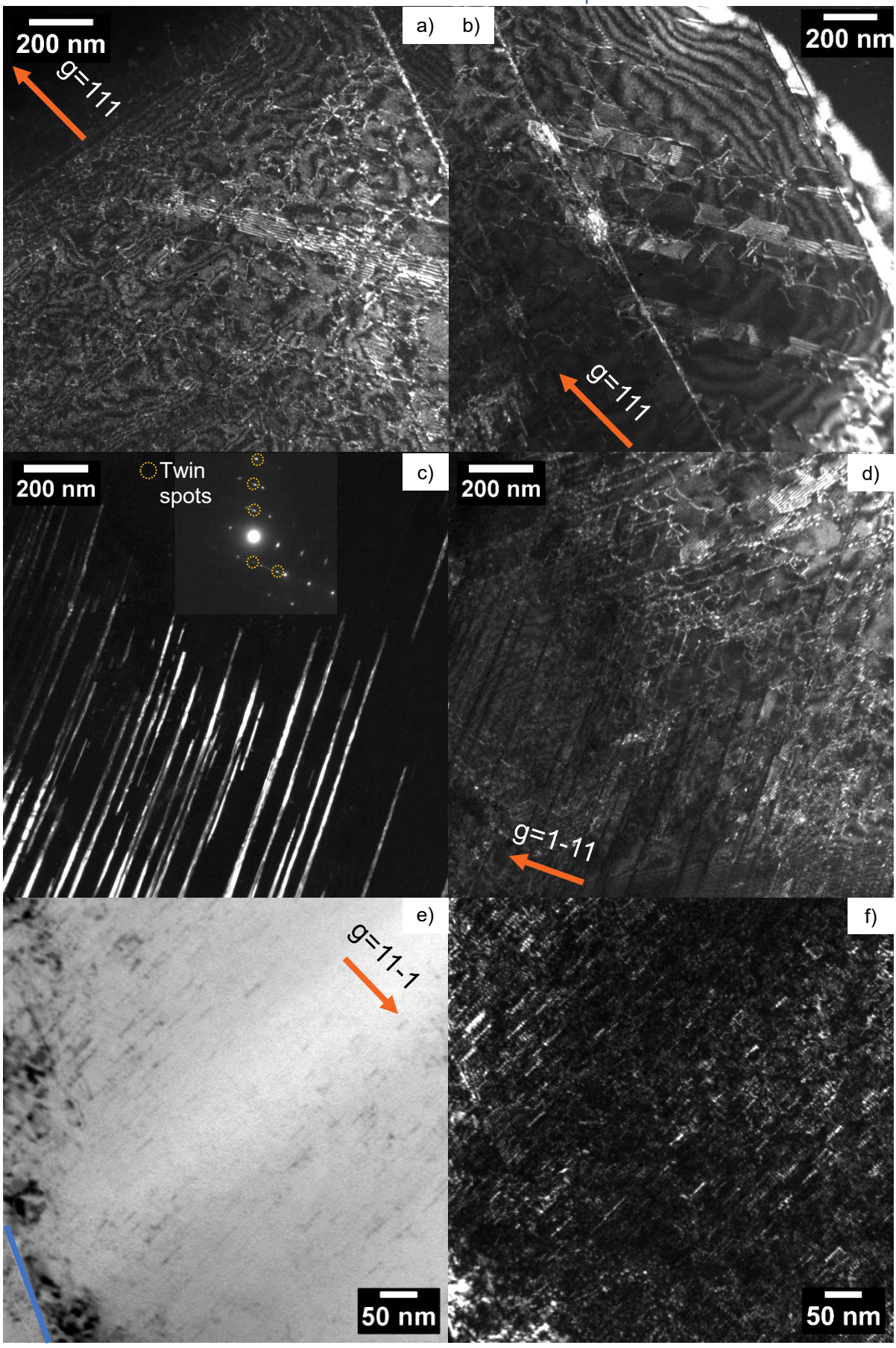

*Figure 4.15: a) and b) are DF TEM images from different regions of a normal diamond grain of SPCD after hot compaction. The g vector of (111) is marked in both images. c) and d) are DF TEM images of twins and dislocations from another normal grain after hot compaction. The diffraction pattern inserted in c) exhibits twin spots (marked by circles). The g vector of (1-11) is marked. The electron beams of a)-d) are parallel to <10-1> of diamond. e) and f) are BF and DF TEM images of a region close to a GB outlined by a blue dashed line in e). Both electron beams are parallel to <112> of diamond.*

Plastic deformation of the diamond occurs during hot compaction. When comparing with the clean BF images of the two reference samples, DF TEM images of a normal diamond grain of SPCD after hot compaction (Figure 4.15 a) and b)) reveal the presence of dislocations, appearing as bright curves and straight lines, deformation twins as long straight lines, and stacking faults as periodic dark and bright fringes. DF TEM images from another normal grain after hot compaction also clearly indicate the presence of a large number of deformation twins and dislocations, as shown in Figure 4.15 c) and d). Dislocations are still observed in regions close to the grain boundary in figure 4.15 e) and f).

#### 4.4.3.4 (S)TEM Results of SPCD

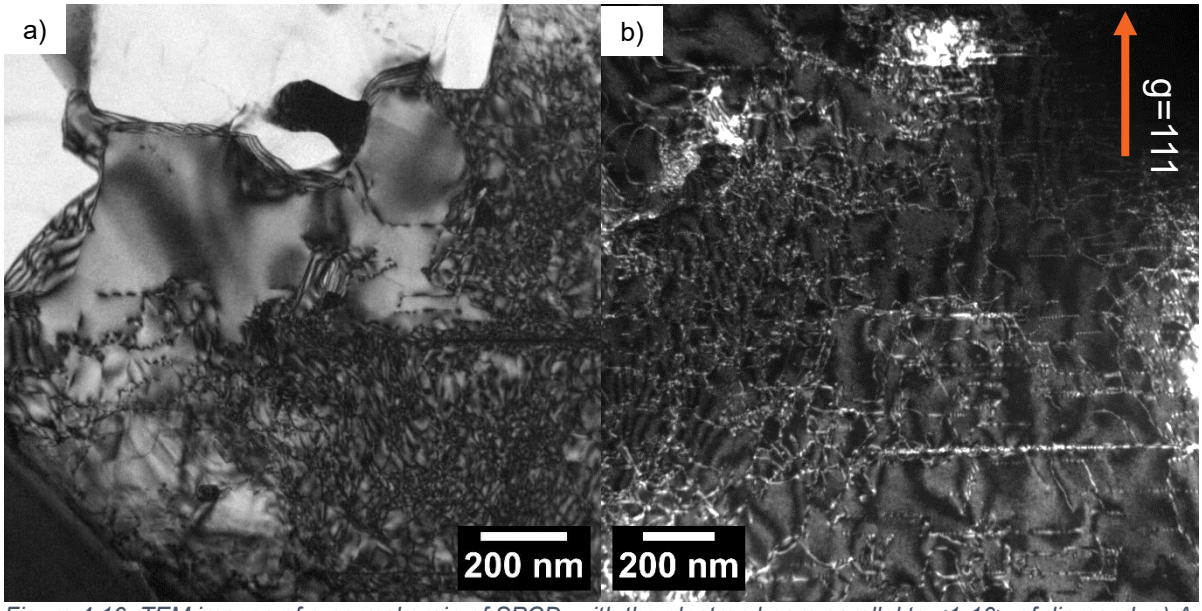


*Figure 4.16: TEM images of a normal grain of SPCD, with the electron beam parallel to <1-10> of diamond. a) A BF TEM image. b) A DF TEM image of the centre of this normal grain, filled with dislocations and twins.*

Figure 4.16 a) and b) are TEM images of different parts of a random selected normal grain of SPCD. After sintering, substantial numbers of dislocations still exist in the core of normal grains of PCD, as illustrated in Figure 4.16 a) and b). Due to dislocation entanglement, bending and dissociation, accurately calculating the regional dislocation density (dislocation length/unit volume) becomes challenging. Therefore, for a random distribution of dislocation

lines, the number emerging/unit area from the TEM sample provides a good estimation. The estimated dislocation density from figure 4.15 a), b), d) and figure 4.16 b) ranges approximately from $8x10^9$ to over $3x10^{10}$ /$cm^2$.

#### 4.4.3.5 (S)TEM Results of SPCD with Additional Graphite Feed

As for the region from SPCDG, a TEM sample across grains 1 and 2 (an orange rectangle outlined in figure 4.17 a) was lifted out and thinned. The measured distances shown in the figure 4.17 b) and c), 4.5 µm and 2.2 µm, are between the closest enclosed binder particles in each grain and the GB between these two grains. The distinct contour is annotated by a red dashed line.

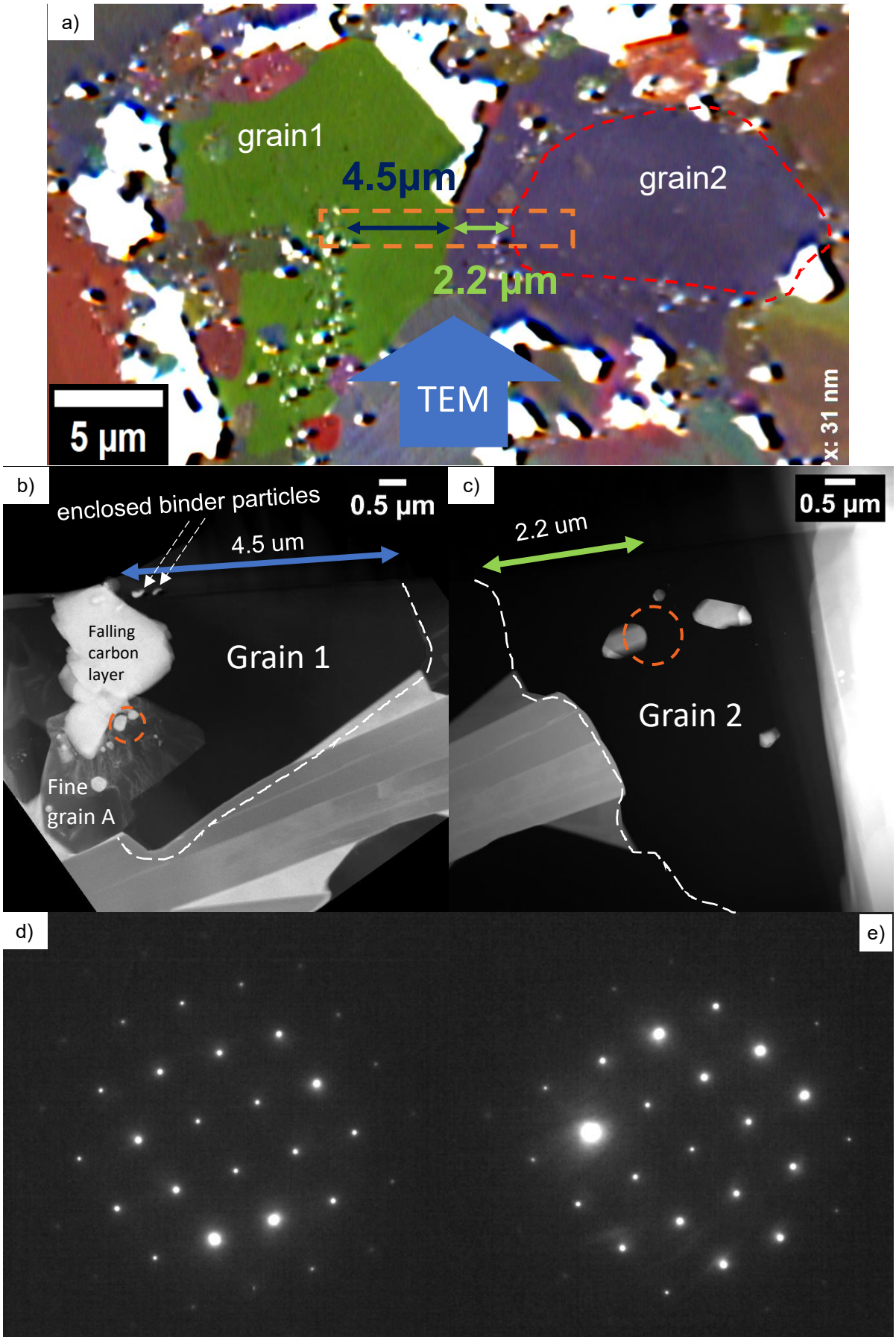
a)
grain1
4.5μm
grain2
2.2 μm
TEM
5 μm
x: 31 nm
b)
enclosed binder particles
0.5 μm
4.5 um
Falling carbon layer
Grain 1
Fine grain A
c)
0.5 μm
2.2 um
Grain 2
d)
e)

*Figure 4.17:a) the replot of part of figure 4.7 a). A TEM sample was taken from the orange rectangle. b) A LAADF image of grain 1. A fine diamond grain A is at the bottom left. The white shade is the falling carbon protective layer. c) A HAADF image of grain 2. Th GBs of both grains 1 and 2 are outlined in white dash lines. d) The diffraction pattern of a region containing both binder and diamond circled in figure 4.17 b). e) The diffraction pattern of a region circled in figure 4.17 c) which contains absolutely both binder and diamond. The zone axis is along <110>. Though it is strictly not possible to confirm both phases contribute to the overlapped DPs. It is shown in appendix A that these DPs indicate that the diamond grain and its enclosed binder particles do share the same orientation. STEM Images were taken by Ruomu Zhang.*

Figure 4.17 b) shows the LAADF image of the cross section of grain 1 in the liftout TEM sample. Besides several enclosed binder particles marked in the top left, the majority of the cross section of grain 1 is binder free. These enclosed binder particles are about 4.5 μm away from the GB between grains 1 and 2 and therefore correspond to those shown at this distance from the GB in figure 4.17 a). In contrast to grain 1, several big binder particles are found in grain 2. Their mean distance from the GB is around 2.2 μm, approximately the distance between the GB and the distinct contour and ring of binder particles in figure 4.17 a).

Figure 4.18 a)-c) are the DF weak beam TEM images of the right, middle and left parts of grain 1. Within it, there is an inhomogeneous distribution of dislocations. A 0.5-1.5 μm thick dislocation-free zone is separated by the white dashed lines from the region containing dislocations in grain 1. Interestingly, two stacking faults outlined by blue dashed lines (figure 4.18 a) & d)) reside in the dislocation-free zone, both contacting the phase boundary.

Moving from the right to the left in grain 1, the dislocation density increases gradually. The estimated dislocation density in the part of grain 1 in figure 4.18 c) is approximately $2x10^9$ /$cm^2$, slightly below the lower limit of the estimated dislocation density in the core of the old diamond in figure 4.15 a), b) and d). No deformation twin is detected in grain 1.

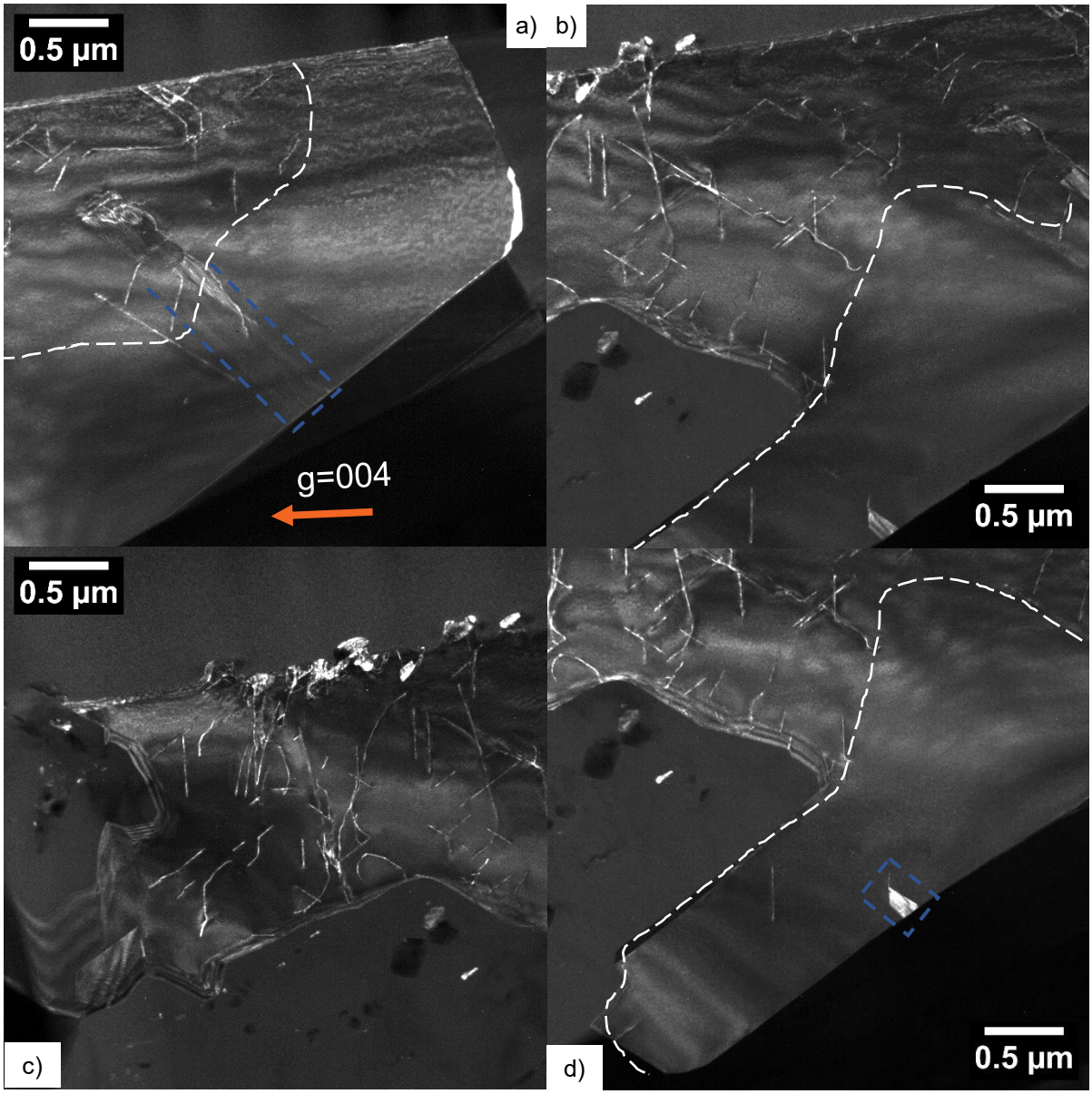


*Figure 4.18: DF weak beam TEM images of grain 1. a), b), c) correspond to the right, middle and left parts of this grain as shown in figure 4.17 b). d) is the region beneath b). The white dashed lines in all 4 figures are the boundary between a dislocation-free zone and the res part of grain 1. All images are normal to the <110> zone axis of diamond and the g vector of (004) is marked in a). Two stacking faults are outlined in blue dashed lines.*

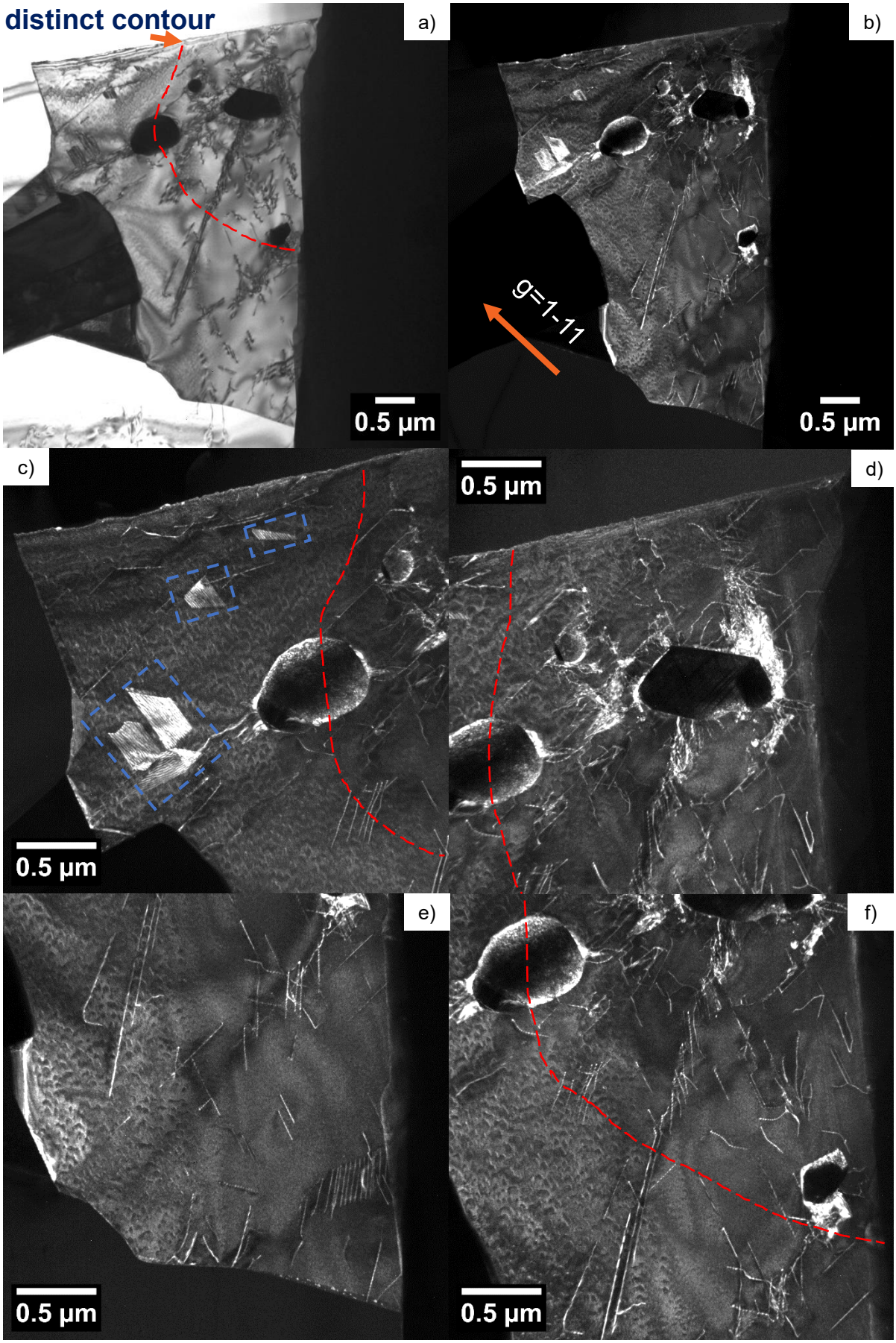


*Figure 4.19: TEM images of grain 2 as shown in figure 4.17 c). a) & b) BF and DF TEM images of the whole*

*cross section of grain 2. The g vector of (1-11) is labelled. c) - f) magnified weak beam DF TEM images of northwest, northeast, southwest and southeast regions of this grain.*

Figure 4.19 a) and b) are BF and DF TEM images of grain 2 under a two-beam condition. An orange arrow denotes the intersection between the distinct contour and the TEM sample. According to the observation that the distinct contour closely aligns with enclosed binder particles, as discussed in section 4.4.1.4, the assumed extended part of the distinct contour within TEM sample are delineated in red dashed line in figure 4.19 a), c), d) and f), approximately across the centres of the two outermost enclosed binder particles.

Grain 2 contains an inhomogeneous distribution of dislocations. Corresponding weak beam DF TEM images (figure 4.19 c) – f)) at a high magnification reveal that dislocations are mainly concentrated within this extended distinct contour. The dislocation density in figure 4.19 d) within the distinct contour is estimated to be $1x10^{10}$ /cm$^2$. Comparatively, in figure 4.19 c) which is mainly outside the distinct contour, although the region is not completely dislocation-free, the density of dislocations is significantly reduced compared to figure 4.19 d). Similar to grain 1, five stacking faults outlined in blue boxes in figure 4.19 c) are found in this low dislocation density region. No deformation twin is detected in the grain 2.

#### 4.4.3.6 Discussion of (S)TEM Results

The distribution of dislocations, deformation twins and stacking faults was confirmed by TEM imaging in four samples. These defects are absent in diamond grits and AGGs. However, high densities of these three defects were found in the normal grains of SPCD.

Concerning the region from SPCDG, there is a defect free zone in grain 1, with its highest estimated local dislocation density in 4.18 c) ($2x10^9$ /cm$^2$) still lower than that of the old diamond (~ $8x10^9$ /cm$^2$). Based on dislocation density analysis, the vast majority of grain 1 is believed to be regrown diamond. The extended part of the distinct contour roughly separates grain 2 into a dislocation sparse region and a region enriched in dislocations, with an estimated dislocation density similar to that of old diamond. Although the dislocation sparse region is not strictly dislocation-free like that in grain 1, the clear difference in dislocation

density between these two regions still evidences diamond regrowth, which has been reported before[36,37]. This suggests that the dislocation sparse region in grain 2 may have been formed via diamond regrowth, whereas the dislocation rich region is old diamond.

The formation of stacking faults is related to the diamond regrowth. Redepositing carbon atoms may deposit at the wrong positions during regrowth, altering the normal ABCABC stacking sequence to ABABC (an intrinsic stacking fault) or ABACABC (an extrinsic stacking fault)[38]. However, they are also formed in the old diamond during hot compaction, so are not a distinctive crystal defect able to distinguish old and regrown diamond.

### 4.4.4 Discussion: Comparing Different Characterization Techniques

Based on the different crystal defects observed in new and old diamond, some criteria can be established to identify the regrown diamond. For the identification of individual regrown diamond grains, the GOS approach proves effective. Coupled with ARGUS imaging, it enables rapid identification and quantitative discrimination of individual regrown diamond grains from old diamond grains if their GOS value is less than the threshold value (1°).

However, its limitations prevent the discrimination of the regrown parts of diamond grains with an overall GOS value larger than 1°. In addition, the local misorientation map cannot locate an interface between regrown and old diamond. This might be attributed to the smooth transition in orientation across the boundary between regrown diamond and old diamond[39].

To address this limitation, hyperspectral SEM-CL can be employed. Depending on the obviously different CL intensities of $NV^0$ centres from both old and regrown diamond, a distinct contour could be determined as an interface between old and regrown diamond. This distinct contour overlapped with the positions of enclosed binder particles. Another distinctive colour centre of regrown diamond revealed by SEM-CL is the NVN centre. It is concluded that the presence of NVN centres is a sign of regrown diamond, though not all regrown diamond exhibits such emissions.

Against this, due to non-radiative recombination at GB[26], visualizing diamond-diamond contacts is challenging with CL, introducing uncertainty when measuring the area of regrown diamond near GB. Some fine diamond grains at GBs, especially if they are regrown, could appear entirely non-luminescent since all electrons relax via non-radiative recombination. Furthermore, the dislocation-related blue band-A is considered not to be a suitable colour centre for studying diamond regrowth, as there is a lack of a guaranteed relation between the presence of dislocations and band-A CL emissions.

The accurate position of dislocations can be acquired by TEM imaging, particularly weak beam DF imaging. The AGGs and diamond grits are determined to be dislocation free, while the dislocation density in the core of old diamond ranges from approximately $8x10^9$ to as above than $3x10^{10}$ /cm$^2$. For the region from SPCDG, a dislocation free zone was observed in grain 1, while in grain 2, a significantly reduced dislocation density was observed in the area outside the distinct contour, compared to that inside it.

However, definitively distinguishing between old and regrown diamond is challenging without a distinct threshold dislocation density value. Some glissile dislocations may introduce uncertainty when attempting to determine this threshold value as these dislocations are capable of migrating from high dislocation density regions into lower density regions. Furthermore, TEM can only study a limited area, and therefore necessitates cumbersome lab work. Stacking faults are also observed to exist in the regrown diamond areas based on TEM imaging.

Between them, the various results give a consistent picture for old and regrown diamond. For the reference AGGs and diamond grits, regarded as regrown diamond, GOS values of their grains are below than 1°. $NV^0$ CL intensities of AGGs are lower than those of the surrounding normal grains, while $NV^0$ CL intensity of diamond grits are negligible compared to their NVN CL intensity. Both reference samples exhibit CL from heterogeneously distributed NVN centres. Lastly, TEM confirms both are free of dislocations, twins, and stacking faults. These differences in microstructure between regrown and old diamond are

summarised in the table below:

| Microstructure features | Regrown diamond | Old diamond |
|---|---|---|
| $NV^0$ centres | Low in density | High in density |
| Dislocations | Low in density or even dislocation free | High in density |
| NVN centres | Distributed unevenly | Absent |
| Global orientation spread (indicating crystallinity) | GOS<1° for a grain with a large fraction of regrown diamond | GOS>1° for a grain with a large fraction of old diamond |

*Table 4.2: the summary of the different microstructure features of regrown and old diamond.*

Conversely, diamond grains in SPCD are high in GOS values (>1°), $NV^0$ CL intensity and dislocation densities, with no NVN CL. All these results confirm that they mostly consist of old diamond.

However, in the region from SPCDG investigated, the results were different for grains 1 and 2. Grain 1 is similar to the two references samples, with a GOS value <1°, low $NV^0$ CL intensity and low in dislocation density with a large dislocation-free zone. This suggests the grain 1 is entirely regrown.

The results inside and outside the distinct contour in grain 2 strongly differ. Outside the distinct contour, the characteristic results match those of the grain 1, while inside the distinct contour, its GOS is >1°; its $NV^0$ CL intensities is of a magnitude higher than those outside and its dislocation density is as high as that of old diamond. It is concluded that the grain 2 is partially regrown with the regrown part outside of the distinct contour. In figure 6.2, such regions are widespread.

## 4.5 Summary

In summary, to preliminarily identify regions of regrown diamond, ARGUS imaging can be utilized to locate areas with reduced misorientation. To further identify the regrown part of a diamond grain, hyperspectral SEM-CL and EBSD are required. The former enables the determination of a distinct contour separating the regrown and old diamond according to the different CL intensities from $NV^0$ centres. The CL emission from NVN centres is also a distinctive sign of regrown diamond. Based on GOS values, the latter can determine entirely

regrown grains or those with the major portion formed through regrowth. TEM imaging provides the difference of dislocation density between regrown and old diamond. However, it neither establishes a quantitative threshold of dislocation density for regrown and old diamond, nor is efficient in terms of lab work.

Since the objective of regrowth identification is relating diamond regrowth to PCD mechanical performance, the aforementioned techniques are limited in their capabilities. An additional quantitative parameter is demanded to effectively assess the degree of diamond regrowth and establish the relationship between diamond regrowth and mechanical performance. Sphericity, a parameter to describe the spheroidization of binder particles, will be introduced in chapter 6 to indicate the degree of diamond regrowth.

## 4.6 Future Work

The future work suggested focuses on the improvement of characterization techniques to better study the regrown diamond.

- With the help of AI imaging, the quantitative analysis of diamond grains could be possible based on the reconstruction of ARGUS images. For example, AI can calculate the extent of direct diamond-diamond contact over the total grain boundary to represent the degree of diamond connection. This ratio is related to not only the diamond regrowth, but also the green body and the size of raw powders etc.
- With the improvement of SEM-CL systems, a lower voltage can be applied to probe the distinct contour in regrown diamond with better spatial resolution.
- With the aid of helium cooling and deconvolution code, it might be possible to resolve CL superpositions of several colour centres in each spectrum.
- With the analysis of Kikuchi patterns, the density and distribution of geometrically necessary dislocations (GND) could be mapped from EBSD data and be shown to help in identifying the regrown diamond.

## 4.7 Reference


(1) Li, L.; Xu, B.; Li, M. Analysis of the Carbon Source for Diamond Crystal Growth. *Chinese Sci. Bull.* **2008**, *53* (6), 937–942.

(2) Sumiya, H.; Harano, K.; Tamasaku, K. HPHT Synthesis and Crystalline Quality of Large High-Quality (001) and (111) Diamond Crystals. *Diam. Relat. Mater.* **2015**, *58*, 221–225.

(3) McKie, A.; Herrmann, M.; Sigalas, I.; Sempf, K.; Nilen, R. Suppression of Abnormal Grain Growth in Fine Grained Polycrystalline Diamond Materials (PCD). *Int. J. Refract. Met. Hard Mater.* **2013**, *41*, 66–72.

(4) Drouin, D.; Hovington, P.; Gauvin, R. CASINO: A New Monte Carlo Code in C Language for Electron Beam Interactions - Part II: Tabulated Values of the Mott Cross Section. *Scanning* **1997**, *19* (1), 20–28.

(5) Edwards, P. R. CHIMP-Cathodoluminescence Hyperspectral Imaging & Manipulation Program. University of Strathclyde, Glasgow 2013.

(6) Harris, A. C.; Weatherall, I. L. Objective Evaluation of Colour Variation in the Sand-Burrowing Beetle Chaerodes Trachyscelides White (Coleoptera: Tenebrionidae) by Instrumental Determination of CIELAB Values. *J. R. Soc. New Zeal.* **1990**, *20* (3), 253–259.

(7) Williamson, S. J.; Cummins, H. Z.; Kidder, J. N. *Light and Color in Nature and Art*; John Wiley and Sons, 1984; Vol. 52.

(8) Mandal, S.; Bhaduri, A. K.; Subramanya Sarma, V. A Study on Microstructural Evolution and Dynamic Recrystallization during Isothermal Deformation of a Ti-Modified Austenitic Stainless Steel. *Metall. Mater. Trans. A Phys. Metall. Mater. Sci.* **2011**, *42* (4), 1062–1072.

(9) Hadadzadeh, A.; Mokdad, F.; Wells, M. A.; Chen, D. L. A New Grain Orientation Spread Approach to Analyze the Dynamic Recrystallization Behavior of a Cast-Homogenized Mg-Zn-Zr Alloy Using Electron Backscattered Diffraction. *Mater. Sci. Eng. A* **2018**, *709* (October 2017), 285–289.

(10) Cao, Y.; Di, H.; Zhang, J.; Zhang, J.; Ma, T.; Misra, R. D. K. An Electron Backscattered Diffraction Study on the Dynamic Recrystallization Behavior of a Nickel-Chromium Alloy (800H) during Hot Deformation. *Mater. Sci. Eng. A* **2013**, *585*, 71–85.

(11) Miller, V. M.; Pollock, T. M. Texture Modification in a Magnesium-Aluminum-Calcium Alloy During Uniaxial Compression. *Metall. Mater. Trans. A Phys. Metall. Mater. Sci.* **2016**, *47* (4), 1854–1864.

(12) Mohapatra, D. R.; Jain, L.; Rai, P.; Hazra, K. S.; Samajdar, I.; Misra, D. S. Development of Crystallographic Texture and In-Grain Misorientation in CVD-Produced Single and Polycrystalline Diamond. *Chemical Vapor Deposition*. 2011, pp 107–113.

(13) Zaitsev, A. M. *Optical Properties of Diamond: A Data Handbook*; Springer Berlin Heidelberg, 2001.

(14) Ruan, J.; Kobashi, K.; Choyke, W. J. On the “Band-A” Emission and Boron Related Luminescence in Diamond. *Applied Physics Letters*. 1992, pp 3138–3140.

(15) Graham, R. J.; Moustakas, T. D.; Disko, M. M. Cathodoluminescence Imaging of Defects and Impurities in Diamond Films Grown by Chemical Vapor Deposition. *J. Appl. Phys.* **1991**, *69* (5), 3212–3218.

(16) Takeuchi, D.; Watanabe, H.; Yamanaka, S.; Okushi, H.; Sawada, H.; Ichinose, H.; Sekiguchi, T.; Kajimura, K. Origin of Band-(Formula Presented) Emission in Diamond Thin Films. *Phys. Rev. B - Condens. Matter Mater. Phys.* **2001**, *63* (24), 1–7.

(17) Melnikov, A. A.; Denisenko, A. V.; Zaitsev, A. M.; Shulenkov, A.; Varichenko, V. S.; Filipp, A. R.; Dravin, V. A.; Kanda, H.; Fahrner, W. R. Electrical and Optical Properties of Light-Emitting p-i-n Diodes on Diamond. *J. Appl. Phys.* **1998**, *84* (11), 6127–6134.

(18) Collins, A. T.; Spear, P. M. The 1.40 EV and 2.56 EV Centres in Synthetic Diamond. *J. Phys. C Solid State Phys.* **1983**, *16* (5), 963–973.

(19) Bocharov, S. N.; Isakov, A. I.; Petrov, Y. Y.; Orekhova, K. N.; Dementeva, E. V.; Burakov, B. E.; Zamoryanskaya, M. V. Study of Radioluminescence and Cathodoluminescence of Artificial Diamond Single Crystals as Prospective Durable Core Material for Nuclear Electric Batteries. *Diam. Relat. Mater.* **2021**, *120* (September), 108658.

(20) Iakoubovskii, K.; Adriaenssens, G. Luminescence Excitation Spectra in Diamond. *Phys. Rev. B - Condens. Matter Mater. Phys.* **2000**, *61* (15), 10174–10182.

(21) Collins, A. T.; Robertson, S. H. Cathodoluminescence Studies of Sintered Diamond. *J. Mater. Sci. Lett.* **1985**, *4* (6), 681–684.

(22) Lysenko, O. G.; Grushko, V. I.; Mitskevich, E. I.; Ilnitska, G. D.; Boyarintsev, A. Y.; Onufriev, Y. D.; Popov, V. F.; Levchuk, L. G.; Kazuchits, N. M.; Rusetsky, M. S.; et al. Luminescent and Radiation Characteristics of Monocrystalline Diamond Powders. *J. Superhard Mater.* **2019**, *41* (1), 17–23.

(23) Collins, A. T. The Characterisation of Point Defects in Diamond by Luminescence Spectroscopy. *Diam. Relat. Mater.* **1992**, *1* (5–6), 457–469.

(24) Kawarada, H.; Yokota, Y.; Mori, Y.; Nishimura, K.; Hiraki, A. Cathodoluminescence and Electroluminescence of Undoped and Boron-Doped Diamond Formed by Plasma Chemical Vapor Deposition. *J. Appl. Phys.* **1990**, *67* (2), 983–989.

(25) Klein, P. B.; Crossfield, M. D.; Freitas, J. A.; Collins, A. T. Donor-Acceptor Pair Recombination in Synthetic Type-IIb Semiconducting Diamond. *Phys. Rev. B* **1995**,

*51* (15), 9634–9642.

(26) Yacobi, B. G.; Holt, D. B. *Cathodoluminescence Microscopy of Inorganic Solids*; Springer US: Boston, MA, 1990.

(27) Lang, A. R. Topographic Methods for Studying Defects in Diamonds. *Diam. Relat. Mater.* **1993**, *2* (2–4), 106–114.

(28) Webb, S. W.; Jackson, W. E. Synthetic Diamond Crystal Strength Enhancement through Annealing at 50 Kbar and 1500 °C. *J. Mater. Res.* **1995**, *10* (7), 1700–1709.

(29) Collins, A. T.; Kanda, H.; Burns, R. C. The Segregation of Nickel-Related Optical Centres in the Octahedral Growth Sectors of Synthetic Diamond. *Philos. Mag. B Phys. Condens. Matter; Stat. Mech. Electron. Opt. Magn. Prop.* **1990**, *61* (5), 797–810.

(30) Van Enckevort, W. J.; Visser, E. P. Photoluminescence Microtomography of Diamond. *Philos. Mag. B Phys. Condens. Matter; Stat. Mech. Electron. Opt. Magn. Prop.* **1990**, *62* (6), 597–614.

(31) Soltamova, A. A.; Il'in, I. V.; Shakhov, F. M.; Kidalov, S. V.; Vul', A. Y.; Yavkin, B. V.; Mamin, G. V.; Orlinskii, S. B.; Baranov, P. G. Electron Paramagnetic Resonance Detection of the Giant Concentration of Nitrogen Vacancy Defects in Sintered Detonation Nanodiamonds. *JETP Lett.* **2010**, *92* (2), 102–106.

(32) Baranov, P. G.; Soltamova, A. A.; Tolmachev, D. O.; Romanov, N. G.; Babunts, R. A.; Shakhov, F. M.; Kidalov, S. V.; Vul', A. Y.; Mamin, G. V.; Orlinskii, S. B.; et al. Enormously High Concentrations of Fluorescent Nitrogen-Vacancy Centers Fabricated by Sintering of Detonation Nanodiamonds. *Small* **2011**, *7* (11), 1533–1537.

(33) Yamamoto, N.; Spence, J. C. H.; Fathy, D. Cathodoluminescence and Polarization Studies from Individual Dislocations in Diamond. *Philos. Mag. B Phys. Condens. Matter; Stat. Mech. Electron. Opt. Magn. Prop.* **1984**, *49* (6), 609–629.

(34) Pennycook, S. J.; Brown, L. M.; Craven, A. J. Observation of Cathodoluminescence at Single Dislocations by STEM. *Philos. Mag. A Phys. Condens. Matter, Struct. Defects Mech. Prop.* **1980**, *41* (4), 589–600.

(35) Edington, J. W. *Interpretation of Transmission Electron Micrographs*; 1975; Vol. 6.

(36) Walmsley, J. C.; Lang, A. R. Characteristics of Diamond Regrowth in a Synthetic Diamond Compact. *J. Mater. Sci.* **1988**, *23* (5), 1829–1834.

(37) Westraadt, J. E.; Dubrovinskaia, N.; Neethling, J. H.; Sigalas, I. Thermally Stable Polycrystalline Diamond Sintered with Calcium Carbonate. *Diam. Relat. Mater.* **2007**, *16* (11), 1929–1935.

(38) Yin, L. W.; Li, M. Sen; Cui, J. J.; Bai, Y. J.; Xu, B.; Gong, J. H.; Hao, Z. Y. Planar Defects and Dislocations in HPHT As-Grown Diamond Crystals. *Diam. Relat. Mater.* **2002**, *11* (2), 268–272.

(39) Britun, V. F.; Oleynik, G. S.; Semenenko, N. P. Deformation Processes during High-Pressure Sintering of the Diamond Powders Produced by Catalytic Synthesis. *J. Mater. Sci.* **1992**, *27* (16), 4472–4476.

# 5 Mechanisms of Diamond Regrowth

## Table of Contents

# 5.1 Introduction

The second objective of this thesis is to investigate mechanism(s) of diamond regrowth during HPHT sintering. One approach to unravel this mystery involves scrutinizing the evolution of the microstructure of PCD materials throughout the entire HPHT sintering process. Samples aborted from different stages of HPHT sintering, including cold compaction, hot compaction and dwell, are examined using multiple characterization techniques. By comparing the different compositions, phase transitions and microstructural features from different samples, this chapter endeavours to elucidate the prevailing diamond regrowth mechanism(s) during HPHT sintering.

# 5.2 Material and Sample Preparation

Eight samples were aborted at different stages of HPHT sintering. Specific information about each aborted stage, including temperature, pressure, and a brief description, can be found in Table 5.1. Upon termination, both the loading and power were stopped instantaneously in the press. Subsequently, the press underwent a natural cooling process to room temperature, while the deloading process is almost linear.

The time point at which each sample was aborted is also labelled in the sintering profile in figure 5.1 below. Not all samples were examined by every characterization technique.

| Number | Abort at which stage | Temperature when aborted | Pressure when aborted | Description |
|---|---|---|---|---|
| 0 | End of cold compaction | 25 °C | 75% $P_{max}$ | Crushed diamond powders |
| 1 | Theoretical start of binder infiltration | 1320 °C (Theoretical eutectic point of Co-C system) | 95% $P_{max}$ | The possible start of the infiltration of liquid binder, a Co-rich liquid with dissolved C and WC. The eutectic point of the Co-WC system is less than 1320°C |
| 2 | Infiltration (possible actual start of hot compaction) | 1350 °C | | Possibly the actual start of the **infiltration** of liquid binder |
| 3 | Start of dwell | $T_{max}$ | $P_{max}$ | The possible start of diamond regrowth. Co-WC is molten and possibly infiltrates the whole PCD skeleton. |
| 4 | Halfway point of dwell | $T_{max}$ | | |
| 5 | End of dwell | $T_{max}$ | | The possible end of diamond regrowth |
| 6 | Halfway through cooling | 70% $T_{max}$ | 95% $P_{max}$ | |
| 7 | End of HPHT sintering | 25 °C | 0 GPa | The SPCD |

*Table 5.1*: Details of 8 PCD samples aborted at different stage of HPHT sintering. The PCD skeleton refers to the assembled diamond and Co admixed powders. There are many gaps within the PCD skeleton. *Tmax ranges from 1500-1800 °C. Pmax ranges from 6.5-8.5 GPa.*

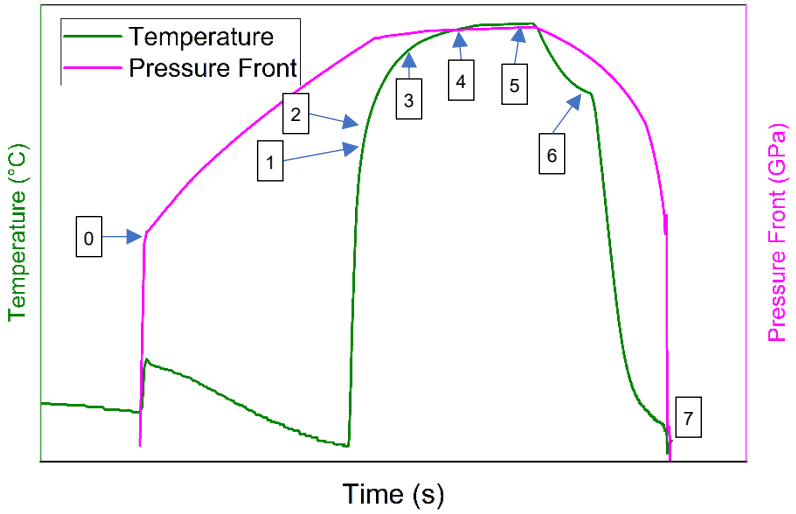


*Figure 5.1: Replot of Figure 3.3 - HPHT Sintering Profile for SPCD sample, showing points at which samples were aborted. Numbers refer to table 5.1.* ***Most of the details were wiped due to confidentiality requirement.***

# 5.3 Experimental

## 5.3.1 Characterization Techniques

Electron Microscopies: The details of all the EM-related characterization have been previously discussed in section 3.3. The details of XRD and ICP-OES can be found in section 3.4.

Dynamic Light Scattering (DLS):

The DLS data were acquired with the help of PhD candidate Liwei Dai from the University of Oxford. A Horiba LA-960 Laser Scattering Particle Size Distribution Analyser (Horiba, Japan) equipped with an ultrasonication function was used to measure the size distribution of diamond powders. Its measurement range is from 10 nm to 0.5 mm diameter. Diamond powders were suspended in deionized (DI) water, which produces a zeta potential of about -50 mV by the adsorption of $-OH^-$ molecules onto the diamond surface[1]. This high zeta potential, combined with the ultrasonication function of the size analyser, effectively prevents the aggregation of diamond powders during measurement.

The concentration of the diamond-DI water suspension was empirically adjusted to fall within the detection range of the size analyser (around 50 g/L). The binning of the size of the diamond particles

is automatically set by the size analyser. Each measurement was repeated 3 times to get an average vol % within each sub-bin.

# 5.4 Results and Discussion

## 5.4.1 Outgassed Powders and Sample 0

Before the start of hot compaction, the diamond/Co admixed powders were pre-treated via outgassing and cold compaction to achieve a green body. These steps have the potential to influence the subsequent diamond regrowth.

### 5.4.1.1 XRD Results of Raw Powders and Sample 0

To examine the different phases during different sintering stages, XRD patterns were obtained from 6 samples. These XRD patterns were normalized with respect to the strongest diamond XRD peak ((111) at 44°). For a direct comparison between them, all the XRD patterns are presented together in this section and will be described in the section corresponding to the representative samples.

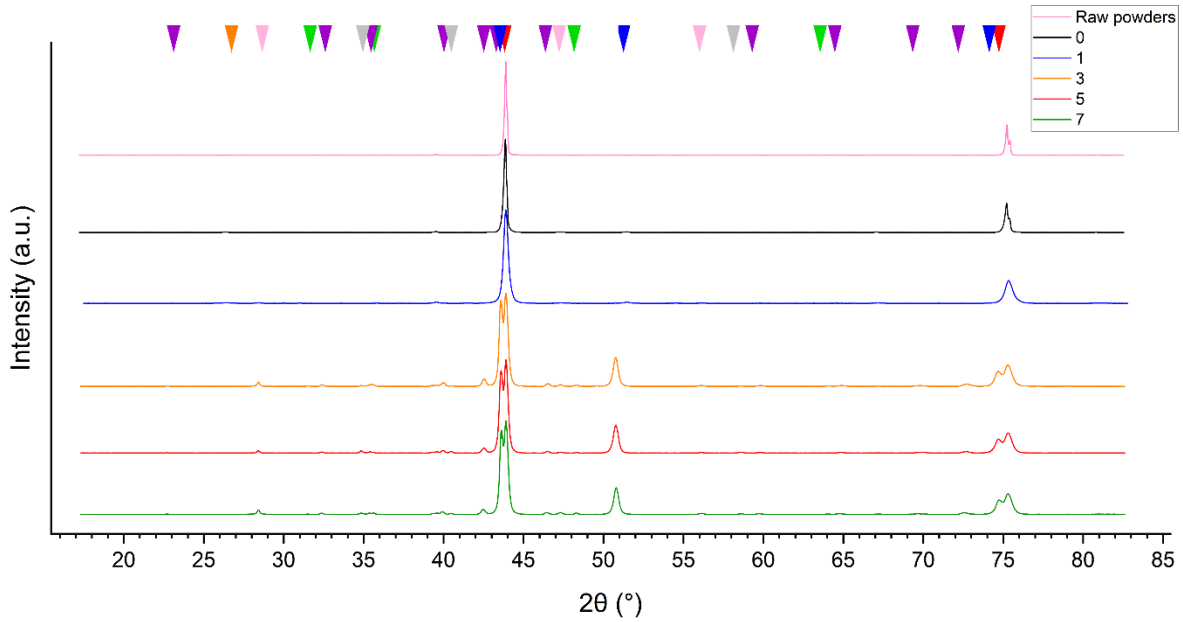


*Figure 5.2: normalized XRD patterns of 6 samples aborted from different stages of sintering. All phases are identified by pointers at the top. Diamond in red; FCC Co in blue; $Co_3W_3C$ in purple; WC in green, NbC in grey, graphite in orange and silicon in pink. The diffraction pattern of sample 2 is almost identical to sample 1. Those of samples 4 & 6 are almost identical to samples 5 & 7*

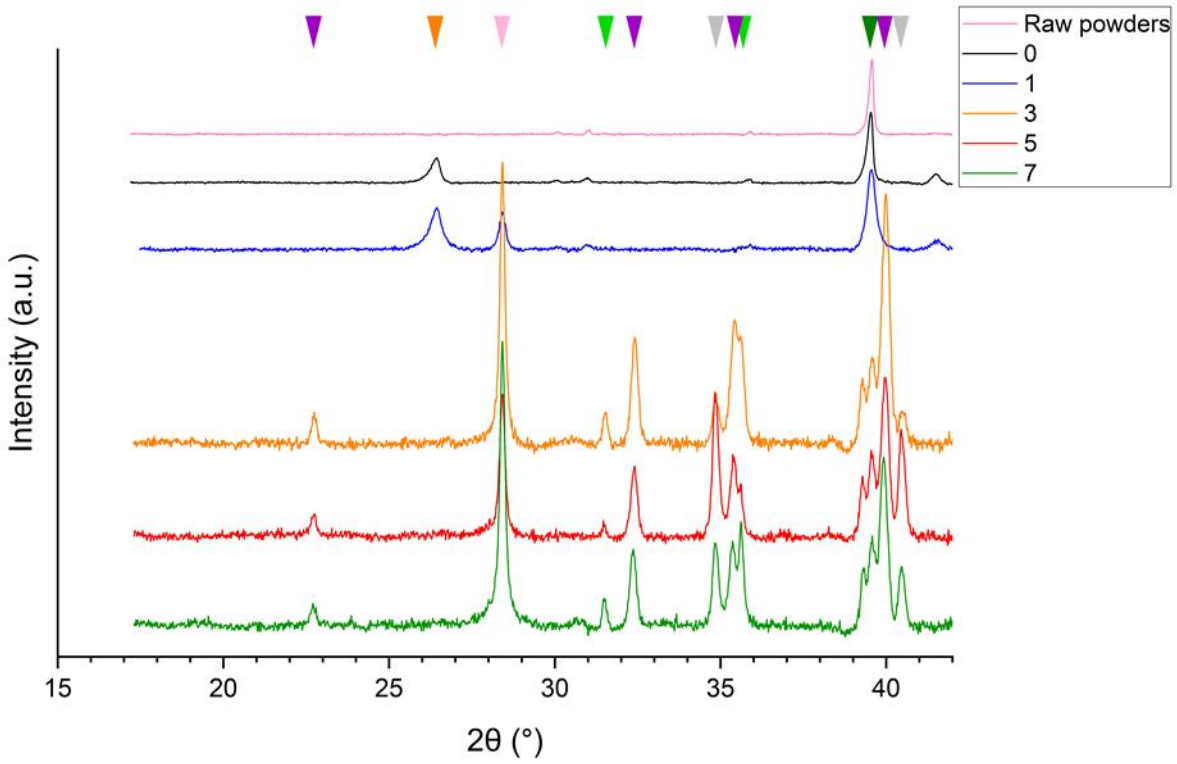


*Figure 5.3: the enlarged range (15°-42°) of figure 5.2. The phase identification is the same as in figure 5.2. It is suspected that an unknown peak identified with an olive pointer at 39.8° might be from XRD sample holder as it is completely disappeared in the XRD pattern from same sample measured by another XRD diffractometer.*

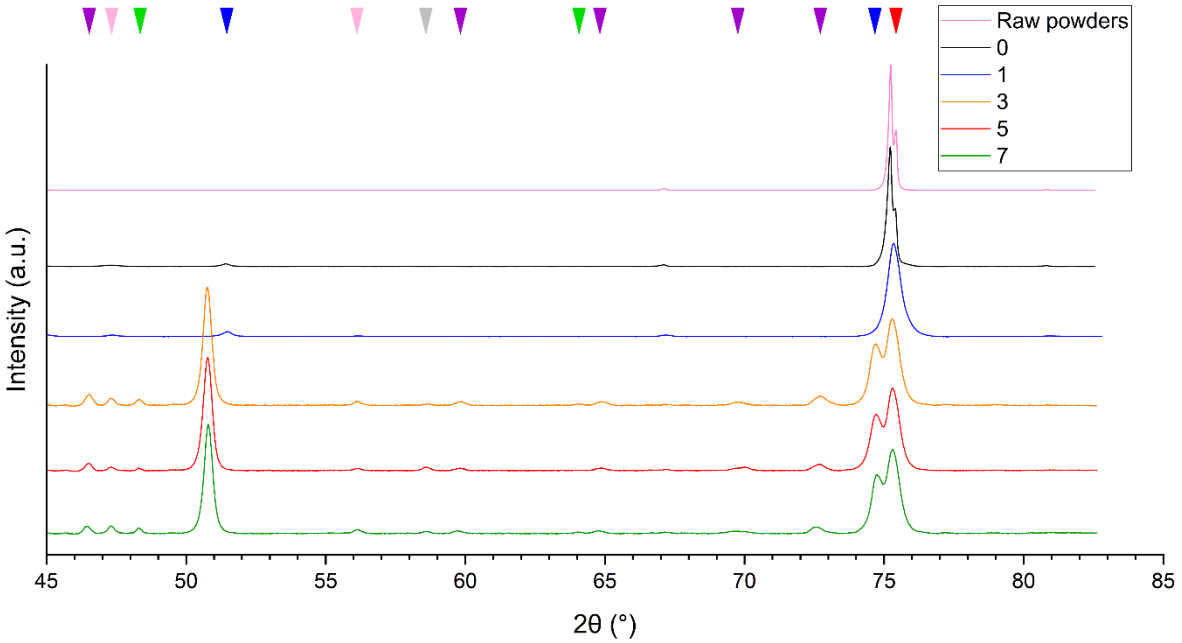


*Figure 5.4: the enlarged range (45°-85°) of figure 5.2. The phase identification is the same as in figure 5.2.*

In figure 5.2, XRD patterns are identified with respect to references from the Crystallography Open Database[2]. A relatively thin layer of single crystal silicon powder was sprinkled onto PCD cutter. This silicon acts as a reference material to correct any potential XRD peak shift. To find the differences

between them, these XRD patterns were further enlarged in the range 15° - 42° and 45° - 85°, plotted in figure 5.3 and figure 5.4 respectively.

The main XRD peaks of raw powders and sample 0 are two diamond peaks at 44.0° and 77.5°. A weak peak of cobalt is also presented at 51.5°. A small (002) graphite peak at 26.6° emerges in sample 0, which is graphite formed during outgassing. Results from Element Six Ltd. on an outgassed powder prior to compaction confirmed the presence of (002) graphite peak.

### 5.4.1.2 DLS Results of Outgassed Powders and Sample 0

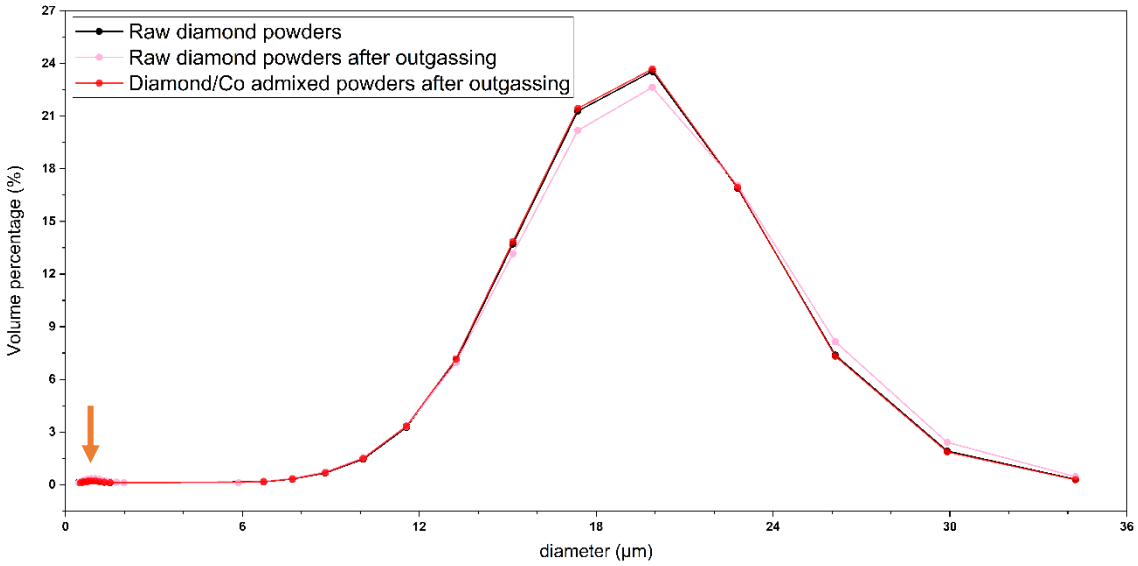


*Figure 5.5: Raw diamond powder distributions before and after outgassing, and the diamond Co admixed powder after*

*outgassing.*

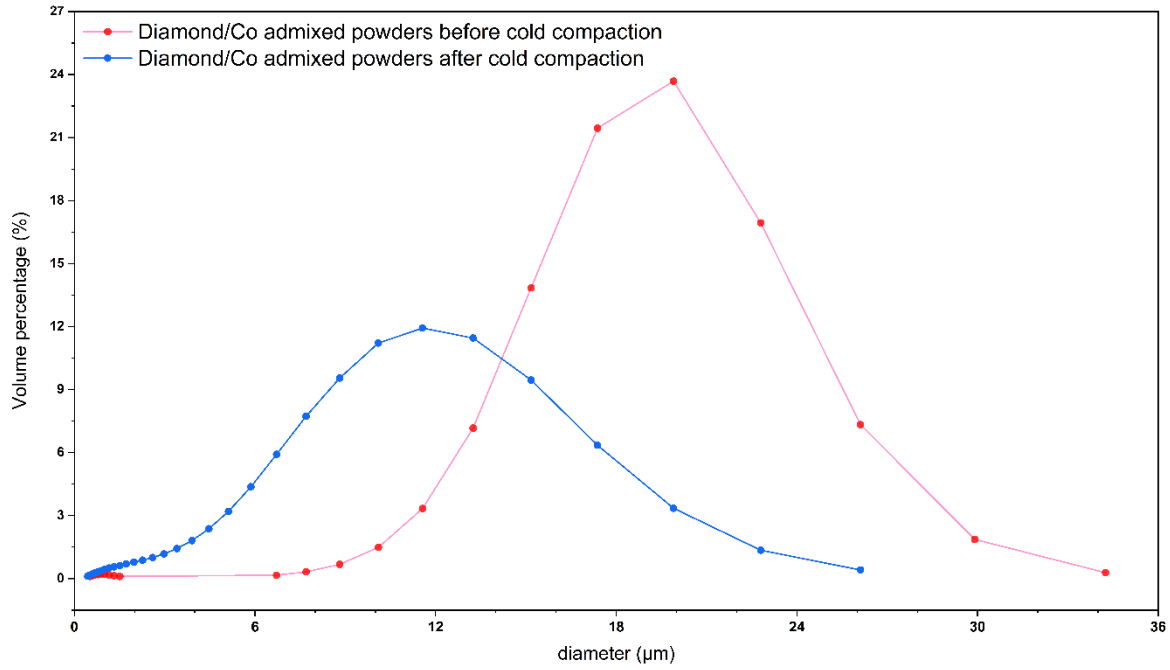


*Figure 5.6: Diamond/Co admixed powders before and after cold compaction.*

Figure 5.5 shows the DLS results of diamond powders before and after outgassing. The DLS of diamond/Co powders after outgassing is also included. The Co powders have little impact on the size distribution curve due to their low vol%.

DLS results show a bi-modal powder distribution. The broad peak corresponds to the 95 vol% coarse powders with a 20 µm average diameter, while the small hump indicated by an orange arrow corresponds to 5 vol% fine powders with a 1 µm average diameter. The powder distribution remains unaltered before and after outgassing, with and without cobalt powders.

From the DLS results in figure 5.6, the initial bi-modal size distribution transforms into a mono-modal distribution, accompanied by a reduction in the overall average grain size from 17.4 ±2.3 µm to 9.0 ± 2.0 µm. The distribution curve also gets flattened and broadened.

#### 5.4.1.3 SEM Images of Outgassed Powders and Sample 0

Diamond powders before and after outgassing and cold compaction are displayed in figure 5.7. The most evident change after outgassing was in the colour of the diamond powders. Diamond powders

changed from a pale yellow to a dark grey after outgassing. This indicates the occurrence of surface graphitization during outgassing[3]. The colour didn't change after cold compaction.

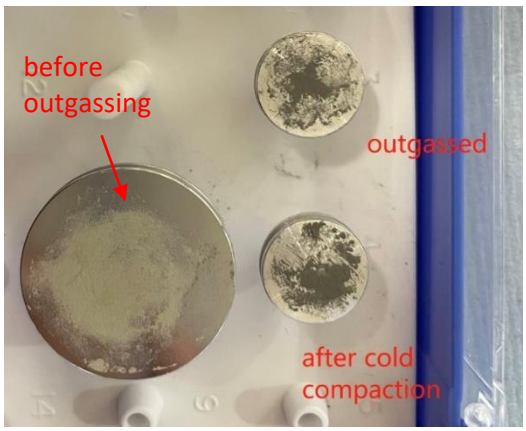


*Figure 5.7: the colours of diamond powders before and after outgassing; before and after cold compaction.*

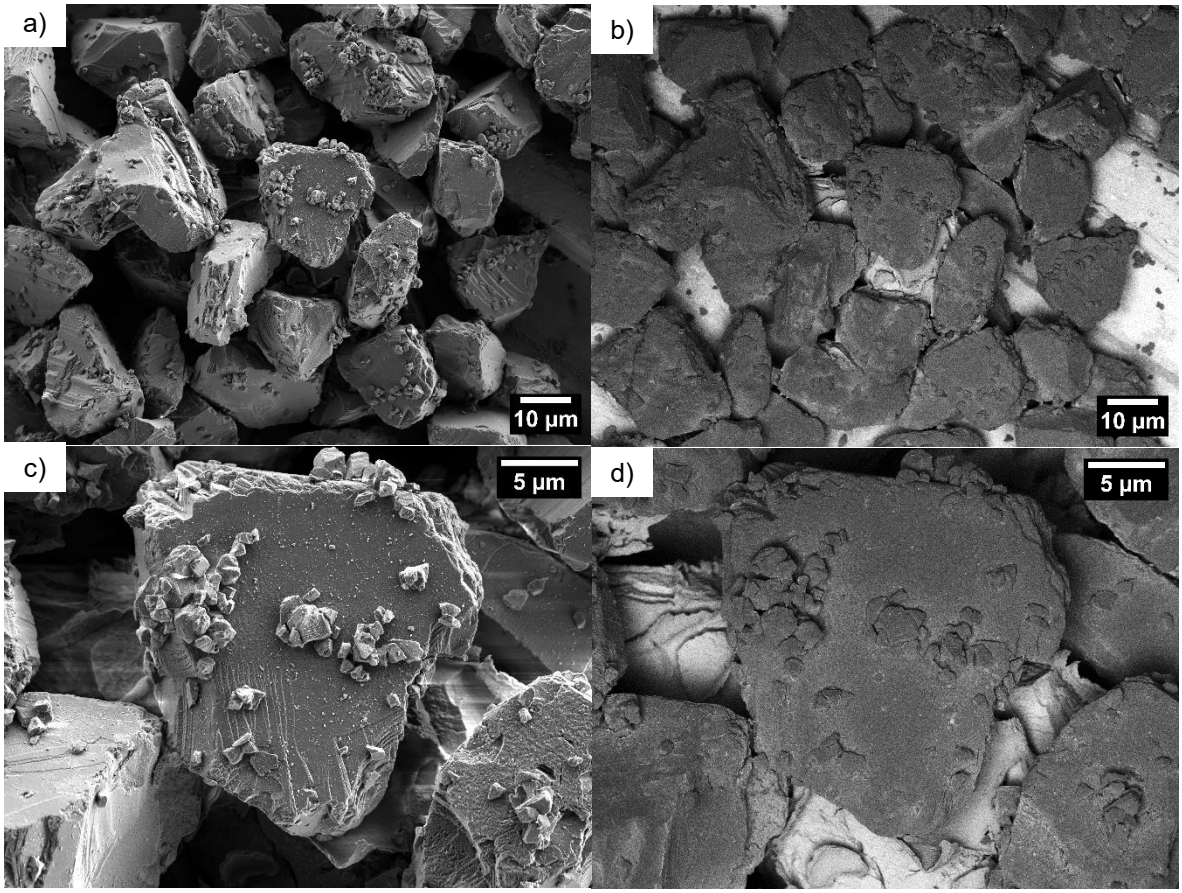


*Figure 5.8*: raw diamond powders **before outgassing**. a) An SE2 image and b) an EsB image at low magnification. c) An SE2 image and d) an EsB image at high magnification.

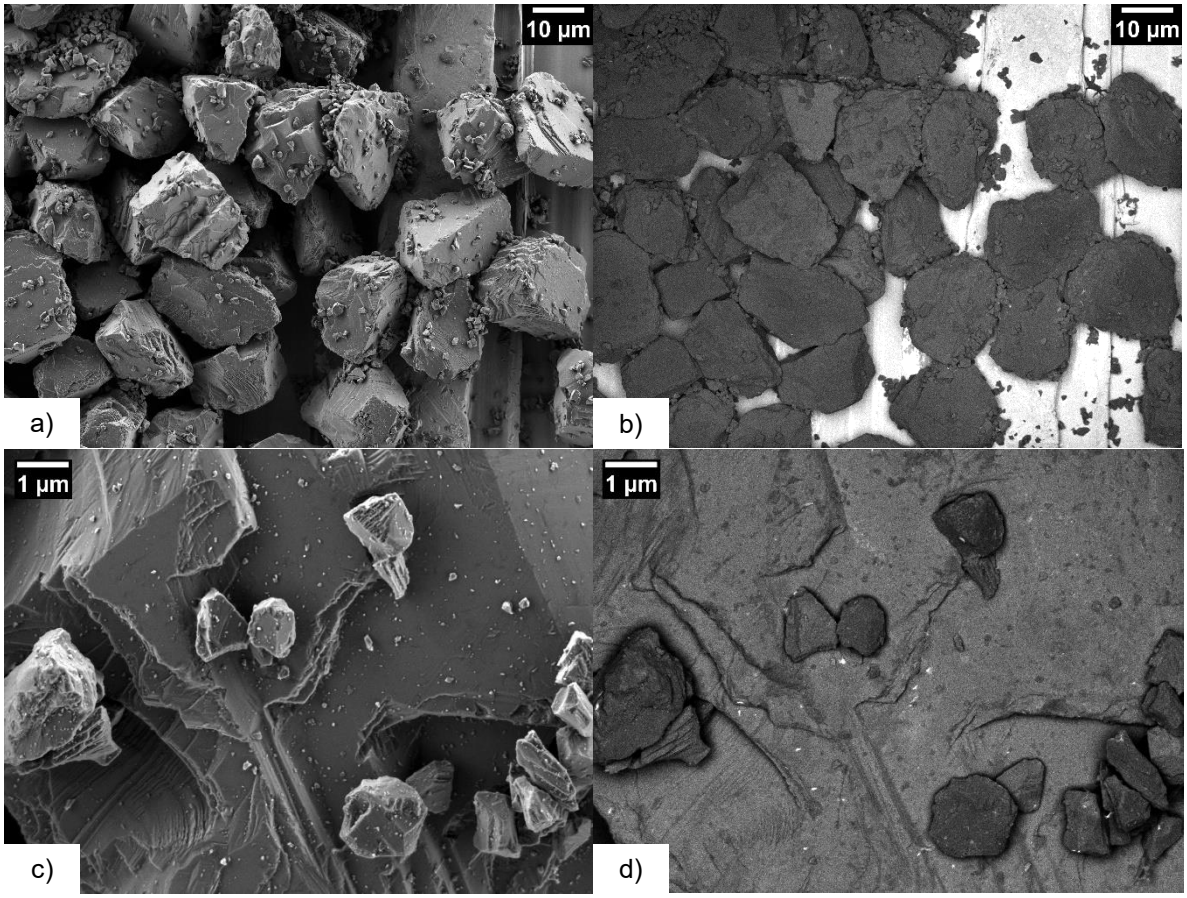


*Figure 5.9: raw diamond powders **after outgassing**. a) An SE2 image and b) An EsB image at low magnification. c) An SE2 image and d) An EsB image at high magnification.*

Diamond powders before outgassing (Figure 5.8 a)-d)) and after outgassing (Figure 5.9 a)-d)) are displayed. The morphologies of diamond powders after outgassing closely resemble those before outgassing. Fine diamond powders evenly adhere to coarse powders, indicating effective admixing.

Figure 5.10 a)- f) are SEM images of diamond/Co powders before outgassing. Figure 5.11 a)- f) are SEM images of diamond/Co powders after outgassing. Before outgassing, admixed Co powders appear spongy, spherical and intact. They are free from any diamond covering. In contrast, after outgassing, admixed Co powders are in a dense, faceted state. Some have fragmented to smaller pieces, which are tightly covered by substances which are suspected to be graphite. These substances show diverse morphologies and contrast, particularly in Inlens images, distinct from the diamond.

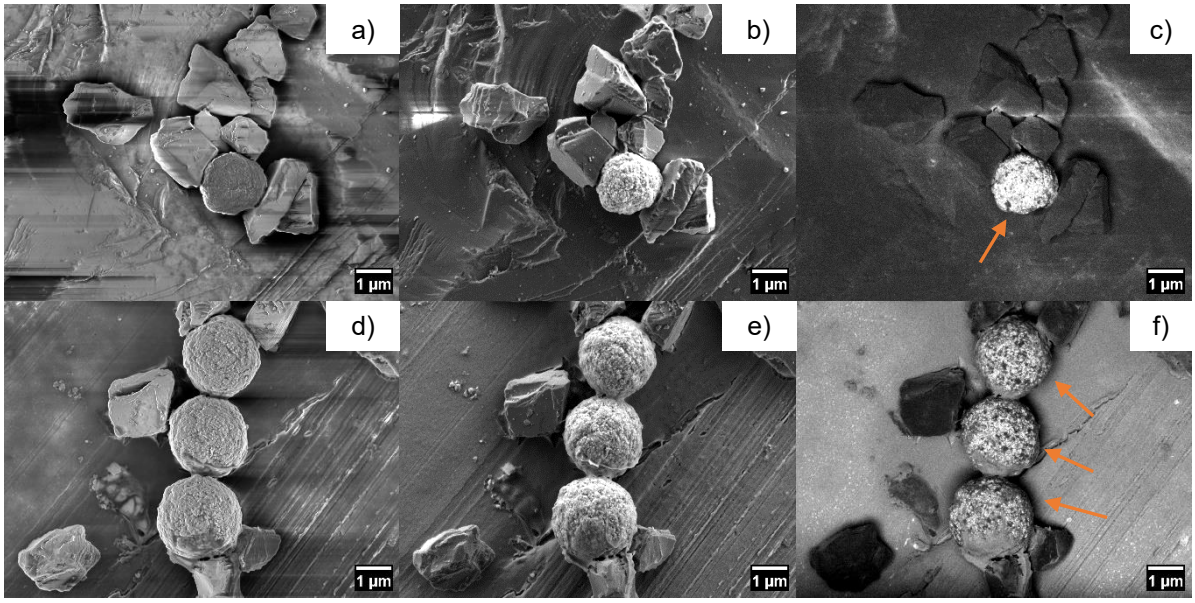


*Figure 5.10: the diamond/Co admixed powders **before outgassing**. a), d) inlens images, b), e) SE2 image and c), f) EsB images of binder particle. Co powders are indicated by orange arrows.*

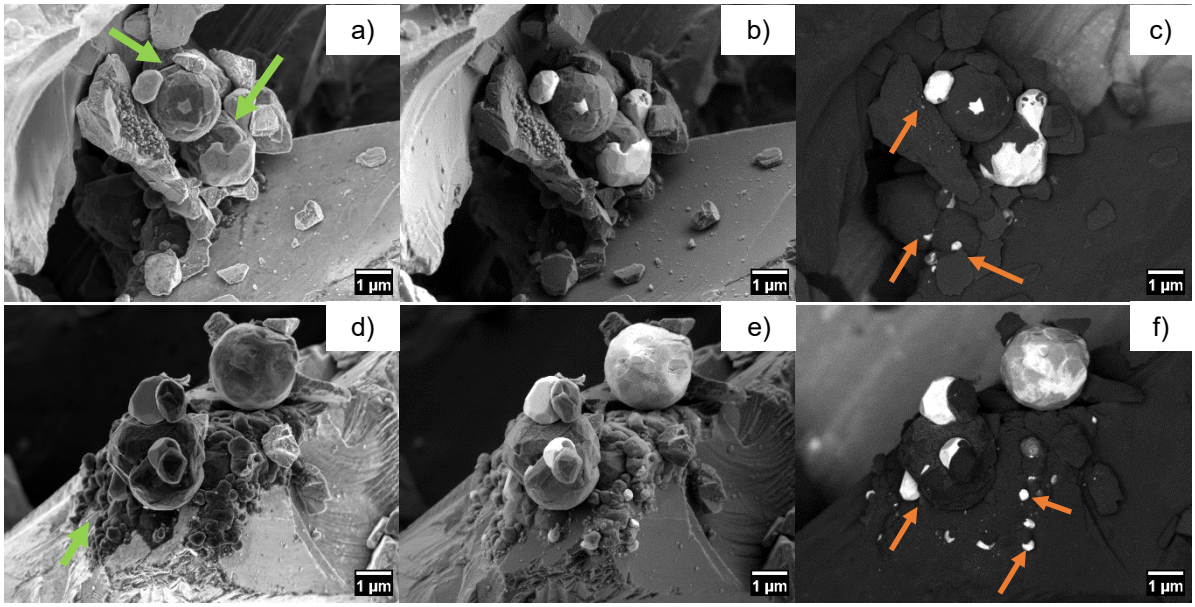


*Figure 5.11: the diamond/Co admixed powders **after outgassing**. a), d) inlens images, b), e) SE2 image and c), f) EsB images of binder particle. Fragmented Co powders are indicated by orange arrows. Suspected graphite is indicated by green arrows.*

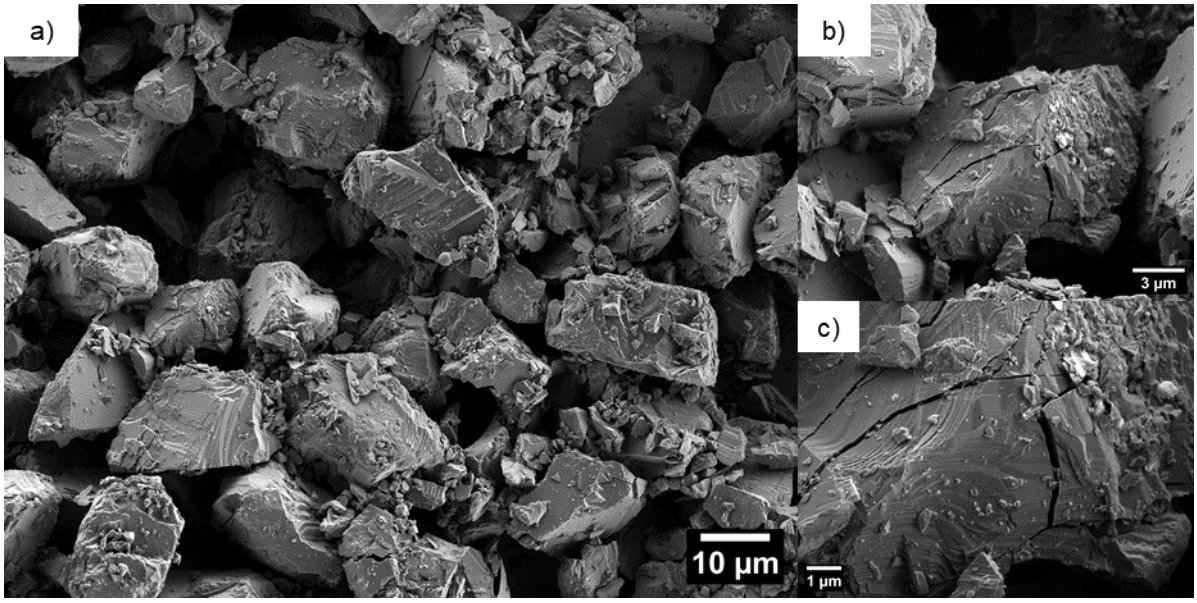

*Figure 5.12: SE2 images of diamond powders after cold compaction. a) at low magnification. b) and c) at high magnifications.*

The morphology of diamond powders after cold compaction is displayed in figure 5.12 a). Evidently, there are various sized of diamond fragments after cold compaction, with their diameters ranging from approximately 100 nm to less than 20 µm. Some have small fracture steps on surfaces. Many microcracks are also found in the coarse diamond powders as shown in figure 5.12 b) and c). Some microcracks are wedged open by diamond debris, while others might have propagated deeply into the core of the particles.

#### 5.4.1.4 Discussion of Outgassed Powders and Sample 0

Generally, after outgassing, there is a layer of graphite covering diamond samples. This graphite was also directly detected using XRD by staff from Element Six Ltd. Additionally, the appearance and disappearance of charging in the SEM on diamond powders before (figure 5.10 a) & d)) and after outgassing (figure 5.11 a) & d)) also supports the formation of surface graphite overlaying diamond powders during outgassing.

The size and morphologies of diamond particles remain unchanged after outgassing. Since the surface graphitization will alter the topography of the diamond surface due to an expansion of volume, the relatively clean diamond surfaces after outgassing imply that the degree of this surface

graphitization is likely limited[4]. However, which graphitization mechanism dominates remains unclear. Both binderless graphitization and binder-assisted graphitization, which are discussed in detail in section 5.4.2.7, occur. The binder-assisted diamond graphitization might be the reason for the morphology change and fragmentation of Co powders[5]. This graphite may act as a lubricant during cold compaction[6] and as a carbon source during diamond regrowth[7].

The two most prominent morphological changes after cold compaction are the altered diamond topography and the reduced size of diamond powders. These changes are in good consistency with a previous study[8]. During cold compaction, due to the substantial externally applied pressure, diamond powders are crushed into small pieces via cleavage fracture along {111} planes, resulting in fracture steps on diamond surfaces[9]. Some crushed diamond fragments fill interstitial gaps and thereby enhance the overall density of the green body[8]. The remaining microcracks could potentially be filled by liquid binder during infiltration. Few crystal defects are introduced to diamond powders during cold compaction[10].

## 5.4.2 Samples 1 and 2

Samples 1 and 2 were terminated at the theoretical start and possibly the practical start of binder infiltration, respectively.

### 5.4.2.1 XRD Result of Sample 1

The (002) graphite peak seen in sample 0 grows stronger in sample 1 in figure 5.4. The only difference between the XRD patterns of sample 0 and 1 is the increased intensity of this (002) graphite peak. By Rietveld refinement analysis of the XRD peak intensity, the estimated amount of graphite almost doubled from 0.93 wt% to 1.80 wt% between cold compaction and binder infiltration (Table 5.2).

| Sample | Graphite/Graphite+Diamond (wt%) |
|---|---|
| 0: end of cold compaction | 0.93 |
| 1: start of binder infiltration | 1.80 |

*Table 5.2: Rietveld refinement analysis of the wt% of graphite among diamond and graphite.*

### 5.4.2.2 ICP-OES Results of Samples 1 and 2

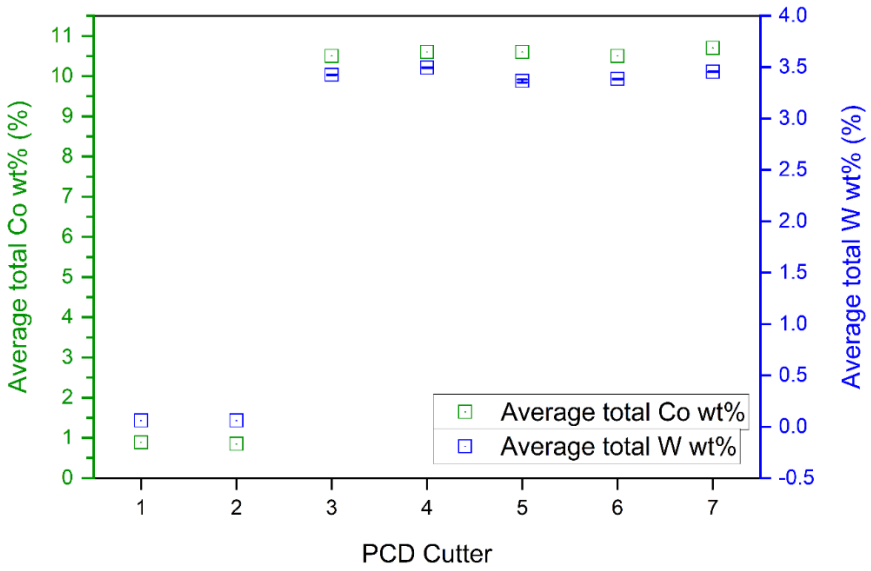


*Figure 5.13: the ICP-OES results of samples aborted at different stages of HPHT sintering after normal leaching which dissolves all un-trapped binder particles or pools in PCD materials*

Compositional analysis of different PCD samples was conducted via ICP-OES. Only the un-trapped binder in PCD materials was dissolved and analysed. ICP-OES results from all samples are presented in figure 5.13.

This graph is divided into two parts. In the first part (samples 1 and 2), there is just about 1 wt% of admixed Co powder and almost no W, indicating no infiltration of binder.

### 5.4.2.3 SEM Images of Samples 1 and 2

Figure 5.14 a) and b) are SE2 images of samples 1 & 2 during hot compaction. The bright phases surrounding the darker diamond grains are remnants of contaminants resulting from mechanical

polishing. Some voids are left after the extraction of diamond grains during mechanical polishing. Most of the diamond grains have little diamond-diamond connection compared to their neighbouring contaminants. These two features indicate both samples 1 and 2 are under-sintered. The average grain size of sample 1 is 8.1±0.4 µm.

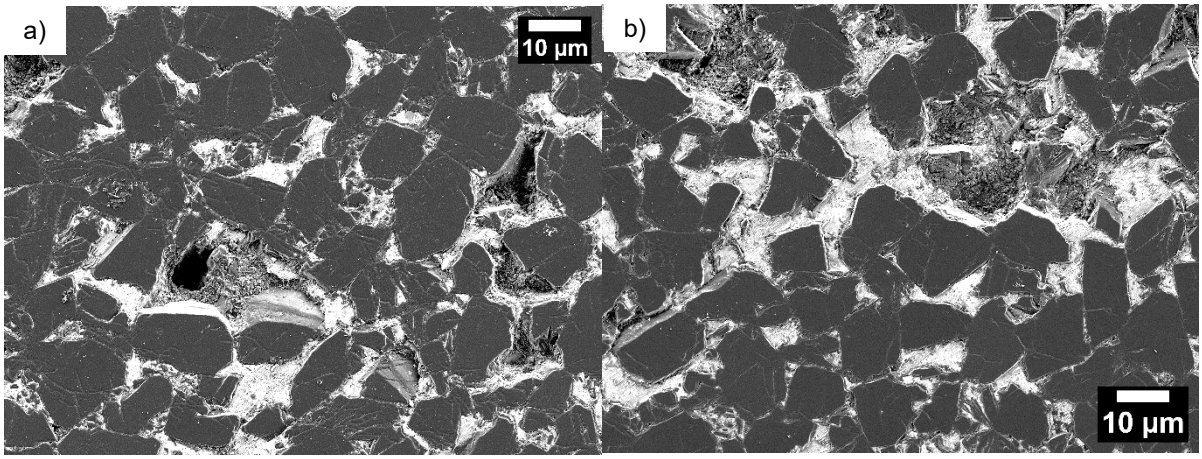


*Figure 5.14: SE2 images of a) sample 1 and b) sample 2*

#### 5.4.2.4 (S)TEM Results of Sample 1

In Figure 5.15, a triple point in sample 1 is located by a LAADF image. Diamond is in grey; binder is in white and the middle region surrounding the binder is suspected to be graphite with its darker contrast due to its inherently less dense atomic arrangement compared to diamond. The three boundaries, SI-1, SI-2 and SI-3 between different phases were characterized by EELS and EDX.

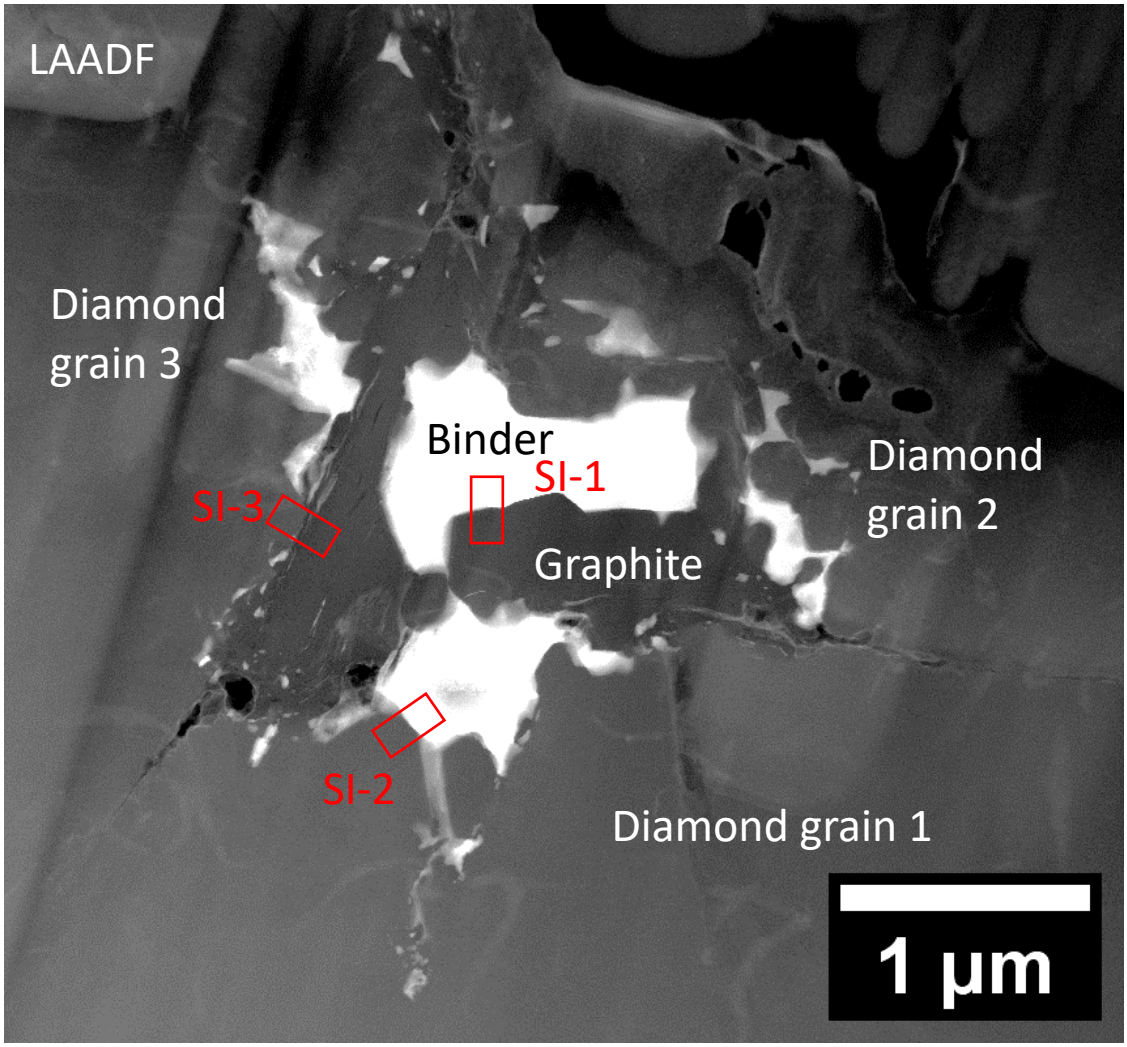


*Figure 5.15: LAADF image of a triple point within diamond grains from sample 1. All the black holes are artefacts arising during sample thinning. Diamond is grey; binder is white and graphite is dark grey in the centre region of the image surrounding the binder. Three diamond grains are labelled 1, 2 and 3. Three regions are outlined in red. SI-1 is a graphite-binder boundary. SI-2 is the diamond-binder boundary and SI-3 is a diamond-graphite boundary.*

The EDX map of SI-1 between binder and suspected graphite (figure 5.16 a)) provides a clear visualization of the different distributions of Co and C on the two sides of this phase boundary. The $L_2$ and $L_3$ edges of Co and the $\pi^*$ peak of graphite were identified from the corresponding EELS spectra of cobalt and carbon (figure 5.16 b) & c)).

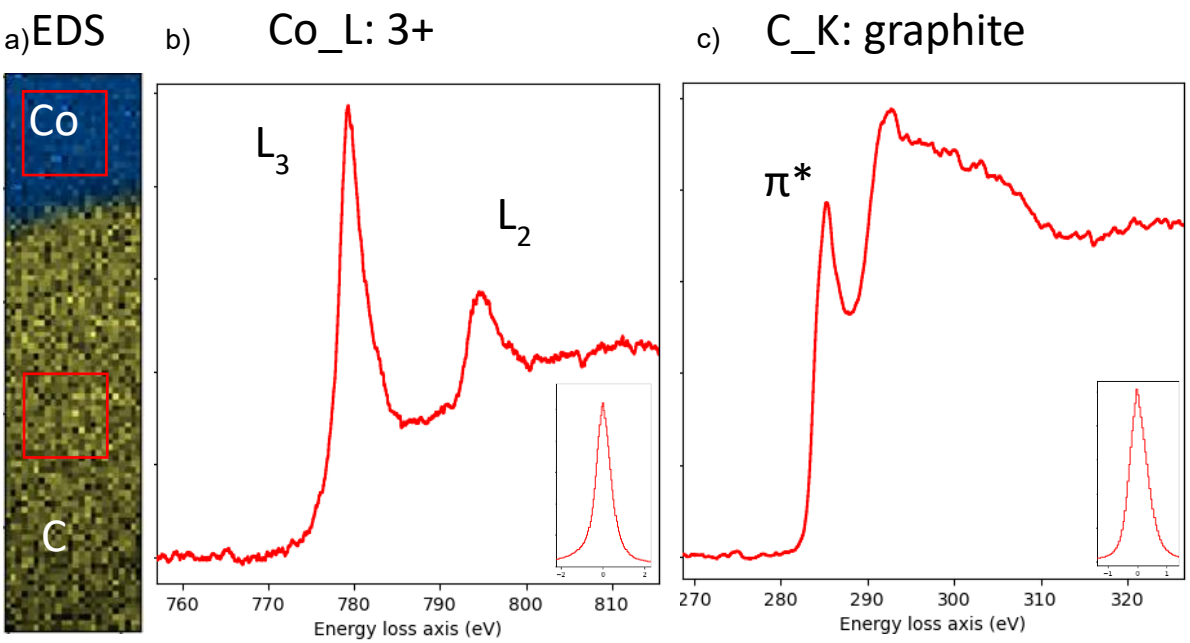


*Figure 5.16: a) The EDS map and b) & c) the EELS cobalt and carbon spectra of SI-1 outlined in* figure 5.17*. The EELS spectra of each element were integrated from the red boxes labelled in a) respectively. The L3 and L2 edges of Co are positioned at 779 eV and 794 eV, respectively. The π* peak of graphite is located at 285 eV. In the bottom right of the EELS spectra are the inserted zero-loss peaks showing good alignment. The width of the EDS map is 71nm.*

From the DF TEM images and diffraction patterns in figure 5.17 a) and b), the big binder pool in the middle of this triple point is identified as a single crystal FCC cobalt binder pool with some deformation twins. Its surrounding graphite comprises several distinct grains. Positioned adjacent to the left side of this binder pool, a part of the region in dark contrast in figure 5.15 is shown in the DF TEM image (figure 5.17 c)), with its diffraction pattern presented in figure 5.17 d). Based on the EELS result and diffraction pattern, this region in dark contrast is strongly indicative of **graphite.** There is no distinctive orientation relationship between the binder pool and its surrounding graphite.

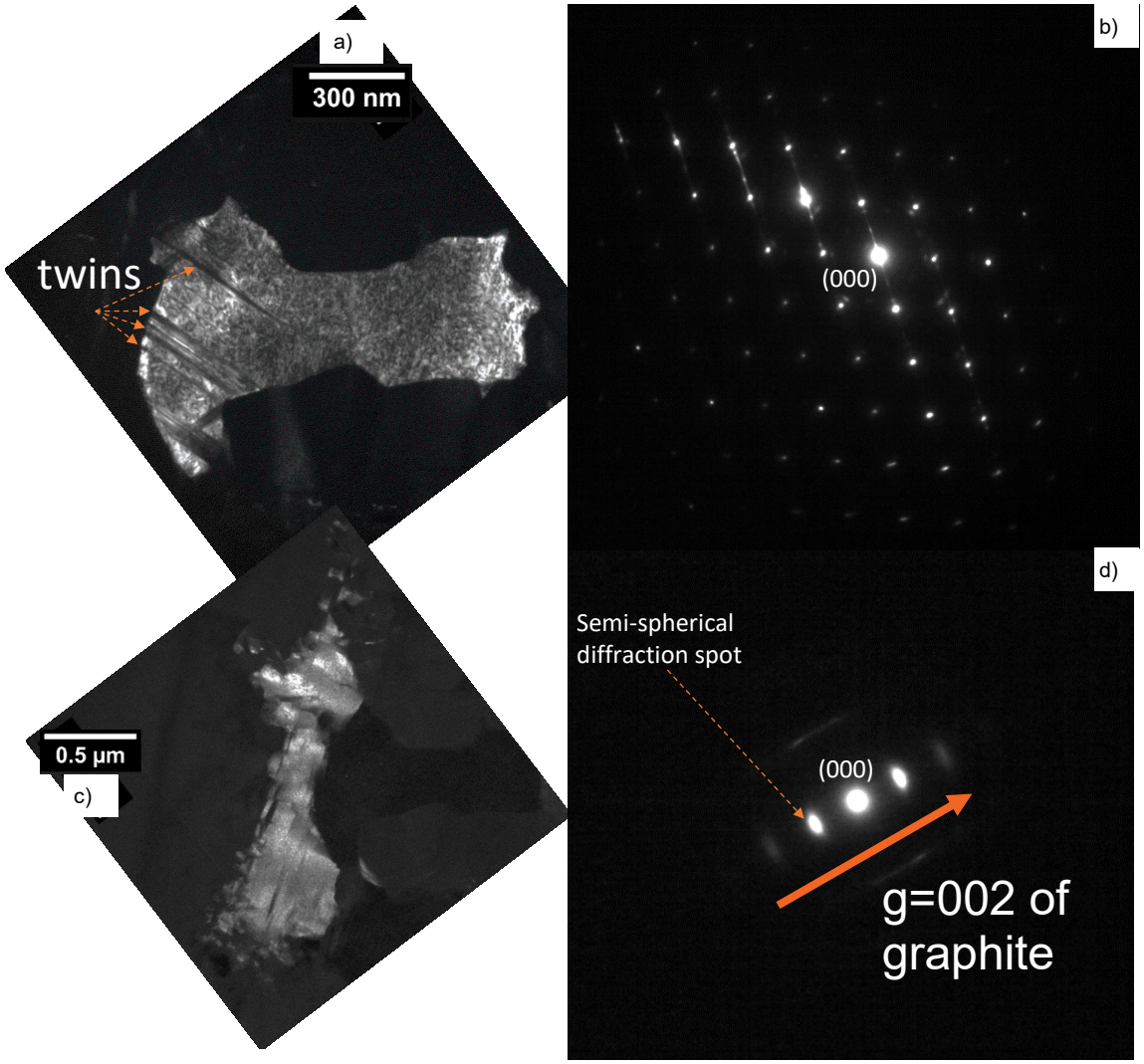


*Figure 5.17: a) A DF TEM image of binder pool in the middle in* figure 5.17 *and b) its diffraction pattern with a <110> zone axis of binder. The streaking points may originate from the twins (black strips labelled in a)). c) A DF TEM image of graphitic like carbon and d) its diffraction pattern.*

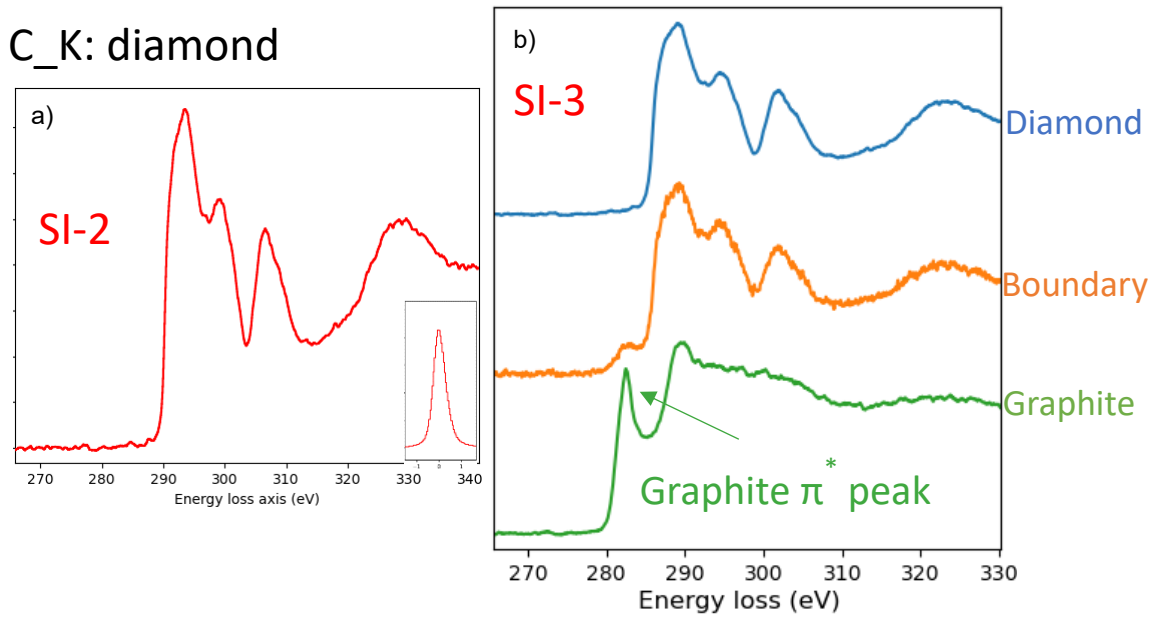

*Figure 5.18: a) & b) the EELS spectra at the diamond-binder interface in SI-2 and across SI-3. In the bottom right of the EELS spectrum of SI-2 is the inserted zero-loss peak showing good alignment.*

At the diamond-binder interface SI-2, in figure 5.18 a), no π* peak is detected by EELS when scanning from diamond to binder, indicating a direct contact between diamond and binder with no interposed graphite. In figure 5.18 b), the STEM probe scanning across the diamond-graphite SI-3 interface yields three EELS spectra, a typical diamond EELS spectrum (blue) with its characteristic three σ* peaks starting from 290 eV[11], a typical graphite EELS spectrum (green) with its strong distinct π* peak at 285 eV[12] and an EELS spectrum at the phase boundary containing all σ* and π* peaks suggesting the coexistence of $SP^3$ and $SP^2$ bonds. A HRs image would be required to further study the atomic arrangement at this boundary.

### 5.4.2.5 (S)TEM Results of Sample 2

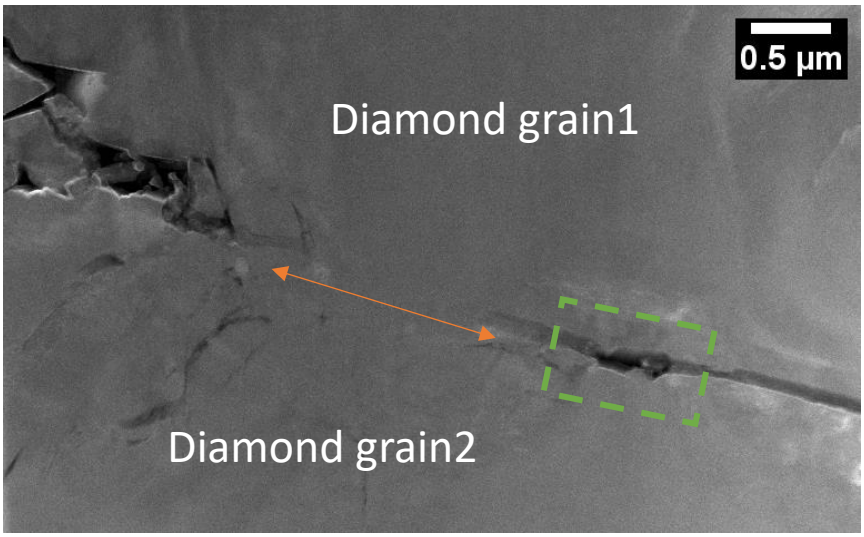


*Figure 5.19: the LAADF image of a diamond connection in sample 2. One side of the connection is marked with a green rectangle.*

In figure 5.19, a diamond-diamond connection is captured in sample 2. Within this connection, a hole between diamond grains to one side of the connection (outlined in a green box) is selected for EDX and EELS analysis.

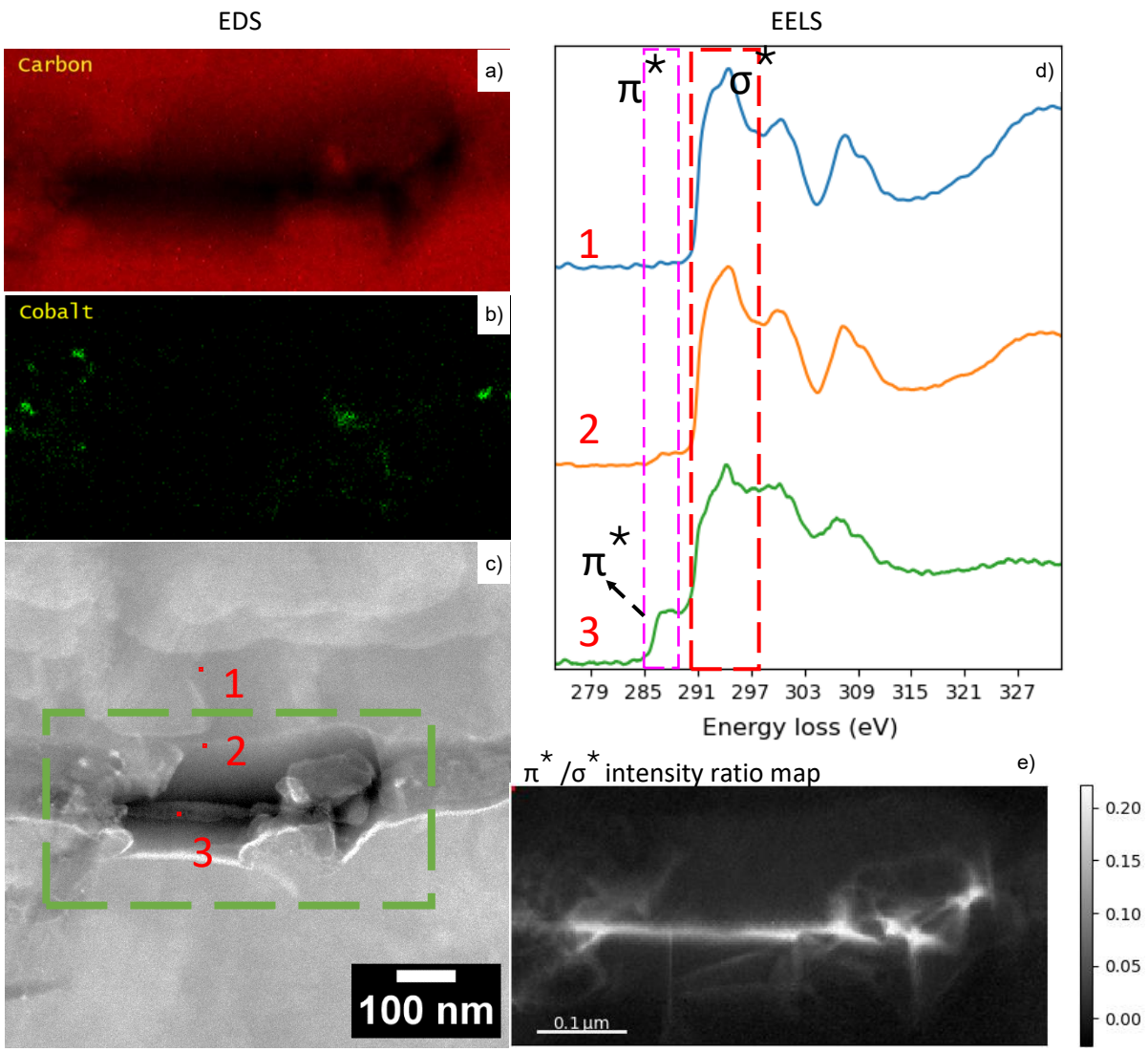


*Figure 5.20: a) and b) are the C and Co EDX maps corresponding to the region outlined in* figure 5.19. *c) A LAADF image of this region. d) Three EELS spectra corresponding to the 3 points in c). e) The π*/σ* intensity ratio map showing the relative intensity from graphite.*

From EDX maps in figure 5.20 a) and b) of this green box, there are only a few tiny and sparsely distributed Co pieces. The LAADF image (figure 5.20 c)) demonstrates a thin layer of graphite like carbon within this hole (marked by the point 3). Three points were selected for EELS analysis. In figure 5.20 d), the green EELS spectrum from point 3 demonstrates a strong π* peak, indicating this thin layer consists of graphite, though this spectrum retains a more diamond-like electronic structure, primarily due to the overlap between graphite and diamond. To plot the position of graphite like carbon, a π*/σ* intensity ratio map (figure 5.20 e)) is generated from the EELS data, calculated by taking the ratio of the integral of π* (the pink box) and σ* peaks (the red box). From

this π*/σ* ratio map, this graphite like carbon is relatively thin and uniform, which is different from the graphite observed around the binder particles/pools.

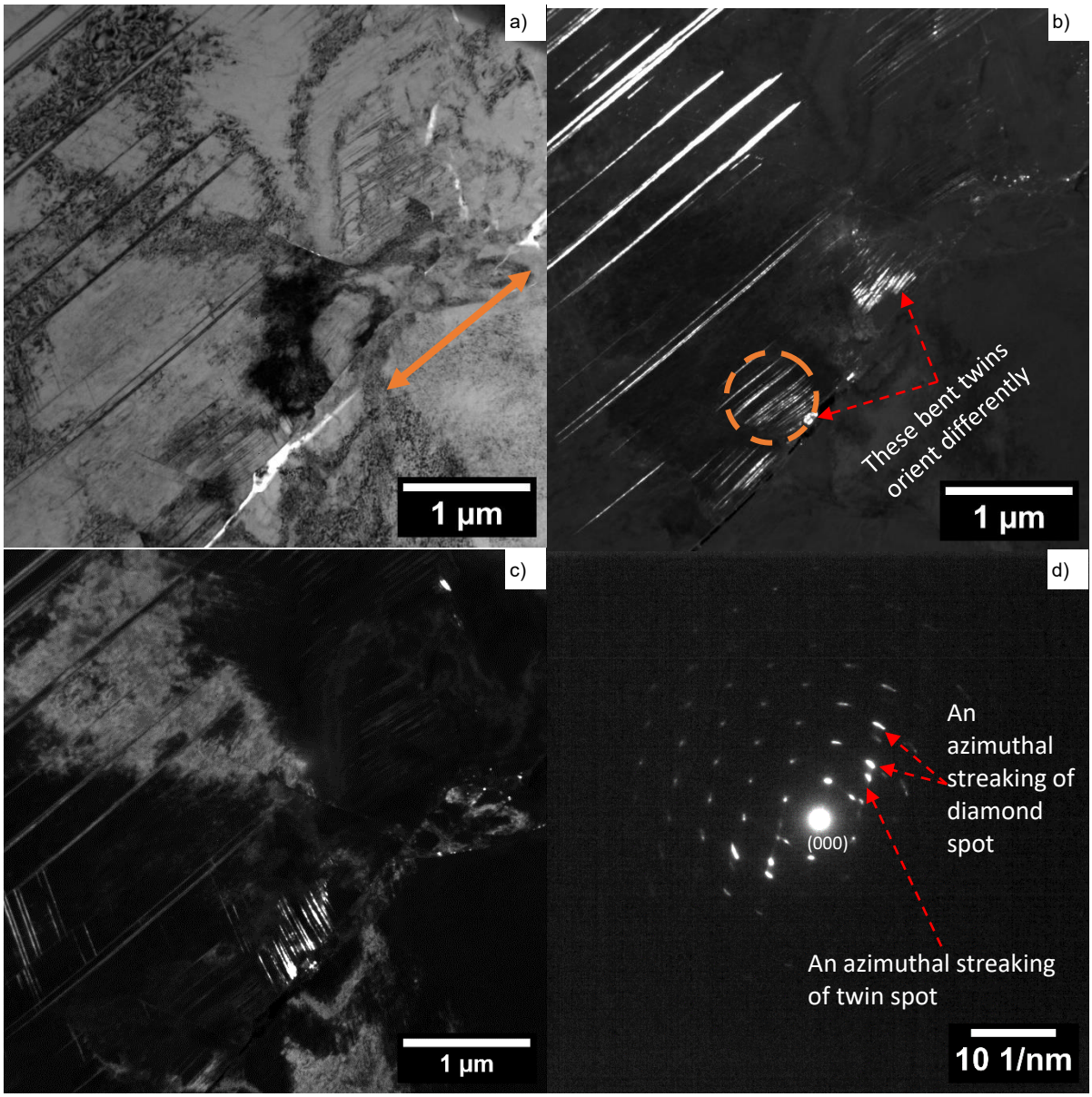


Figure 5.*21: TEM images of the diamond-diamond connection (labelled in orange) in* figure 5.*19. a) A BF TEM image. ). b) A DF image showing one set of twins. c) A DF image showing the other set of twins. d) Azimuthal streaking diffraction pattern from the orange circle in b.) All TEM images are vertical to <110> of top diamond grain.*

Figure 5.21 a) shows the same binder-free diamond-diamond connection shown in figure 5.19. Two DF TEM images reveal the location of bent 70.5° <110> twins near this diamond-diamond connection. At the top left corner of figure 5.21 b), the 70.5° <110> twins are straight. As the diamond-diamond connection is approached, the 70.5° <110> twins gradually bend, evident in both figure 5.21 b) and c). Notably, the orientations of bent twins are not parallel to that of the straight twins though they share the same {111} twin plane.

Moreover, the bent twins are not oriented toward a consistent direction. For the twins marked by red lines, some are oriented in one direction, while others are oriented in another direction 5° - 15° away from the first direction. Figure 5.21 d) is a diffraction pattern taken from a region containing bent twins (outline in orange circle in figure 5.21 b)). The azimuthal streaking of diamond and twin spots are labelled in this diffraction pattern. The third set of 70.5° <110> twins is not imaged due to limitations in TEM sample tilting. From EDX and EELS results (not shown), no graphite nor binder was observed at the diamond-diamond connection.

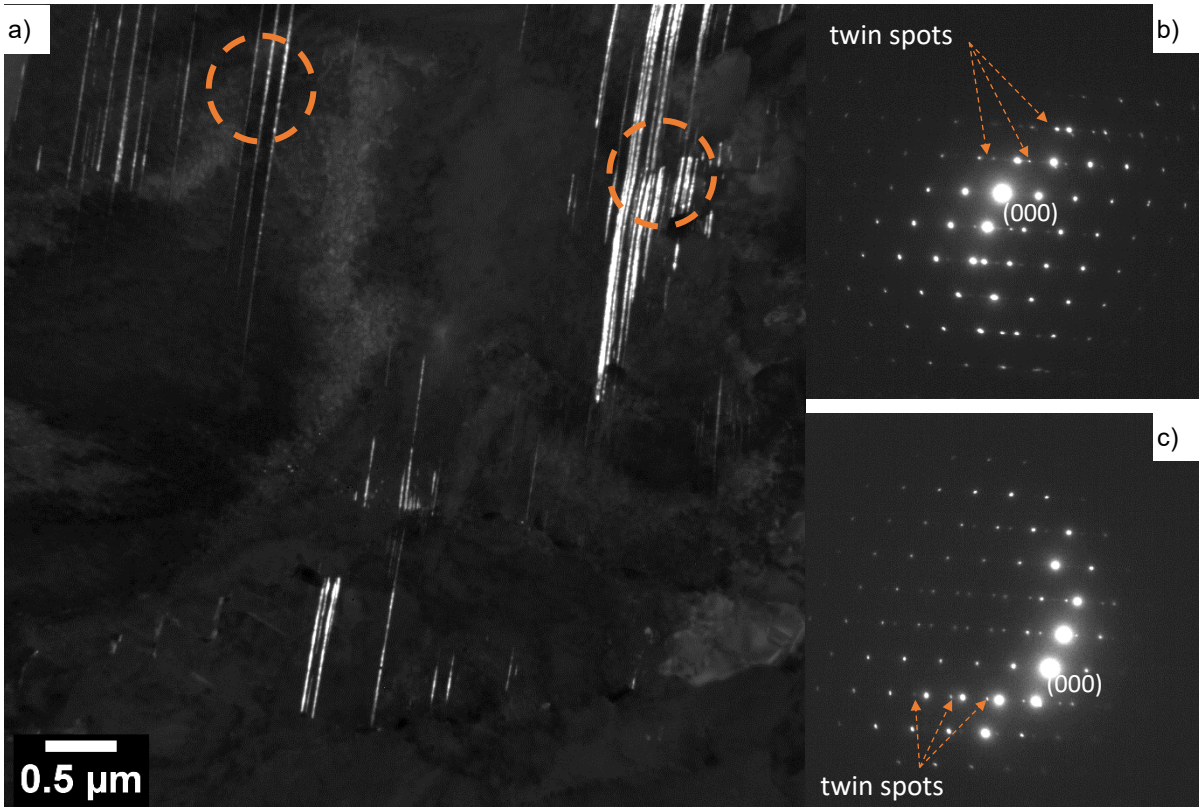


Figure 5.22: *a) A DF TEM image of straight 70.5° <110> twins from the old diamond of another fully sintered SPCD. b) The diffraction pattern from the left circle in a). c) The diffraction pattern from the right circle in a).*

With reference to bent twins, a collection of straight 70.5° <110> twins from a large and heavily plastically deformed old diamond grain (TEM images showing a high dislocations density in old diamond grain not shown) from a fully sintered SPCD material is shown in figure 5.22 a). The same set of twins through the entire grain are all consistently oriented in the downward direction. Massive isolated and entangled dislocations were observed around and overlapping with these twins (DF TEM image not shown here). The sizes of the selective area apertures to obtain diffraction patterns of straight (figure 5.22) and bent (figure 5.21) twins were the same. Contrary to the azimuthal

streaking in the diffraction pattern from bent 70.5° <110> twins, in figure 5.22 b) and c), no azimuthal streaking of diffraction spots from these straight 70.5° <110> twins is present from the different selected regions. In summary, no bent twins are found in these heavily plastically deformed old diamond grains.

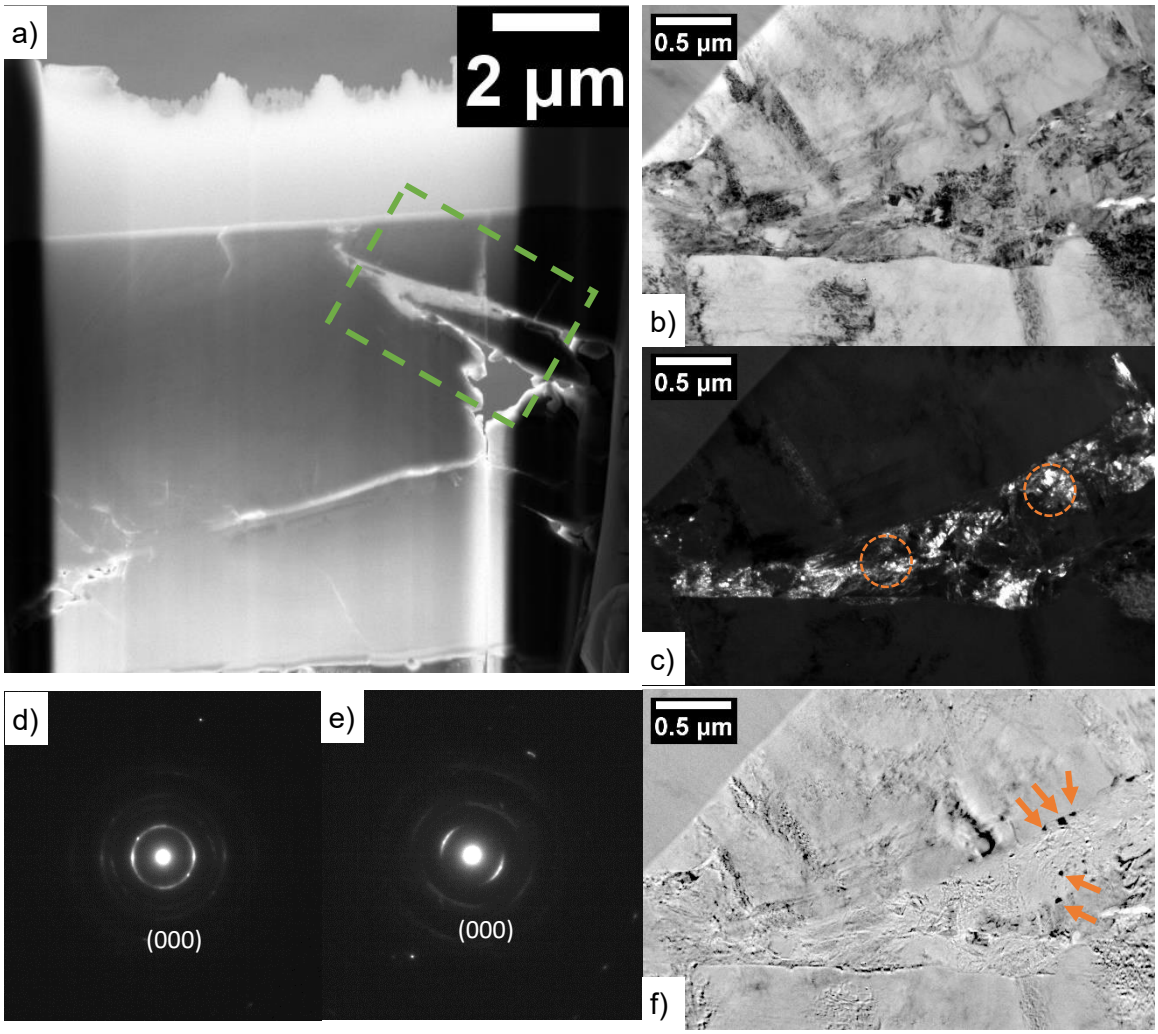


*Figure 5.23: a) SE2 image of a TEM sample from sample 2. b) & c) BF and DF TEM images of this graphite region. d) & e) Diffraction patterns of polycrystal graphite from the left and right orange circles of same aperture size in c). f) A Z contrast TEM image of this graphite region with binder particles labelled by orange arrows.*

SE2 image in figure 5.23 a) highlights a thin region in sample 2 outlined within green dashed lines. The corresponding DF and BF TEM images of this region, inserted in figure 5.23 b) and c), show no discernible gaps between this region and the diamond grains. The electron diffraction patterns in figure 5.23 d) and e) from the left and right orange circled regions show the crystal structure of graphite. This thin graphite region consists of many disordered polycrystalline graphite grains. Only a

few isolated binder particles marked by orange arrows are along the diamond-graphite phase boundary in figure 5.23 f).

#### 5.4.2.6 3D Tomography of Sample 2

To estimate the spatial distribution of isolated binder particles/pools in 3D, the relative position of the reshaped or fragmented binder particles was precisely determined by FIB-SEM 3D tomography. Considering the sintering temperature of sample 2 is 30 °C above the Co-C eutectic point, a larger volume from sample 2 was selected, sectioned and imaged. From this volume, a rectangular sub-volume away from the border containing all nearby isolated binder particles was extracted and visualized in 3D (figure 5.24). Each isolated particle has been colourized differently. The biggest binder particle here is the brown particle at the left bottom corner in each image of figure 5.24. Its dendrite-like configuration signifies the penetration of melt binder particles into interstitial gaps between diamond powders during hot compaction. All other binder particles are relatively small. From the XY cross-section in figure 5.25, all binder particles are nearly enclosed by the phase possessing the same contrast as diamond. An example of the surrounding phase of the biggest binder is outlined in orange. This is analogous to the microstructure in figure 5.15, where the binder is surrounded by graphite, indicating this phase is likely graphite.

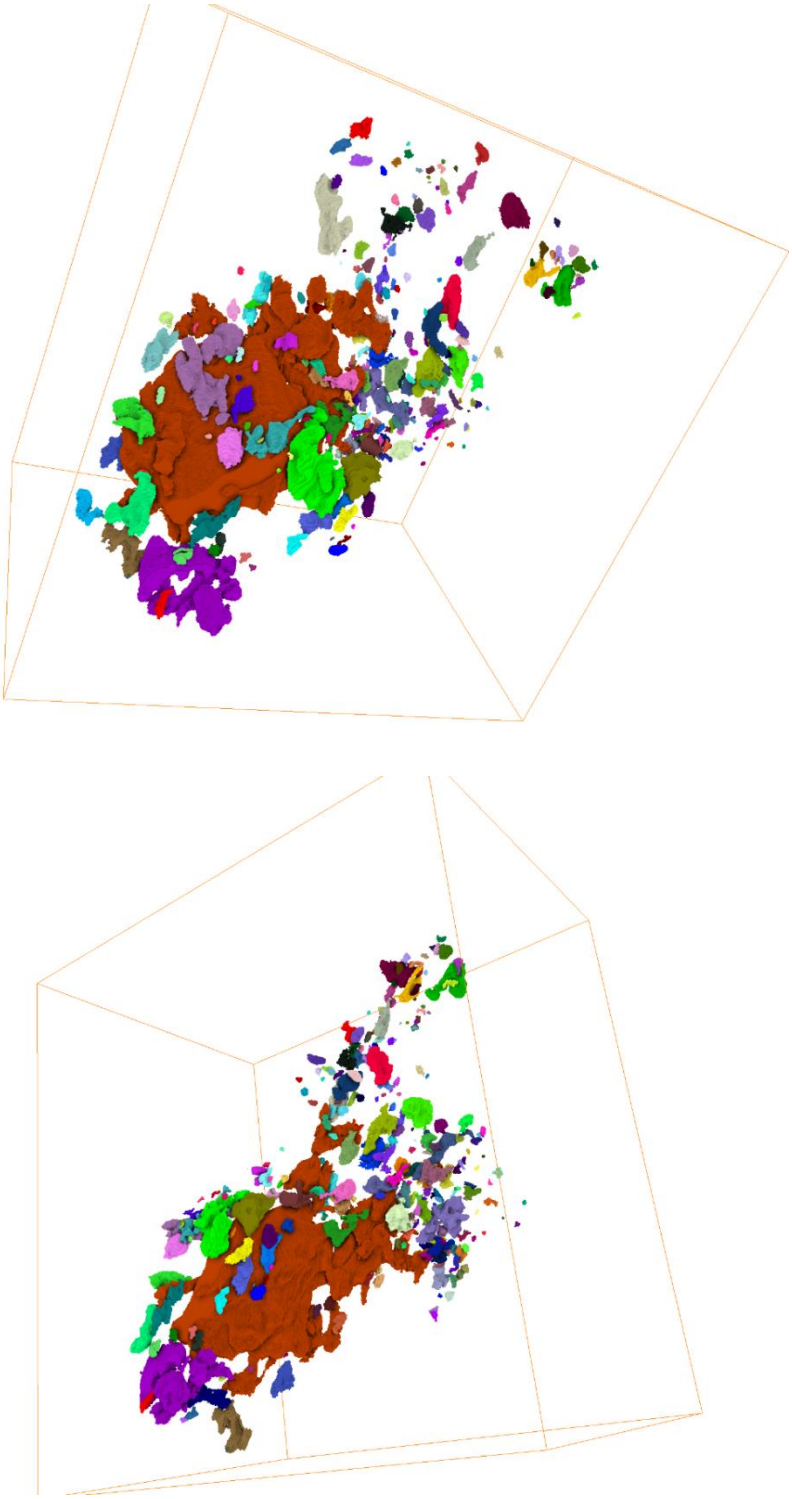

*Figure 5.24: 3D tomography of fragmented binder particles from sample 2. Top and bottom images are viewed from different angles. The length is 7.75 µm, height is 8.69 and thickness is 5.62 µm.*

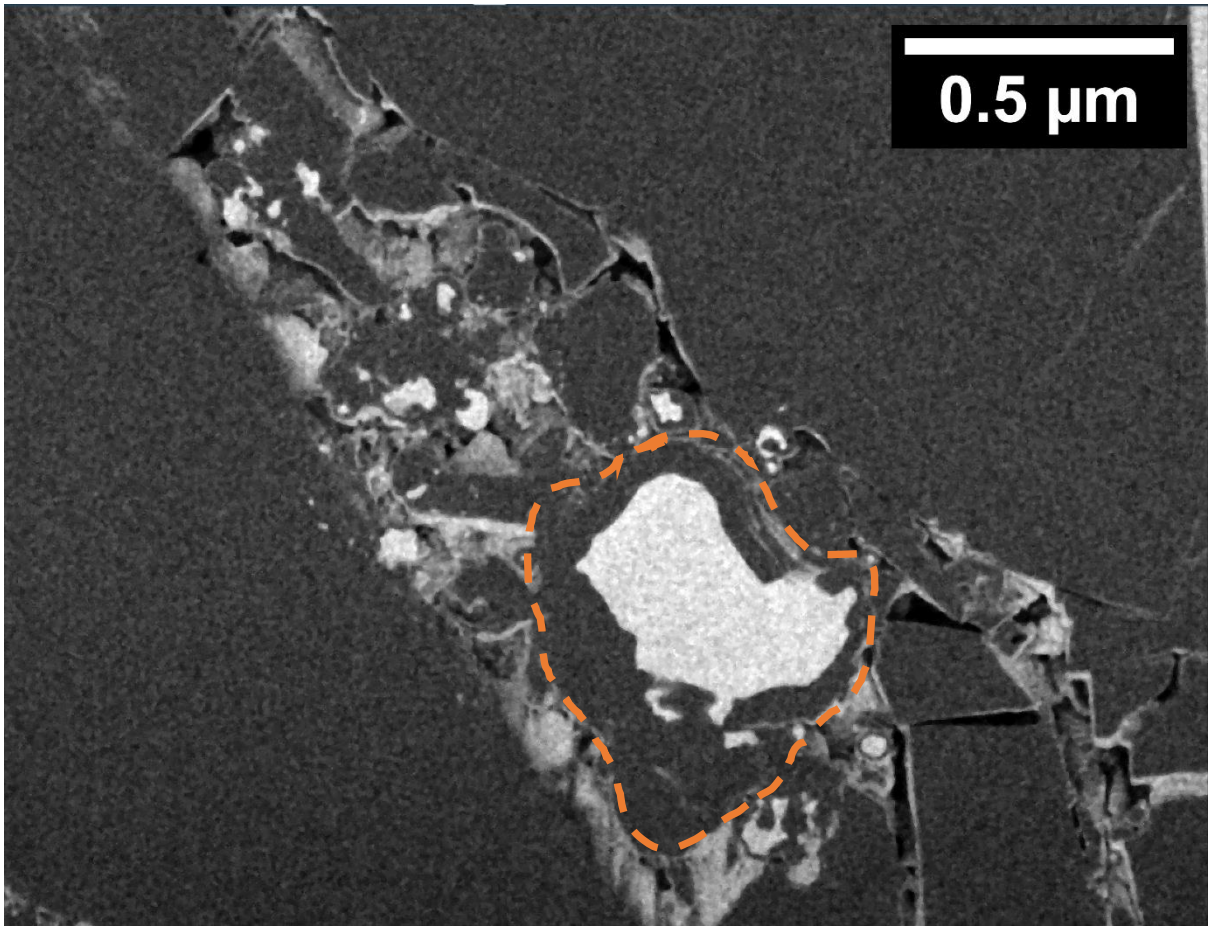


*Figure 5.25: An EsB image of an XY cross section of the 3D volume in* figure 5.21.

### 5.4.2.7 Discussion of Samples 1 and 2

XRD patterns reveal the appearance of graphite in sample 1. While the absolute amount of graphite is relatively low compared to diamond, it only occupies interstitial voids between powders. Graphite-diamond dissolution and reprecipitation regrowth therefore occurs only at these voids. It is the amount of graphite in these voids that determines the extent of diamond regrowth via graphite-diamond dissolution and reprecipitation.

This occupancy can be expressed as $\frac{V_{graphite}}{V_{void}+V_{graphite}}$ upon infiltration. $V_{graphite}$ can be estimated via Rietveld refinement performed on Sample 1. $V_{void}+V_{graphite}$ can be approximated to the sum of $V_{WC}$ , $V_{Co\text{-}infiltrated}$ (both determined from ICP-OES) and $V_{regrown\ diamond\ from\ graphite}$ at the beginning of dwell, by assuming the sum of graphite and void volumes roughly equivalent to those of infiltrated binder and regrown diamond. The $\frac{V_{graphite}}{V_{void}+V_{graphite}}$ ratio is approximately 32 vol%, indicating that the graphite-

diamond dissolution and reprecipitation regrowth would occur in more than one-third of the total void space. When the graphite is converted to regrown diamond, it accounts for about 21% of the space occupied by it and the binder. The graphite observed in both samples 1 and 2 identified by (S)TEM supports this claim. As reviewed in section 2.2.3.2, there are two graphitization mechanisms: binderless graphitization and the binder-assisted graphitization.

#### 5.4.2.7.1 Binder-Assisted Graphitization

The available evidence strongly suggests that the identified graphite in sample 1 is a product of binder-assisted graphitization. XRD and ICP-OES results indicate the binder infiltration had not yet occurred within samples 1 and 2. All binder in these two samples come from the initially admixed Co particles. Though some Co particles fragmented during outgassing, most of them remained in fragments and did not penetrate between the diamond grains. However, the distinctive morphology of irregularly shaped, dendrite-like and meniscus-like binder particles/pools from LAADF images and 3D tomography, all strongly imply they were in the liquid state which suggests that the temperature had reached the eutectic temperature of the C/Co system. The liquid binder wetted diamond surfaces, catalysed the diamond to graphite transformation and finally was separated by the newly formed graphite, such as the largest binder pool in figure 5.17.

Similar semi-spherical graphitic like carbon diffraction spots to those in figure 5.17 d), were obtained from FFTs of HRs images by Tulic *et al.*[13]. They observed a gradually increased semi-spherical compressive strain mainly along the graphite [002] direction. They ascribed this compression in graphite to both the volume expansion from diamond to graphite and the constraint from nearby diamond particles. However, these semi-spherical graphite diffraction spots could be due to the graphite distortion during carbon atoms reprecipitation. In conclusion, the graphite from binder-assisted graphitization is highly disordered.

#### 5.4.2.7.2 Binderless Graphitization

Both the absence of large binder particles and the thin and uniform shape of the graphite like carbon layer in figure 5.20 c) and e) strongly suggest that this carbon layer is from the direct transformation of the diamond surface. This is plausible as the PT conditions (non-contact region with no pressure and temperature more than 1320 °C) favour the formation of graphite from diamond[14]. However, graphite does not fill the holes between the two diamond grains in the LAADF image (figure 5.20 c)) and other gaps were observed in SEM images (figure 5.14). As reviewed in section 2.2.3.2, the kinetics of binderless graphitization depends on the size of diamond particles, facets of diamond and temperature. Here, the lack of large scale of binderless graphitization is attributed to a low kinetics.

However, a large region of graphite is found in figure 5.21. It could stem from both graphitization mechanisms. Firstly, it might stem from binder-assisted graphitization, with most of the binder being expelled by the newly formed graphite away from the original diamond-binder contact, leaving a few enclosed binder particles along the boundary.

Alternatively, this large region of graphite could result from binderless graphitization from some specific facets like {111} which graphitize more rapid[4,15]. Because of the high surface-to-volume ratio, finer diamond powders are more prone to graphitization[16]. Fine diamond powders between coarse diamond powders after cold compaction would lead to polycrystal graphite filling the gaps between coarse diamond powders. Unfortunately, no evidence shows which graphitization mechanism dominates.

However, regardless of the specific graphitization mechanism, the salient point is the formation of a large piece of graphite filling the gaps, which will significantly affect the subsequent diamond regrowth.

### 5.4.3 Sample 3

Sample 3 was terminated at the start of dwell when both temperature and pressure reach maximum.

#### 5.4.3.1 XRD Result of Sample 3

In figure 5.4, the most obvious change in all XRD patterns is the emergence of new XRD peaks starting with sample 3. These new XRD peaks correspond to new phases introduced, including WC from the substrate, NbC through binder-catalysed interactions between the Nb canister and diamond, and η phase $Co_3W_3C$, as a product of the interaction between Co, C and W.

Another change in XRD pattern of sample 3 is related to Co. The intensities of the (200) and (220) Co XRD peaks at 50.7° and 74.8° suddenly increase at sample 3 due to binder infiltration and keep constant in the rest of the samples, suggesting the completion of binder infiltration ahead of the start of the dwell (sample 3). The (002) Co peak also shifts from 51.5° in sample 1 to 50.7° in sample 3, indicating an expansion of the Co lattice.

However, the graphite XRD peak completely vanishes in sample 3 and never reappears thereafter.

#### 5.4.3.2 ICP-OES Result of Sample 3

In figure 5.13, between samples 2 and 3, the cobalt content rises significantly to around 10.5 wt%, accompanied by the tungsten content reaching around 3.5 wt%, again indicating the occurrence of binder infiltration.

#### 5.4.3.3 SEM Images of Sample 3

The newly formed NbC layer in sample 3, initially revealed by XRD, is imaged in figure 5.26 a) and b). The NbC layers in samples 3-7 are similar to one another (SEM images not shown). This NbC layer separates the PCD and the Nb canister. The microstructure of sample 3 is shown in figure 5.26 c). It

has already appeared dense. No holes or voids were observed when preparing the TEM sample from sample 3. The average grain size of sample 3 is 6.4±0.4 µm.

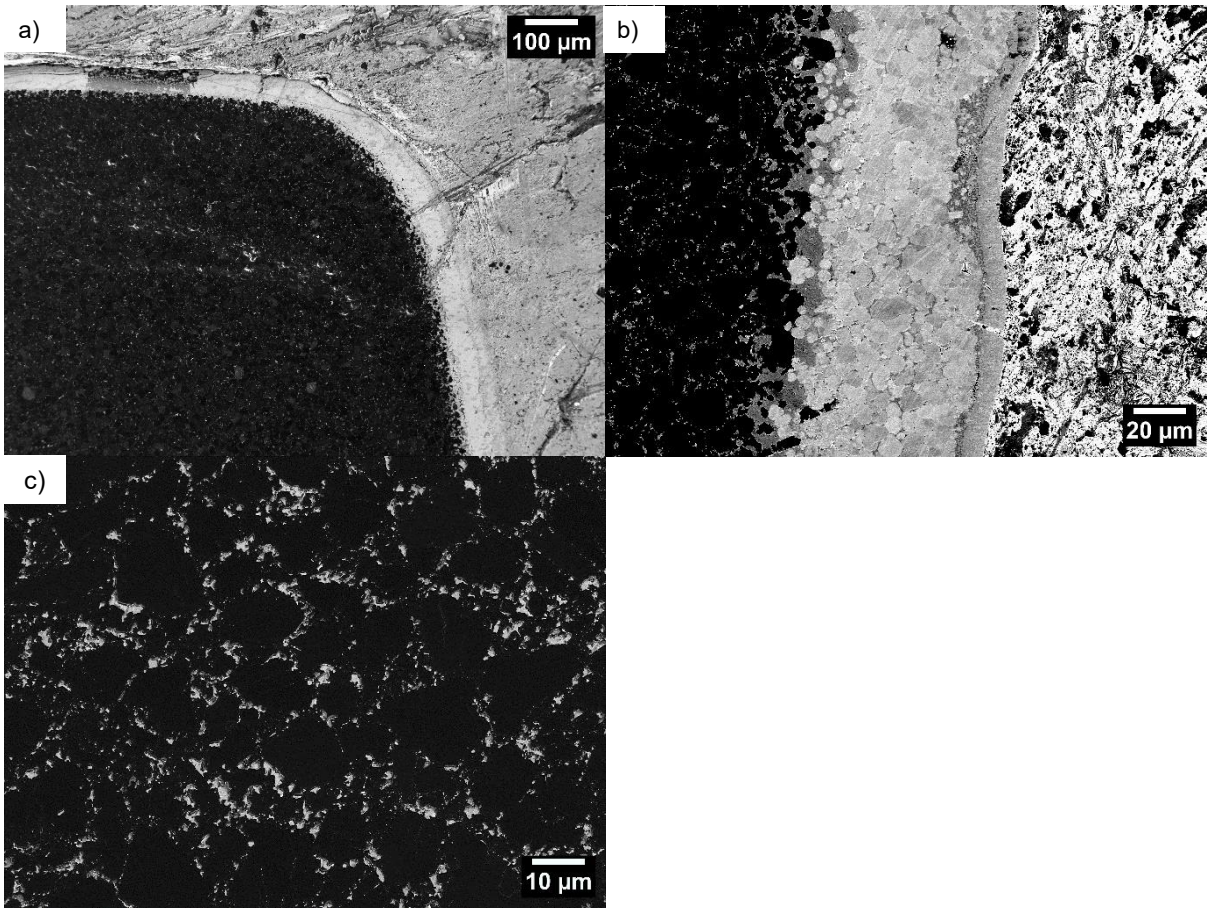


*Figure 5.26:a) SE2 image of the uniform NbC shell surrounding the black PCD skeleton in sample 3. b) The angle selective backscatter image of a magnified NbC shell. Diamond is black, Co is dark grey, NbC is light grey and Nb is white. c) An SE2 image of sample 3.*

### 5.4.3.4 EDX of NbC Layer

Figure 5.27 a) is a part of the NbC layer in figure 5.26 a). Figure 5.27 b)-d) are the corresponding EDX carbon, cobalt and niobium maps of this NbC layer, while figure 5.27 e) & f) are the EDX spectra of the NbC layer and the adjacent Nb canister on the right side, showing the elemental distributions of carbon, cobalt and tungsten.

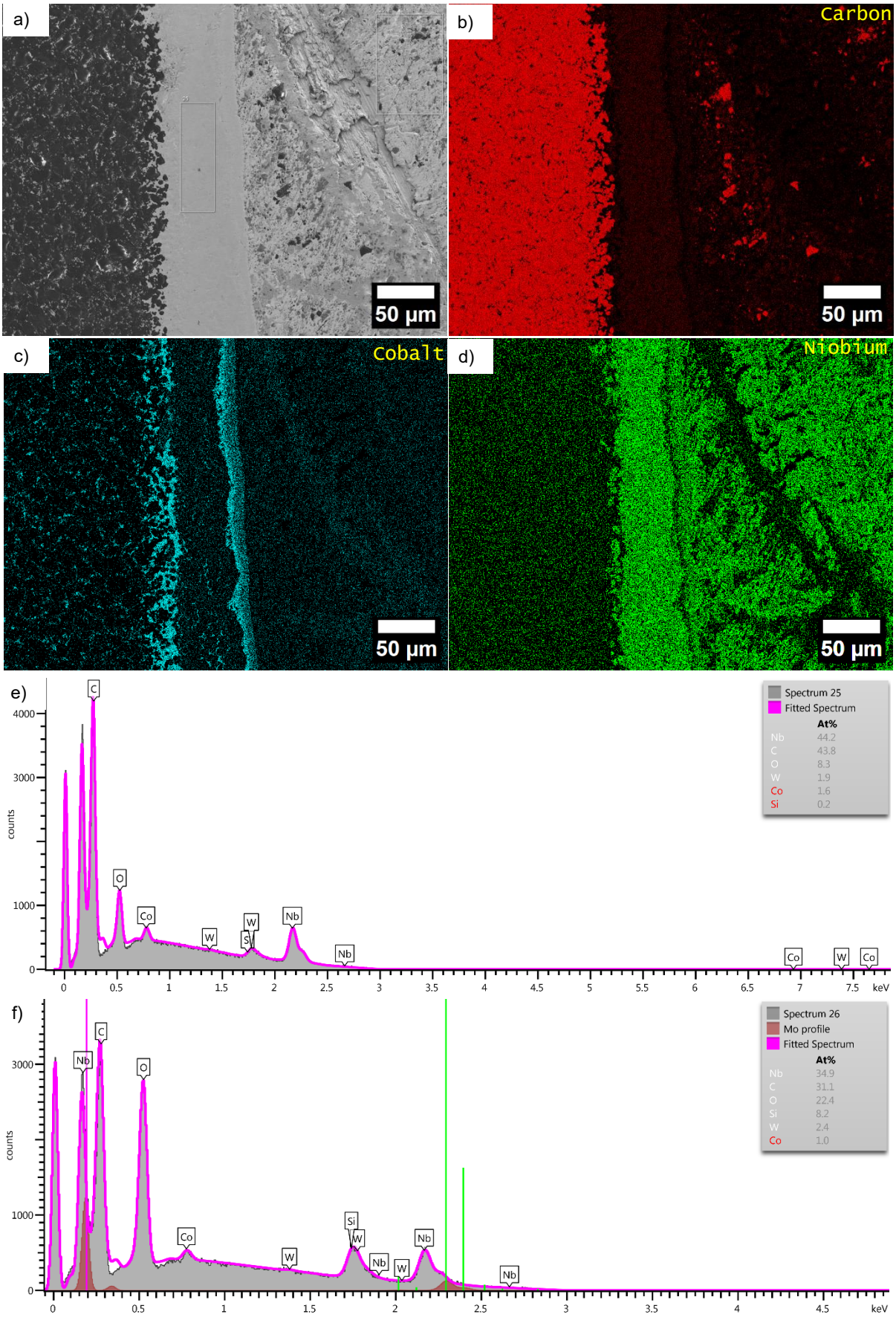
a)
50 µm
b)
Carbon
50 µm
c)
Cobalt
50 µm
d)
Niobium
50 µm
e)
counts
keV
Spectrum 25
Fitted Spectrum
At%
Nb 44.2
C 43.8
O 8.3
W 1.9
Co 1.6
Si 0.2
f)
counts
keV
Spectrum 26
Mo profile
Fitted Spectrum
At%
Nb 34.9
C 31.1
O 22.4
Si 8.2
W 2.4
Co 1.0

*Figure 5.27: a) SE2 image of a diamond-NbC-Nb region from* figure 5*.26. b), c), & d), The carbon, cobalt, and niobium EDX map respectively. e) The EDX spectrum from the middle NbC layer marked in the middle in a). f) The EDX spectrum from the Nb region marked in a).*

#### 5.4.3.5 (S)TEM Results of Sample 3

To study the diamond regrowth, a GB formed after binder infiltration in sample 3 is focused on. Figure 5.28 a) is a BF TEM image under a g=004 two-beam condition, with its corresponding DF image in figure 5.28 b). Both BF and DF TEM images illustrate the distribution of dislocations, with their density gradually decreasing from the core of the grain towards its periphery. The vicinity of the GB is almost dislocation-free. Along the periphery of this dislocation-free zone, a line of enclosed binder particles is outlined by a green dashed line shown in figure 5.28 c). All enclosed binder particles share one identical orientation which is the same as that of their diamond host. An example diffraction pattern (figure 5.28 e)) of a region containing both binder and diamond circled in figure 5.28 c) shows a full overlap of diamond and binder diffraction spots. Some straight 70.5° <110> deformation twins crossing from the core of grain to the GB are displayed in 5.26 d). The corresponding diffraction pattern is displayed in figure 5.28 f) with some twin spots highlighted.

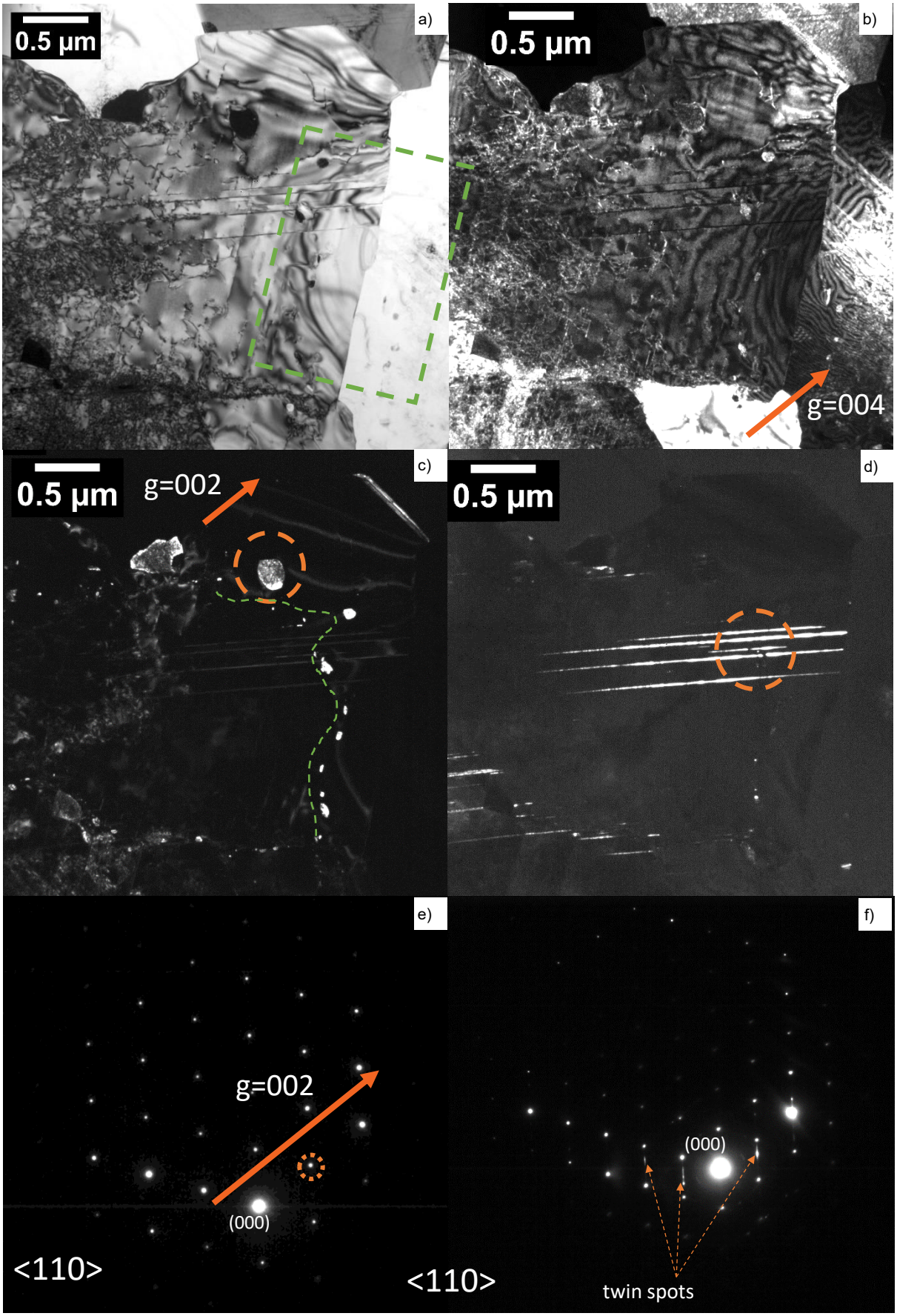


Figure 5.*28: TEM images of sample 3 after binder infiltration. a) A BF TEM image. A region containing GB is outlined. b) The corresponding DF image. c) A DF TEM image of enclosed binder particles within this grain.* The 002 binder diffraction spot *is*

*circled in e). An area of binder and diamond is circled. d) A DF image of 70.5° <110> deformation twins in this grain. An area of twins is circled. e) A diffraction pattern of the area circled in c). f) A diffraction pattern of twins circled in d).*

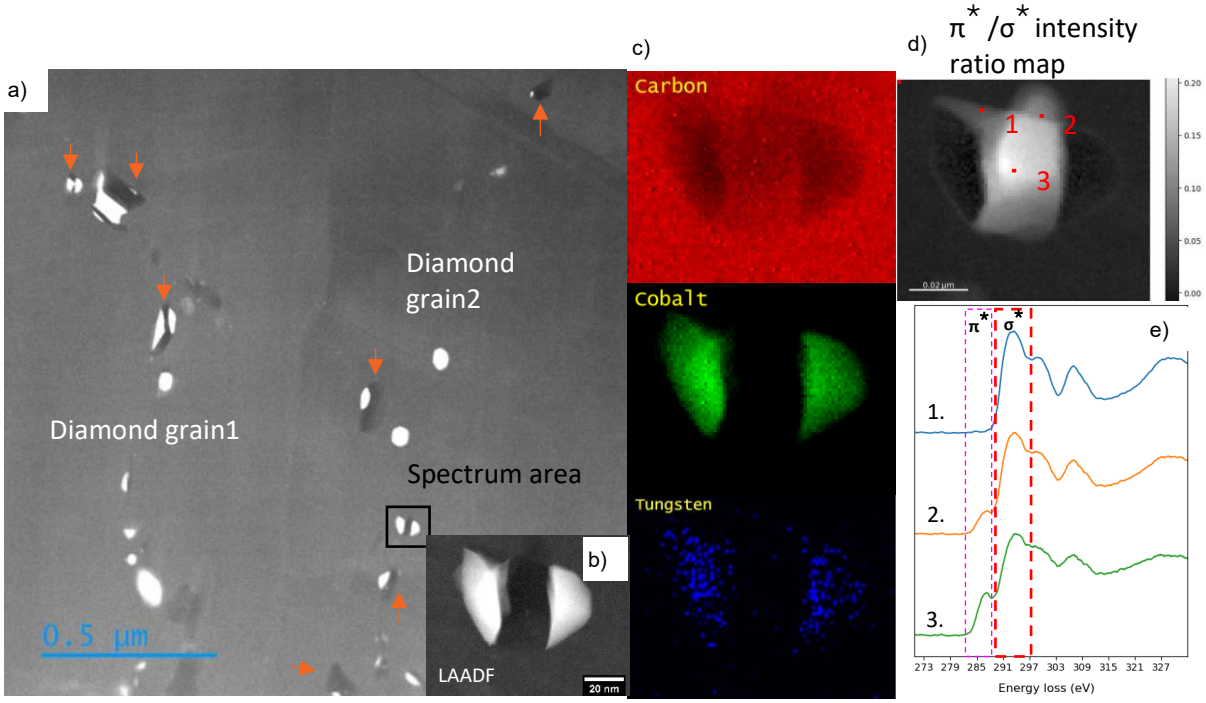


Figure 5.*29: a) the LAADF image of the targeted GB marked in* figure 5.*26 a). b) an enlarged LAADF image of a spectrum area and c) its corresponding carbon, cobalt and tungsten EDS maps. The length of these EDX maps is 87 nm. d) A π*/σ* intensity ratio map showing the relative intensity from graphite in the spectrum area. e) three representative EELS spectra correspond to 3 points labelled in d).*

The region of interest marked by the green box in figure 5.28 a) is examined. It contains a GB and a line of enclosed binder particles in each grain either side of the GB. Figure 5.29 a) is the LAADF image of this region of interest. It is confirmed that neither graphite nor binder is detected within this clean GB. However, graphite, distinctively shown in dark contrast, is found in contact with the enclosed binder particles on both sides of the GB, arrowed in the figure. A typical binder-graphite-binder microstructural feature is selected as a spectrum area, shown in the enlarged LAADF image (Figure 5.29 b)). Figure 5.29 c) shows the corresponding EDX element maps of carbon, cobalt and tungsten of this spectrum area, indicating a homogeneous distribution of both major cobalt and minor tungsten elements within the two binder particles. The π*/σ* intensity ratio map derived from the EELS data is plotted in figure 5.29 d). Figure 5.29 e) are three representative EELS spectra from the diamond, graphite edge and graphite centre. A discernible trend is noticed from spectrum 1 to spectrum 3, wherein the graphite π* peak progressively intensifies, but the diamond σ* peak

gradually weakens, showing the gradual change of diamond to graphite when moving towards the centre between these two binder particles.

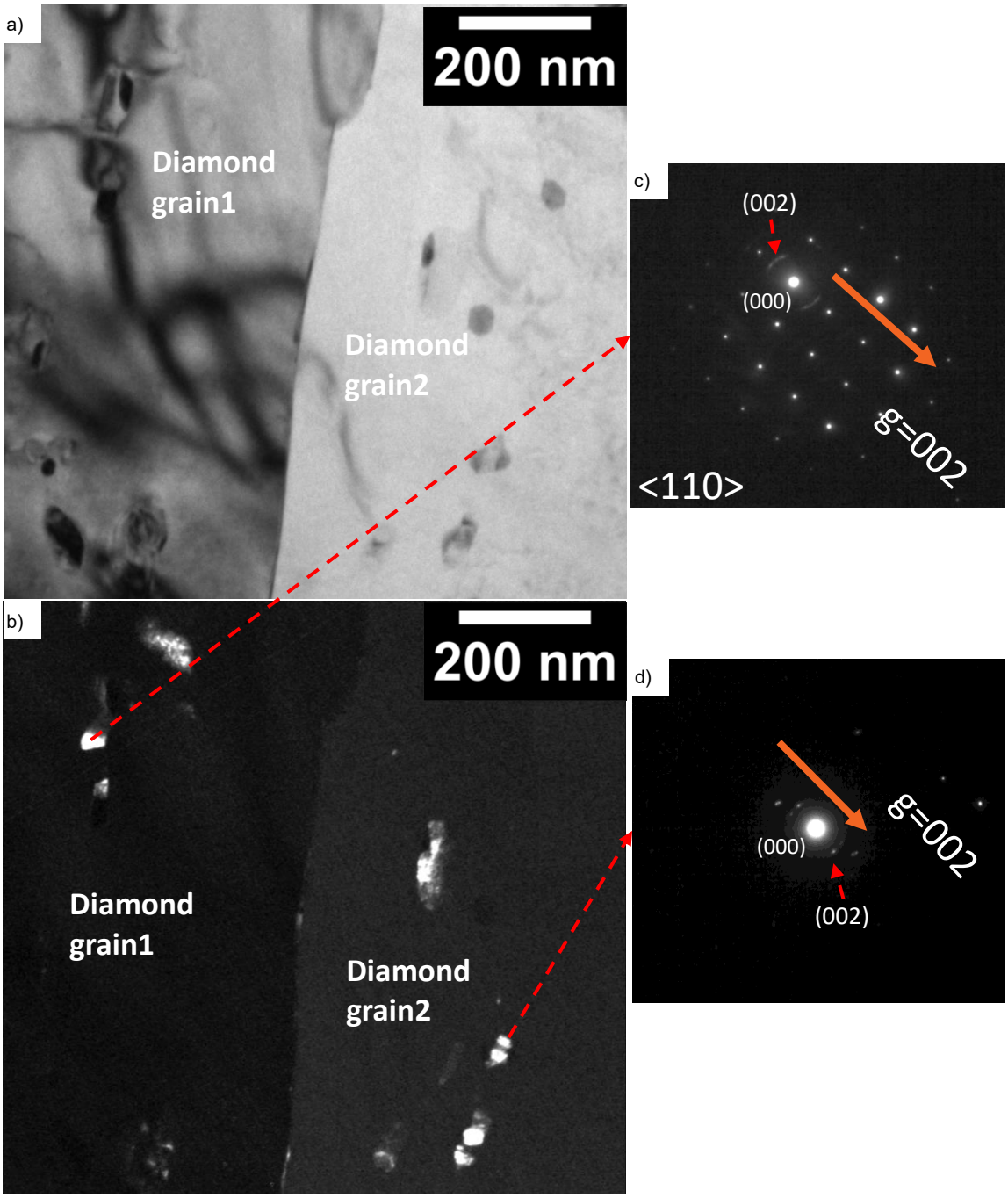


Figure 5.*30: a) A BF image of the magnified GB in* figure 5.*27. b) Its corresponding DF image from 002 graphite diffraction spot showing the residual graphite. c) The diffraction pattern of diamond and graphite from grain 1. d) The diffraction pattern of the spectrum area. The weak diffraction spots from graphite are indicated by red arrows. Both TEM images are vertical to<110> of diamond grain 1.*

In figure 5.30 a) and b), BF and DF TEM images were taken to examine the orientation relationships between diamond grains, enclosed binder particles and residual graphite in this region of interest. All the enclosed binder particles have the same orientation identical to their diamond host

(corresponding DF TEM images not shown). From figure 5.30 c) and d), the diffraction patterns of graphite in grain 1 and 2, the distorted (002) spots from graphite appear close to the (000) spot due to the large d spacing in (002) plane of graphite. However, from these two diffraction patterns, irrespective of the diamond grain, the orientation of the graphite differs from that of its diamond host. Moreover, the most interesting finding is the consistent orientation of all residual graphite as shown in figure 5.28 b). Specifically, the residual graphite particles on both sides of this GB share one identical orientation, which is independent of the host diamond grains and enclosed binder particles.

#### 5.4.3.6 Discussion of Sample 3

##### 5.4.3.6.1 Liquid Binder Infiltration

With the increase of temperature in sample 3, binder infiltration occurs. Many new phases, according to the XRD pattern, are introduced. Liquid binder dissolves WC and brings it to the PCD skeleton. The WC later precipitates out upon cooling[17]. η phase $Co_3W_3C$ is formed at a temperature probably above 1500 °C under a high pressure and is metastable at low temperature after fast cooling[18,19]. The formation of NbC might be related to the complex interactions within the Nb-C-Co system[20–22].

An expansion of the Co lattice is confirmed from the shift of the Co XRD peak. The dominant contribution to this lattice expansion is the solid solution of tungsten in cobalt. When they annealed the PCD materials at 800 °C for two hours to drive the solid solution tungsten out from the cobalt as a precipitate, Westraadt *et al.* [23] found the lattice expansion of cobalt disappears and the (002) Co XRD peak was back to 51.5°.

The increased contents of both cobalt and tungsten in the ICP-OES results are consistent with the increased Co and WC XRD peak intensities, indicating the occurrence of binder infiltration between sample 2 and 3. Considering the interval between samples 2 and 3 is only 150s, it can be inferred

that the binder infiltration occurs rapidly within this time frame, sweeping from the bottom toward the top of the PCD skeleton.

Since the maximum temperature reached by sample 2 is 30 °C above the eutectic point of the Co-C system at atmospheric pressure and also exceeds the eutectic point of the Co-WC system at atmospheric pressure [24,25], ICP-OES results suggest that the practical eutectic point of the Co-WC system under 7.7 GPa is higher than that calculated under atmospheric pressure.

A uniform NbC layer is seen as the final product after the complex interactions within the Nb-C-Co system after binder infiltration. The observed uniformity of the NbC layer also supports the rapid infiltration. Otherwise the slow infiltration would result in an uneven NbC layer, thicker at the bottom and thinner at the top due to the different interaction time.

From SEM images and EDX maps the Co layers on the two sides of the NbC layer in figure 5.27 c) are believed to be precipitation from the Nb-C-Co melt after cooling[22]. Since the eutectic points of both NbC-Co and Nb-Co systems are below 1350 °C, the maximum temperature reached in sample 2[22,26], the absence of the NbC XRD peak in sample 2 implies the essential catalytic role of the infiltrating Co in the formation of NbC.

Albeit without the images directly showing the progress of infiltration, it is still possible to simply understand this binder infiltration based on the abrupt change in ICP-OES and XRD results between samples 2 and 3 and the formation of a uniform NbC layer. As the temperature rises sufficiently to induce a partial liquid fraction of the Co-WC alloy within the substrate, the huge external pressure squeezes the liquid Co-WC solution in the substrate to propel it through the PCD skeleton. The capillary pressure within voids will also aid the infiltration of liquid Co-WC solution due to the small wetting angle (~ 26°) between liquid Co and diamond[27]. The viscosity in the binder is too small to prevent this infiltration driven by the external pressure[28]. This process is accelerated kinetically by the continuously increasing temperature. This understanding is also supported by a simplified infiltration model by German[28].

#### 5.4.3.6.2 Microstructural Features of Regrown Diamond

The microstructure shown in figure 5.26 c) is similar to that of the fully sintered sample in chapter 4, indicating that sample 3 has already densified. As discussed in sections 2.1 and 4.4.3.5, the absence of dislocations is a feature of regrown diamond[29]. Moreover, according to sections 4.4.2.4 and 4.4.3.5, the distinct contours separating old and regrown diamond usually overlaps with the enclosed binder particles. In figure 5.28 c), the green dashed line overlaps with the enclosed binder particles and separates the almost dislocation-free region from the region with numerous dislocations and is evidently another such contour. Therefore, it is reasonable to conclude that, in grain 1 in figure 5.28 c), the region outside the green dashed line is regrown diamond.

As for residual graphite, it also overlaps with the green dashed line. Minnaar *et al.*[30] reported the discovery of similar residual graphite in regrown diamond.

Thus, both enclosed binder particles and residual graphite are microstructural features characteristics of the interface between old and regrown diamond.

The most interesting finding is the nearly identical orientation of these residual graphite crystals. These orientation relationships indicate that the residual graphite along both sides of the GB might have originated from one large single crystal of graphite occupying the space between these two grains before diamond regrowth. During diamond regrowth, some parts of this single crystal graphite were somehow preserved within different diamond grains. A mechanism to explain this is suggested in section 5.5.1.

## 5.4.4 Samples 5 and 7

Sample 5 was terminated at the end of dwell and sample 7 was a fully sintered SPCD.

### 5.4.4.1 XRD Results of Samples 5 and 7

In figure 5.4, there is little difference in XRD pattern between samples 3,5 and 7.

### 5.4.4.2 ICP-OES Result of Samples 5 and 7

In figure 5.13, the wt% of both cobalt and tungsten remain constant, at around 10.5% and 3.5% for samples 3-7.

### 5.4.4.3 SEM Images of Samples 5 and 7

Figure 5.31 a) and b) are SEM images of samples 5 and 7. Their microstructures are similar to each other and also to that of sample 3. The average grain sizes of samples 5 and 7 are 5.8±0.4 µm and 5.8±0.3 µm, respectively.

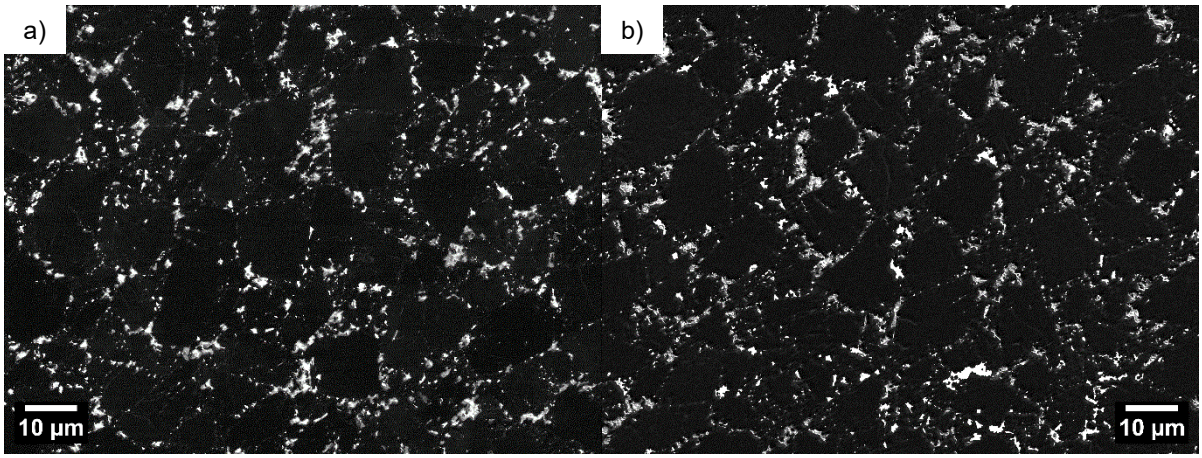


*Figure 5.31: SE2 images of a) sample 5. b) sample 7.*

### 5.4.4.4 (S)TEM Results of Samples 5 and 7

Figure 5.32 a) is a LAADF image of a region of aggregated fine diamond grains in sample 5 next to a coarser grain to the right of the figure. Orange arrows indicate residual graphite particles detected via EELS. A GB from the right hand coarse grain results in straight phase boundaries. A green dashed line outlines the position of enclosed binder particles within this coarse grain. On the left side, according to the corresponding BF TEM image (not shown) multiple fine diamond grains are present, hosting randomly distributed binder particles. The corresponding DF TEM image in figure 5.32 b) reveals the spatial distribution of residual graphite particles along both sides of the GB. Again, within this limited area, all residual graphite particles display a near-identical orientation different to those of both diamond and binder. Figure 5.32 c) illustrates a diffraction pattern from the circled region in

figure 5.32 a) consisting of diamond, graphite and binder. The bright diffraction spots within green circles correspond to diamond, whereas faint spots arise from graphite due to the double diffraction of electron beams[31]. This indicates an overlap between diamond and graphite in this region.

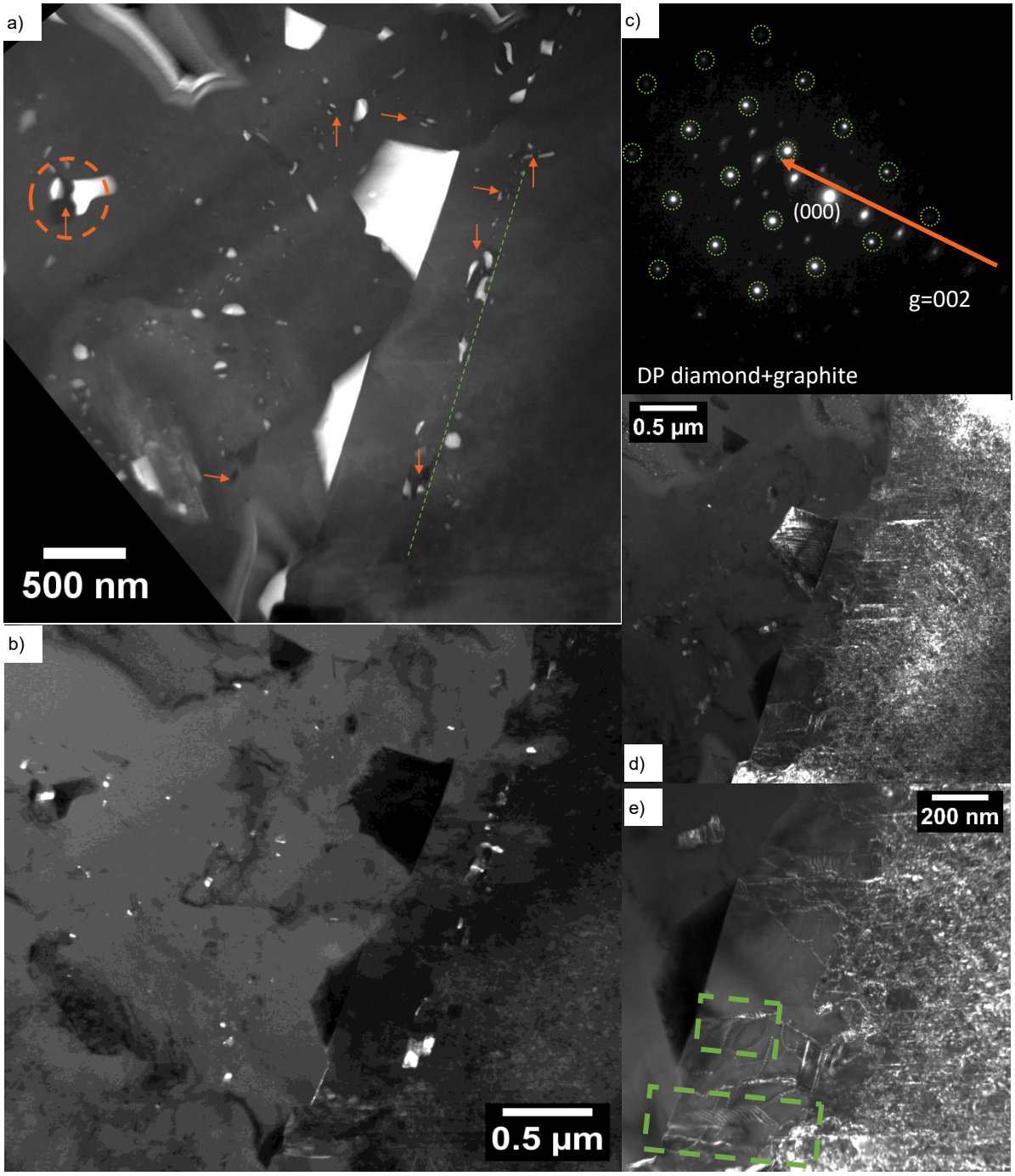


*Figure 5.32:a) A LAADF STEM image of a fine diamond grains aggregated region in sample 5. b) the corresponding DF TEM image from 002 graphite diffraction spot. c) the diffraction pattern of the circled area in a). The g=002 of graphite is marked. d) A DF TEM image showing the dislocation density in the right diamond grain. e) the enlarged DF TEM image of d) showing a region with sporadic dislocations. All TEM images are vertical to <110> of the right coarse diamond grain.*

Massive entangled dislocation networks are shown in the right hand coarse grain in the (111) weak beam DF TEM images in figure 5.32 d). The enlarged view in figure 5.32 e) offers a closer view. The

high density of dislocations leads to a blurred contrast in the old diamond on the right side in figure 5.32 d). Again, the green dashed line in figure 5.32a) across both the enclosed binder particles and residual graphite exactly separates the dislocation rich old diamond and dislocation sparse regrown diamond within these coarse grains.

Similar to the positions of stacking faults reported in section 4.4.3.5., some stacking faults (outlined in green boxes figure 5.32 e)) are also found within a low dislocation region close to the GB.

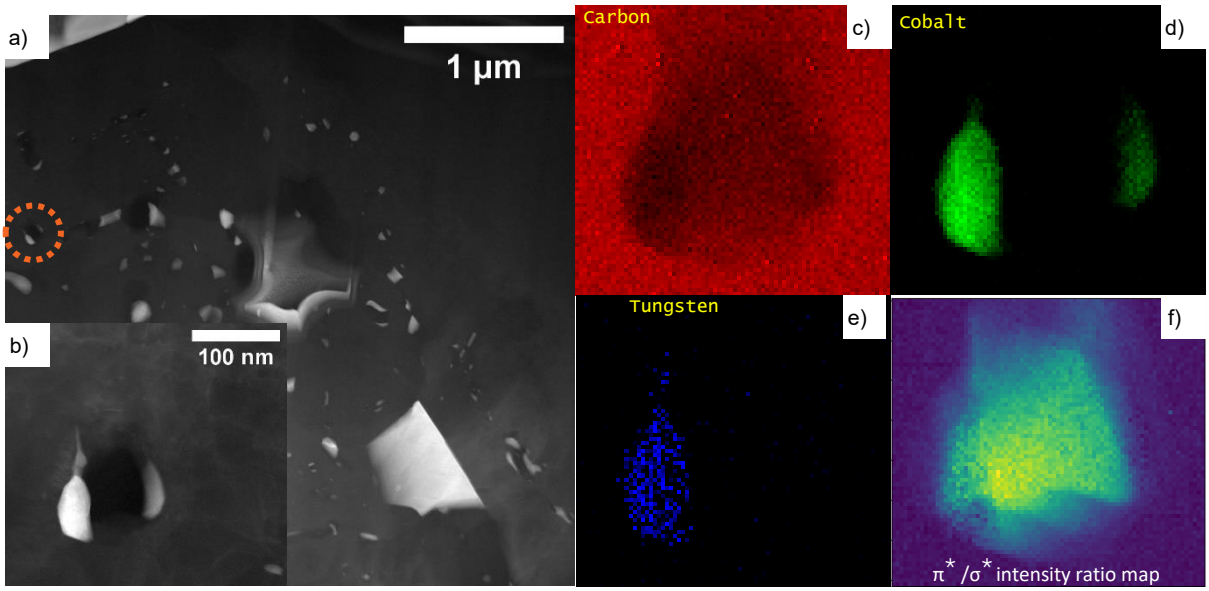


Figure 5.*33: a) A LAADF STEM image of a feature slightly above the region shown in* figure 5.32 *a). b) An enlarged LAADF image of a target feature circled in a). c), d) and e) EDX maps of carbon, cobalt and tungsten respectively. The width of EDX maps is 173 nm. f) The π*/σ* intensity ratio map showing the relative intensity from graphite.*

EELS and EDX were employed to probe another distinct binder-graphite-binder microstructure feature located just above the region selected in sample 5. The location of this feature is highlighted in the LAADF STEM image in figure 5.33 a), while an enlarged LAADF image is presented in figure 5.33 b). Figure 5.33 c), d) and e) correspond to the EDX carbon, cobalt and tungsten maps respectively. Figure 5.33 f) presents the π*/σ* intensity ratio map, again, showing the graphite is tightly encased by the binder particles on both sides. An inhomogeneous distribution of tungsten is evident within these two binder particles from the tungsten EDX map, with almost no tungsten characteristic X-rays from the right binder particle.

A region with two fine diamond grains from sample 7 is shown in figure. The BF TEM image in figure 5.34 a) and DF images in figure 5.34 b) & c) highlight the distribution of dislocations within two neighbouring grains, A and B. The dislocation densities are high in the top and low in the bottom within grains A and B. As in other regions, the DF TEM image in figure 5.34 d) reveals that all the residual graphite particles within these two grains share the same orientation. The enclosed binder particles in grain A are shown in figure 5.34 e). These enclosed binder particles within grains A and B exhibit the same orientation as that of their diamond host.

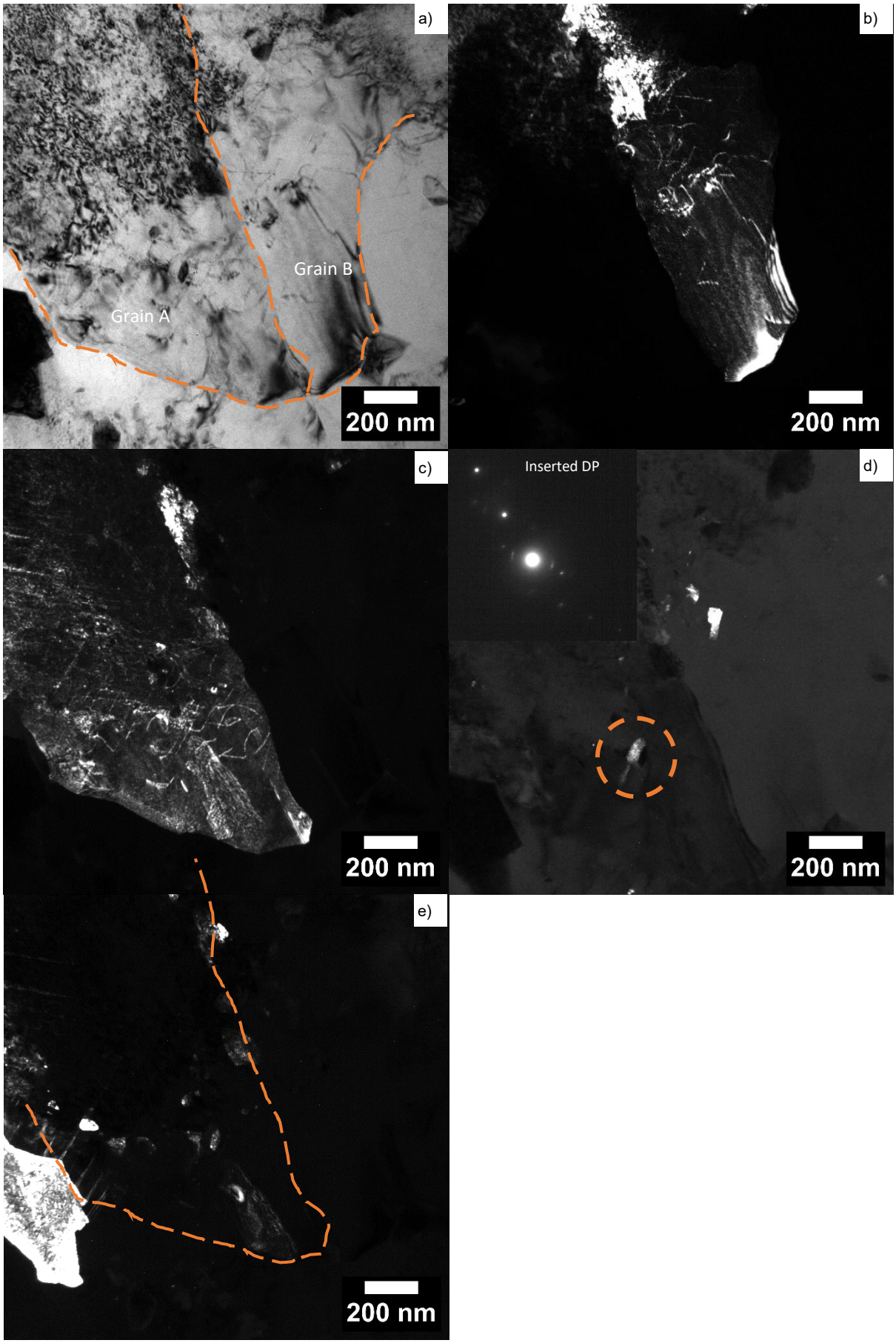


Figure 5.*34: a) A BF TEM image of two fine diamond grains in sample 7. GBs are outlined in orange dashed lines. b) A DF*

*TEM image from the 111 diamond diffraction spot of the grain B. c) A DF TEM image from the 111 diamond diffraction spot of the grain A. d) A DF TEM image from the 002 graphite diffraction spot. The inserted diffraction pattern is from the circled region in d). The bright diffraction spots are from diamond, while the faint ones are from graphite. e) A DF TEM image of enclosed binder particles in grain A. The GB of grain A is outlined in orange line.*

#### 5.4.4.5 Discussion of Samples 5 and 7

From SEM images, linear intercept analysis, XRD and ICP-OES results, the compositions and microstructures of sample 3, 5 and 7 are similar throughout the whole dwell. Therefore, the impact of dwell on the microstructure of PCD materials remain unclear at this stage.

The binder-graphite-binder microstructural features were also discovered in sample 5. However, an inhomogeneous distribution of tungsten in these two binder particles is revealed by EDX map (5.33 e)). One reason for this inhomogeneous distribution might be the different sources for the two binder particles. However, the other reason might just be that the right binder particle is thicker, as indicated by its low contrast in figure 5.33 b) and its weak characteristic X-rays intensity for Co in figure 5.33 d).

Regrown diamond regions were also found in samples 5 and 7. In the coarse grain investigated in sample 5 and at the bottom of grains A and B for sample 7, the low dislocation density, presence of enclosed binder particles and residual graphite, which are two microstructural features concluded from sample 3, all prove these regions are regrown diamond. For the residual graphite particles from samples 5 or 7, according to the DF TEM images of each sample, they all share almost one identical orientation which is different from their diamond hosts. However, all enclosed binder particles were examined to exhibit the same orientation as their diamond hosts. These orientation relationships are still consistent with sample 3.

# 5.5 Regrowth Mechanisms

## 5.5.1 Regrowth Mechanism Ⅰ: Graphite-Diamond Dissolution-Reprecipitation

Based on the dimension of the regions of graphite developed during hot compaction and the specific microstructural features, especially the enclosed binder, residual graphite particles and distribution of dislocations in samples 3, 5 and 7, a dissolution and reprecipitation process for diamond regrowth is proposed and depicted in figure 5.35. The direct transformation of graphite to diamond will be covered in section 5.5.2. and therefore, is not illustrated in these sketches.

Figure 5.35 a) represents the microstructure at the end of cold compaction. At this point, the diamond particles are coated in graphite from the outgassing treatment. The externally applied pressure is concentrated at the contact points between the diamond particles. The exposed surface between have no normal stress and are therefore below the Berman-Simon (B-S) line.

Figure 5.35 b) shows the microstructure during hot compaction. When the temperature rises to the eutectic point of Co-C system. Further graphitization is happening to gradually fill the interstitial voids. During the subsequent hot compaction in figure 5.35 b), diamond surfaces with pressure below the B-S line start to graphitize. Some surfaces not in contact with admixed cobalt graphitize binderlessly, such as the thin graphite layer in figure 5.20 c). For surfaces in contact with admixed cobalt, binder-assisted graphitization occurs locally through the dissolution of diamond carbon atoms, diffusion of these atoms in solid cobalt[5], and reprecipitate as graphite. Upon reaching the eutectic point of Co-C system at around 1320 °C, the high temperature, combined with the increased contact between diamond and cobalt due to liquification, significantly enhances the reactivity of Co and promotes further local binder-assisted graphitization[32]. 3D tomography (figure 5.24) reveals the

fragmentation of admixed binder particles. Individual liquid binder particles penetrate into the diamond grains.

Figure 5.35 c) refers to the microstructure after the temperature reaches the eutectic point of Co-WC system. The liquid binder infiltrates from substrates and approaches the admixed binder. One consequence of graphitization is the formation of a relatively large piece of single crystal graphite filling gaps between diamond grains, as shown in figure 5.35 c), similar to the microstructure in the green box shown in figure 5.23 a). At a timepoint once the temperature is beyond the Co-WC eutectic point in the substrate, the liquid Co-WC binder infiltrates into the PCD skeleton from the substrate[28].

The turning point comes when the temperature is beyond the eutectic point of Co-WC system and the pressure reaches the B-S line at this corresponding temperature (figure 5.25 d)). Diamond regrowth is about to commence because diamond becomes the thermodynamically stable phase. This rise in pressure is because the infiltration of the liquid binder homogeneously redistributes the hydraulic pressure throughout the PCD material[33]. Macroscopically, the PCD skeleton is entirely filled by the infiltrating liquid binder and the transformation of graphite to diamond is reversed to a graphite-to-diamond transformation catalysed by the liquid binder. Microscopically, graphite is completely surrounded by the compressive neighbouring diamond grains and the compressive liquid binder. This compression raises the local pressure above the B-S line to trigger diamond regrowth at the expense of the graphite. Some graphite protrusions into diamond grains, as shown in figure 5.35 d), were formed from previous binder-assisted graphitization.

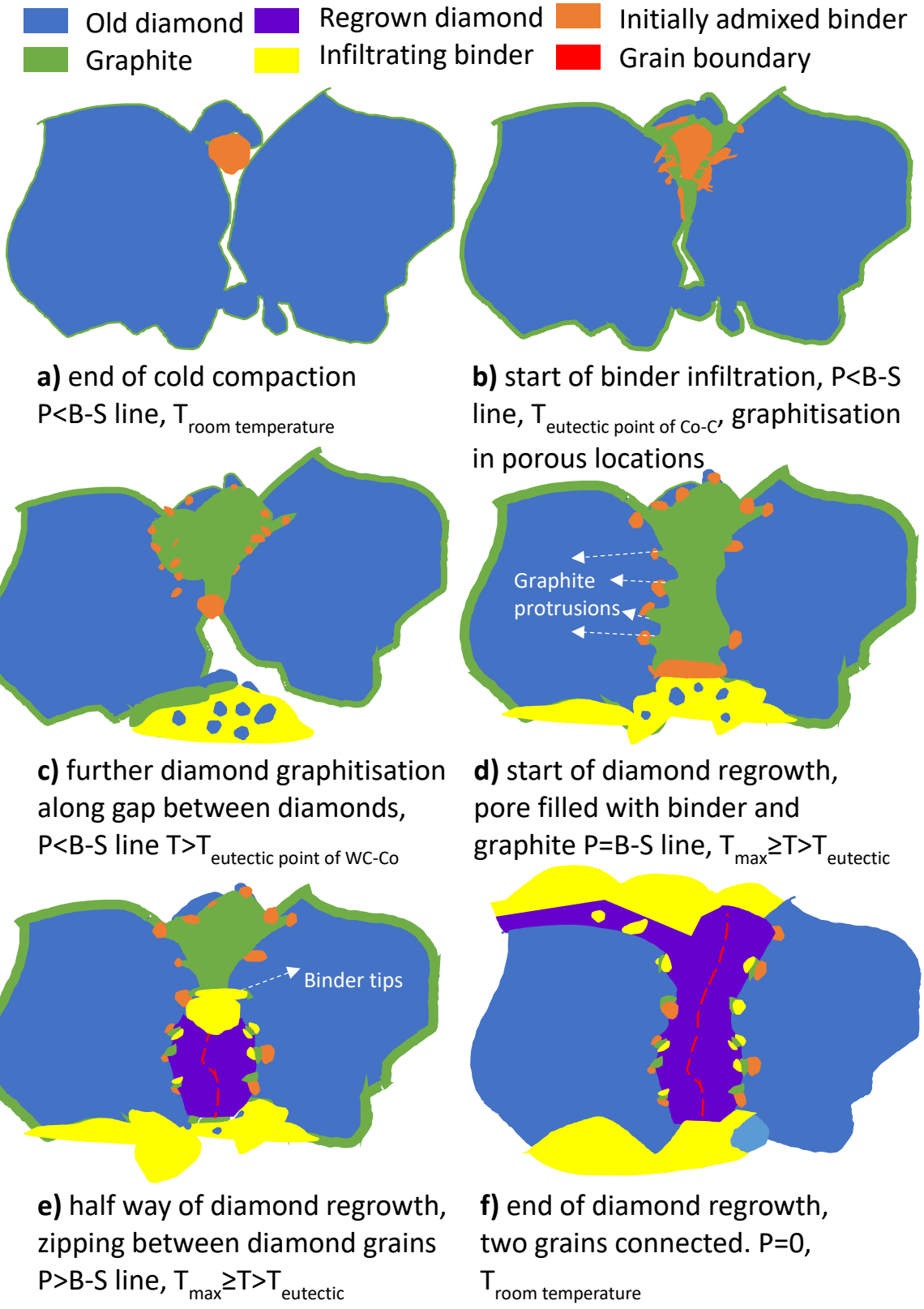


Figure 5.*35: a)-f) sketches of cross sections describe the dissolution and reprecipitation process of diamond regrowth. The stage and P, T conditions of each sketch are listed below. The pressure here refers to the local pressure on the exposed diamond surfaces. To simplify sketches, except a few diamond-diamond contacts, it assumes most of the diamond surfaces are not in contact with each other initially, but will be swept by binder in f).*

Figure 5.35 e) is the microstructure of the mid-point of diamond regrowth. Regrown diamond grows, catalysed by a liquid binder pool ahead. Dissolved carbon atoms diffuse through the liquid binder medium to epitaxially redeposit onto nearby diamond surfaces, joining them together at a clean GB. The whole regrowth process is similar to the reversed process of the nickel assisted graphitization proposed by Tulic *et al*.[13].Though the detail of this reprecipitation process remains unclear, it is believed that this epitaxial reprecipitation process is rapid and leads to the formation of the characteristic binder-graphite-binder microstructure, as shown in figure 5.29 b). One binder particle located away from the GB is likely an isolated component originating from the admixed binder powders, while the other binder particle close to the GB is thought to be a tip of a large, mobile infiltrating liquid binder pool dissolving the graphite protrusions (in figure 5.35 d)). As the liquid binder advances along the graphite, the reprecipitation of carbon atoms causes quick diamond regrowth to intercept these advancing binder tips (highlighted in figure 5.35 e)), rendering these binder tips enclosed. The graphite protrusions ahead of these binder tips are therefore remained in diamond.

Since diamond regrowth is through the consumption of the large single crystal of graphite between these two diamond grains, all residual graphite pieces in figure 5.35 e) at the boundary between regrown and old diamond share a nearly identical orientation. One thing that needs to be emphasized in e) is that the yellow, middle region infiltrating binder must be in connection with other infiltrating liquid binder in 3D. This continuous connection is essential, as isolated liquid binder cannot sustain sufficient pressure to continue diamond regrowth due to insufficient compression.

The rapid processes of liquid binder infiltration and diamond regrowth by dissolution-reprecipitation show that the regrowth might have been already largely completed at the start of the dwell. Little change in XRD patterns, compositional analysis results and microstructure features between sample 3 and sample 5 uphold this hypothesis.

At the end of diamond regrowth in figure 5.35 f), diamond grains are connected by regrown diamond. Apart from the residual graphite enclosed within diamond grains, the majority of the previously generated graphite has been transformed back to regrown diamond, corresponding to the disappearance of the graphite XRD peak in sample 3. This indicates that graphite to diamond dissolution and reprecipitation might be one of the dominant diamond regrowth mechanisms.

However, various microstructures could be formed at the end of diamond growth. Figure 5.35 f) is an example of a clean GB microstructure between two coarse grains. In other scenarios, different microstructures emerge, including binder particles on GBs (figure 5.32 a)) and large binder pools filling a triple point, enormous of which were seen in some SEM and TEM images (not shown here). These different microstructures may depend on the quantity of graphite before regrowth happens.

In the end, as discussed in section 5.4.4.5, further work is required to fully understand the change of microstructure during dwell.

In closing this section, it is worth pointing out the key role of the binder, which plays three key roles during this dissolution-reprecipitation process:

- Catalyst: catalyses diamond ⇌ graphite transformation under different conditions through the dissolution and reprecipitation mechanism.
- Diffusion path: redistributes diamond to fill the holes and increase the density of the PCD materials.
- Hydraulic fluid: increases and evenly distributes (hydraulic) pressure within the PCD materials.

### 5.5.2 Regrowth Mechanism || : The Direct Transformation of Graphite to Diamond

In comparison to the non-streaking twin diffraction spots from the straight 70.5° <110> twins in figure 5.22 a), the azimuthal streaking of twin spots suggests the presence of disoriented twins at the diamond-diamond connection in figure 5.21. The azimuthal streaking of diamond diffraction spots is related to a large misorientation within the same selected region, which is an indication of the higher degree of plastic deformation in the directly transformed regrown diamond[34]. Due to the relatively large misorientation, some twins near the diamond-diamond connection only have faint contrast in DF as their diffracted beam is oriented differently, near or even partially outside the objective aperture.

The presence of the bent twins is a sign of the direct transformation of graphite. Luo *et al.*[35] discovered the bent twins in nano diamonds from the directly transformed graphite and explained the formation of these bent twins via first-principles calculations. Consequently, in this study, the interconnection of diamond grains in figure 5.19 is very likely regrown diamond from the direct transformation of graphite formed during outgassing. This deduction is from several crucial pieces of evidence, including the bent 70.5° <110> twins at the connection in figure 5.21, the absence of both binder particles and graphite at the connection, and the presence of untransformed graphite at the periphery of the connection in figure 5.20 c).

The occurrence of the direct transformation of graphite to diamond within PCD materials can be simply described as below. The initial regrown diamond formation takes place at the point-to-point graphite contact between diamond grains, whose surface has previously transformed to graphite during outgassing. The contacts are under pressures higher than the mean externally applied pressure. This regrown diamond formation comes from the consumption of the graphite, resulting in an imperfect atomic arrangement characterized by abundant bent 70.5° <110> twins[35]. Since the

graphite layer is thin on diamond facets in figure 5.20 c), the regrowth of diamond is limited in thickness.

Some may argue that the bent twins originate from the bending of straight twins, rather than being formed during the direct graphite transformation regrowth. However, three results refute this argument. Firstly, the straight 70.5° <110> twins in figure 5.22 a) are buried among adjacent massive dislocations, yet no bent twins from TEM images or streaking twin diffraction spots from diffraction patterns are observed. Secondly, there is a high concentration of misorientation at the binder-free diamond-diamond connection, indicated by azimuthal streaking of diamond diffraction spots. However, this high concentration of misorientation is absent for heavily plastically deformed old diamond. In figure 5.22, no azimuthal streaking of diamond diffraction spots is observed from heavily plastically deformed old diamond, even with the same size of selective area aperture when studying the bent twins. Thirdly and most distinctively, no dislocations are observed near the bent twins at the binder-free diamond-diamond connection, despite the high local stress.

However, the subsequent processes following this direct transformation are not well understood. A possible scenario is that the expansion of the diamond connection formed could involve the plastic deformation of diamond grains flattening the contacts to fill gaps ahead of the two sides of this connection, which is similar to the phenomenon described by Ashby[36]. But this scenario appears less plausible.

Firstly, the expansion of the diamond-diamond connection will lead to a reduction in pressure between diamond grains. Once the stress falls below the yield stress of diamond, this expansion ceases.

Secondly, in the microstructural study of PCD materials, no 2-3 micron or even larger GB with itself and its surrounding environment being binder-free is ever observed in fully sintered SPCD materials. Instead, the frequently observed microstructure involves discontinuous binder particles dispersed

along or around GB. This also suggests that, in SPCD, the binder-assisted dissolution-reprecipitation mechanism is the dominant one during diamond regrowth.

Considering the competitive nature between the two diamond regrowth mechanisms described, a plausible scenario is that once a small diamond-diamond connection is formed via direct transformation, its expansion is possibly quite slow. Both sides of it will be soon wetted by the infiltrating liquid binder. The growth mechanism would eventually switch to the binder-assisted dissolution-reprecipitation mechanism.

### 5.5.3 Regrowth Mechanism ||| : Grain Growth via Movement of Grain Boundaries at Solid/Solid Interfaces

A less frequently discussed regrowth mechanism is diamond grain growth via movement of grain boundaries at solid/solid interfaces [37]. To study this mechanism, the average grains size of each sample was measured as summarised in Table 5.3 below and their interception distributions are plotted in figure 5.36. Except for samples 0 and 1, the average grain size of the other samples is almost constant. The reduction of grain size from sample 0 to 1 is due to diamond fracture during the hot compaction. Smaller grains were pulled out during mechanical polishing of sample 1, leading to a higher average grain size.

Because the most evident microstructural feature from grain growth is the increase of average grain size, the opposite change of grain size in this study does not align with the expected outcome of grain growth during the HPHT LPS sintering of PCD materials[38]. The grain size of samples with different dwell time in the next chapter also demonstrate no difference in average grain size. The relatively high energy barrier for grain boundary migration might be the reason that prevents the grain growth in PCD materials[35]. The carbon atom on the diamond surface has to undergo de-bonding from their original grain and then form new covalent bonds with the new grain. With the

extra de-bonding step, this potentially requires an even higher energy compared to the direct transformation of graphite to diamond[35].

| Sample | Average grain size (µm) | Number of interceptions |
|---|---|---|
| 0 | 8.9 | From DLS; more than 1000 |
| 1 | 8.1±0.5 | 988 |
| 3 | 6.4±0.4 | 999 |
| 5 | 5.8±0.4 | 1078 |
| 7 | 5.8±0.3 | 1090 |

*Table 5.3: average grain size measured from the linear intercept analysis and the number of interceptions of each sample.*

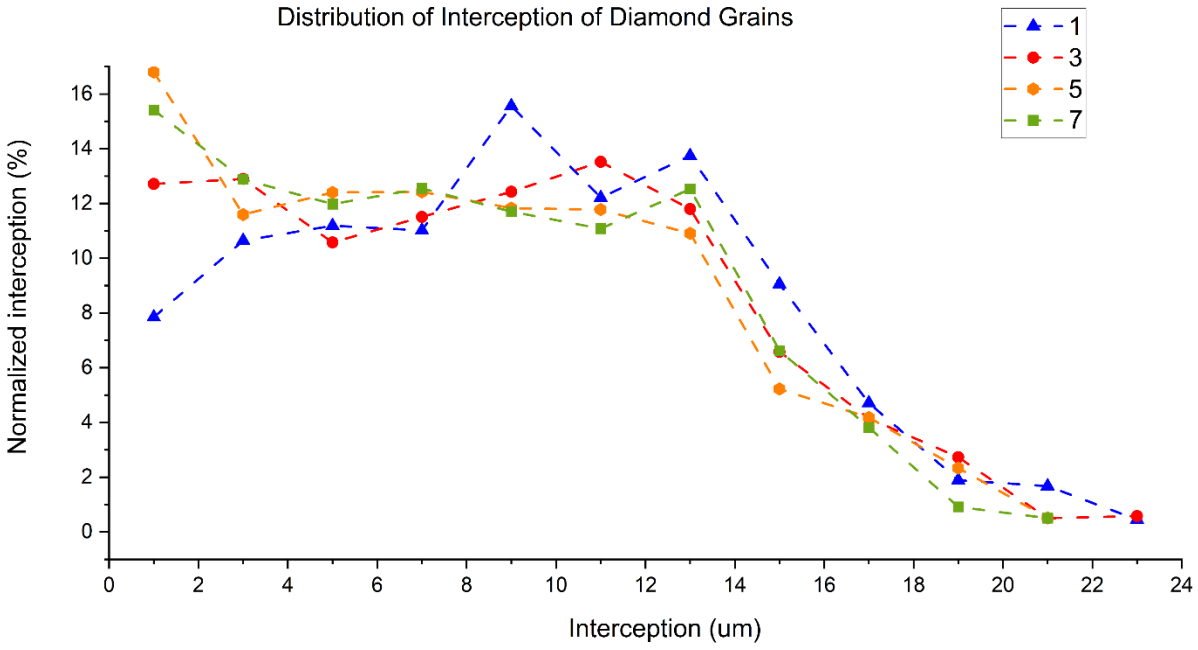


*Figure 5.36: the distribution of interception of sample 1, 3, 5 and 7.*

### 5.5.4 Regrowth Mechanism Ⅳ: Classical Dissolution and Reprecipitation (from Diamond to Diamond)

The process of classical dissolution and reprecipitation[39] (by dissolving diamond in binder to reprecipitate regrown diamond onto old diamond) certainly occurs during sintering and it is likely the predominant regrowth mechanism during the dwell stage (discussed in next chapter). The regrown diamond from classical dissolution and reprecipitation mechanism is microstructurally similar to that from graphite-diamond dissolution and reprecipitation, despite the lack of residual graphite and enclosed binder particles. Nonetheless, the fraction of regrown diamond resulting from the classical dissolution and reprecipitation **between binder infiltration and the dwell stage may be minimal**. This assessment is based on two reasons. Firstly, the kinetics of the classical dissolution and reprecipitation might be relatively low, potentially impeded by the low solubility of diamond in cobalt[28]. The presence of undissolved diamond particles within both the AGG and binder pools after a full sintering process corroborates this hypothesis. Secondly, the interval between infiltration and dwell is notably short (under 150s). However, during a more than 10 or even 50 times longer dwell at $T_{max}$, analysis from SEM, ARGUS, EBSD and TEM don't show a significantly enlarged rim of regrown diamond in comparison with samples subjected to shorter dwell. The linear intercept analysis does not indicate a noticeable increase in average grain size after these long-time dwells. Likewise, Ostwald ripening, as one of the classical dissolution and reprecipitation mechanisms, will occur to a limited extent due to the small fraction of nano-sized diamond grains[39] (~0.1 %, estimated from the dynamic light scattering result of diamond powders after cold compaction) and the carbon saturation in liquid binder by dissolving graphite during infiltration.

## 5.6 Summary

By studying the microstructure of PCD samples from different HPHT sintering stages, this chapter has probed the underlying mechanisms of diamond regrowth. Four regrowth mechanisms have been discussed: graphite-diamond dissolution-reprecipitation, direct transformation of graphite to diamond, grain growth via movement of grain boundaries at solid/solid interfaces and classical dissolution and reprecipitation, with the emphasis mainly on the first one. The graphite-diamond dissolution-reprecipitation mechanism is described as a diamond-to-graphite-to-diamond process facilitated by catalytic binders. Based on the change of microstructure, the diamond is thought to be initially graphitized during pre-treatment and hot compaction, achieved through homogeneous binderless graphitization and inhomogeneous binder-assisted graphitization. Depending on the stage at which the sintering is aborted, before infiltration, the newly formed graphite can fill between 32 vol% the void space in samples discussed in this thesis. Subsequently, this graphite is dissolved by the rapid liquid binder infiltration and the dissolved carbon atoms then epitaxially reprecipitate onto diamond surfaces as regrown diamond. This occurs once the local pressure redistributed by the liquid binder exceeds the B-S line. Ultimately, this graphite-diamond dissolution-reprecipitation is a process of the redistribution of diamond carbon atoms to form regrown diamond to connect diamond grains among the PCD structure during the HPHT sintering. Enclosed binder particles and residual graphite within diamond are the microstructural features of regrown diamond. The majority of the dissolution-reprecipitation diamond regrowth process is described in figure 5.35.

It is shown that the majority of the graphite-diamond dissolution-reprecipitation diamond regrowth has rapidly completed before the dwell stage. The binder has three roles throughout diamond regrowth: catalyst, diffusion path and hydraulic fluid. However, the change of microstructure during dwell needs further investigation.

Some evidence supports the occurrence of the direct transformation of graphite to diamond mechanism, though many questions remain about what happens after the formation of the diamond-diamond connection. Identifying this connection is challenging as definitive evidence largely revolves around the observation of bent twins via TEM.

The results of linear intercept analysis of diamond grains do not show any grain growth mechanism.

Understanding diamond regrowth can be useful. Firstly, it serves as a theoretical benchmark for investigating PCD material sintering. The corresponding PCD microstructures can be predicted when changes are made to the original feed or sintering conditions. Secondly, it sets prerequisites for selecting new binders, which must fulfil the three roles crucial for solid diamond regrowth. Lastly, it guides the tailoring of the HPHT sintering profile to approach a balance between the PCD sintering and its enormous energy consumption. This paves the way for greener manufacturing.

## 5.7 Future Work

Future studies in this field should concentrate on investigating these points:

- Exploring the detail of liquid binder infiltration from the substrate, including the starting temperature, the time span and the kinetics.
- Detailing the reprecipitation process
- Theoretical modelling of the graphite-diamond transformation: predicting local conditions and time points at which the graphite-diamond transformation is reversed.
- Kinetic study of dissolution-reprecipitation diamond regrowth.
- Competition among different regrowth mechanisms.
- Effect of alternative catalysts: exploring the potential influence on diamond regrowth of alternative catalysts, like Ni and Fe.

## 5.8 Reference


(1) Dzepina, B.; Sigalas, I.; Herrmann, M.; Nilen, R. The Aqueous Electrophoretic Deposition (EPD) of Diamond-Diamond Laminates. *Int. J. Refract. Met. Hard Mater.* **2013**, *36*, 126–129.

(2) Gražulis, S.; Daškevič, A.; Merkys, A.; Chateigner, D.; Lutterotti, L.; Quirós, M.; Serebryanaya, N. R.; Moeck, P.; Downs, R. T.; Le Bail, A. Crystallography Open Database (COD): An Open-Access Collection of Crystal Structures and Platform for World-Wide Collaboration. *Nucleic Acids Res.* **2012**, *40* (D1), D420–D427.

(3) Kamali, A. R. Black Diamond Powder: On the Thermal Oxidation and Surface Graphitization. *Appl. Surf. Sci.* **2021**, *551* (January).

(4) Bokhonov, B. B.; Dudina, D. V.; Sharafutdinov, M. R. Graphitization of Synthetic Diamond Crystals: A Morphological Study. *Diam. Relat. Mater.* **2021**, *118* (August).

(5) Tian, Y.; Wang, J.; Zhang, J.; Guan, S.; Zhang, L.; Wu, B.; Su, Y.; Huang, M.; Zhou, L.; He, D. Solubility and Stability of Diamond in Cobalt under 5 GPa. *Diam. Relat. Mater.* **2020**, *110* (September), 1–7.

(6) Jianxin, D.; Hui, Z.; Ze, W.; Aihua, L. Friction and Wear Behavior of Polycrystalline Diamond at Temperatures up to 700 °c. *Int. J. Refract. Met. Hard Mater.* **2011**, *29* (5), 631–638.

(7) Walmsley, J. C.; Lang, A. R. Characteristics of Diamond Regrowth in a Synthetic Diamond Compact. *J. Mater. Sci.* **1988**, *23* (5), 1829–1834.

(8) Bobrovnitchii, G. S.; Osipov, O. S.; Filgueira, M. Some Peculiarities of the Diamond Micro-Powder Sintering. *Int. J. Refract. Met. Hard Mater.* **2003**, *21* (5–6), 251–258.

(9) Guan, S.; Peng, F.; Liang, H.; Fan, C.; Tan, L.; Wang, Z.; Zhang, Y.; Zhang, J.; Yu, H.; He, D. Fragmentation and Stress Diversification in Diamond Powder under High Pressure. *J. Appl. Phys.* **2018**, *124* (21).

(10) Nie, A.; Bu, Y.; Huang, J.; Shao, Y.; Zhang, Y.; Hu, W.; Liu, J.; Wang, Y.; Xu, B.; Liu, Z.; et al. Direct Observation of Room-Temperature Dislocation Plasticity in Diamond. *Matter* **2020**, *2* (5), 1222–1232.

(11) Egerton, R. F.; Whelan, M. J. Electron Energy Loss Spectra of Diamond, Graphite and Amorphous Carbon. *J. Electron Spectros. Relat. Phenomena* **1974**, *3* (3), 232–236.

(12) Turner, S. Structure, Shape, Defects and Impurities in Nanodiamonds Investigated by HRTEM and STEM-EELS. *Nanodiamonds Adv. Mater. Anal. Prop. Appl.* **2017**, *3* (1), 57–84.

(13) Tulić, S.; Waitz, T.; Čaplovičová, M.; Habler, G.; Varga, M.; Kotlár, M.; Vretenár, V.; Romanyuk, O.; Kromka, A.; Rezek, B.; et al. Covalent Diamond-Graphite Bonding: Mechanism of Catalytic Transformation. *ACS Nano* **2019**, *13* (4), 4621–4630.

(14) Kondo, K.; Sawai, S.; Akaishi, M.; Yamaoka, S. Deformation Behaviour of Shock-Synthesized Diamond Powder under High Pressures and High Temperatures. *J. Mater. Sci. Lett.* **1993**, *12* (17), 1383–1385.

(15) Khmelnitsky, R. A.; Gippius, A. A. Transformation of Diamond to Graphite under Heat Treatment at Low Pressure. *Phase Transitions* **2014**, *87* (2), 175–192.

(16) Akaishi, M.; Kanda, H.; Sato, Y.; Setaka, N.; Ohsawa, T.; Fukunaga, O. Sintering Behaviour of the Diamond-Cobalt System at High Temperature and Pressure. *J. Mater. Sci.* **1982**, *17* (1), 193–198.

(17) Fernandes, C. M.; Senos, A. M. R. Cemented Carbide Phase Diagrams: A Review. *Int. J. Refract. Met. Hard Mater.* **2011**, *29* (4), 405–418.

(18) García, J.; Collado Ciprés, V.; Blomqvist, A.; Kaplan, B. Cemented Carbide Microstructures: A Review. *Int. J. Refract. Met. Hard Mater.* **2019**, *80* (December 2018), 40–68.

(19) Scott, T. The Effect of High Temperature on Polycrystalline Diamond, Oxford, 2019.

(20) Cuppari, M. G. di V.; Santos, S. F. Physical Properties of the NbC Carbide. *Metals (Basel).* **2016**,

*6* (10).

(21) Dmitrieva, G.; Cherepova, T. Melting Diagram of Cobalt-Rich Alloys in the System C–Co–Nb. *Chem. Met. Alloy.* **2015**, *8* (3/4), 83–90.

(22) Huang, S. G.; Van der Biest, O.; Li, L.; Vleugels, J. Properties of NbC-Co Cermets Obtained by Spark Plasma Sintering. *Mater. Lett.* **2007**, *61* (2), 574–577.

(23) Westraadt, J. E.; Sigalas, I.; Neethling, J. H. Characterisation of Thermally Degraded Polycrystalline Diamond. *Int. J. Refract. Met. Hard Mater.* **2015**, *48*, 286–292.

(24) Guillermet, A. F. Thermodynamic Properties of the Co-W-C System. **1989**, *20* (May).

(25) Diagram, E. The C-Co (Carbon-Cobalt) System. **1991**, *12* (4), 417–424.

(26) Okamoto, H. Co-Nb (Cobalt-Niobium). *J. Phase Equilibria Diffus.* **2010**, *31* (1), 94–95.

(27) Andreyev, A. V. The Wetting and Bonding of Diamond Films by High Melting Point Metals in the Range of Diamond Thermodynamic Stability. *Diam. Relat. Mater.* **1994**, *3* (10), 1262–1264.

(28) German, R. M. Sintering Window and Sintering Mechanism for Diamond. *Int. J. Refract. Met. Hard Mater.* **2023**, *117*, 151–160.

(29) Walmsley, J. C. The Microstructure of Ultrahard Material Compacts Studied by Transmission Electron Microscopy. *Mater. Sci. Eng.* **1988**, *105–106* (PART 2), 549–553.

(30) Minnaar, E. G.; Westraadt, J. E.; Neethling, J. H. Microstructural Characterization of Polycrystalline Diamond Sintered at Ultrahigh Pressures. *Microsc. Microanal.* **2017**, *23* (S1), 2288–2289.

(31) Edington, J. W. *Interpretation of Transmission Electron Micrographs*; 1975; Vol. 6.

(32) Sung, C. M.; Tai, M. F. Reactivities of Transition Metals with Carbon: Implications to the Mechanism of Diamond Synthesis Under High Pressure. *Int. J. Refract. Met. Hard Mater.*

**1997**, *15* (4), 237–256.

(33) German, R. M.; Suri, P.; Park, S. J. Review: Liquid Phase Sintering. *J. Mater. Sci.* **2009**, *44* (1), 1–39.

(34) Britun, V. F.; Oleynik, G. S.; Semenenko, N. P. Deformation Processes during High-Pressure Sintering of the Diamond Powders Produced by Catalytic Synthesis. *J. Mater. Sci.* **1992**, *27* (16), 4472–4476.

(35) Luo, K.; Liu, B.; Hu, W.; Dong, X.; Wang, Y.; Huang, Q.; Gao, Y.; Sun, L.; Zhao, Z.; Wu, Y.; et al. Coherent Interfaces Govern Direct Transformation from Graphite to Diamond. *Nature* **2022**, *607* (7919), 486–491.

(36) Ashby, M. F. The Deformation of Plastically Non-Homogeneous Materials. *Philos. Mag.* **1970**, *21* (170), 399–424.

(37) Park, J. K.; Akaishi, M.; Yamaoka, S.; Fukunaga, O.; Eun, K. Y.; Yoon, D. N. Formation of Bridges between Diamond Particles during Sintering in Molten Cobalt Matrix. *J. Mater. Sci.* **1992**, *27* (17), 4695–4697.

(38) Cantwell, P. R.; Tang, M.; Dillon, S. J.; Luo, J.; Rohrer, G. S.; Harmer, M. P. Grain Boundary Complexions. *Acta Mater.* **2014**, *62* (1), 1–48.

(39) McKie, A.; Herrmann, M.; Sigalas, I.; Sempf, K.; Nilen, R. Suppression of Abnormal Grain Growth in Fine Grained Polycrystalline Diamond Materials (PCD). *Int. J. Refract. Met. Hard Mater.* **2013**, *41*, 66–72.

# 6 Spheroidization of Binder Particles During Dwell

## Table of Contents

## 6.1 Introduction

As concluded in chapter 5, in PCD materials, diamond regrowth is mainly governed by binder-assisted dissolution-reprecipitation and direct transformation of graphite to diamond. However, little microstructural difference is found between samples terminated during or after dwell. As noted at the end of Chapter 4, it is challenging to directly identify regrown diamond and assess the diamond-diamond connectivity (DDC) which can be roughly understood in terms of the thermodynamic stability of the diamond-liquid binder system under HPHT conditions. DDC is at its lowest at the onset of classical dissolution and reprecipitation diamond regrowth (approximately the end of binder infiltration when all graphite has been dissolved and reprecipitated). It increases as the total energy of the diamond-liquid binder system decreases via the replacement of high energy interfaces by low energy interfaces through the redistribution of carbon atoms during diamond regrowth. Ideally, when the diamond-binder system achieves the most thermodynamically stable state, the classical dissolution and reprecipitation diamond regrowth effectively ceases and DDC reaches its highest point.

The corresponding microstructures with different DDC are sketched in figure 6.1. Before dwell, the corresponding microstructural evolution because of diamond regrowth can be thought of the change from figure 6.1 a) to figure 6.1 b). During dwell, the change of microstructure can be potentially reflected by the change of DDC, i.e. from figure 6.1 b) to figure 6.1 c). With the increase of DDC, the amount of diamond-diamond connection increases due to the segmentation of binder pools and reshaping of binder particles. Unfortunately, it is difficult to quantify DDC directly.

The contiguity of diamond-diamond contact normalized with phase boundary can directly express the degree of DDC. However, two challenges arise. Firstly, determining connectivity statistically requires a large quantity of data from many high-resolution images and measurements are typically carried out manually[1]. This process is time-consuming and labour-intensive, which is not conducted due to the DPhil time constraint. Secondly, it also necessitates high quality high-resolution images

clearly showing both the phase boundaries and diamond connectivity, especially those nano sized binder particles along GB as shown from TEM images in chapter 5. The resolution of ARGUS images at 10 kV is roughly 31 nm, which may introduce inaccuracies when mapping these nano binder particles.

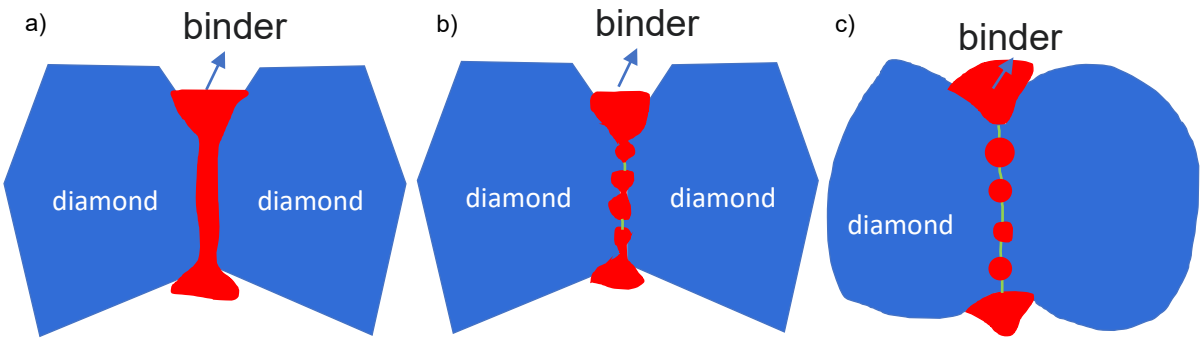


*Figure 6.1: simplified sketches of DDC of different microstructures. The green line is the GB between two diamond grains. a) At the onset of diamond regrowth. DDC is the lowest. b) The onset of dwell. Some GBs between two diamond grains form as diamond is regrowing. DDC increases at this stage. c) A probable microstructure of a thermodynamically stable diamond-liquid binder system. DDC is the highest. These simplified sketches ignore the graphite and correspond to a regrowth scenario where binder particles remain in GBs.*

An indirect way to study DDC is to investigate the evolution of the geometry of binder particles. Liquid binder always accompanies and catalyses the diamond regrowth between diamond grains. During sintering, liquid binder pools will have a tendency to change their geometry to minimize the local interfacial energy[2]. Therefore, liquid binder will tend to change from an irregular geometry at the beginning of liquid phase sintering toward a regular geometry to minimize the local interfacial area. For example, during initial sintering, the liquid binder phase will infiltrate the gaps between diamond grains to form a continuous network structure. This will catalyse diamond regrowth to connect diamond grains and its minimisation of interfacial area will finally result in discrete binder particles along grain boundaries. Hence the overall geometry of small binder particles might be linked with the degree of regrowth.

Sphericity, a morphological parameter describing the three-dimensional spherical nature of particles, is highlighted as an indicator of this interfacial energy-driven regrowth process for binder particles. Its quantitative expression is discussed in section 6.3.1. The sphericity of binder particles

can be statistically measured by high-resolution FIB-SEM 3D tomography with a voxel size of 10*10*20 nm.

## 6.2 Material and Sample Preparation

To extend the potential differences in microstructure before dwell and after dwell, two types of samples were prepared. One type includes samples with a standard dwell and with a 10 x longer dwell to facilitate the microstructural change during dwell. The other type includes samples with no extra graphite and 5 wt% extra graphite to facilitate the microstructural change before dwell.

Therefore, in addition to SPCD, now termed TP2-0 in this chapter, and SPCDG, now termed TP2-5, this chapter introduces two new samples named TP2-0 lt and TP2-5 lt to investigate the latter possibility. The "lt" suffix indicates a 10x longer dwell time compared to SPCD. Table 6.1 summarizes the differences for these four sample types.

| | **Standard dwell time** | **10 times longer dwell time** |
|---|---|---|
| **No graphite** | TP2-0 (same as SPCD) | TP2-0 lt |
| **Extra graphite (5wt%)** | TP2-5 (same as SPCDG) | TP2-5 lt |

*Table 6.1: composition and processing details of four types of samples*

## 6.3 Experimental

### 6.3.1 Characterization Techniques

The details of the EM-related general characterization that are concerned with in this chapter have been previously discussed in section 3.3, including ARGUS imaging, linear intercept analysis, FIB-SEM 3D tomography, TEM. The details of XRD and ICP-OES can be found in section 3.4.

To study the sphericity of individual binder particles or pools, their volume and surface area were extracted from the 3D tomography results to calculate their corresponding sphericity. The mathematical expression of sphericity is:

$$\frac{the\ surface\ area\ of\ a\ sphere\ with\ the\ same\ volume\ as\ a\ given\ particle}{the\ actual\ surface\ area\ of\ this\ given\ particle} = \frac{\pi^{1/3}(6V)^{2/3}}{A}$$

where V is the volume of the binder particle counted by the sum of voxels and A is the surface area of the binder particle integrated via the positions of surface voxels[3]. The sphericity of some representative geometries is listed in table 6.2 below.

| Geometry | Sphere | Octahedron | Cube | Tetrahedron |
|---|---|---|---|---|
| Sphericity | 1 | 0.846 | 0.806 | 0.671 |

*Table 6.2: sphericities of some representative geometries.*

## 6.4 Results

### 6.4.1 Microstructure

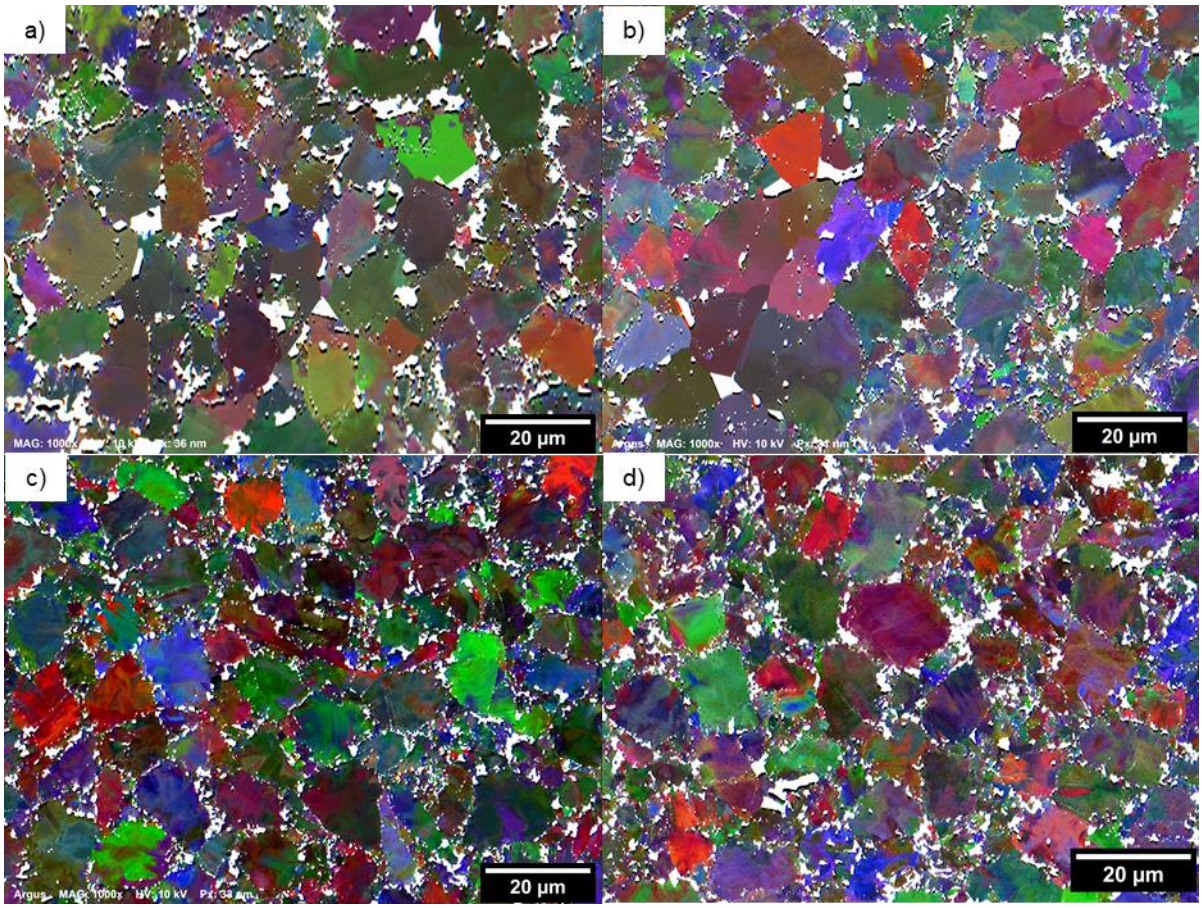


*Figure 6.2: ARGUS images of a) TP2-5. b) TP2-5 lt. c) TP2-0. d) TP2-0 lt.*

To compare the different microstructures of these four samples, their corresponding ARGUS images are provided in figure 6.2 a)-d). In the ARGUS image, each colour represents a specific crystallographic orientation, showing diamond grains. The ARGUS images of TP2-5 and TP2-5 lt show numerous enclosed binder particles within diamond grains, resulting in some diamond-diamond connections (clean GBs). In contrast, the ARGUS images of TP2-0 and TP2-0 lt exhibit a similar microstructure, with the majority of the binder particles or pools distributed along or within the GB.

### 6.4.2 Grain Size

The estimated average diamond grain size of each sample was measured via the linear intercept analysis introduced in 3.2.4. The results are plotted in figure 6.3 a) and b). The grain size of TP2-0 and TP2-0 lt are closely comparable, while those of TP2-5 and TP2-5 lt are similar to one another, indicating that the long dwell time has minimal impact on the diamond grain size. However, there is about a 2.5 µm difference in grain size between the PCD samples with or without graphite. This is because there are relatively less fine diamond grains (interception less than 4 µm) in PCD samples with graphite, as shown in figure 6.3 b), indicating that diamond grains grow larger on the consumption of extra graphite. The largest grain size of each sample exceeds 20 µm.

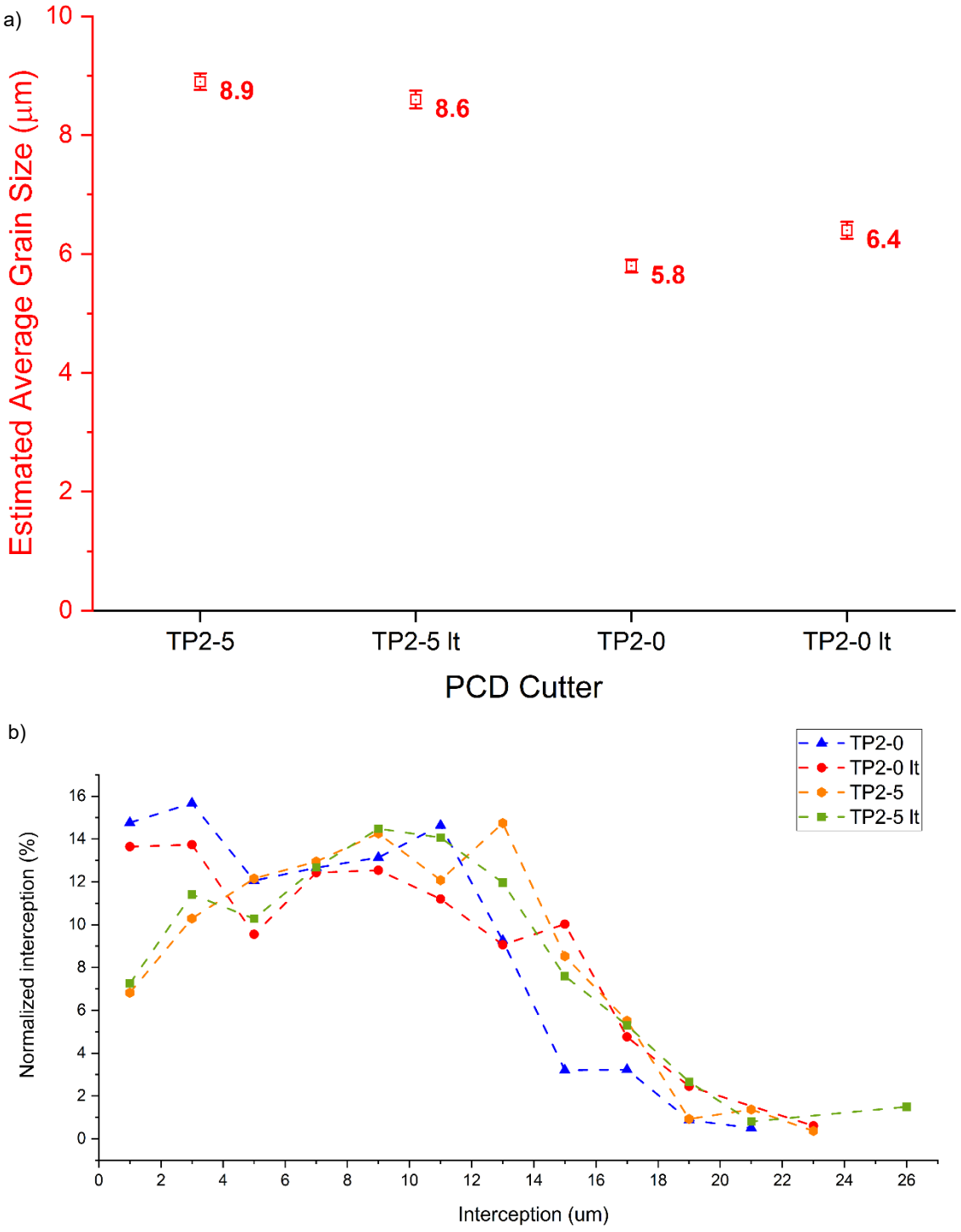


*Figure 6.3: a) The estimated average grain size of diamond, with the standard error, measured from the linear intercept analysis. b) the distribution of grain interceptions in each sample. The number of intercepts for each sample ranges from 900 to 1200.*

### 6.4.3 Sphericity of Binder Particles

In addition to differences in the distribution of the binder particles or pools, their geometry might be diverse as well. To statistically study the geometry of isolated binder particles, 5 volumes were randomly selected for 3D FIB-SEM tomography from the four samples: TP2-5 (two different volumes), TP2-0, TP2-0 lt, and an under-sintered sample 2 (sintering terminated at the start of hot compaction) from chapter 5. 3D FIB-SEM tomography of TP2-5 lt was not conducted due to project timeline constraints.

In the sphericity analysis, binder particles with volumes less than $1x10^{-4}$ $\mu m^3$ (50 voxels, about 0.06 µm in diameter) were excluded, as their limited number of voxels introduced inaccuracy in measuring volume and surface area. Moreover, binder particles larger than 0.1 $\mu m^3$ ($5x10^4$ voxels, about 0.6 µm in diameter) were also excluded due to the small population size that limits their statistical significance. The binder particles that were in contact with the boundaries of the sample volumes were removed, leaving only the isolated binder particles within.

Figures 6.4, 6.5 and 6.6 display the 3D tomography images of TP2-0, TP2-5 set 2 and TP2-0 lt. Each isolated binder particle or pool is coloured differently to distinguish it from the surrounding ones. The varying numbers of binder particles or pools between the samples are partly due to differences in sectioning depth.

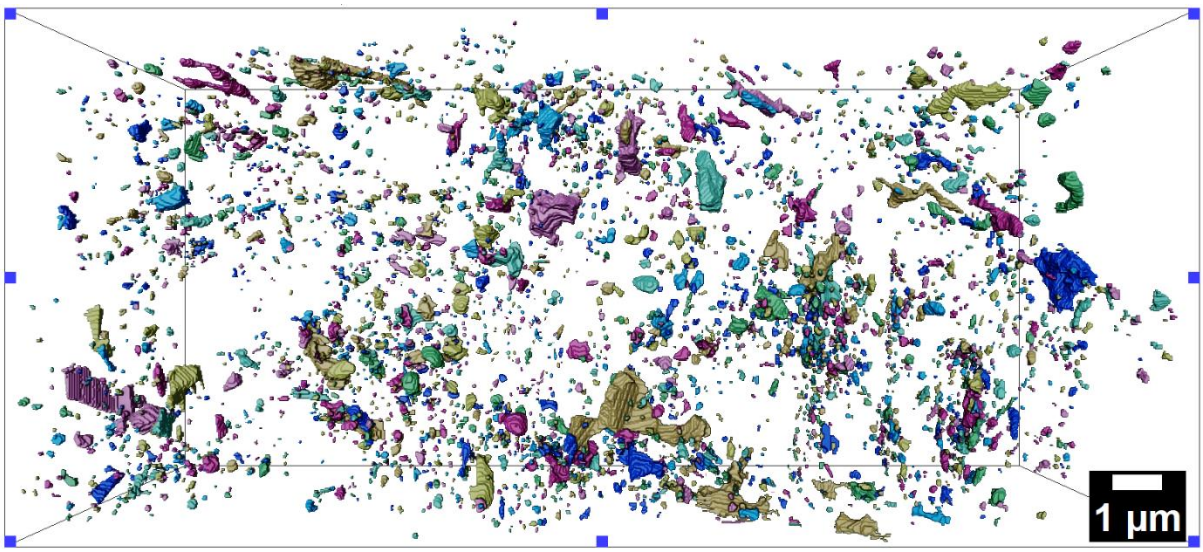


*Figure 6.4: front view from 3D tomography of isolated binder particles or pools of TP2-0. There are about 4000 binder particles or pools within this volume.*

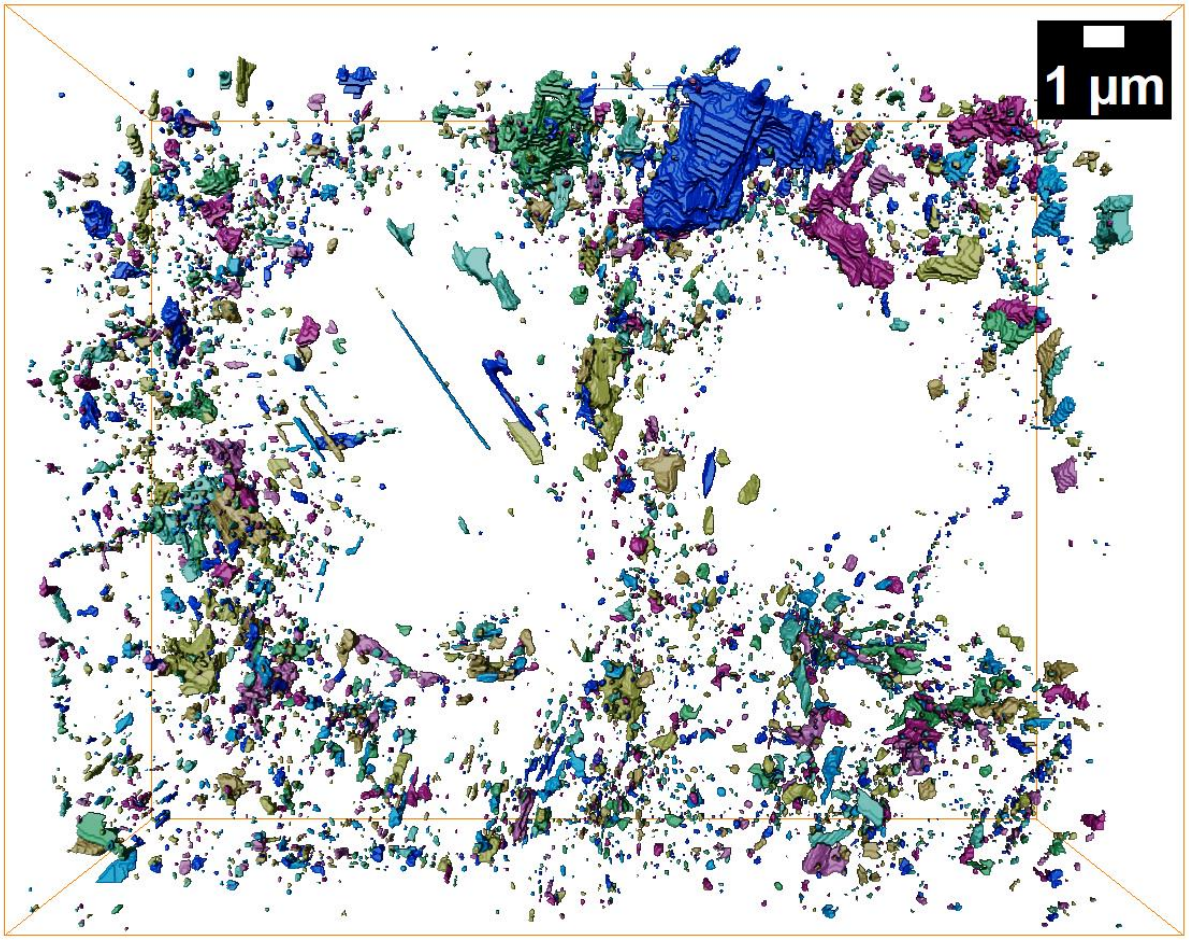


*Figure 6.5: front view from 3D tomography of isolated binder particles or pools of TP2-5 set 2. There are about 800 binder particles or pools within this volume.*

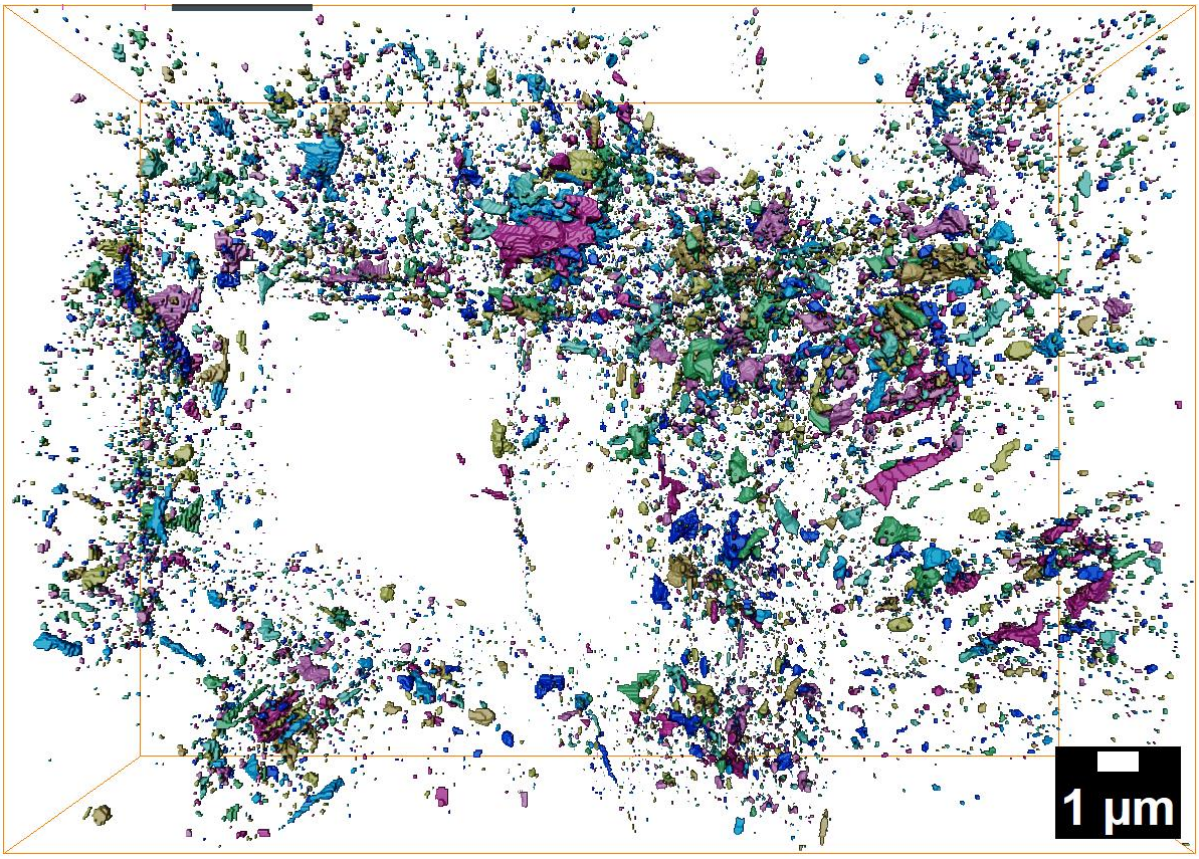


*Figure 6.6: front view from 3D tomography of isolated binder particles or pools of TP2-0 lt. There are about 12000 binder particles or pools within this volume.*

To clearly illustrate the trend of the sphericity as a function of binder volume, figure 6.7 is divided into three ranges: $1x10^{-4}$ < range 1 ≤ $1x10^{-3}$ µm $^3$, $1x10^{-3}$ < range 2 ≤ $1x10^{-2}$ µm $^3$and $1x10^{-2}$ < range 3 ≤ $1x10^{-1}$ µm $^3$. A linear scale of X-axis is selected as for each region it is easier to interpret the change of sphericity as a function of binder volume, compared to a logarithmic scale. Each range is further divided into nine sub-bins. The average sphericity and its standard error are calculated from all the binder particles in the same sub-bin. Therefore, the average sphericity of the same sub bin across different samples can be compared, reducing the influence from different binder sizes.

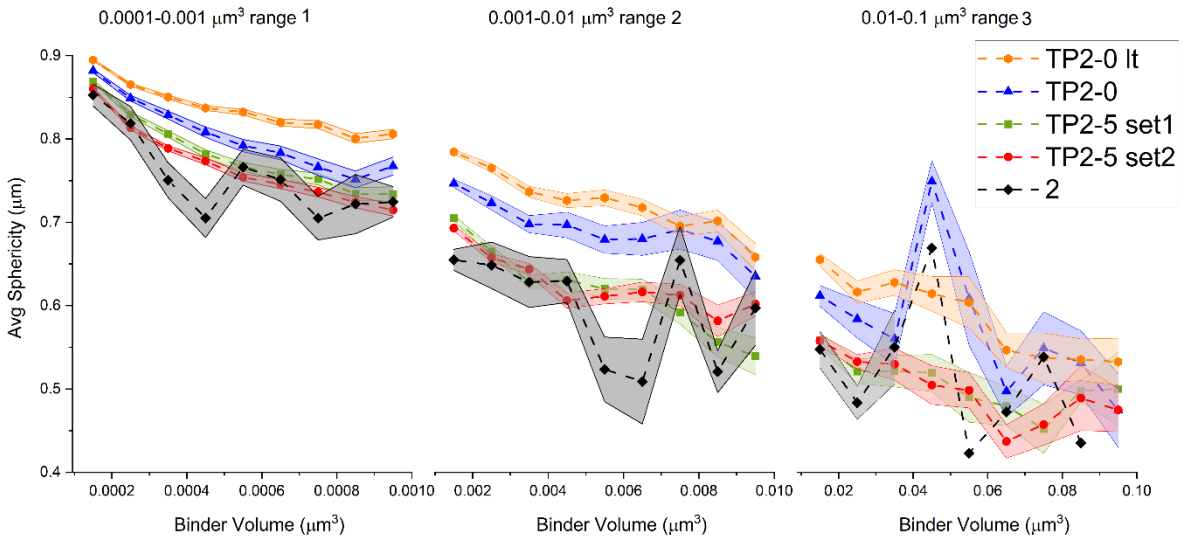


*Figure 6.7: A sphericity analysis of five sets of data from four samples. The semi-transparent region is the standard error. The standard error in some sub bins of range 3 of sample 2 is absent due to the lack of quantity in relatively large binder particles.*

Generally, TP2-0 lt exhibits the highest average sphericity across all three ranges, followed by TP2-0 and TP2-5 (set 1 and 2), while sample 2 displays the lowest average sphericity. The relatively large fluctuation in the trend of sample 2 is attributed to the small population size (about 300 binder particles). The small population is also the reason behind the relatively large fluctuations for all samples in range 3.

Furthermore, in all data sets, the average sphericity gradually decreases with an increase in binder volume, indicating that binder particles become more irregular the larger they are.

Lastly, the two data sets from TP2-5 exhibit a significant overlap. The difference in their average sphericity is evidently smaller compared to the difference between any data sets from two different samples. This demonstrates the reproducibility of the measurements.

Other results were also extracted from the 3D tomography. With the exception of sample 2 which has a limited binder particle population, the count percentage in each sub-bin with the same binder volume is similar across the remaining three samples. No single sub-bin of the same binder volume displays a markedly higher count percentage compared to the other samples. This shows that all sintered samples contain the same number and volume distribution of particles. There are, however,

substantially more binder particles in range 1 than in range 3. Moreover, the spatial distribution of binder particles is similar among all four samples. Lastly, no pores, voids or cracks were detected during sectioning for the three fully sintered samples.

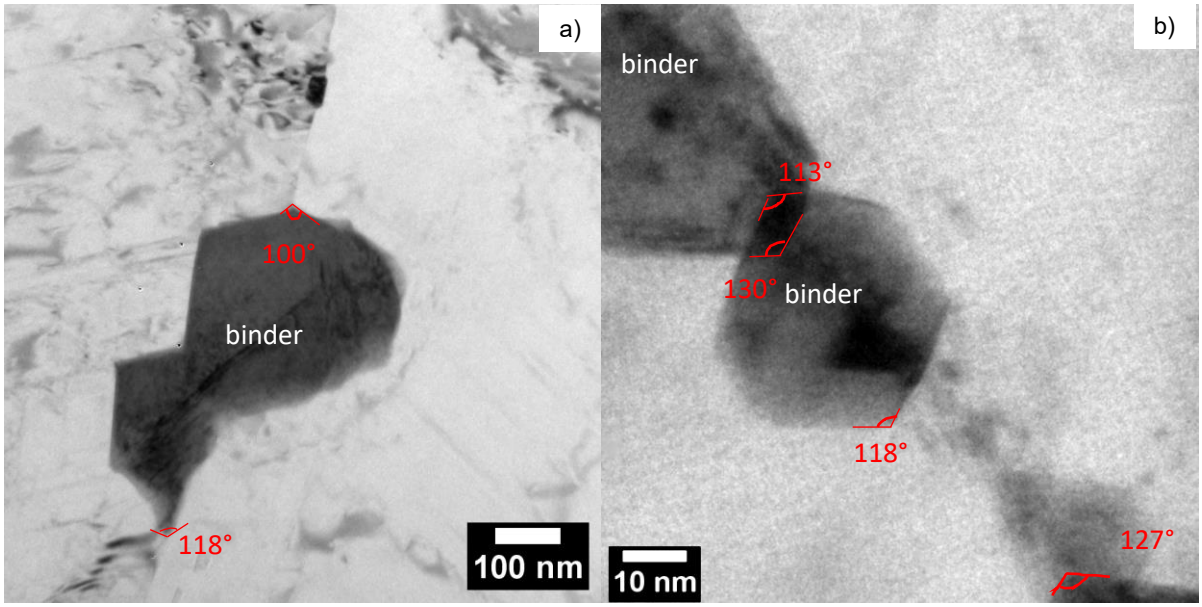


*Figure 6.8: a) and b) are BF TEM images showing some measured dihedral angles of binder particles in 2D. All these TEM samples are fabricated from TP2-0.*

Figure 6.8 a) and b) show some binder particles within GBs after standard dwell. Some dihedral angles have been marked and roughly measured. It should be noted that the actual dihedral angles may be slightly higher due to the blunting of corners, making accurate measurement challenging.

Another noteworthy aspect of the binder particles is their geometries. For the binder particle in figure 6.8 a), its left interface comprises several straight facets, while its right interfaces are rounded. Regarding the binder particles in figure 6.8 b), all of them exhibit polyhedral with short facets.

## 6.4.4 Phase and Compositional Analysis

### 6.4.4.1 Phase Analysis

To investigate the potential presence of different phases among these four samples, XRD patterns were obtained for each sample. In figure 6.9, all phases are identified with different coloured pointers on top. Notably, no graphite XRD peak was observed for the 2 samples (TP2-5 & TP2-5 lt)

with extra graphite. Furthermore, XRD patterns from all four samples closely resemble each other especially between the main XRD peaks from diamond (red pointers) and cobalt (blue pointers). There is also little difference in the other phases detected.

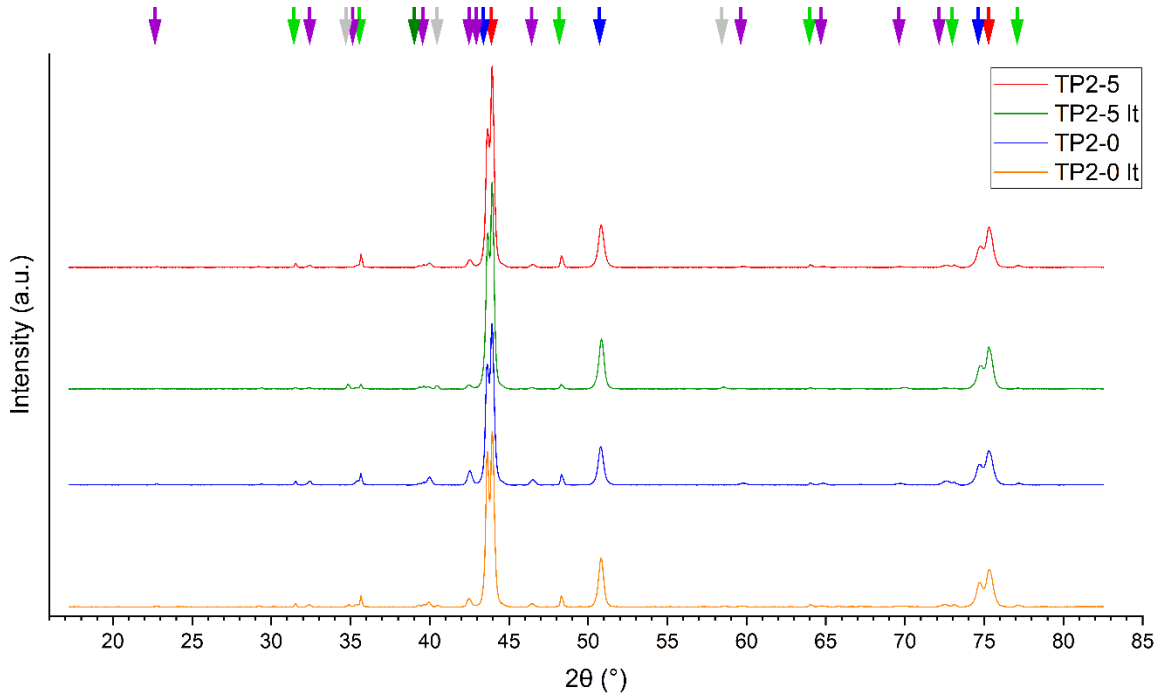


*Figure 6.9: XRD patterns of the four samples. All phases are identified by pointers at the top. Diamond in red; FCC Co in blue; $Co_3W_3C$ in purple; WC in green and NbC in grey. An unknown peak at 39.8° indicated in olive might be from the XRD sample holder.*

### 6.4.4.2 Composition

To further investigate the volume percentages of both cobalt and tungsten carbide in PCD materials, ICP-OES was conducted by staff from Element Six Ltd. The compositional data are presented in figure 6.10. The vol% of cobalt ranges from 6 to 7 vol%, while tungsten carbide falls within the range from 0.5 to 1 vol%. There is little significant difference in vol% of cobalt or in vol% of tungsten carbide between the four samples.

As listed in table 6.3, the vol% of both cobalt and tungsten carbide were also extracted from 3D tomography data for TP2-0, TP2-5 and TP2-0 lt. For each sample, their vol% of both cobalt and tungsten carbide obtained from 3D tomography closely match the corresponding vol% from ICP-OES.

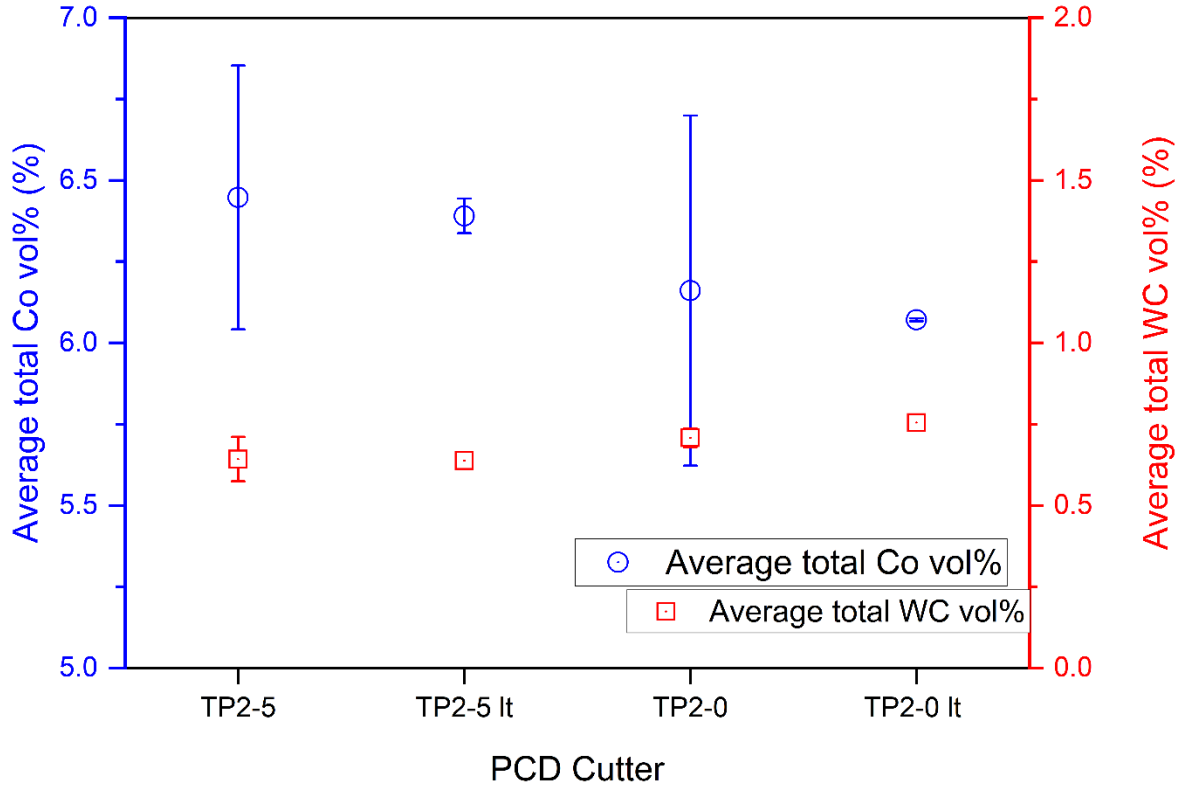


*Figure 6.10: ICP-OES results of four samples after fully leaching. Results are presented in volume percentage.*

| 3D tomography | TP2-5 | TP2-0 | TP2-0 lt |
|---|---|---|---|
| Co vol% | 6.3% | 6.7% | 6.3% |
| WC vol% | 0.4% | 0.6% | 0.4% |

*Table 6.3: volume percentages of cobalt and tungsten carbide measured from 3D tomography.*

## 6.5 Discussion

### 6.5.1 Validity of the Sphericity Analysis

To the author's knowledge, this is the first time that analysis of the sphericity of binder particles has been used to study the kinetics of liquid phase sintering. A comparable study by M. Pontoreau *et al*[4] utilized X-ray 3D tomography based sphericity analysis to investigate phase transformation kinetics in gas-atomized Ti-6Al-4V powders.

The similar composition results from ICP-OES, a widely recognized and accurate chemical composition analysis method, and FIB-SEM 3D tomography demonstrate good reliability of the tomography results. The near overlap of the sphericity data between the two TP2-5 sets and the obvious sphericity difference between either TP2-5 set and the other samples indicate the reproducibility of the sphericity analysis.

### 6.5.2 Sphericity and DDC

One of the factors that determines the sphericity of binder particles during HPHT liquid phase sintering is the dihedral angle between Co and diamond[2]. This influences the vertiex geometry of binder particles in contact with diamond GBs. The equilibrium dihedral angle $\varphi$ can be calculated using the following equation:

$$(\gamma_{gb}) = 2\gamma_{Co-diamond} \cos\frac{\varphi}{2}$$

Where $\gamma_{gb}$ is the grain boundary energy of diamond, typically 0.5-1 times the surface energy of diamond which varies with different diamond {hkl} planes[2,5]. $\gamma_{Co-diamond}$ is the interfacial energy between cobalt and diamond. Using the value of $\gamma_{Co-diamond}$ (4.63 J/m$^2$) [6] and the average surface energy of diamond (6.3 J/m$^2$)[5,6], the calculated average $\varphi$ ranges from around 94° to 140°. This aligns with dihedral angles measured from the isolated binder particles in figure 6.8. However, this average $\varphi$ range is 6 to 9 times larger than the reported average $\varphi$ (15°) of cobalt-diamond by German[7]. However, the $\varphi$ results from his measurements rely on relatively low-resolution EBSD maps rather than HR TEM images. In EBSD maps, small binder particles in GBs consist of a few pixels, reducing the accuracy of particle geometry and dihedral angle values.

Another factor governing the edges and faces of binder particles is the local interfacial energy[2,8]. During the dwell, the micron or nano sized binder particles will accommodate their geometry to minimize the local interfacial energy[2,9]. The reduction of total interfacial energy is expressed as:

$$\Delta(\gamma A) = A\Delta\gamma + \gamma\Delta A$$ [2]

Where γ is the specific interfacial energy (J/m$^2$) for different interfaces and A is the total interfacial area (m$^2$). This minimization of interfacial energy in PCD involves reducing γ by replacing the mismatched/high energy {hkl} diamond-binder interfaces with low energy ones, and by reducing A between binder and diamond. Sometimes, these pathways can compete, resulting in some binder particles at GBs consisting of low {hkl} facets on one side, but curved interfaces on the other side, as shown in figure 6.8 a). Or they can be synergistic, leading to a binder particle with a polyhedron geometry with faceted faces, as shown in figure 6.8 b).

Therefore, sphericity can partly indicate the amount of diamond-diamond connections formed during dwell since the diamond-binder phase boundary is partially replaced by newly formed diamond-diamond connections. However, this indication is confined to the comparison among PCD samples with the same compositions.

In general, both the dihedral angle and the local interfacial energy drive binder particles to transform from irregular geometries just after the binder infiltration towards regular and more discontinuous geometries during dwell. Therefore, despite the complex factors determining the precise geometries of individual particles, **average sphericity is likely to serve as a parameter to reflect diamond-diamond connectivity during dwell**.

The increase sphericity of TP2-0 to TP2-0 lt, shown in figure 6.7, shows that longer sintering time enables liquid binder particles to evolve toward stable regular geometries under the two driving forces discussed.

The kinetics of the change of binder geometry is dependent on the liquid binder diffusion distance[2]. With short diffusion distances, small binder particles achieve thermodynamically stable regular geometries faster than large particles. This explains the reason why the smaller the binder particles, the higher their average sphericity.

However, as discussed in chapter 5, enclosed binder particles are consequences of diamond regrowth before dwell. From the large amount of enclosed binder particles in figure 6.2 a) and b), a large extent of diamond regrowth is expected to have occurred in the samples with extra graphite, corresponding to a greater vol % of regrown diamond in these samples. Nonetheless, the average sphericities of two sets of TP2-5 are lower than those of TP2-0 and TP2-0 lt in which enclosed binder particles were not frequently observed. This indicates that sphericity does not directly reveal the DDC before dwell.

The relationship between DDC before and after dwell and their indicators is concluded in figure 6.11.

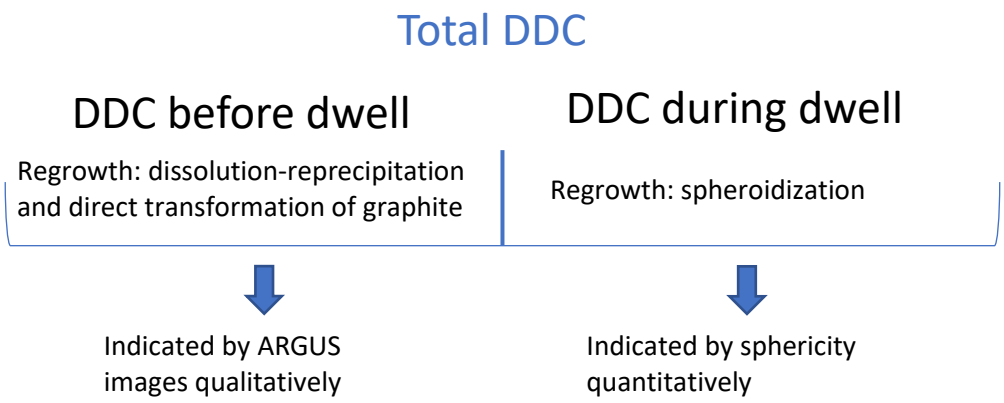


*Figure 6.11: the relationships between different DDC, regrowth mechanisms and their indicators.*

Compared to spheroidization, variables in composition, such as the extra graphite, exert a larger impact on **total DDC**. In figure 6.2, obviously the amount of diamond-diamond connection in TP2-5 is higher than in TP2-0 lt.

## 6.6 Summary

Sphericity analysis based on FIB-SEM 3D tomography was applied to investigate the sphericity of binder particles from 4 PCD samples with different amount of extra graphite and sintering time. By comparing composition results from 3D tomography and from standard ICP-OES and repeating the measurement of the average sphericity from random regions in the same sample, it is concluded that the sphericity analysis is valid and reproducible.

In terms of the thermodynamics and kinetics of diamond regrowth during dwell, average sphericity can serve as a parameter to indirectly reflect DDC of PCD samples after dwell. DDC can partly indicate the relative amount of diamond-diamond connections formed during dwell between samples with the same composition.

## 6.7 The Relationships between the Three Regrowth Mechanisms

In conclusion, when a substantial amount of graphite occupies voids in the PCD table prior to infiltration, the predominant diamond regrowth mechanism after infiltration is the graphite-diamond dissolution and reprecipitation, driven by the different solubilities of graphite and diamond. Owing to the high solubility of graphite in liquid Co, this process is considered rapid compared to the classical dissolution of diamond and reprecipitation. It initiates immediately at the end of infiltration and possibly ceases even before reaching Tmax (in under 150s) once all graphite has been dissolved.

On the other hand, with a relatively small quantity of graphite, though this graphite will be quickly transferred to diamond, the predominant diamond regrowth mechanism may shift to the classical dissolution and reprecipitation driven by the minimization of interfacial energy. The extent of diamond regrowth via this mechanism is time dependent. It also starts at the end of infiltration, but can continue for even a few hours[10]. Its kinetics might mainly depend on the dissolution of diamond in the molten binder. The presence of nano-sized diamond grains, debris and sharp diamond corners could expedite this process via Ostwald ripening[11].

Prior to both mechanisms discussed above, the direct transformation of graphite to diamond occurs at the diamond-graphite-diamond contact points where local pressure is highly concentrated (more than 10 GPa). However, because of the thin graphite layer formed during vacuum heat treatment and in the absence of binder catalysis, the extent of this mechanism is restricted to the thin graphite

layer within high pressurized diamond-diamond contacts. This transformation ceases at the end of the infiltration.

These relationships are illustrated in figure 6.12.

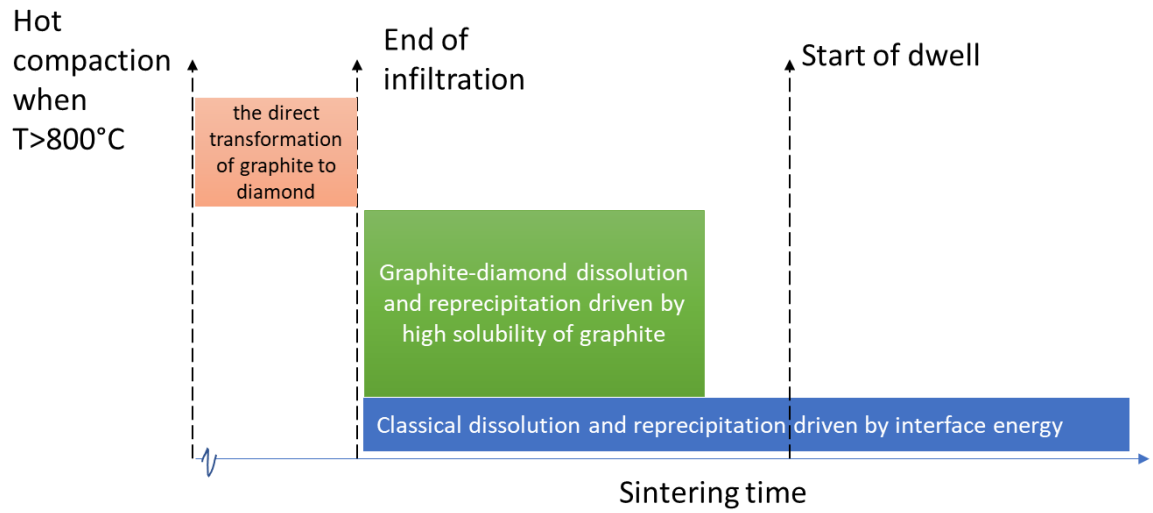


*Figure 6.12: the predominant regrowth mechanism at each sintering stage.*

## 6.8 Future work

The future work suggested focuses on:

- Investigate relationships between diamond regrowth and other manufacturing variables, like temperature and pressure.
- Correlate the indirect characterization of diamond regrowth with direct characterization, with the aid of AI and low voltage ARGUS images obtained from a better detector, measuring the diamond-diamond contiguity measuring the diamond-diamond contiguity from high quality high-resolution ARGUS images clearly showing both phase boundaries and diamond grain boundaries.
- Explore other manufacturing processes to only enhance the diamond-diamond connections, such as dispersing nano sized graphite to fill gaps between diamond grains.

## 6.9 Reference


(1) Hansen, N. Polycrystalline Strengthening. *Metall. Trans. A* **1985**, *16* (12), 2167–2190.

(2) Kang, S. J. L. *Sintering: Densification, Grain Growth and Microstructure*; 2005.

(3) ThermoFisher Scientific. Thermo Scientific Avizo Software 9. 2018, p 169.

(4) Pontoreau, M.; Coffigniez, M.; Trillaud, V.; Bourlot, C. Le; Lachambre, J.; Gremillard, L.; Perez, M.; Maire, E.; Adrien, J.; Steyer, P.; et al. In Situ Synchrotron Study of Sintering of Gas-Atomized Ti-6Al-4 V Powders Using Concomitant Micro-Tomography and X-Ray Diffraction: Effect of Particle Size and Interstitials on Densification and Phase Transformation Kinetics. *Acta Mater.* **2023**, *246* (January), 118723.

(5) Zhang, J. M.; Ma, F.; Xu, K. W.; Xin, X. T. Anisotropy Analysis of the Surface Energy of Diamond Cubic Crystals. *Surf. Interface Anal.* **2003**, *35* (10), 805–809.

(6) Andreyev, A. V. The Wetting and Bonding of Diamond Films by High Melting Point Metals in the Range of Diamond Thermodynamic Stability. *Diam. Relat. Mater.* **1994**, *3* (10), 1262–1264.

(7) German, R. M. Sintering Window and Sintering Mechanism for Diamond. *Int. J. Refract. Met. Hard Mater.* **2023**, *117*, 151–160.

(8) De Jonghe, L. C.; Rahaman, M. N. Sintering of Ceramics. In *Handbook of Advanced Ceramics: Materials, Applications, Processing and Properties*; 2003; Vol. 1–2, pp 187–264.

(9) Rahaman, M. N. *Sintering of Ceramics*; 2007.

(10) Park, J. K.; Akaishi, M.; Yamaoka, S.; Fukunaga, O.; Eun, K. Y.; Yoon, D. N. Formation of Bridges between Diamond Particles during Sintering in Molten Cobalt Matrix. *J. Mater. Sci.* **1992**, *27* (17), 4695–4697.

(11) McKie, A.; Herrmann, M.; Sigalas, I.; Sempf, K.; Nilen, R. Suppression of Abnormal Grain Growth in Fine Grained Polycrystalline Diamond Materials (PCD). *Int. J. Refract. Met. Hard Mater.* **2013**, *41*, 66–72.

# 7 The Relationships Between Diamond Regrowth and Mechanical Performance of PCD Materials

## Table of Contents

# 7.1 Introduction

The final objective of this thesis is to explore the potential relationships between diamond regrowth and the mechanical performance of PCD materials. From section 2.3 and previous discussion, as a consequence of regrowth, individual diamond grits will be connected to form a continuous structure, potentially strengthening the mechanical performance. However, as established in chapters 5 and 6, diamond regrowth mechanisms before and after dwell are different, and result in different microstructures, involving differences in DDC. The four samples with various graphite additions and dwell times investigated in chapter 5 are carried forward to this chapter and their microstructures are correlated with their mechanical properties, represented by vertical borer analysis (VBA) and 3-point bend testing.

# 7.2 Material and Sample Preparation

The same four samples are from section 6.2.

# 7.3 Experimental

## 7.3.1 Mechanical Testing

### 7.3.1.1 3-Point Bend Testing

The transverse rupture strengths (TRS) of PCD samples were measured by 3-point bend testing using a Shimadzu AGS-X Universal Electromechanical Test Frame (Shimadzu, Japan). PCD beams were cut from PCD materials, lapped and polished to minimize any surface roughness. Beam dimensions were in 13 x 1.6 x 0.8 mm. During testing, beams were positioned symmetrically on two support pins so the loading pin contacted the centre of the beam (figure 7.1). A ball bearing on top removed any

misalignment of the top loading support. This testing configuration enabled mode I fracture. The loading speed was 1 µm/s, which is between the values from several TRS studies on similar PCD materials[1,2].

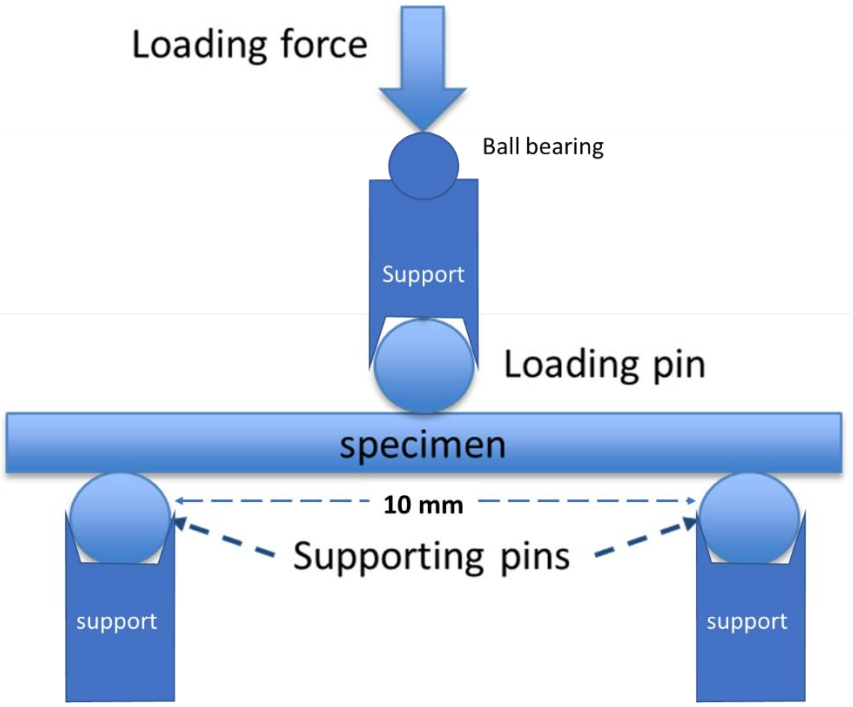


*Figure 7.1: A schematic of the 3-point bend testing setup.*

The force and displacement were recorded during testing. For each type of PCD materials, at least 5 effective results were collected to calculated an average value and a standard error. The TRS is calculated via the equation:

$$\sigma_t = \frac{3FL}{2bd^2}$$

where $\sigma_t$ is the transverse rupture stress, F is the maximum loading during testing, L is the distance between the two supporting pins, b is the width of the beam and d is the depth of the beam. Fractography was performed on the fracture surface of beams to find the potential fracture origin (flaw) via SEM.

Regarding to the data processing, the bend testing result of a PCD beam was marked as effective only if there was no presence of AGGs on the fracture surface of the beam. The presence of AGGs

also introduces significantly larger binder pools. Abnormally large diamond grains, binder pools and their interfaces are possible origins for the largest residual flaws, influencing TRS values[3]. PCD beams with AGGs on fracture surface account for 10.3% (3/29) of the total amount of beams.

#### 7.3.1.2 Vertical Borer Analysis

Vertical borer analysis was used to evaluate the wear resistance of these four samples. It measures the area of the wear scar after grinding PCD materials onto a reference granite wheel with a constant rotation speed for a fixed distance. The rotation speed was 55 rpm with a PCD material feed rate (6.35 mm/rev) driving PCD samples from the edge towards the centre of the granite wheel. The depth of cut was 0.25 mm. A water coolant was employed to dissipate the frictional heat and to maintain the temperature at the PCD-granite contact in the range of 300 - 400 °C while grinding (data from Element Six Ltd). For each type of PCD sample, the analysis was repeated three times to obtain an average value and an error bar. The wear scar was located and measured by optical microscopy. This experiment was performed by staff at Element Six Ltd.

To minimise variations resulting from different granites, a normalization method is adopted to effectively compare the wear resistance of PCD materials tested on different granites. Firstly, a standard cutter is tested on different granites to obtain average wear scar areas $A_s$, $A_1$ and $A_2$ for $granite_{standard}$, $granite_1$ and $granite_2$ respectively. For new $cutter_1$ on $granite_1$, its wear scar area is $A_{c1}$. The normalized wear scar area of $cutter_1$ with respect to the $granite_{standard}$ is then $A_{c1}*(A_s/A_1)$. For another new $cutter_2$ on $granite_2$, its wear scar area is $A_{c2}$ and its normalized wear scar area of is $A_{c2}*(A_s/A_2)$. Therefore, the two normalized wear scars can be compared as though tested with the same reference granite.

## 7.4 Results

### 7.4.1 Evaluation of Mechanical Performance

To assess the mechanical performance of the four samples, the average wear scar area (WSA) and the average transverse rupture strength (TRS) were obtained by 3-point bending tests and vertical borer analysis (VBA) respectively, as shown in figure 7.2.

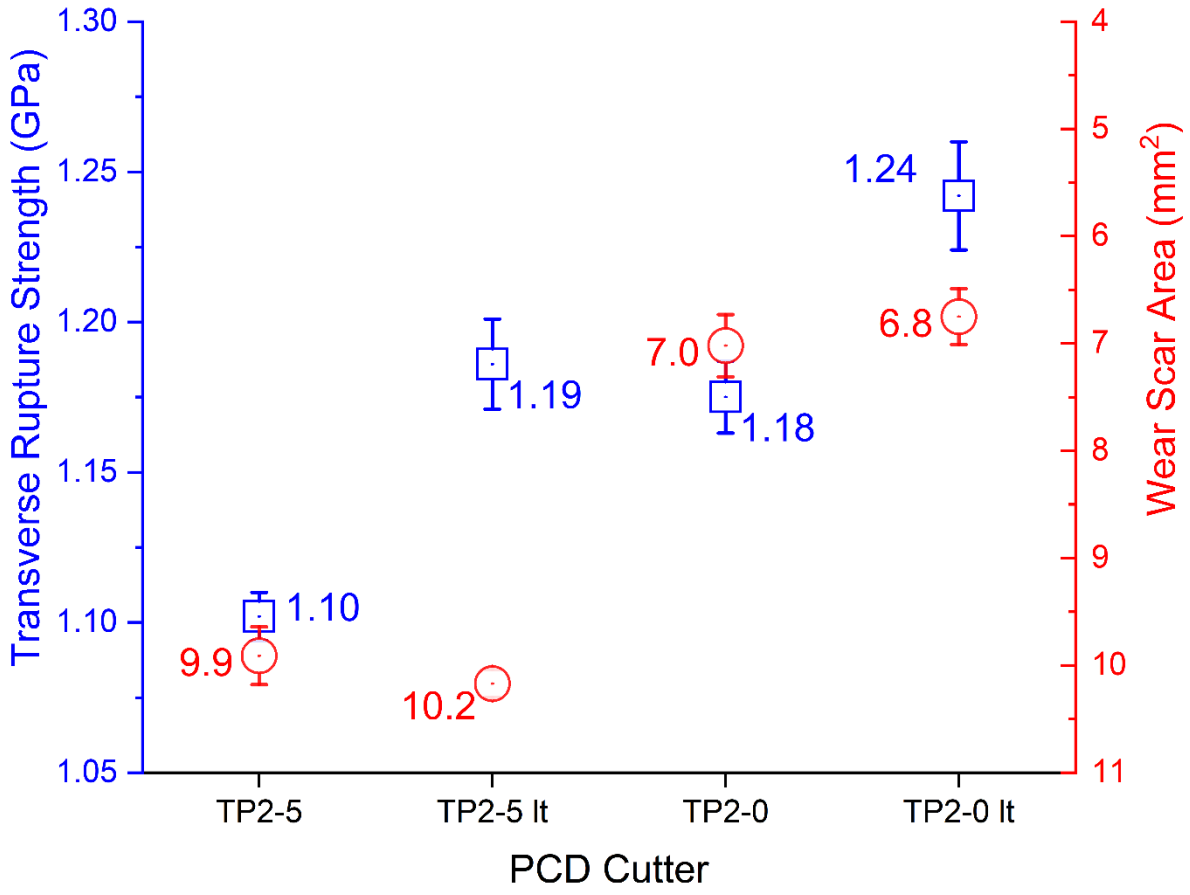


*Figure 7.2: The average TRS and WSA of four samples. The magnitude of the right axis is reversed as the smaller the average wear scar area, the better the wear resistance. TRS results of samples with AGGs were excluded.*

The similarly WSA of both TP2-5 and TP2-5 lt indicate relatively poor wear resistance compared to the lower WSA of TP2-0 and TP2-0 lt. The average WSA increases by over 45% with extra graphite, representing a significant reduction in wear resistance.

Regarding the average TRS, TP2-5 shows the lowest average TRS of four samples, while TP2-5 lt and TP2-0 showed comparable average TRS values. TP2-0 lt displayed the highest average TRS. Due to long dwell, the average TRS increase 7.6% and 5.7% for samples with and without graphite.

Based on the average TRS, the critical crack size can be estimated via the equation[4]:

$$K_{\mathrm{I}c} = \mathrm{Y}\sigma\sqrt{a}$$

where $K_{1c}$ is fracture toughness of samples, Y is the geometry factor ($2.24/\sqrt{\pi}$ for a semi-circular crack[4]), σ is the average TRS and a is the radius of this semi-circular crack. Using the value of $K_{\mathrm{I}c}$ (8.89 MN/m$^{3/2}$) of a PCD material with the same cobalt binder element and similar nominal grain size and substrate[3], the estimated critical edge flaw size for each sample is listed in table 6.1. The critical flaw size of TP2-5 is the largest, corresponding to its lowest TRS value. The critical crack sizes of TP2-5 lt and TP2-0 are similar, whereas TP2-0 lt has the smallest critical flaw size.

| **Sample** | **TP2-5** | **TP2-5 lt** | **TP2-0** | **TP2-0 lt** |
|---|---|---|---|---|
| Estimated critical semi-circular flaw size (μm) | 41±1 | 36±2 | 36±2 | 32±3 |

*Table 6.1: the estimated size of a semi-circular crack for the four PCD samples.*

## 7.4.2 Fracture Surfaces of TRS Beams

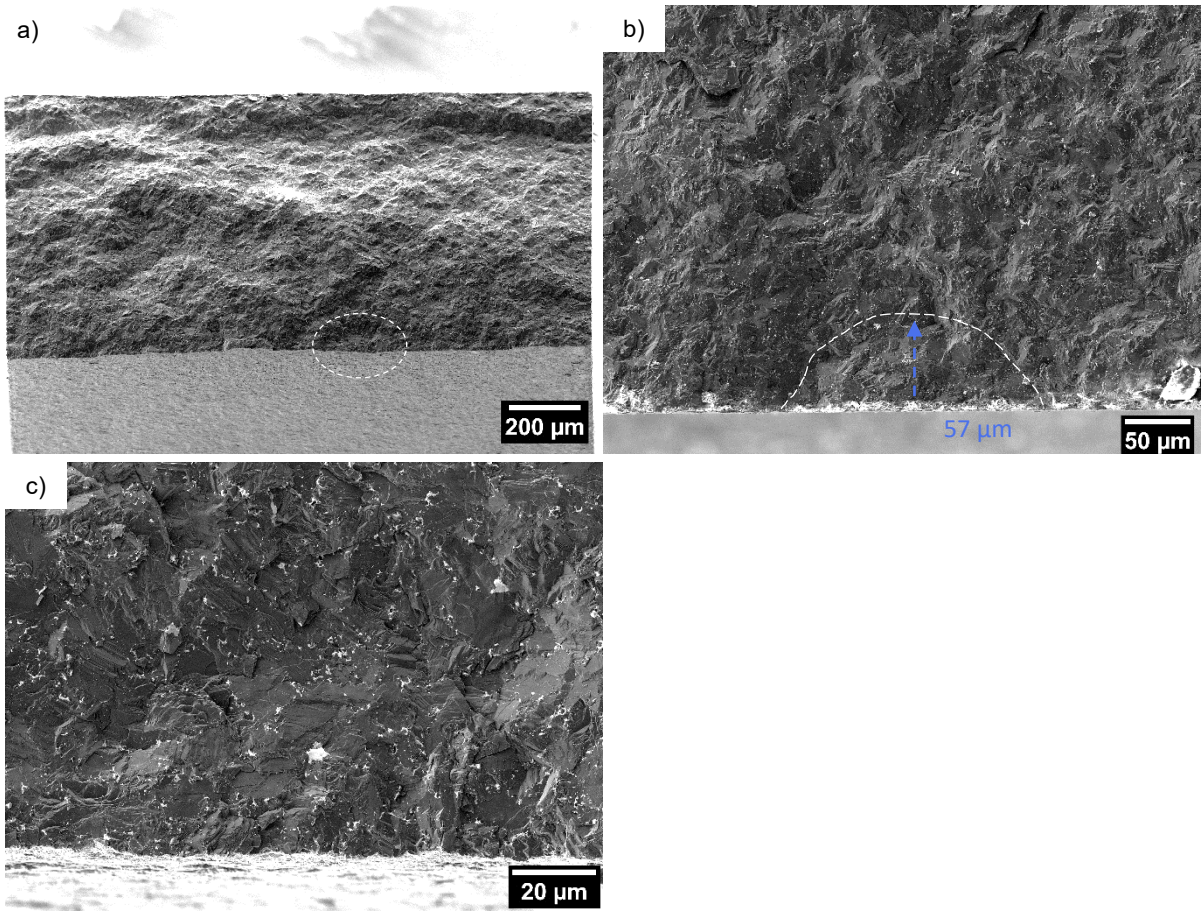


*Figure 7.3: a) An SE2 image of a typical fracture surface of PCD beams (TP2-0 lt) at low magnification. The bottom side was in tension during 3-point bending test. A suspected fracture origin is circled. b) An SE2 image of this suspected fracture origin at 250 x magnification. The white dash line aligns the edge of this fracture origin. c) This suspected fracture origin at 800 x magnification.*

A typical fracture surface is displayed in figure 7.3. No clear fracture mirror is shown on the fracture surface of PCD materials[5]. At low magnification (figure 7.3 a)), the suspected fracture origin exhibits a relatively flat region in the tension side of the PCD beam. At high magnification (figure 7.3 b)), the edge of this suspected fracture origin is roughly outlined by the white dashed line. Its radius is around 57 µm. From the rest of the fracture surfaces, the estimated size of fracture origin ranges from 50 to 70 µm. Though there is a difference between size of fracture origin measured from SEM images and the calculated one, this difference is less than factor of 2 and is probably due to a low toughness from the literature and the inaccuracy of the estimation of size of fracture origin

At 800 x magnification in figure 7.3 c), the features on the fracture surface show no compelling evidence for extensive intergranular fracture, indicating a mixed fracture mode with transgranular

fracture predominating. More importantly, except for the fracture surfaces exhibiting AGGs, the fracture surfaces from different samples all resemble this typical fracture surface, indicating no fundamental mechanisms of fracture between samples.

### 7.4.3 Wear Scars

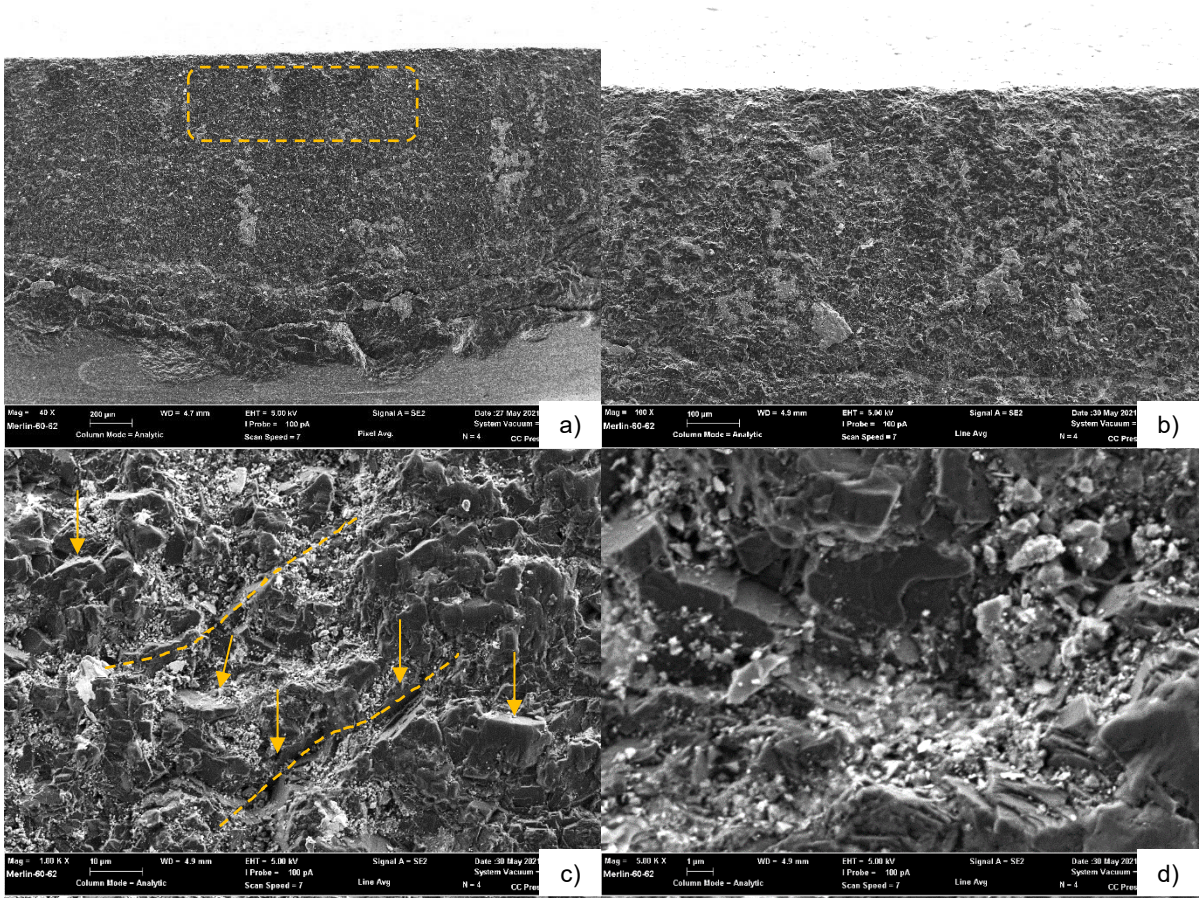


*Figure 7.4: SE2 images of the wear scar of **TP2-0 It** cutters after VBA. a) Overview of the wear scar. b) 100 x magnification. c) 1000 x magnification. d) 5000 x magnification.*

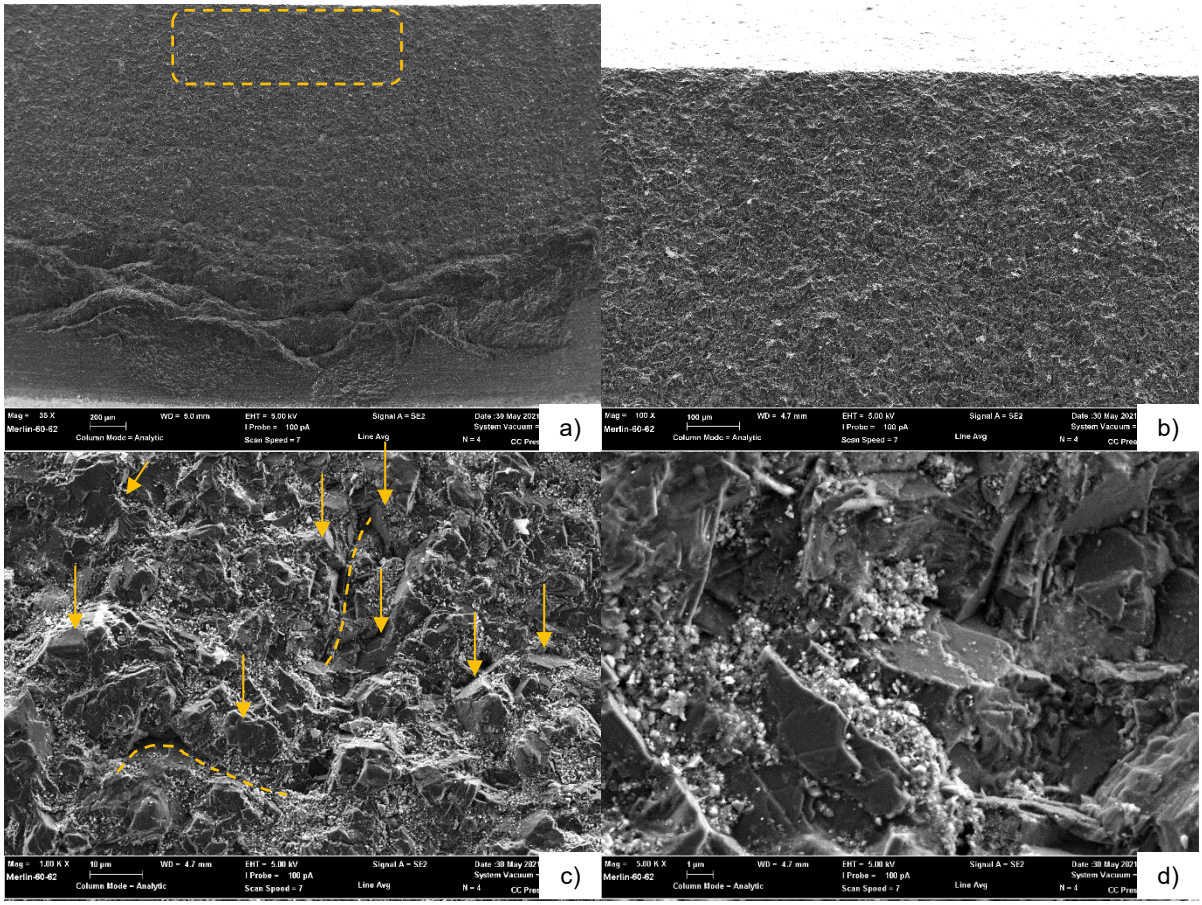


*Figure 7.5: SE2 images of the wear scar of **TP2-5 lt** cutters after VBA. a) Overview of the wear scar. b) 100 x magnification. c) 1000 x magnification. d) 5000 x magnification.*

Figure 7.4 and 7.5 show the top regions (orange boxes) of wear scar of TP2-0 lt and TP2-5 lt, respectively. Their wear scars look similar at all different magnifications. The light grey substances are debris from granite. At low magnifications, both samples show a smooth finish on the top of wear scar in figure 7.4 a) & b) and 7.5) & b), respectively. However, at high magnification in figure 7.4 c) and 7.5 c), some exposed facets, indicated by orange arrows, are visible. Local crack paths spanning several grains (outlined by orange dashed lines) are also located, across several grains. Further magnified (figure 7.4 d) and 7.5 d)), steps are observed on the faceted surfaces.

### 7.4.4 Distribution of Microcracks

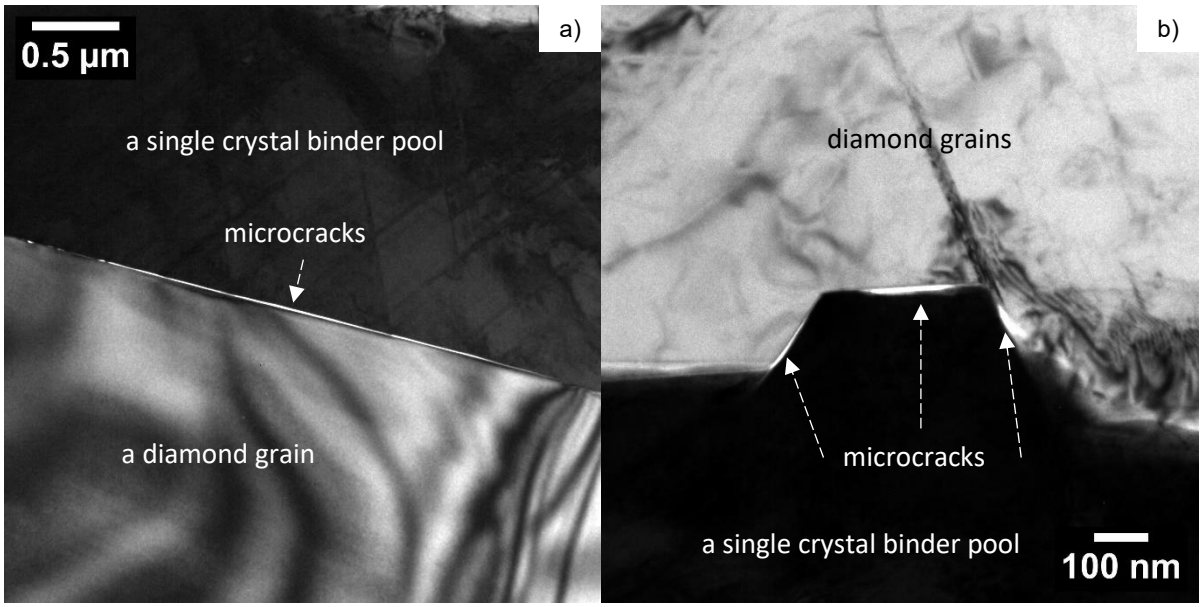


*Figure 7.6: BF TEM images of microcracks along diamond-binder phase boundaries. Microcracks are bright lines as they are hollow in TEM samples. The TEM sample is from TP2-5.*

In figure 7.6, some microcracks were found along the diamond-binder phase boundaries between diamond and relatively large binder pools (> 7-8 µm in length in TEM samples). The length of these cracks ranges from several hundred nanometres to a few microns. However, microcracks were found only along the facetted phase boundaries of large binder pools. No detectable crack was found via SEM or 3D tomography for all four samples.

## 7.5 Discussion: Relationships between Diamond Regrowth and Mechanical Performance

#### 7.5.1.1 DDC and Transverse Rupture Strength

The TRS of PCD materials depends on many factors, including fracture toughness[3], total amount of binder[3], its distribution[3], bonding strength between diamond grains[6] and any other factors affecting the maximum crack size in PCD[7], such as grain size[1,8] and the seldom considered DDC.

From the ICP-OES and 3D tomography results, the total amount of binder is nearly identical for the four samples investigated. The fractography suggests the fracture mode, which is mostly dominated

by bonding strength between diamond grains, and therefore related to the toughness, does not significantly change between the different types of samples. The change of TRS in four samples, therefore, barely relates to these factors.

One difference in the TRS results is between the samples with and without extra graphite. Considering the same sintering profile, the average TRS of samples with extra graphite is lower than samples without graphite, showing a 6.7% difference in TRS between TP2-5 and TP2-0 and a 4% difference between TP2-5 lt and TP2-0 lt.

Their different microstructures caused by the extra graphite may lead to different TRS values. The first difference in microstructure is the total DDC. In figure 6.2 a) and b), there are more diamond-diamond connections in samples with extra graphite, indicating their fracture toughness might be higher which should result in a higher average TRS. However, this contradicts the lower TRS values of both samples with extra graphite.

The second difference in microstructure is the average grain size. The average grain size of samples without graphite is smaller than that of samples with extra graphite. The difference in average grain size between TP2-5 and TP2-0 is 35% and between TP2-5 lt and TP2-0 lt is 25%. According to both Lammer and Petrovic [1,3], TRS of PCD materials is inversely proportional to the square root of the average diamond grain size which is associated with the residual flaw size. Thus, a lower TRS might be related to a large average grain size. Based on the measured grain size for the four samples investigated, this proportion would result in reductions of about 19% and 13% in TRS from TP2-5 to TP2-0 and from TP2-5 lt to TP2-0 lt, respectively, so the simplistic assumption that the critical flaw size is directly proportional to the grain size is more than sufficient to explain the results. It is noted that the estimated critical flaw size is 50% larger than the largest size of diamond grain measured, which indicates that although the critical flaw size may be connected with the grain size, the detailed relationship is more complicated and may not be a direct proportionality.

The last difference in microstructure is the presence and geometries of coarse binder pools with volumes significantly larger than 1 $\mu m^3$, as shown in figure 6.3 a) and b). Though the distribution of small binder particles (< 1 $\mu m^3$) in 3D tomography is similar between the four samples, more coarse binder pools appear in samples with extra graphite and these coarse binder pools are usually with long facets compared to those from samples without graphite. Via TEM (figure 7.6), some microcracks were found along the facetted phase boundary of coarse binder pools. However, in figure 6.2 a) and b), the long facets are usually smaller than the estimated critical crack size, suggesting they are not the dominant factor.

Some may argue the largest binder can act as the critical flaw because its Young's modulus is 20 to 25 % of PCD[9]. This is unlikely, however, as there is no compelling fractography evidence showing the fracture origin as a large binder pool in this study or in the literature.

In conclusion, the TRS difference between samples with and without extra graphite are mostly related to both the average grain size and the presence of facets of coarse binder pools. DDC is not the dominant factor in this case. DDC still might be a potential factor that leads to different microstructures and then different TRS.

However, to find the relationship between DDC and TRS of PCD materials, it is better to compare samples with DDC as the only variable, such as samples dwelled differently. Samples with a long dwell show a higher TRS than those with a standard dwell. The TRS of TP2-5 lt is improved by around 8% compared to TP2-5 and that of TP2-0 lt is improved by around 5% compared to TP2-0.

The only obvious difference in microstructure in this case is DDC changed during dwell, reflected by the different sphericity in figure 6.7. As previously discussed, other factors, including average grain size, fracture surface, the concentration of binder, its distribution, the density and geometries of coarse binder pools, are similar for the samples that underwent different sintering profiles. Thus, the increase of TRS from TP2-0 to TP2-0 lt is attributable to the corresponding increase in DDC. For the

same reason, compared to TP2-5, the potentially increased DDC in TP2-5 lt might lead to the increase in its TRS.

However, it remains unclear how TRS of PCD materials is affected by DDC. One potential explanation is the increase in fracture toughness. As discussed in section 6.5.2, a high DDC can indicate more diamond-diamond connections, which in turn, improves the fracture toughness. Confirming this relationship requires the actual determination of fracture toughness, which is difficult for PCD and was not attempted here because of the time constraint. Another potential explanation is the potential reduction of the size of the largest residual flaw along phase boundaries by the bending or segmentation of the long facetted diamond-binder phase boundaries, correlating to the increase of DDC.

#### 7.5.1.2 DDC and Wear Resistance

Many studies have claimed DDC as the critical feature for wear resistance of PCD materials[10–12], despite the lack of a method to assess DDC.

However, the VBA results here do not indicate a relationship with DDC. The wear resistance of both TP2-0 and TP2-0 lt are nearly identical, while there is a clear difference in their average sphericity, and hence their DDC. Similarly, the long dwell expected to improve DDC of TP2-5 lt does not enhance its wear resistance over TP2-5. Though the extra graphite is usually thought to enhance the wear resistance of PCD materials due to an increase of diamond-diamond connections[11,13], in this study samples with extra graphite do exhibit more diamond-diamond connections, whereas their wear resistances are lower.

Instead, in this study, the average grain size and faceted coarse binder particles appear as the dominant factors that determine the wear resistance of the four samples. TP2-5 and TP2-5 lt show lower wear resistance than TP2-0 and TP2-0 lt. Correspondingly, TP2-5 and TP2-5 lt exhibit larger grain sizes (figure 6.3) and the presence of faceted coarse binder pools (figure 6.2).

The prevalent wear mechanisms of PCD materials include grain pull-out, binder-assisted graphitisation, whole-grain fracture and microchipping [8]. Grain pull-out would produce an intergranular wear surface. Similarly, substantial binder particles along grain boundaries could yield an intergranular wear surface through binder-assisted graphitization, especially for samples without extra graphite. However, the examined wear surfaces in figure 7.4 and 7.5 do not show an intergranular feature, indicating neither mechanism is the dominant one in these four samples. The other two mechanisms are closely related to the size and distribution of flaws, which, as previously discussed, are significantly affected by the average grain size and faceted coarse binder particles. This assertion also aligns with many conclusions from literature[8,14].

In the author's opinion, the relationship between DDC and wear resistance depends on the stage of sintering reached. The assumed relationships between DDC/wear resistance and sintering time are plotted in figure 7.7, in which a special timepoint referring to when the PCD materials become fully dense after binder infiltration but before dwelling, is labelled. Before this timepoint, DDC remains essential to the wear resistance of PCD materials. Akaishi *et al.*[12] attributed the poor wear resistance of PCD materials to weakly bonded bodies due to under-sintering. However, when surpassing this timepoint, although the relatively high DDC could keep increasing slowly via spheroidization, wear resistance barely changes with sintering time because it is now dominated by other factors, such as average grain size and the presence of faceted coarse binder pools. In this study, because all four samples were dwelled for relatively long periods after fully binder infiltration, their wear resistance is no longer linked to their DDC beyond this point.

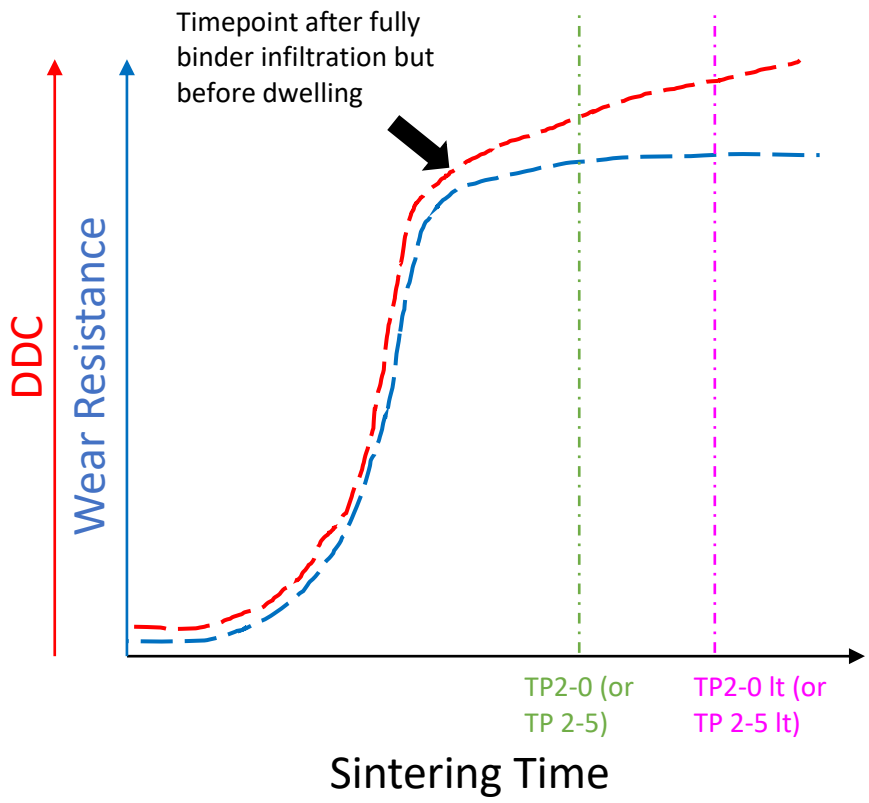


*Figure 7.7: the relationships between DDC, wear resistance and sintering time. Two lines intercepting both the wear resistance curve and DDC curve are marked indicating the sintering time of sample with different dwell time.*

## 7.6 Summary

In light of mechanical testing results and the different DDC from these four samples, the relationships between DDC and TRS/wear resistance of PCD materials were examined.

Although the extra graphite introduces more diamond-diamond connections, then higher DDC, it is determined that both the average grain size and the presence of facets of coarse binder pools are the predominant factors influencing TRS of PCD materials.

However, by comparing TRS of samples with different dwell time, it is claimed that TRS of PCD materials is positively linked with DDC. DDC could increase the fracture toughness and/or reduce the maximum residual flaw size to increase the TRS. More evidence is needed to further elucidate this relationship between DDC and TRS.

DDC could be a secondary factor in wear resistance determination. Other factors, such as average grain size and coarse binder pools, are the primary factors that dominate the wear resistance of PCD materials.

## 7.7 Reference


(1) Petrovic, M.; Ivankovic, A.; Murphy, N. The Mechanical Properties of Polycrystalline Diamond as a Function of Strain Rate and Temperature. *J. Eur. Ceram. Soc.* **2012**, *32* (12), 3021–3027.

(2) Belnap, D.; Griffo, A. Homogeneous and Structured PCD/WC-Co Materials for Drilling. *Diam. Relat. Mater.* **2004**, *13* (10), 1914–1922.

(3) Lammer, A. Mechanical Properties of Polycrystalline Diamonds. *Mater. Sci. Technol. (United Kingdom)* **1988**, *4* (11), 949–955.

(4) Hertzberg, R. W.; Vinci, R. P.; Hertzberg, J. L. *Deformation and Fracture Mechanics of Engineering Materials*.

(5) Quinn, G. D. *Fractography of Ceramics and Glasses*.

(6) Qiu, T.; Feng, J.; Cai, B.; Fan, G.; Zhang, W.; Liu, Y. Microstructural Evolution of Diamond-Based Composites at High Temperature and High Pressure. *Materials (Basel).* **2022**, *15* (24).

(7) Richard W. Hertzberg, Richard P. Vinci, J. L. H. *Deformation and Fracture Mechanics of Engineering Materials*; 2012.

(8) Scott, T. A. The Influence of Microstructure on the Mechanical Properties of Polycrystalline Diamond: A Literature Review*. *Adv. Appl. Ceram.* **2018**, *117* (3), 161–176.

(9) Westraadt, J. E.; Dubrovinskaia, N.; Neethling, J. H.; Sigalas, I. Thermally Stable Polycrystalline Diamond Sintered with Calcium Carbonate. *Diam. Relat. Mater.* **2007**, *16* (11), 1929–1935.

(10) Bellin, F.; Dourfaye, A.; King, W.; Thigpen, M. The Current State of PDC Bit Technology. *World Oil* **2010**, *231* (11), 67–71.

(11) Chen, Z.; Ma, D.; Wang, S.; Dai, W.; Li, S.; Zhu, Y.; Liu, B. Effects of Graphene Addition on Mechanical Properties of Polycrystalline Diamond Compact. *Ceram. Int.* **2020**, *46* (8), 11255–11260.

(12) Akaishi, M.; Ohsawa, T.; Yamaoka, S. Synthesis of Fine-Grained Polycrystalline Diamond Compact and Its Microstructure. *J. Am. Ceram. Soc.* **1991**, *74* (1), 5–10.

(13) Bobrovnitchii, G. S.; Osipov, O. S.; Filgueira, M. Some Peculiarities of the Diamond Micro-Powder Sintering. *Int. J. Refract. Met. Hard Mater.* **2003**, *21* (5–6), 251–258.

(14) Yahiaoui, M.; Paris, J. Y.; Delbé, K.; Denape, J.; Gerbaud, L.; Colin, C.; Ther, O.; Dourfaye, A. Quality and Wear Behavior of Graded Polycrystalline Diamond Compact Cutters. *Int. J. Refract. Met. Hard Mater.* **2016**, *56*, 87–95.

# 8 Conclusions

# Table of Contents



The current work has advanced the understanding in of three key questions related to diamond regrowth in HPHT PCD materials. The key discoveries or answers regarding each question are summarised below:

## 8.1 Identification of Regrown diamond

Criteria based on the distinct crystal defects have been established to identify the regrown diamond

- Orientation-sensitive ARGUS imaging can preliminarily locate the suspected regrown diamond regions due to a reduced misorientation.
- An EBSD based approach can be used to identify the entire regrown grain by determining its Grain Orientation Spread (GOS) value. Diamond grains with a GOS value less than 1° are determined as regrown grains.
- The interface between regrown and old diamond, termed a “distinct contour” in this thesis, can be located by SEM-CL. One order of magnitude of difference in the NV0 CL intensity has been observed on either side of the distinct contour, with the regrown diamond emitting

significantly lower NV0 CL. The NVN centre is a characteristic colour centre for regrown diamond.

- Via TEM imaging, compared to heavily plastically deformed old diamond, regrown diamond is found to contain less or nearly no dislocations.

It is recommended that to fully identify regrown diamond, both EBSD and SEM-CL are required to find both the GB and the distinct contour of regrown diamond.

## 8.2 Mechanisms of Diamond Regrowth

Three regrowth mechanisms, graphite-diamond dissolution-reprecipitation, direct transformation of graphite and classical dissolution and reprecipitation have been confirmed

- It has been found that the graphite-diamond dissolution-reprecipitation mechanism includes an initial step of diamond graphitization via both binder-assisted and binderless processes, followed by graphite dissolution in the binder and epitaxial reprecipitation of carbon atoms to connect individual diamond grains. This regrowth mechanism can be generally described as a diamond-to-graphite-to-diamond process facilitated by the catalytic binder. A detailed model of this regrowth mechanism is proposed.
- Direct transformation of graphite to diamond has also been identified at the diamond-diamond connection via distinctive bent twins formed before the binder infiltration.
- During dwell, the classical dissolution and reprecipitation diamond regrowth is driven by the minimization of interfacial energy which leads to the spheroidization of binder particles and the increase of diamond-diamond connections. These two processes can be described by the sphericity of binder particles. It is revealed that the sphericity increases with the extension of dwell time, indicating the formation of more diamond-diamond connections. However, extra graphite feed reduces sphericity.

- These three mechanisms dominate the diamond regrowth at different stages of sintering. Their relationships have been concluded in figure 6.12.

## 8.3 Relationships Between Diamond Regrowth and Mechanical Performance

- For TRS of PCD materials, long dwell times increase the TRS by forming more diamond-diamond connections to increase toughness and/or potentially reduce the size of the largest residual flaw.
- Extra graphite, which increases the total amount of diamond-diamond connection, leads to a decrease in TRS. This decrease is attributed to the accompanying increase in grain size and possibly the presence of facets of coarse binder pools; both may increase the size of the largest residual flaw.
- No relationship is found between longer dwell times and the wear resistance of PCD materials.
- Extra graphite lowers the wear resistance of PCD materials. The higher average grain size and the higher density of faceted coarse binder particles due to extra graphite are the two factors contributing to this reduced wear resistance.

# Appendix

## Appendix A:

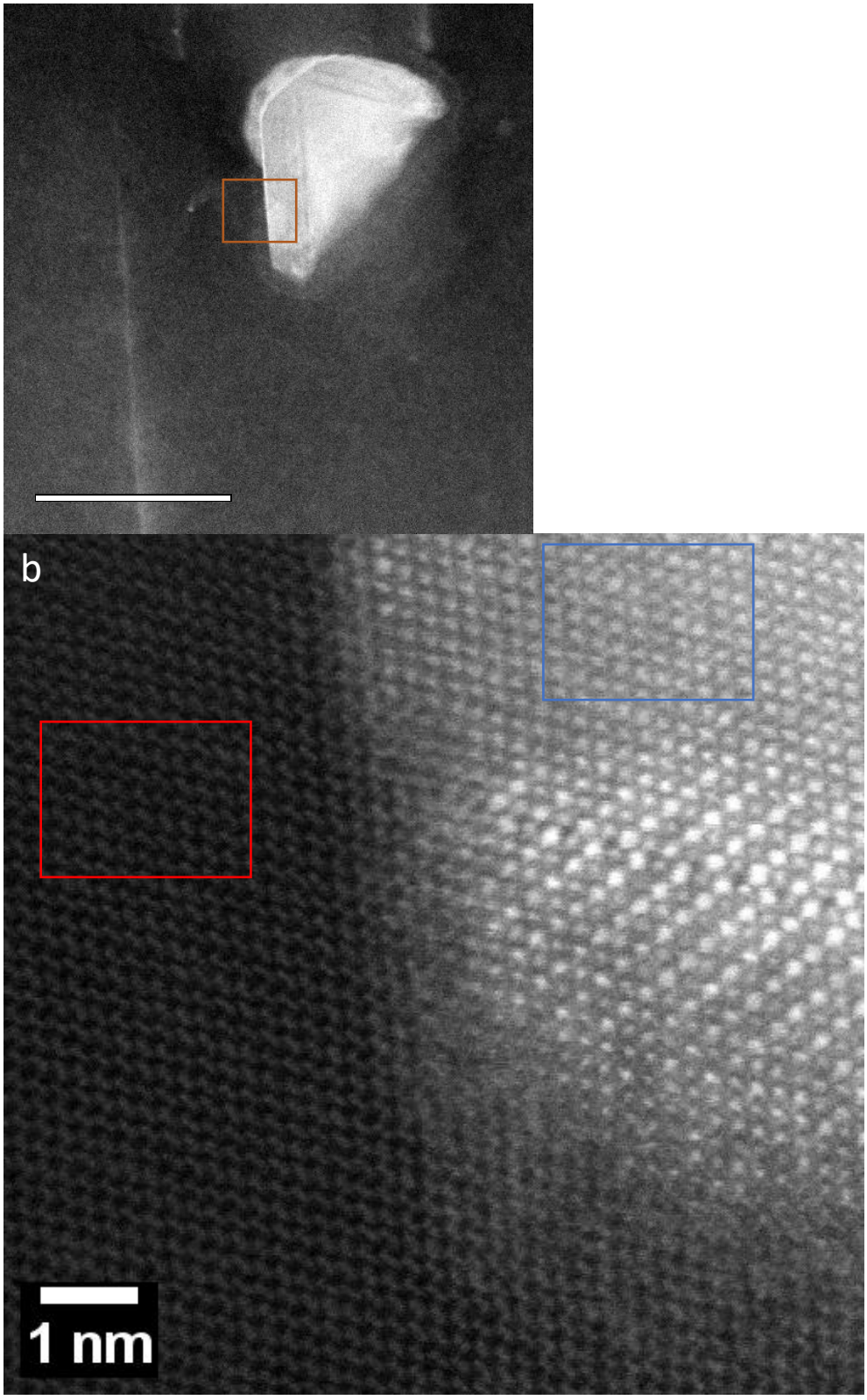

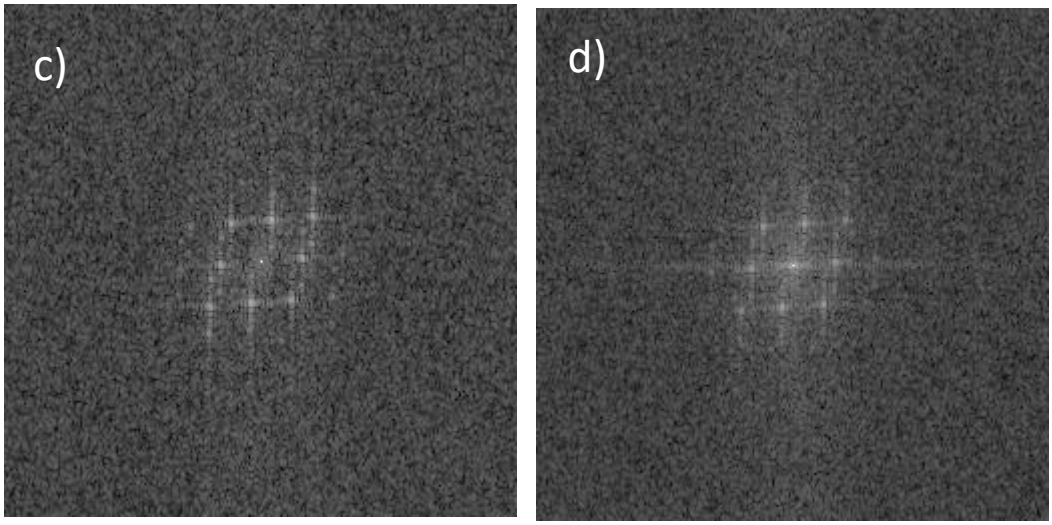


*Figure 1A: a) a LADDF STEM image showing an enclosed binder within its diamond matrix. B) the HRs HADDF image of a diamond-binder interface from a selected region in a). Within binder, the large bright atoms in binder are W and small bright atoms in binder are Co. In diamond, two carbon atoms form the dumbbell shaped motif. (confirmed by STEM EDX). C) the revered fast Fourier transformation from red selected region in b). d) the revered fast Fourier transformation from blue selected region in b). The zone axis is <110>.*

Figure 1A displays a region of regrown diamond with an enclosed binder particle. The HRs STEM image reveals the atomic arrangement near the diamond-binder interface. Two regions were selected for reverse fast Fourier transformation (FFT) to obtain the corresponding diffraction patterns. It is noticed that these two diffraction patterns from different phases, c) diamond and d) binder, are identical. This indicates diamond and the enclosed binder particle share the same orientation. Such alignment explains why DPs overlap when taking a DP from a region including both diamond and the enclosed particle.